REDUCTION OF VIBRATION TRANSMISSION AND FLEXURAL WAVE PROPAGATION IN COMPOSITE SANDWICH PANELS

by

V. V. SATISH K MOTIPALLI

B.E., Andhra University, 2000

M.S., Kansas State University, 2002

AN ABSTRACT OF A DISSERTATION

submitted in partial fulfillment of the requirements for the degree

DOCTOR OF PHILOSOPHY

Department of Mechanical and Nuclear Engineering
College of Engineering

KANSAS STATE UNIVERSITY
Manhattan, Kansas

2015

Abstract

Thin walled structures such as plates and shells have application in many fields of engineering because these structures are light weight and can support large loads when designed suitably. In real world, loads may cause these structures to vibrate which can be undesirable causing fatigue and failure of the structure. Such undesirable vibrations need to be reduced or eliminated.

In this work, analytical studies of flexural wave propagation for idealized geometries are conducted and finite element method (FEM) is used to explore the effects of composite panel designs of finite size for the reduction of vibration transmission.

In the analytical studies, the influence of the material properties on the reflection and transmission characteristics are explored for an infinite bi-material plate, and infinite plate with a strip inhomogeneity. In the analytical study of an infinite thin plate with a solid circular inclusion, the far and near field scattering characteristics are explored for different frequencies and material properties. All the analytical studies presented here and reported in the literature consider infinite plates to characterize the flexural wave propagation. Obtaining closed form solutions to characterize the flexural wave propagation in a finite plate with inclusions is mathematically difficult process. So, FEM is used to explore the composite panel designs. The understanding gained about the material properties influence on the flexural wave propagation from analytical studies helped with the choice of materials for FEM simulations.

The concept of phononic crystals is applied to define the design variations that are effective in suppressing vibration transmission. Various design configurations are explored to study the effects of various parameters like scatterer's material properties, geometry and spatial pattern. Based on the knowledge gained through a systematic parametric study, a final design of

the composite sandwich panel is proposed with an optimum set of parameters to achieve the best vibration reduction.

This is the first study focused on reducing vibration and wave transmission in composite rotorcraft fuselage panels incorporating the concept of phononic crystals. The optimum sandwich panel design achieved 98% vibration transmission reduction at the frequency of interest of 3000 Hz.

REDUCTION OF VIBRATION TRANSMISSION AND FLEXURAL WAVE PROPAGATION IN COMPOSITE SANDWICH PANELS

by

V. V. SATISH K MOTIPALLI

B.E., Andhra University, 2000

M.S., Kansas State University, 2002

A DISSERTATION

submitted in partial fulfillment of the requirements for the degree

DOCTOR OF PHILOSOPHY

Department of Mechanical and Nuclear Engineering
College of Engineering

KANSAS STATE UNIVERSITY
Manhattan, Kansas

2015

Approved by:

Co-Major Professor
X. J. Xin

Approved by:

Co-Major Professor
Liang-Wu Cai

Copyright

Abstract

Thin walled structures such as plates and shells have application in many fields of engineering because these structures are light weight and can support large loads when designed suitably. In real world, loads may cause these structures to vibrate which can be undesirable causing fatigue and failure of the structure. Such undesirable vibrations need to be reduced or eliminated.

In this work, analytical studies of flexural wave propagation for idealized geometries are conducted and finite element method (FEM) is used to explore the effects of composite panel designs of finite size for the reduction of vibration transmission.

In the analytical studies, the influence of the material properties on the reflection and transmission characteristics are explored for an infinite bi-material plate, and infinite plate with a strip inhomogeneity. In the analytical study of an infinite thin plate with a solid circular inclusion, the far and near field scattering characteristics are explored for different frequencies and material properties. All the analytical studies presented here and reported in the literature consider infinite plates to characterize the flexural wave propagation. Obtaining closed form solutions to characterize the flexural wave propagation in a finite plate with inclusions is mathematically difficult process. So, FEM is used to explore the composite panel designs. The understanding gained about the material properties influence on the flexural wave propagation from analytical studies helped with the choice of materials for FEM simulations.

The concept of phononic crystals is applied to define the design variations that are effective in suppressing vibration transmission. Various design configurations are explored to study the effects of various parameters like scatterer's material properties, geometry and spatial pattern. Based on the knowledge gained through a systematic parametric study, a final design of

the composite sandwich panel is proposed with an optimum set of parameters to achieve the best vibration reduction.

This is the first study focused on reducing vibration and wave transmission in composite rotorcraft fuselage panels incorporating the concept of phononic crystals. The optimum sandwich panel design achieved 98% vibration transmission reduction at the frequency of interest of 3000 Hz.

Table of Contents

List of Figures

List of Tables

Acknowledgements

I would like to first express my deepest gratitude to my advisors, Dr. X.J. Xin and Dr. Liang-Wu Cai, for their technical guidance, invaluable suggestions and constant support. I would like to thank Dr. Bradley Kramer, Dr. Daniel Andresen and Dr. Shuting Lei for serving on my supervisory committee. My special thanks to Dr. Brian Washburn for serving as an outside chairperson. I would like to thank Dean Dr. Carol Shanklin for her guidance in completing the paperwork needed for the graduate school.

I would like to thank late Dr. Prakash Krishnaswami who has inspired me to continue my education after finishing Master's degree under his guidance. I thank Dr. Kirby Chapman for giving me an opportunity to work at National Gas Machinery Laboratory as an Information Technologist. I would also like to extend my thanks to Advanced Manufacturing Institute for providing me financial support through graduate research internship. I would like to thank Department of Mechanical and Nuclear Engineering for providing me financial support through teaching assistantship.

I thank Dr. Tim Bremner, my past supervisor, at Hoerbiger Corporation of America for providing me the support necessary to complete the dissertation. I would also like to extend my special thanks to Mr. Bruce Driggett, Mr. Christoph Magnet, Mr. James Findlay, and Mr. Daniel Westwood for facilitating the extended leave of absence for me to come back to school to finish my dissertation. My special thanks all my colleagues at Hoerbiger for their support. I thank Mr. Rainer Ponzel for giving me the first job opportunity to work at Hoerbiger Corporation as Technical Specialist.

I would like to thank my parents and brother for their unconditional love, encouragement and support throughout my life. I am grateful to my wife, Sunitha, for her support, cooperation

and being there for me whenever needed. It is quite unthinkable that I could have accomplished this without her support. I thank my in-laws for their support.

I thank all my friends especially Shekhar, Jeet, Seemanti, and Shilpa for their support and companionship during and after my stay at KSU. I owe my very special thanks to Lakshmi, Dr. Pagadala and their kids (Abhinav and Ananya) for welcoming me and Sunitha into their home. I would also like to thank Anupama, Praveen, Samatha and Harish for making my stay at KSU a pleasant one. I appreciate the faculty families Muthukrishnan's, Krishnaswami's and Pahwa's for welcoming us (me and Sunitha) into their homes, helping and advising us whenever needed.

Finally, I would like to thank Sherry, Carol, Heather, Mitzi and every one in Mechanical and Nuclear Engineering for their support.

Dedication

To

My wife,

parents, and teachers.

1 Introduction

1.1 Background

Thin walled structures such as plates and shells have applications in many fields of engineering. The wide spread use of thin plates and shells is attributed to their intrinsic properties of high load bearing to weight ratios. These properties of the structures make them suitable for building structures in aerospace, automotive, and civil and mechanical engineering applications where lightweight of the structure is critical [1].

In the real world, loads may cause the structures to vibrate and transmit sounds. In some cases the vibration is undesirable, causing fatigue, performance degradation or even failure. Such vibrations need to be reduced or be eliminated. In other cases the vibration of the structures could be desirable like the sounds radiated by vibrating musical instruments [2, 3]. Most sound radiated by vibrating thin structures like beams, plates and shells is caused by bending or flexural waves in the structures. Flexural waves deform the structure transversely and cause the cross sections of structure to rotate about the neutral axis as shown in Figure 1.1.

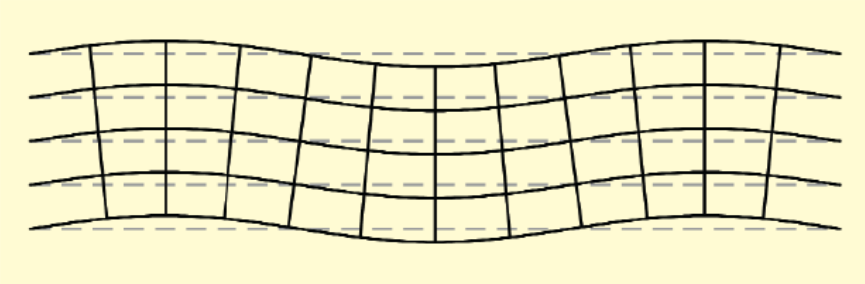

Figure 1.1: Ref. [4] – A flexural, bending wave propagating through a thin plate or beam (amplitudes highly exaggerated)

Flexural wave propagation is far more complicated as the speed of the wave depends not only on the material properties (Young's modulus, density) but also on the cross-sectional

geometry. In addition, the speed of the flexural waves are dispersive and vary with the frequency of oscillation [2, 4].

1.2 Literature Review

Over the years various approaches have been investigated for vibration reduction and isolation. In this section, the conventional vibration reduction approaches, and their relative advantages and disadvantages are discussed. A new approach, the concept of phononic crystals for vibration reduction will be presented. Phononic crystals with local resonance and the associated bandgaps are identified as good candidates for blocking or filtering dynamic disturbances such as sound insulation and vibration damping. The literature review of both analytical and experimental work concerning phononic crystals for vibration reduction is discussed.

1.2.1 Vibration Reduction/Isolation

Vibration reduction management can be broadly divided into two forms: isolation and damping. Isolation is the prevention of vibrations from entering the system, and damping is absorbing and dissipating the vibration energy in a different form of energy such as heat. Although these are different forms, they often are used in conjunction to achieve the desired performance [5, 6].

Numerous approaches have been investigated for vibration reduction over the years. These approaches can be broadly be classified into passive and active categories. In active vibration control, the vibration is detected through a sensor, and the signal is then inverted, amplified and fed back to the actuator to reduce the vibration. Passive vibration reduction is achieved through using passive techniques such as using rubber pads, mechanical springs, foams, etc. In general passive methods are effective at higher frequencies where the dimensions of the

components are comparable with the wavelength of the vibration. Active methods, on the other hand, are effective at lower frequencies where the wave lengths of the vibration are large relative to the size of the structure. The choice of method for vibration reduction is different for different applications, depending on the frequency, direction, and magnitude of vibrations present and the desired level of attenuation of those frequencies [7-9].

One of the common and simple vibration reduction methods is to use visco-elastic material (VEM) and attach it to the component surface using a strong bonding agent, heat treated or bolted as shown in Figure 1.2. This is referred to as free-layer or extensional damping and is a passive method. Several types and shapes are available; some are adhesive in nature, and some enamel. The principle is that the energy is dissipated as a result of extension and compression of the damping visco-elastic material under flexural stress from the base structure as shown in Figure 1.2.

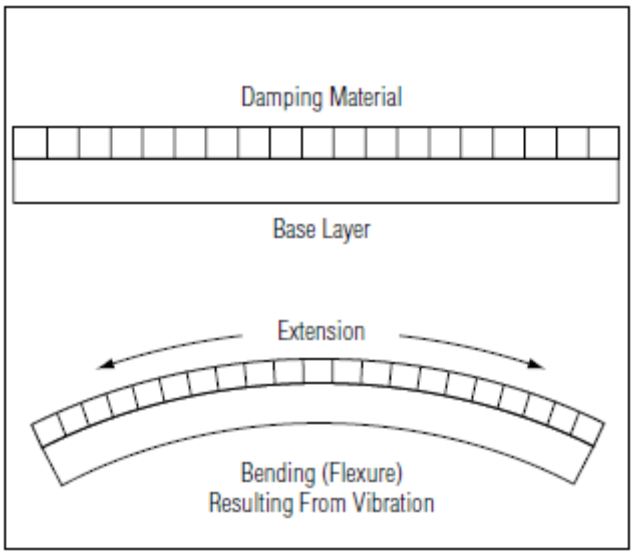

Figure 1.2: Ref. [6] - Free layer damping

Another method is constrained layer damping (CLD), generally used for stiff structures. In this method, the visco-elastic material (damping layer) is sandwiched between a base structure and the constraining layer, and the energy is dissipated through the shear deformation within the visco-elastic layer when the system vibrates as shown in Figure 1.3.

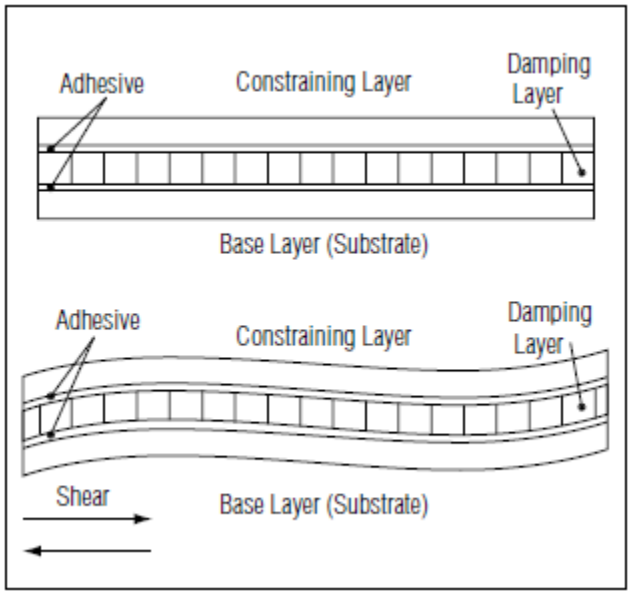

Figure 1.3: Ref. [6] – Constrained layer damping

The embedded layer damping method is very similar to CLD except that the visco-elastic layer is embedded in the component somewhere. This method has gained interest especially as the composite materials are being widely used which have the ability to co-cure the visco-elastic materials. Studies have shown that the post cured visco-elastic materials retain more damping capability than when co-cured along with the composite because of the penetration of the VEM in the composite matrix [10, 11].

Magnetic constrained layer damping (MCLD) uses the damping layer consisting of specially arranged network of permanent magnets. This method has shown improved damping characteristics compared to conventional passive constrained layer damping because of the attraction in the magnetic layers [12].

In the active vibration control, a built-in sensor, monitors the dynamic changes of the structure and converts the changes into electric signal. This electrical signal is then passed through a control system which implements the control law and generates a modified signal. This modified signal is passed to the actuator by developing control forces to maintain desirable performance. A general layout of an active control system with a sensor and an actuator is shown in Figure 1.4. Piezoelectric materials are commonly used as the sensors and actuators which are integrated into the flexible structure. Over the years, various control techniques and different feedback algorithms have been developed (such as coupled control, independent control, model space control methods) [11].

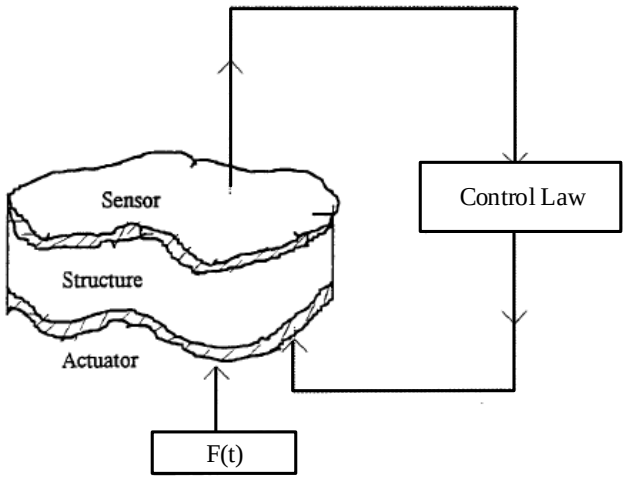

Figure 1.4: Ref. [13] - General layout of an active control system with a sensor and an actuator

Some hybrid approaches also have been developed which exploit the best from both the passive and active vibration control methods. Active constrained layer damping (ACLD) is one such method where visco-elastic damping layer is sandwiched between two piezoelectric layers. The first layer is directly bonded to the plate to sense its vibration and the second layer acts as an

actuator to actively control the shear deformation of the damping layer according to the plates response as shown in Figure 1.5.

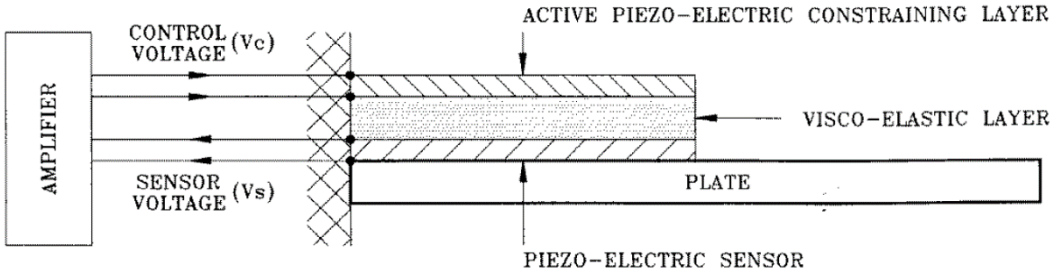

Figure 1.5: Ref. [14] - Active constrained layer damping

Another method is intelligent constrained layer (ICL) where the vibrating plate is treated with a visco-elastic damping layer constrained by a piezoelectric film which is utilized to generate additional damping. The vibration response of the structure is measured and is passed to the controller. The feedback controller regulates the in-plane deformation of piezoelectric layer to perform active vibration control [12].

Each of the active and passive methods have their own advantages and disadvantages. The active methods show high performance especially at the low frequencies and are adaptable. The active methods require power and could de-stabilize the system by adding power rather than dissipating. Implementing active control systems is expensive and more complex compared to the passive systems. The passive systems are more efficient at high frequencies and are stable. Passive systems are low cost solutions and require no power to operate. But these systems add more weight to the base structure and require more space in general. Hybrid methods take advantage of the best from both worlds. So, these achieve vibration reduction for a broader range of frequencies, and provide high vibration reduction to the weight ratio [7].

1.2.2 Phononic Crystals

Metamaterials are artificially fabricated materials that are designed to control, direct, and manipulate sound waves as might occur in gases, liquids, and solids. Acoustic metamaterial ideas was originally proposed by Veselago in 1967 [15], but not realized until some 33 years later. Pendry produced the basic elements of metamaterials during the last part of the 1990s [16]. These materials were combined to realize negative index materials first in the year 2000 and 2001 which produced a negative refraction thereby broadening possible optical and material responses. The research in acoustic metamaterials has the goal of broader material response with sound waves.

Acoustic metamaterials are also referred to as sonic or phononic metamaterials. The phononic metamaterials that are periodically structured with an assembly of at least two different materials is defined as phononic crystal (PC). A phononic crystal is essentially made of inclusions arranged periodically in a propagating medium (or matrix). For example a two dimensional phononic crystals arranged in a triangular lattice and square lattice is shown in Figure 1.6.

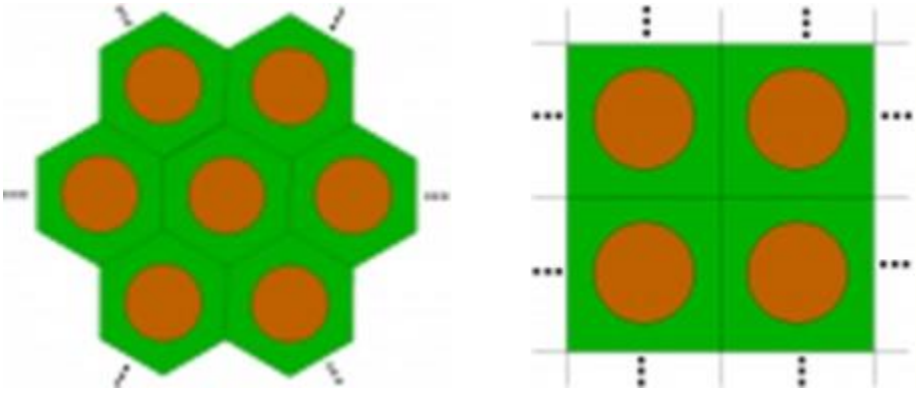

Figure 1.6: Ref. [17] - Two dimensional phononic crystal in triangular lattice (left) and square lattice (right) arrangements

A real phononic crystal sculpture shown in Figure 1.7, composed of a two dimensional periodic arrangement of steel tubes by Sempere sits in a park in Madrid became a basis for study of phononic crystal [17]. In 1995, Meseguer and colleagues determined experimentally the aural filtering properties of the sculpture, by disposing microphones around the sculpture. Their measurements showed that attenuation occurs at certain frequencies, a phenomenon that cannot be explained by absorption, since the steels tubes are extremely stiff and behave as very efficient scatterers for sound waves [17].

Figure 1.7: Ref. [17] - Sculpture by Eusebio Sempere (1923-1985), Madrid, Spain

Early work in phononic crystals can arguably be traced back to the beginning of the 1990's with the publication of papers by Sigalas and Economou at the University of Heraklion in Crete (Greece), and by Kushwaha et al. at the University of Lille in France [17]. John and Rangarajan [18], Economou and Zdetsis [19] worked on the localization of classical waves and pointed out the possible connection of localization with the existence of gaps in the spectrum of periodic inhomogeneous medium. It was observed that these gaps in the spectrum and the localized states were found as the medium is gradually introduced with a disorder in terms of the

position, geometry and the composition. Sigalas and Economou [20, 21] have first shown in 1992 that frequency gaps do appear for elastic and acoustic waves, propagating in structures consisting of identical spheres placed periodically within a host material.

Phononic crystals in a matrix with high impedance contrast of mass densities and/or elastic moduli will give rise to new acoustic dispersions and band gaps. Regions of frequency where there is a strong attenuation or forbidding of wave propagation are called as the band gaps or forbidden gaps. These band gaps occur due to two mechanisms: the Bragg scattering and the existence of local resonances [22]. In the local resonance mechanism, the bandgaps are resulted because of the local resonances that are induced by the inclusions. At resonance, the energy of the waves propagating in the matrix can be efficiently stored and delayed [23].

In Bragg's scattering mechanism, the band gaps originate from the multiple interference of the waves scattered by the periodicity of the inclusions (also referred as scatterers). Because of the periodic distribution of the inclusions, these interferences can be either constructive or destructive depending on the frequency of the waves. Figure 1.8 and Figure 1.9 show the constructive and destructive interferences of the reflected waves respectively.

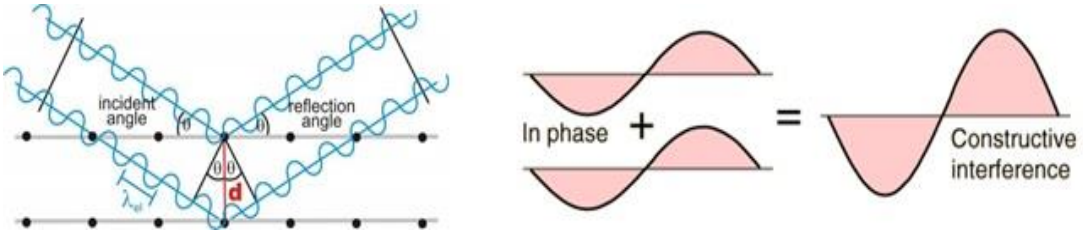

Figure 1.8: Constructive interference

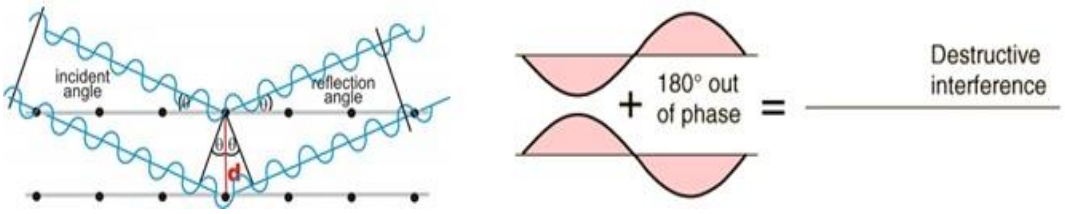

Figure 1.9: Destructive interference

In the case of destructive interferences, the waves are strongly attenuated or forbidden as they travel through the phononic crystals and this phenomenon is called formation of band gaps. The existence of band gaps that forbid the propagation of waves with any polarization and propagation direction suggests the possibility to manipulate the energy flows in the associated frequency ranges. Moreover, diversity and complexity of the wave behaviors have attracted great efforts to investigate the acoustic band-gap phenomena in various phononic crystal structures [17, 24].

Tuning of band gaps of phononic crystals is strongly dependent upon the structural geometries of phononic crystals, including the scatterer's shape, lattice form, filling fraction, and the material differences between the scatterer and the matrix [25-28].

Many researchers have explored the wave attenuation in phononic crystals. Pichard et al. [29] reported the study of the acoustic propagation in two dimensional sonic crystal made of square shape scatterers. The results showed that scatterer rotation in the unit cell influences the band gap width and demonstrated the efficiency of this type of sonic crystal as tunable crystal in the audible frequency range. Zhou et al. [30] studied the material parameters (mass density ratio, shear modulus ratio, Poisson's ratios) of the scatterer and matrix materials effects on the band gap formation for different filling fractions. The results showed that the density ratio had a bigger impact for the anti-plane mode, while the density ratio and the shear modulus ratio had big impact on controlling the band. Band structure has been investigated for a phononic crystal

with a periodic array of cylindrical dots with different shapes such as circular, square, and rotated square deposited on a homogeneous membrane [31].

Hsu et al. [24] explored the elastic wave propagation in phononic crystal strip cut from silicon phononic crystal plate with square lattice vacuum holes. The influence of different cuttings is studied and observed to be crucial for the band gap formation through analyzing the band structure and transmission spectra. Shen and Cao [32] explored the band gap formation using a layered structure of finite size as a medium using the multiple periodicity and acoustic impedence difference as factor for engineering. Two different materials with large acoustic impedance difference are considered. An experimental set-up using glass plates and water is used. The results were compared with analytical solution formulated using transfer matrix technique. It was observed that by changing the dimensions and type of materials used in the structure, the acoustic band-gap engineering concept of using multiple periodicity can be generalized to higher or lower frequency ranges.

Shen and Cao [33] reported bandgap formation in a periodic structure with unit cells containing two, four and six sub layers of different thicknesses. Two different types of materials (water and glass) were used for this study. Transfer matrix method and Floquet's theorem were used to derive the dispersion relation for the acoustic wave propagation and these results were verified with the experimental measurements. The results showed that narrow passbands are produced when the unit cell is subdivided into more than four sub layers. The ratio of the total stopband width versus passband width increases significantly from the case of two sublayer cells to the case of six sublayer cells.

Ye and Hoskinson [34] reported the acoustic bandgap and localization in a 2D system of air cylinders in water, with comparison to the complete acoustic band gap of the corresponding

regular arrays. The numerical calculations predicted that the localization is relatively independent of the precise location or the organization of the scatterers. The localization occurs within the region of frequencies, coincident with the complete bandgap predicted by the conventional bandgap structure for periodic lattice of scatterers calculations.

The work reported by Zhang et al. [35], studied the evidence of surface acoustic wave band gaps in phononic structures in thin plates. The phononic crystals were manufactured by patterning periodic air-filled holes in thin plates. In this study, a laser ultrasonics instrument was utilized to characterize the surface acoustic wave band properties of the phononic crystals. Wide multiple surface acoustic wave band gaps were evident in the experiments, together with some special band structures, such as narrow pass bands within certain band gaps. Flexural wave propagation and vibration transmission in a locally resonant thin plate with a 2D periodic array of attached spring–mass resonators was studied by Xiao et al. [36]. The well-known plane wave expansion method was extended to treat such a periodic plate system containing lumped resonant elements, and to calculate the imaginary part of Bloch wave vectors that can be used to quantify the wave attenuation performance of band gaps. Vibration transmission in finite locally resonant plates was examined using the finite element method. The presence of vibration transmission gaps in finite LR plates confirms the existence of band gaps predicted by the plane wave expansion method.

Flexural vibration band gaps are studied in a thin epoxy plate with periodic square array of lead discs hemmed around by rubber [37]. The band structures are calculated theoretically using a periodic expansion by means of the Bloch theorem. The numerical results showed that the full band gaps of flexural vibration do exist in the thin plate. These results are compared to the band gap results in a thin steel plate and concluded that the width of the first full band gap is

rather larger in the thin epoxy plate than in the thin steel plate. The results showed that the frequencies of band gap decrease as lattice constant increases but increase as the thickness increases.

Pennec et al. [38] worked on two-dimensional bulk phononic crystals i.e. two-dimensional arrays of inclusions assumed of infinite extent along the three spatial directions. A square array of carbon cylinders embedded in an infinite epoxy background is considered. Results showed that the bandwidth of the forbidden band depends strongly on the nature of the constituent materials (solid or fluid), as well as the contrast between the physical characteristics (density and elastic moduli) of the inclusions and of the matrix, the geometry of the array of inclusions, the inclusion shape and the filling factor of inclusions. This research also reported on filtering and multiplexing of acoustic waves. For a solid/solid set-up two-dimensional phononic crystal composed of steel cylinders in epoxy is considered. Acoustic waveguides and resonators were created in this structure by removing cylinders. A waveguide with a sharp bend appears to transmit acoustic waves without significant loss over most of the passing band of a linear guide.

El-Naggar et al. [39] theoretically investigated bandgaps of phononic crystals with square steel rods embedded in epoxy matrix super cell plane wave expansion method. Comparison analysis with circular cross section steel rods was also presented. The results showed that the band gaps can be tuned by the variation of the shape of the rods, the lattice structure, the filling factor and the plate thickness. A comparison between square and circular cross sectional rods reveals that the former has superior normalized gap width than the latter in case of a square lattice. This situation is switched in case of a triangular lattice.

Yao et al. [40] studied flexural vibration band gaps formation in a ternary locally resonant phononic crystal in a thin plate using the improved plane wave expansion method. The

effects of various physical and geometric parameters have been studied. Parameters studied in this work are density, elastic modulus, filling ratio with the goal of finding the lower and wider frequency bang gap. The ternary phononic crystal considered in this study is steel rods covered with rubber in concrete plate. Numerical results showed the existence of band gaps and also showed that the band gap is strongly dependent on the filling fraction, radius ratio, the mass density and the Young's modulus contrasts between the core and the coating.

Liu et al. [41] showed that the effective mass densities can become negative close to local responses. An analytical model was developed for a low frequency wave propagation for composite materials that exhibit band gap dues to resonance. Both 2D and 3D systems were considered in this work. The 3D system consisted of hard spheres each coated with a soft material embedded in matrix material. In the 2D system, three component composite model with concentric hard cylinders coated with soft material was embedded in matrix material. The results showed that the band gap regions disappear if the coated layer is replaced with a stiffer material instead of the soft material. Huang et al. [42] showed that a metamaterial containing multiple microstructures with a spectrum of local resonance frequencies provides the capability of drastically reducing the magnitude of stress waves generated by dynamic sources. Research reported by Lee et al. [43] fabricated a new acoustic metamaterial that exhibits negative mass density at zero and near zero frequencies. This structure blocked acoustic waves below a critical frequency *of* 735 Hz. This material allowed continuous control of mass density by varying the external parameters. The authors believed that this materials can play an important role in achieving acoustic cloaking and acoustic super lensing.

Lee et al. [44] presented an acoustic metamaterial that exhibits a negative effective modulus in a frequency range from 0 to 450 Hz. The metamaterial considered in this work is a

one-dimensional acoustic metamaterial with an array of side holes on a tube. Some studies have reported phononic crystals that exhibit negative effective modulus and achieved wave attenuation in certain frequency ranges [44, 45]. The work reported in [46] demonstrated a phononic crystal possessing simultaneously negative bulk modulus and mass density.

Tailored phononic crystals can be used in a wide range of applications. For example, the phononic crystals can be used as acoustic isolators to reflect all the incoming sound waves within certain frequency ranges. Some preliminary results based on the explorations of new designs for highway noise barriers based on the phononic band gap phenomenon were published in [47]. Introduction of defects within the phononic crystal allows sound waves within the frequencies of bandgap formation to be trapped or guided along the defects as shown in Figure 1.10. These guided defects are called wave guides as they will lead to develop selective frequency filters [38, 48]. Kafesaki et al. [49] calculated the elastic wave transmission through a straight wave guide created in a two-dimensional phononic crystal by removing a row of cylinders. Some other applications are ambient sound shielding, sound and vibration protection devices, acoustic lasers, perfect acoustic mirrors, shock proofing, slow wave effects, acoustic imaging, acoustic cloaking, etc. [44]. Figure 1.11shows the phononic crystals used as wave traps and acoustic mirrors.

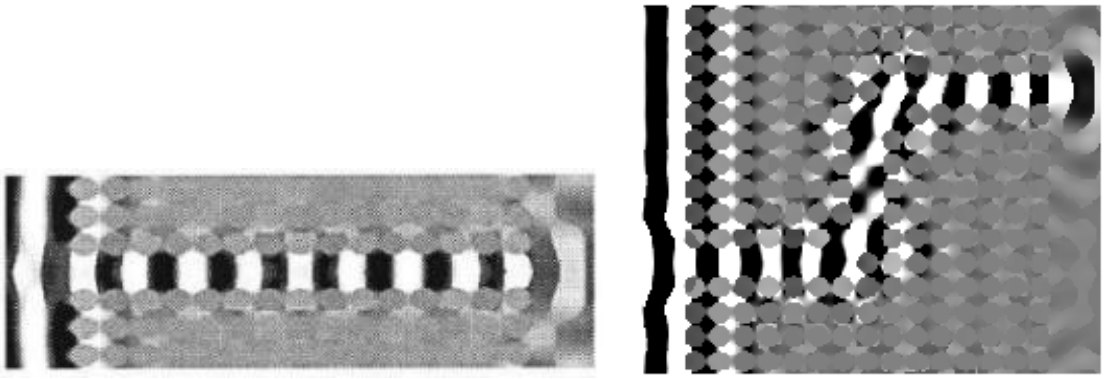

Figure 1.10: Linear wave guide (left) and bent wave guide (right)

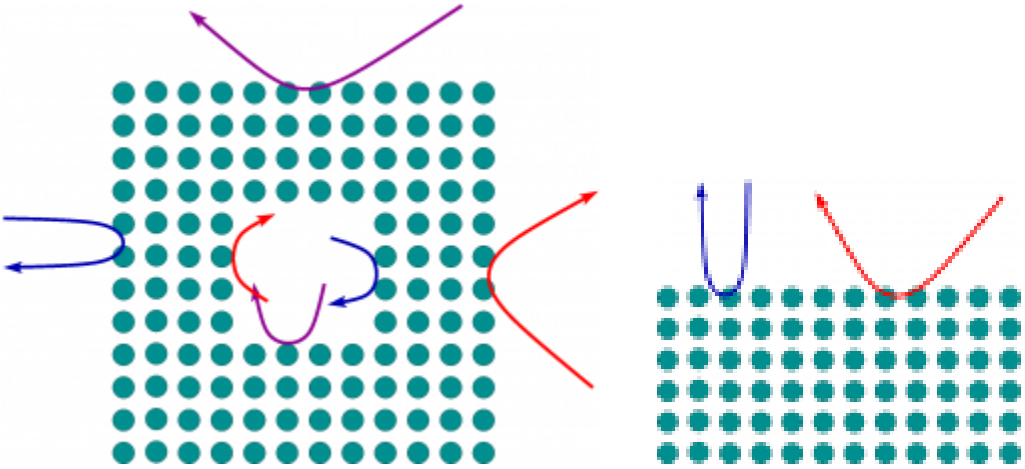

Figure 1.11: Phononic crystals used as wave traps (left) and acoustic mirror (right)

All the work reported in the literature, both analytical and experimental show that phononic crystals with local resonance and the associated bandgaps form good candidates for blocking or filtering dynamic disturbances such as sound insulation and vibration damping [22, 50]. The material properties and the geometrical configuration of the scatterers affect the wave propagation in the host, and their proper combination helps minimize vibration transmission. This work is focuses on the effects of the controlling parameters including scatterers material properties, geometry, and spatial pattern on vibration reduction in a finite sandwich panel. The phononic crystal concept is applied as a guiding principle to define various design configurations of sandwich panel that are effective in suppressing vibration transmission.

1.3 Motivation

Large structural roof panels in commercial and military rotorcraft fuselages are mechanically interconnected with the transmission, allowing strong gear meshing tones emanating from the transmission to pass into the panels and radiate into the cabin. Also, sound

radiated directly by the transmission housing impacts the ceiling panels, which transmit a portion of that sound into the interior. Composite sandwich panels are used for these roof panels because of their lightweight. Though the composite panels help reduce weight, they lead to increased sound radiation. Traditionally layers of foam and thin plates are attached to these composite panels to reduce the sound transmission, make the panels bulky, heavy and expensive [51].

A new method of vibration reduction to reduce vibration and sound transmission is explored in this study. The concept of sonic crystals will be incorporated to design an optimum composite roof panel that will achieve the best vibration reduction.

1.4 Research Objective

In this work, analytical studies of flexural wave propagation for idealized geometries are conducted and finite element method (FEM) is used to explore the effects of composite panel designs of finite size for the reduction of vibration transmission and flexural wave propagation.

In the analytical studies, the influence of the material properties on the reflection and transmission characteristics are explored for an infinite bi-material plate, and infinite plate with a strip inhomogeneity. In the analytical study of an infinite thin plate with a solid circular inclusion, the far and near field scattering characteristics are explored for different frequencies and material properties. All the analytical studies presented here and analytical formulations reported in the literature consider infinite plates to characterize the flexural wave propagation. Obtaining closed form solutions to characterize the flexural wave propagation in a finite plate with inclusions is mathematically difficult process. So, FEM is used to explore the composite panel designs. The understanding gained about the material properties influence on the flexural wave propagation from analytical studies helped with the choice of materials for FEM simulations.

In the finite element method (FEM) investigation, the effects on the reduction of vibration transmission and flexural wave propagation in composite sandwich panels with different design variations are explored. The concept of phononic crystals will be used as the filtering principle to determine these design variations. FEM simulations are conducted to evaluate the effectiveness of each of these designs in suppressing vibration transmission. Various design configurations will be considered to explore the effects/contributions of different parameters like scatterer's material properties, geometry and spatial pattern. Based on knowledge gained (contributions of the parameters) through the systematic parametric study, an optimal design of the composite sandwich panel will be proposed.

1.5 Dissertation Outline

Following the introduction in Chapter 1, Chapter 2 describes the flexural wave propagation in thin plates. The governing equation for transverse deflections in a thin plate is derived to characterize the wave propagation and solved in closed form for specific cases. Chapter 3 discusses various design configurations and their FEM model set-ups. Using these simulation models various systematic parametric studies are conducted to explore the contributions of different parameters like scatterer's material properties, geometry and spatial pattern on the reduction of vibration transmission. The results from these parametric studies are presented in Chapter 4. Based on the learnings and knowledge gained by the influence of parameters on the vibration transmission reduction, an optimum design model of the composite sandwich panel is proposed. The details of the optimum design model and the comparisons with the unmodified base sandwich panel are presented in Chapter 5. Chapter 6 concludes the dissertation by summarizing the results and proposing various suggestions for future work.

2 Flexural Wave Propagation in Thin Plates

In this chapter, the governing equation for transverse deflections in a thin plate is derived. This governing equation is formulated to characterize the wave propagation. For a number of specific cases including an infinite bi-material plate, infinite plate with a strip inhomogeneity, and an infinite thin plate with a solid circular inclusion, closed form solutions are obtained. The analytical results provide guidance to the subsequent investigations using the finite element method.

2.1 Governing Equation for Deflection in Thin Plates

In this section the general considerations for motion in thin plates are discussed and the governing equation for the transverse deflections is derived based on Kirchhoff's plate theory assumptions.

Consider an isotropic thin plate with constant thickness h, density ρ, Young's modulus E, and Poisson's ratio ν with the mid-plane in the x-y plane and the z-axis is perpendicular to it as shown in Figure 2.1. The plate thickness is small compared to the other in-plane dimensions. A load $p(x, y)$ is applied perpendicular to the mid-plane of the plate. Consider a differential element $h\ dx\ dy$ as shown in Figure 2.2 with various shear forces, bending and twisting moments, and the external load.

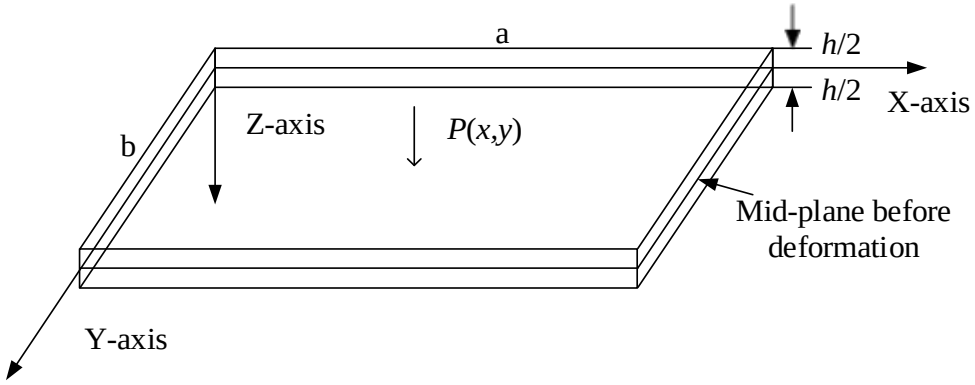

Figure 2.1: Schematic of thin plate

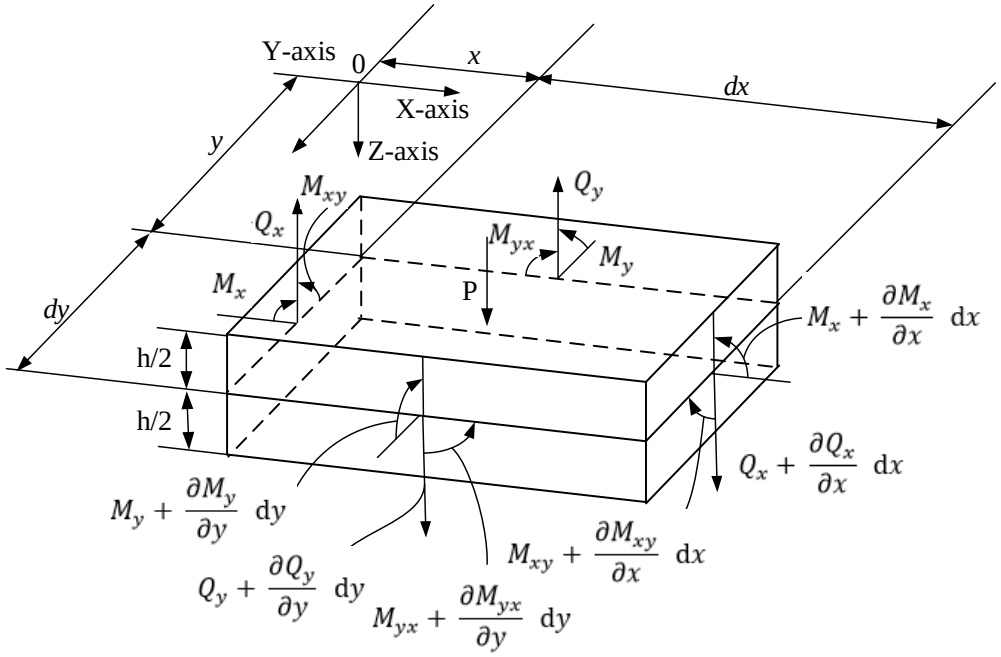

Figure 2.2: Element of the plate subjected to forces and moments

2.1.1 Basic Assumptions

Following are the fundamental assumptions based on Kirchhoff's plate theory of thin plates [1]:

a. The material of the plate is elastic, homogeneous, and isotropic.

b. The plate is initially flat.

c. The deflection (the normal component of the displacement vector) of the mid-plane is small compared with the thickness of the plate. The slope of the deflected surface is therefore very small and the square of the slope is a negligible quantity in comparison with unity.

d. The straight lines, initially normal to the mid-plane before bending, remain straight and normal to the mid-plane during the deformation and the length of such elements is not altered. This means that the vertical shear strains γ_{xz} and γ_{yz} are negligible and the normal strain ε_z may be omitted. This assumption is referred to as the ‘‘*hypothesis of straight normals*’’.

e. The stress normal to the mid-plane, σ_z, is small compared with the other stress components ($\sigma_x, \sigma_y, \tau_{xy}$) and may be neglected in the stress–strain relations.

f. Since the displacements of a plate are small, it is assumed that the mid-plane remains unstrained after bending.

These assumptions result in the reduction of a three-dimensional plate problem to a two-dimensional one.

2.1.2 Stresses and Strains

Let u, v, w be the components of the displacement vector of the points on the mid-plane of the plate in x, y, z directions respectively. Based on assumption (d) the following relation can be derived:

$$u = -z\,\frac{\partial w}{\partial x},\quad v = -z\,\frac{\partial w}{\partial y} \tag{2.1}$$

where u, v are the displacements of the points at a distance z from the mid-plane, and w is the deflection or the normal component of the displacement which is function of *x* and *y* only. From the definition of the strain components the following relations are obtained:

$$\varepsilon_x = \frac{\partial u}{\partial x} = -z\,\frac{\partial^2 w}{\partial x^2} \tag{2.2}$$

$$\varepsilon_y = \frac{\partial v}{\partial y} = -z\,\frac{\partial^2 w}{\partial y^2} \tag{2.3}$$

$$\gamma_{xy} = \frac{\partial u}{\partial y} + \frac{\partial v}{\partial x} = -2z\,\frac{\partial^2 w}{\partial x \partial y} \tag{2.4}$$

From the Hooke's law, the stress components can be written as follows:

$$\sigma_x = \frac{E}{1-\nu^2}\left(\varepsilon_x + \nu\varepsilon_y\right) = -\frac{Ez}{1-\nu^2}\left(\frac{\partial^2 w}{\partial x^2} + \nu\frac{\partial^2 w}{\partial y^2}\right) \tag{2.5}$$

$$\sigma_y = \frac{E}{1-\nu^2}\left(\varepsilon_y + \nu\varepsilon_x\right) = -\frac{Ez}{1-\nu^2}\left(\frac{\partial^2 w}{\partial y^2} + \nu\frac{\partial^2 w}{\partial x^2}\right) \tag{2.6}$$

$$\tau_{xy} = \frac{E}{2(1+\nu)}\,\varepsilon_{xy} = -\frac{Ez}{1+\nu}\left(\frac{\partial^2 w}{\partial x \partial y}\right) \tag{2.7}$$

2.1.3 Resultant Forces and Moments

The resultant stresses and the moments are the total statically equivalent forces and moments applied to the mid-plane. These stress resultants and moments are referred to as the shear forces per unit length Q_x and Q_y , the bending moments per unit length $M_x \; and \; M_y$ and the twisting moments per unit length M_{xy} and M_{yx} respectively as shown in Figure 2.2. These forces and moments can be expressed in stress components as follows:

$$\begin{Bmatrix} M_x \\ M_y \\ M_{xy} \end{Bmatrix} = \int_{-h/2}^{h/2} \begin{Bmatrix} \sigma_x \\ \sigma_y \\ \tau_{xy} \end{Bmatrix} z\,dz \tag{2.8}$$

and

$$\begin{Bmatrix} Q_x \\ Q_y \end{Bmatrix} = \int_{-h/2}^{h/2} \begin{Bmatrix} \tau_{xz} \\ \tau_{yz} \end{Bmatrix} dz \tag{2.9}$$

Substituting the expressions for $\sigma_x, \sigma_y, \tau_{xy}$ in terms of the deflection of the plate from equations (2.5) through (2.7) in the above relations shown in equation (2.8) will result in the following:

$$M_x = \int_{-h/2}^{h/2} \sigma_x \, z dz = -\frac{E}{1-\nu^2}\left(\frac{\partial^2 w}{\partial x^2} + \nu \frac{\partial^2 w}{\partial y^2}\right) \int_{-h/2}^{h/2} z^2 \, dz \tag{2.10}$$

$$M_y = \int_{-h/2}^{h/2} \sigma_y \, z dz = -\frac{E}{1-\nu^2}\left(\frac{\partial^2 w}{\partial y^2} + \nu \frac{\partial^2 w}{\partial x^2}\right) \int_{-h/2}^{h/2} z^2 \, dz \tag{2.11}$$

$$M_{xy} = \int_{-h/2}^{h/2} \tau_{xy} \, z dz = -\frac{E}{1+\nu}\left(\frac{\partial^2 w}{\partial x \partial y}\right) \int_{-h/2}^{h/2} z^2 \, dz \tag{2.12}$$

Equations (2.10) through (2.12) are simplified into the following:

$$M_x = -\frac{EI}{1-\nu^2}\left(\frac{\partial^2 w}{\partial x^2} + \nu \frac{\partial^2 w}{\partial y^2}\right) \tag{2.13}$$

$$M_x = -\frac{EI}{1-\nu^2}\left(\frac{\partial^2 w}{\partial y^2} + \nu \frac{\partial^2 w}{\partial x^2}\right) \tag{2.14}$$

$$M_x = -\frac{EI}{1+\nu}\left(\frac{\partial^2 w}{\partial x \partial y}\right) \tag{2.15}$$

where *I* is the moment of inertia of the per unit length of the plate. Define the flexural rigidity, denoted as *D*, as follows:

$$D = \frac{Eh^3}{12(1-\nu^2)} \tag{2.16}$$

With this notation $M_x, M_y,$ and M_{xy} can be written as follows:

$$M_x = -D\left(\frac{\partial^2 w}{\partial x^2} + \nu\frac{\partial^2 w}{\partial y^2}\right) \tag{2.17}$$

$$M_y = -D\left(\frac{\partial^2 w}{\partial y^2} + \nu\frac{\partial^2 w}{\partial x^2}\right) \tag{2.18}$$

$$M_{xy} = M_{yx} = -D(1-\nu)\left(\frac{\partial^2 w}{\partial x \partial y}\right) \tag{2.19}$$

2.1.4 Governing Equation for Deflection

For the system of the forces and moments shown in Figure 2.2, the following three independent dynamic conditions can be set-up:

(1) Considering the dynamic force equilibrium in the *z*-axis gives:

$$-Q_x\,\mathrm{d}y + \left(Q_x + \frac{\partial Q_x}{\partial x}\,\mathrm{d}x\right)\mathrm{d}y - Q_y\,\mathrm{d}x + \left(Q_y + \frac{\partial Q_y}{\partial y}\,\mathrm{d}y\right)\mathrm{d}x + p\,\mathrm{d}x\,\mathrm{d}y = \rho h\,\frac{\partial^2 w}{\partial t^2} \tag{2.20}$$

which results in

$$\frac{\partial Q_x}{\partial x} + \frac{\partial Q_y}{\partial y} + p = \rho h\,\frac{\partial^2 w}{\partial t^2} \tag{2.21}$$

(2) Considering the moment equilibrium about the *x*-axis gives:

$$-M_y\,\mathrm{d}x + \left(M_y + \frac{\partial M_y}{\partial y}\,\mathrm{d}y\right)\mathrm{d}x + M_{xy}\,\mathrm{d}y - \left(M_{xy} + \frac{\partial M_{xy}}{\partial x}\,\mathrm{d}x\right)\mathrm{d}y - Q_y\,\mathrm{d}x\,\mathrm{d}y = 0 \tag{2.22}$$

which results in

$$\frac{\partial M_y}{\partial y} + \frac{\partial M_{xy}}{\partial x} - Q_y = 0 \tag{2.23}$$

(3) Considering the moment equilibrium about *y*-axis gives:

$$-M_x\,\mathrm{d}y + \left(M_x + \frac{\partial M_x}{\partial x}\,\mathrm{d}x\right)\mathrm{d}x - M_{yx}\,\mathrm{d}x + \left(M_{yx} + \frac{\partial M_{yx}}{\partial y}\,\mathrm{d}y\right)\mathrm{d}x - Q_x\,\mathrm{d}x\,\mathrm{d}y = 0 \tag{2.24}$$

which results in

$$\frac{\partial M_x}{\partial x} + \frac{\partial M_{yx}}{\partial y} - Q_x = 0 \tag{2.25}$$

From equations (2.23) and (2.25), the following relations for Q_x and Q_y are obtained

$$Q_x = \frac{\partial M_x}{\partial x} + \frac{\partial M_{yx}}{\partial y} \tag{2.26}$$

$$Q_y = \frac{\partial M_y}{\partial y} + \frac{\partial M_{xy}}{\partial x} \tag{2.27}$$

Substituting Q_x and Q_y in equation (2.21) results in

$$\frac{\partial^2 M_x}{\partial x^2} + \frac{\partial^2 M_{xy}}{\partial x \partial y} + \frac{\partial^2 M_y}{\partial y^2} = -p + \rho h \frac{\partial^2 w}{\partial t^2} \tag{2.28}$$

Substituting the expressions for M_x, M_y, M_{xy} from equations (2.17) through (2.19) into equation (2.28) yields

$$\frac{\partial^4 w}{\partial x^4} + 2\frac{\partial^4 w}{\partial x^2 \partial y^2} + \frac{\partial^4 w}{\partial y^4} = \frac{p}{D} - \frac{\rho h}{D} \frac{\partial^2 w}{\partial t^2} \tag{2.29}$$

This is the governing differential equation for the deflections of a thin plate based on the Kirchhoff's assumptions. This equation can also be written as follows:

$$\mathrm{D}\nabla^4 w + \rho h \frac{\partial^2 w}{\partial t^2} = p \tag{2.30}$$

where

$$\nabla^4( ) = \frac{\partial^4}{\partial x^4} + 2\frac{\partial^4}{\partial x^2 \partial y^2} + \frac{\partial^4}{\partial y^4}$$

is called the biharmonic operator. More background on the theory of elasticity and the details of all the equations and relations can be found in these references [1, 52, 53].

2.2 Flexural Wave Propagation in a Bi-material Infinite Plate

In this section, a method of solution to characterize the flexural wave propagation in an infinite bi-material plate has been described. Closed form solutions have been obtained for the following two cases: a plane wave traveling in *x*-direction incident normal to the interface, and a

plane wave propagating at an angle θ with *x*-axis incident on the interface. In both cases, the influence of the materials properties of the media on the reflection and transmission characteristics are explored.

2.2.1 Normal Incidence

Consider an infinite thin bi-material plate composed of two different materials separated along the *y*-axis as shown in Figure 2.3. Medium 1 has mass density ρ_1, Young's modulus E_1, and Poisson's ratio $\nu_1$and medium 2 has mass density ρ_2, Young's modulus E_2, and Poisson's ratio ν_2.

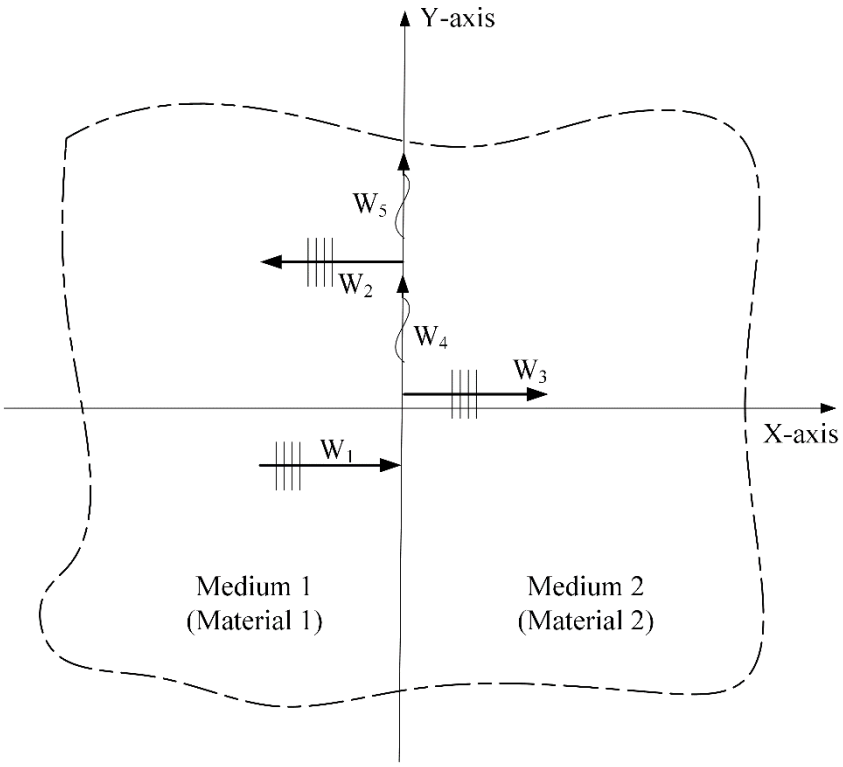

Figure 2.3: Infinite bi-material thin plate with normal incident wave

The equation of motion for transverse displacement has been derived in the above section and is shown in equation (2.30). Assume a traveling harmonic plane wave propagating in *x*-direction impinges onto the interface between the two materials ($x = 0$) as shown in Figure 2.3. Such a wave can be expressed as

$$w(x,t) = A_0 e^{\hat{\imath}(kx-\omega t)} \tag{2.31}$$

The waves generated and the continuity conditions at the interface depend on only on *x* space variable. Considering the case of no external force applied on the plate, the equation (2.30) can be represented in one-dimensional space as

$$\frac{\partial^4 w}{\partial x^4} + \frac{\rho h}{D}\frac{\partial^2 w}{\partial t^2} = 0 \tag{2.32}$$

Substituting the wave form shown in equation (2.31) into the equation (2.32) gives

$$(ik)^4 A_0 e^{\hat{\imath}(kx-\omega t)} + \frac{\rho h}{D}(-i\omega)^2 A_0 e^{\hat{\imath}(kx-\omega t)} = 0 \tag{2.33}$$

Since $A_0 e^{\hat{\imath}(kx-\omega t)}$ is not always zero, equation (2.33) results in

$$k^4 = \frac{\rho h \omega^2}{D} \tag{2.34}$$

$$k_{1,2} = \pm \sqrt[4]{\frac{\rho h \omega^2}{D}};\ k_{3,4} = \pm i \sqrt[4]{\frac{\rho h \omega^2}{D}} \tag{2.35}$$

which gives

$$k_{1,2} = \pm\alpha;\ k_{3,4} = \pm i\alpha \tag{2.36}$$

where

$$\alpha = \sqrt[4]{\frac{\rho h \omega^2}{D}}$$

This implies that all the possible waves will have the following forms:

$$e^{\hat{\imath}(\alpha x-\omega t)}, e^{-\hat{\imath}(\alpha x+\omega t)}, e^{-\alpha x} e^{-\hat{\imath}\omega t}, e^{\alpha x} e^{-\hat{\imath}\omega t} \tag{2.37}$$

The first two forms represent traveling waves and the latter two are non-traveling and are referred to as evanescent waves which vary exponentially with distance from the interface.

Consider a unit amplitude plane wave W_1 traveling in *x*-direction and incident normal to the interface between the two materials ($x = 0$) as shown in Figure 2.3. A reflected wave W_2, a

transmitted wave W_3, along with evanescent waves W_4 and W_5 in *y*-direction (along the interface), are generated as shown in Figure 2.3.

These waves can be represented as follows:

$$W_1 = e^{\hat{\imath}(k_1 x - \omega t)} \tag{2.38}$$

$$W_2 = Re^{-\hat{\imath}(k_1 x + \omega t)} \tag{2.39}$$

$$W_3 = Te^{\hat{\imath}(k_2 x - \omega t)} \tag{2.40}$$

$$W_4 = E_1 e^{k_1 x} e^{-i\omega t} \tag{2.41}$$

$$W_5 = E_2 e^{-k_2 x} e^{-i\omega t} \tag{2.42}$$

where W_1, W_2, and W_4 are the are waves that are valid in medium 1 ($x < 0$) and W_3 and W_5 are waves are valid in medium 2 ($x > 0$), R, T are the reflection and transmission coefficients and E_1, E_2 are the evanescent wave coefficients, and $k_{1,2}$ are the wave numbers in medium 1 and 2 respectively. The total wave in medium 1 is the sum of the incident, reflected and the evanescent wave (W_4) that decays in the negative *x*-direction.

$$U_1 = W_1 + W_2 + W_4 \tag{2.43}$$

$$U_1 = e^{\hat{\imath}(k_1 x - \omega t)} + Re^{-\hat{\imath}(k_1 x + \omega t)} + E_1 e^{k_1 x} e^{-i\omega t} \tag{2.44}$$

The total wave in medium 2 is the sum of the transmitted and the evanescent wave (W_5) that decays in the positive *x*-direction.

$$U_2 = W_3 + W_5 \tag{2.45}$$

$$U_2 = Te^{\hat{\imath}(k_2 x - \omega t)} + E_2 e^{-k_2 x} e^{-i\omega t} \tag{2.46}$$

At the interface of the two materials ($x = 0$), the displacement, the slope, the bending moment, and the shear force must be continuous. These give the following continuity conditions at the interface of the two materials:

$$U_1|_{x=0} = U_2|_{x=0} \tag{2.47}$$

$$\left[\frac{\partial U_1}{\partial x}\right]|_{x=0} = \left[\frac{\partial U_2}{\partial x}\right]|_{x=0} \tag{2.48}$$

$$\left[-D_1 \frac{\partial^2 U_1}{\partial x^2}\right]|_{x=0} = \left[-D_2 \frac{\partial^2 U_2}{\partial x^2}\right]|_{x=0} \tag{2.49}$$

$$\left[-D_1 \frac{\partial^3 U_1}{\partial x^3}\right]|_{x=0} = \left[-D_2 \frac{\partial^3 U_2}{\partial x^3}\right]|_{x=0} \tag{2.50}$$

Substituting U_1 and U_2 from equations (2.44) and (2.46) in the continuity equations (2.47) through (2.50) will result in the following equations:

$$e^{-\hat{\imath}\omega t}\left[e^{\hat{\imath}k_1 x} + Re^{-\hat{\imath}k_1 x} + E_1 e^{k_1 x}\right]|_{x=0} = e^{-\hat{\imath}\omega t}[Te^{\hat{\imath}k_2 x} + E_2 e^{-k_2 x}]|_{x=0} \tag{2.51}$$

$$\begin{aligned} e^{-\hat{\imath}\omega t}[\hat{\imath}k_1 e^{\hat{\imath}k_1 x} - \hat{\imath}k_1 Re^{-\hat{\imath}k_1 x} + k_1 E_1 e^{k_1 x}]|_{x=0} \\ = e^{-\hat{\imath}\omega t}[\hat{\imath}k_2 Te^{\hat{\imath}k_2 x} - k_2 E_2 e^{-k_2 x}]|_{x=0} \end{aligned} \tag{2.52}$$

$$\begin{aligned} -D_1 e^{-\hat{\imath}\omega t}[(\hat{\imath}k_1)^2 e^{\hat{\imath}k_1 x} + \left(-\hat{\imath}k_1\right)^2 Re^{-\hat{\imath}k_1 x} + {k_1}^2 E_1 e^{k_1 x}]|_{x=0} \\ = -D_2 e^{-\hat{\imath}\omega t}[(\hat{\imath}k_2)^2 Te^{\hat{\imath}k_2 x} + {k_2}^2 E_2 e^{-k_2 x}]|_{x=0} \end{aligned} \tag{2.53}$$

$$\begin{aligned} -D_1 e^{-\hat{\imath}\omega t}[(\hat{\imath}k_1)^3 e^{\hat{\imath}k_1 x} + \left(-\hat{\imath}k_1\right)^3 Re^{-\hat{\imath}k_1 x} + {k_1}^3 E_1 e^{k_1 x}]|_{x=0} \\ = -D_2 e^{-\hat{\imath}\omega t}[(\hat{\imath}k_2)^3 Te^{\hat{\imath}k_2 x} - {k_2}^3 E_2 e^{-k_2 x}]|_{x=0} \end{aligned} \tag{2.54}$$

Substituting $x = 0$, letting r_k denote the ratio of the wave numbers (k_2/k_1) and r_D denote the ratio of flexural densities (D_2/D_1) in the above equations (2.51) through (2.54) and re-arranging the terms, the following set of four equations result:

$$-R - E_1 + T + E_2 = 1 \tag{2.55}$$

$$R + \hat{\imath}E_1 + r_k T + \hat{\imath}r_k E_2 = 1 \tag{2.56}$$

$$-R + E_1 + r_D {r_k}^2 T - r_D {r_k}^2 E_2 = 1 \tag{2.57}$$

$$R - \hat{\imath}E_1 + r_D {r_k}^3 T - \hat{\imath}r_D {r_k}^3 E_2 = 1 \tag{2.58}$$

The equations (2.55), through (2.58) can be solved to obtain

$$R = \frac{2r_D r_k(1 - {r_k}^2) + i(1 - r_D {r_k}^2)^2}{(1 + 2r_D r_k + 2r_D {r_k}^2 + 2r_D {r_k}^3 + {r_D}^2 {r_k}^4)} \tag{2.59}$$

$$T = \frac{2(1 + r_k)(1 + r_D {r_k}^2)}{r_k(1 + 2r_D r_k + 2r_D {r_k}^2 + 2r_D {r_k}^3 + {r_D}^2 {r_k}^4)} \tag{2.60}$$

$$E_1 = \frac{(1 + i)(1 - {r_D}^2 {r_k}^4)}{(1 + 2r_D r_k + 2r_D {r_k}^2 + 2r_D {r_k}^3 + {r_D}^2 {r_k}^4)} \tag{2.61}$$

$$E_2 = \frac{2(1 - ir_k)(r_D {r_k}^2 - 1)}{r_k(1 + 2r_D r_k + 2r_D {r_k}^2 + 2r_D {r_k}^3 + {r_D}^2 {r_k}^4)} \tag{2.62}$$

From equations (2.59) and (2.60), it can be observed that the reflection coefficient is a complex number which means there is a phase shift in the reflected wave whereas transmission coefficient is always a positive number. When $r_k < 1$ which means $k_2 < k_1$ the reflection wave is in phase with the incident wave. When $r_k > 1$ which means $k_2 > k_1$ there is a phase difference of π between the reflected and the incident waves.

Consider a thin infinite plate of thickness 'a' with both medium 1 and 2 made of the same material $\rho_1 = \rho_2, E_1 = E_2, \nu_1 = \nu_2$ which implies $r_D = 1$ and $r_k = 1$. Since both the medium 1 and 2 are made of same material it is expected that there will be total transmission of the wave and no reflection. Substituting $r_D = 1$ and $r_k = 1$, in the equations (2.59) through (2.62), R=0, T=0, E_1=0, and E_2=0.

Figure 2.4 shows a surface plot of the magnitude of reflection coefficient plotted against the ratio of flexural rigidities of medium 2 to medium 1(D_2/D_1) and the ratio of densities of medium 2 to medium 1(ρ_2/ρ_1). The range from 0.01 to 100 is considered for D_2/D_1. The range from 0.01 to 100 is considered for ρ_2/ρ_1. It can be observed from Figure 2.4 that the reflection coefficient increases as each of the medium is more rigid than the other. In a similar way, the reflection coefficient increases as each of the medium becomes denser compared to the other. It

can also be observed that there is zero reflection and total transmission in the case when the ratio of the densities and ratio of the flexural rigidities of both the medium are equal to 1.

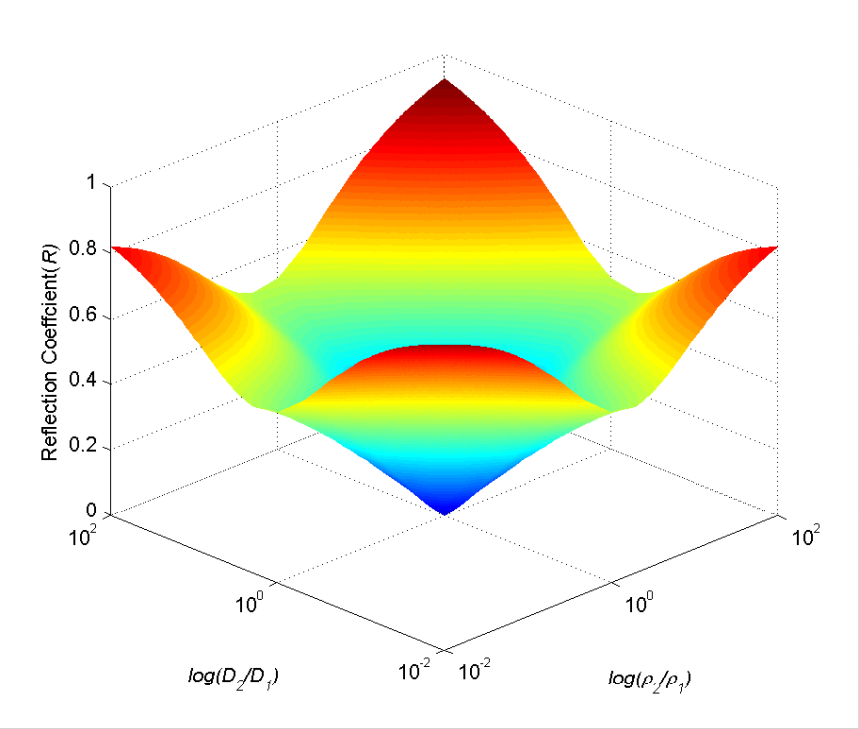

Figure 2.4: Reflection coefficient (R) vs $log(D_2/D_1)$ [10^{-2} to 10^2], $log(\rho_2/\rho_1)$ [10^{-2} to 10^2]

Figure 2.5 shows a surface plot of the transmission coefficient plotted against the ratio of flexural rigidities of medium 2 to medium 1(D_2/D_1) and the ratio of densities of medium 2 to medium 1(ρ_2/ρ_1). The range from 0.01 to 100 is considered for D_2/D_1. The range from 0.01 to 100 is considered for ρ_2/ρ_1. It can be observed from Figure 2.5 that the transmission coefficient decreases as the material of medium 2 is more rigid than medium 1. The transmission coefficient decrease as medium 2 is denser compared to medium 1 as can be seen in Figure 2.5.

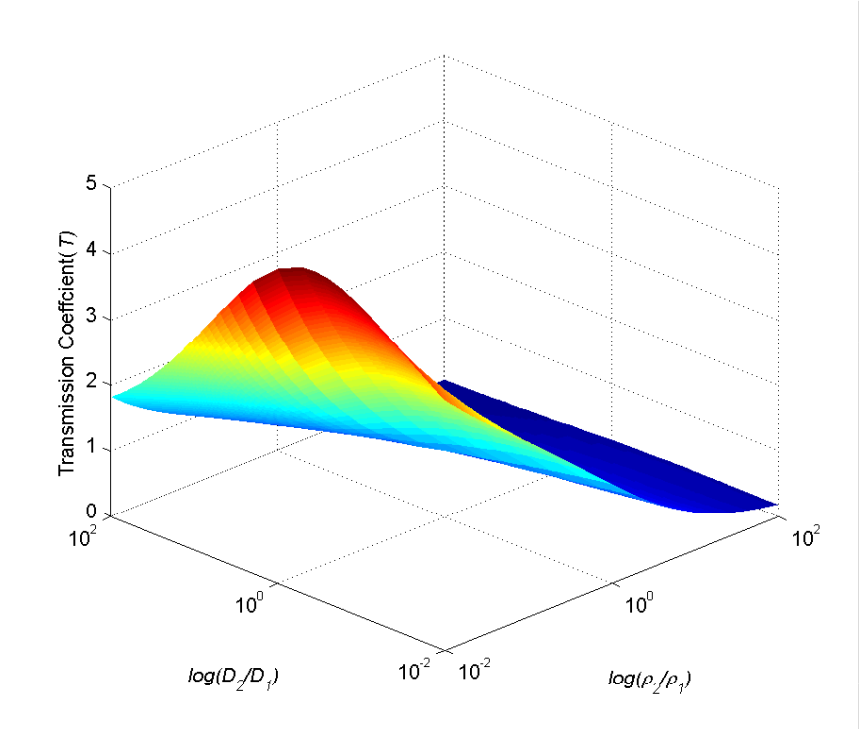

Figure 2.5: Transmission coefficient (T) vs $log(D_2/D_1)$ [10^{-2} to 10^2], $log(\rho_2/\rho_1)$ [10^{-2} to 10^2]

Figure 2.6 and Figure 2.7 show surface plots of the evanescent coefficients E_1 and E_2 plotted against the ratio of flexural rigidities of medium 2 to medium 1(D_2/D_1) and the ratio of densities of medium 2 to medium 1(ρ_2/ρ_1) respectively. The range from 0.01 to 100 is considered for D_2/D_1. The range from 0.01 to 100 is considered for ρ_2/ρ_1. It can be observed from Figure 2.6 the evanescent coefficient E_1 increases as each of the medium is more rigid than the other and increases as each of the medium is denser than the other. Figure 2.7 shows that the evanescent coefficient E_2 decreases as the material of medium 2 is more rigid than medium 1 and also reduces as medium 2 is denser compared to medium 1.

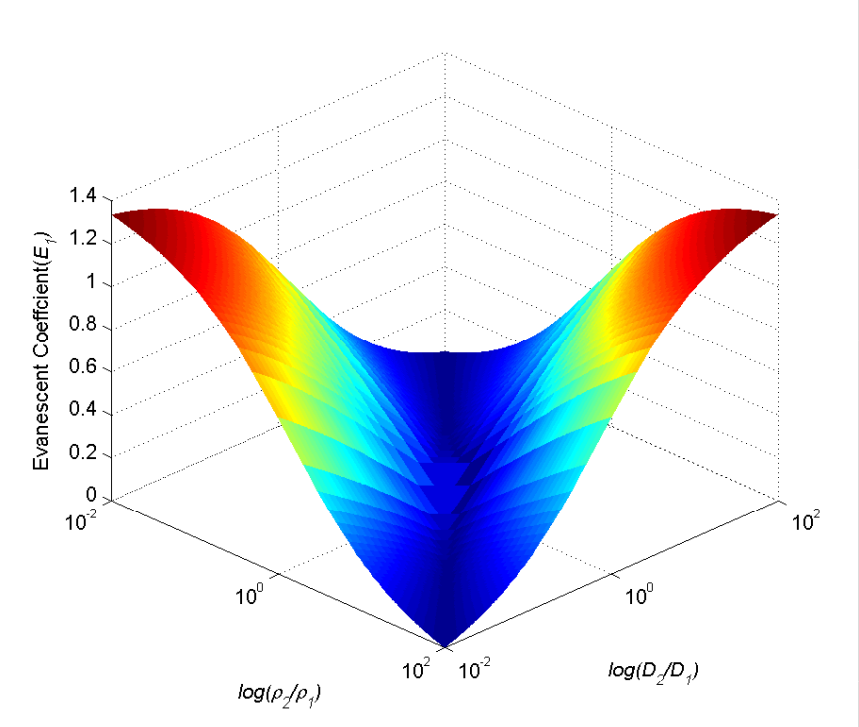

Figure 2.6: Evanescent coefficient (E_1) vs $log(D_2/D_1)$ [10^{-2} to 10^{2}], $log(\rho_2/\rho_1)$ [10^{-2} to 10^{2}]

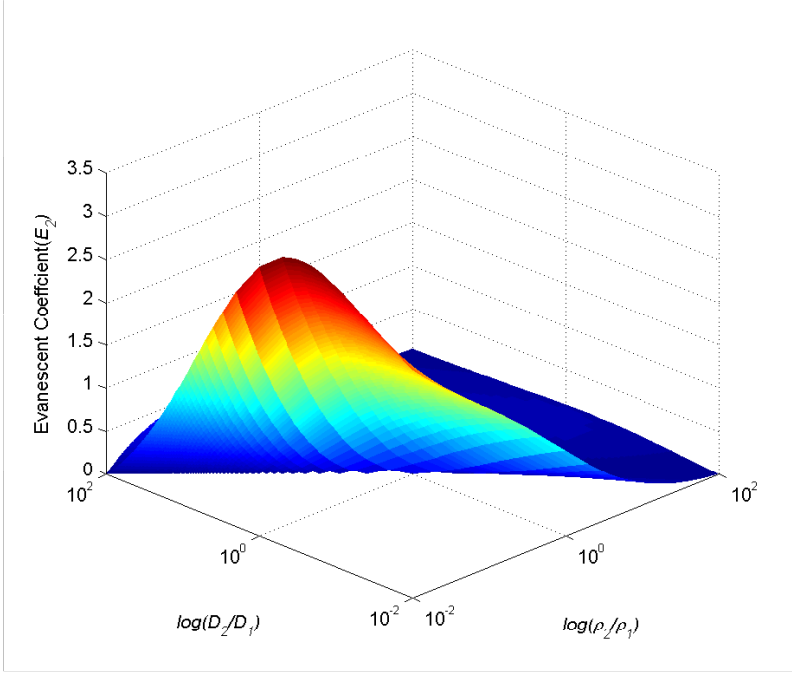

Figure 2.7: Evanescent coefficient (E_2) vs $log(D_2/D_1)$ [10^{-2} to 10^{2}], $log(\rho_2/\rho_1)$ [10^{-2} to 10^{2}]

2.2.2 Oblique Incidence

The equation of motion for transverse displacement of thin plate has been derived in the above section and is shown in equation (2.30). Considering the case of no external force applied on the plate, equation (2.30) is simplified as

$$\frac{\partial^4 w}{\partial x^4} + 2\frac{\partial^4 w}{\partial x^2 \partial y^2} + \frac{\partial^4 w}{\partial y^4} + \frac{\rho h}{D}\frac{\partial^2 w}{\partial t^2} = 0 \tag{2.63}$$

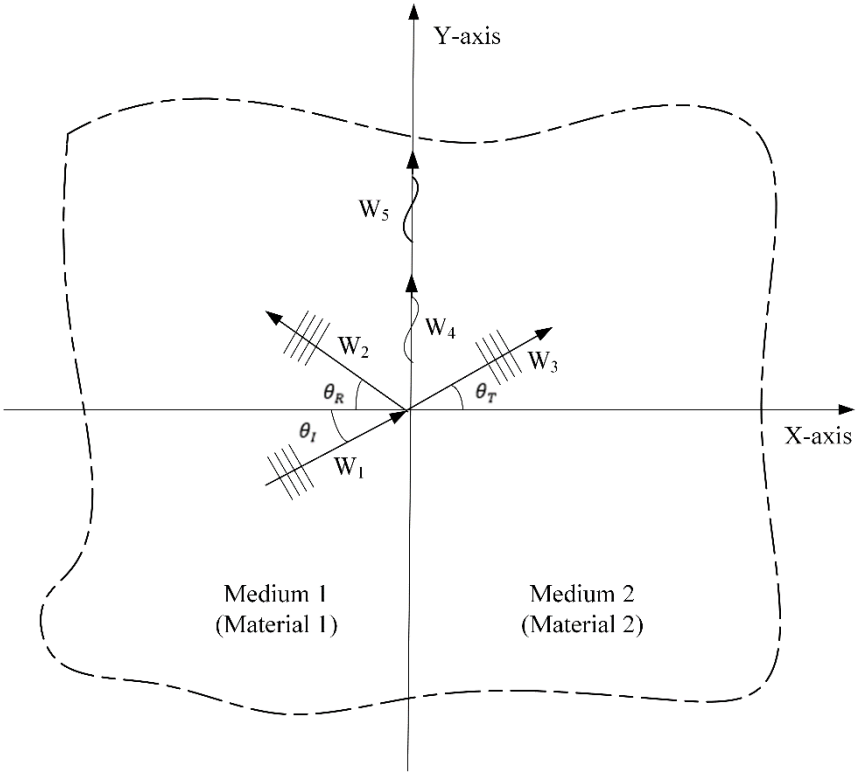

Figure 2.8: Infinite bi-material thin plate with oblique incident wave

Assume a traveling harmonic plane wave propagating at an angle θ with *x*-axis. This wave can be represented as

$$w(x, y, t) = A_0 e^{\hat{\imath}(k_x x + k_y y - \omega t)} \tag{2.64}$$

where $k_x = k\cos\theta$, $k_y = k\sin\theta$ and k is the wave number. Substituting the wave form (2.64) into the equation (2.63) gives

$$({k_x}^2 + {k_y}^2)^2 A_0 e^{\hat{\imath}(k_x x + k_y y - \omega t)} + \frac{\rho h}{D}(-i\omega)^2 A_0 e^{\hat{\imath}(k_x x + k_y y - \omega t)} = 0 \tag{2.65}$$

Since $A_0 e^{\hat{\imath}(k_x x + k_y y - \omega t)}$ is not always zero, equation (2.65) results in

$$k^4 = \frac{\rho h \omega^2}{D} \tag{2.66}$$

$$k_{1,2} = \pm \sqrt[4]{\frac{\rho h \omega^2}{D}};\ k_{3,4} = \pm i \sqrt[4]{\frac{\rho h \omega^2}{D}} \tag{2.67}$$

which gives

$$k_{1,2} = \pm\alpha;\ k_{3,4} = \pm i\alpha \tag{2.68}$$

where

$$\alpha = \sqrt[4]{\frac{\rho h \omega^2}{D}}$$

The possible waves will have the following forms

$$e^{\hat{\imath}(\alpha x \cos\theta + \alpha y \sin\theta - \omega t)}, e^{-\hat{\imath}(\alpha x \cos\theta + \alpha y \sin\theta + \omega t)}, e^{(\alpha x \cos\theta + \alpha y \sin\theta - \hat{\imath}\omega t)}, e^{-(\alpha x \cos\theta + \alpha y \sin\theta + \hat{\imath}\omega t)} \tag{2.69}$$

The first two forms of solutions represent traveling waves and the latter two are non-traveling and are referred to as evanescent waves.

Now consider evanescent waves. The different possible wave forms can be represented as

$$w(x, y, t) = A_0 e^{\hat{\imath}k_x x} e^{-k_y y} e^{-\hat{\imath}\omega t} \tag{2.70}$$

$$w(x, y, t) = A_0 e^{\hat{\imath}k_x x} e^{k_y y} e^{-\hat{\imath}\omega t} \tag{2.71}$$

$$w(x, y, t) = A_0 e^{-k_x x} e^{\hat{\imath}k_y y} e^{-\hat{\imath}\omega t} \tag{2.72}$$

$$w(x, y, t) = A_0 e^{k_x x} e^{\hat{\imath}k_y y} e^{-\hat{\imath}\omega t} \tag{2.73}$$

The waves shown equations (2.70) and (2.71) represent the evanescent waves traveling along *x*-axis and decay exponentially in the negative and positive *y*-direction. The waves shown

equations (2.72) and (2.73) represent the evanescent waves traveling along *y*-axis and decay exponentially in the negative and positive *x*-direction as you move away from the *y*-axis.

Consider a unit amplitude plane wave W_1 traveling at an angle θ_I with *x*-axis impinges onto the interface between the two materials ($x = 0$). A reflected wave W_2 traveling at an angle θ_R with *x*-axis, a transmitted wave W_3 traveling at an angle θ_T with *x*-axis, and the evanescent waves W_4 and W_5 along *y*-axis are generated as shown in Figure 2.8. Based on all the waveforms that can possibly exist in the system, we can assume the waves are represented as follows:

$$W_1 = e^{\hat{\imath}[k_1(x\cos\theta_I + y\sin\theta_I) - \omega t]} \tag{2.74}$$

$$W_2 = Re^{-\hat{\imath}[k_1(x\cos\theta_R + y\sin\theta_R) + \omega t]} \tag{2.75}$$

$$W_3 = Te^{\hat{\imath}[k_2(x\cos\theta_T + y\sin\theta_T) - \omega t]} \tag{2.76}$$

$$W_4 = E_1 e^{k_1 x} e^{\hat{\imath} k_3 y} e^{-\hat{\imath}\omega t} \tag{2.77}$$

$$W_5 = E_2 e^{-k_2 x} e^{\hat{\imath} k_4 y} e^{-\hat{\imath}\omega t} \tag{2.78}$$

where R, T are the reflection and transmission coefficients and E_1, E_2 are the evanescent wave coefficients, θ_R, θ_T are the respective reflection and transmission angles; k_1 and k_2 are the wave numbers in medium 1 and 2; k_3 and k_4 are the wave numbers of the evanescent waves along the interface. The total wave in medium 1 is the sum of the incident, reflected and evanescent wave (W_4) that decays in the negative *x*-direction.

$$U_1 = W_1 + W_2 + W_4 \tag{2.79}$$

$$U_1 = e^{\hat{\imath}[k_1(x\cos\theta_I + y\sin\theta_I) - \omega t]} + Re^{-\hat{\imath}[k_1(x\cos\theta_R + y sin\theta_R) + \omega t]} + E_1 e^{k_1 x} e^{\hat{\imath} k_3 y} e^{-\hat{\imath}\omega t} \tag{2.80}$$

The total wave in medium 2 is the sum of the transmitted and evanescent wave (W_5) that decays in the positive *x*-direction.

$$U_2 = W_3 + W_5 \tag{2.81}$$

$$U_2 = Te^{\hat{\imath}[k_2(x\cos\theta_T + y\sin\theta_T) - \omega t]} + E_2 e^{-k_2 x} e^{\hat{\imath} k_4 y} e^{-\hat{\imath}\omega t} \tag{2.82}$$

At the interface of the two materials ($x = 0$), the displacement, the slope, the bending moment, and the shear force must be continuous. These give the following continuity conditions at the interface of the two materials:

$$U_1|_{x=0} = U_2|_{x=0} \tag{2.83}$$

$$\left[\frac{\partial U_1}{\partial x}\right]|_{x=0} = \left[\frac{\partial U_2}{\partial x}\right]|_{x=0} \tag{2.84}$$

$$\left[-D_1 \frac{\partial^2 U_1}{\partial x^2}\right]|_{x=0} = \left[-D_2 \frac{\partial^2 U_2}{\partial x^2}\right]|_{x=0} \tag{2.85}$$

$$\left[-D_1 \frac{\partial^3 U_1}{\partial x^3}\right]|_{x=0} = \left[-D_2 \frac{\partial^3 U_2}{\partial x^3}\right]|_{x=0} \tag{2.86}$$

Substituting U_1 and U_2 from equations (2.80) through (2.82) in the continuity equations (2.83) through (2.86) and $x = 0$ will result in the following equations:

$$e^{-\hat{\imath}\omega t}[e^{\hat{\imath} k_1 y\sin\theta_I} + Re^{-\hat{\imath} k_1 y\sin\theta_R} + E_1 e^{\hat{\imath} k_3 y}] = e^{-\hat{\imath}\omega t}[Te^{\hat{\imath} k_2 y\sin\theta_T} + E_2 e^{\hat{\imath} k_4 y}] \tag{2.87}$$

$$\begin{aligned} e^{-\hat{\imath}\omega t}[(\hat{\imath} k_1\cos\theta_I)e^{\hat{\imath} k_1 y\sin\theta_I} + (-\hat{\imath} k_1\cos\theta_R)Re^{-\hat{\imath} k_1 y\sin\theta_R} + k_1 E_1 e^{\hat{\imath} k_3 y}] \\ = e^{-\hat{\imath}\omega t}[(\hat{\imath} k_2\cos\theta_T)Te^{\hat{\imath} k_2 y\sin\theta_T} - k_2 E_2 e^{\hat{\imath} k_4 y}] \end{aligned} \tag{2.88}$$

$$\begin{aligned} -D_1 e^{-\hat{\imath}\omega t}[(\hat{\imath} k_1\cos\theta_I)^2 e^{\hat{\imath} k_1 y\sin\theta_I} + (-\hat{\imath} k_1\cos\theta_R)^2 Re^{-\hat{\imath} k_1 y\sin\theta_R} + {k_1}^2 E_1 e^{\hat{\imath} k_3 y}] \\ = -D_2 e^{-\hat{\imath}\omega t}[(\hat{\imath} k_2\cos\theta_T)^2 Te^{\hat{\imath} k_2 y\sin\theta_T} + {k_2}^2 E_2 e^{\hat{\imath} k_4 y}] \end{aligned} \tag{2.89}$$

$$\begin{aligned} -D_1 e^{-\hat{\imath}\omega t}[(\hat{\imath} k_1\cos\theta_I)^3 e^{\hat{\imath} k_1 y\sin\theta_I} + (-\hat{\imath} k_1\cos\theta_R)^3 Re^{-\hat{\imath} k_1 y\sin\theta_R} + {k_1}^3 E_1 e^{\hat{\imath} k_3 y}] \\ = -D_2 e^{-\hat{\imath}\omega t}[(\hat{\imath} k_2\cos\theta_T)^3 Te^{\hat{\imath} k_2 y\sin\theta_T} + {k_2}^3 E_2 e^{\hat{\imath} k_4 y}] \end{aligned} \tag{2.90}$$

For the displacement continuity equation (2.87) to hold true for all 'y', the y factors of the exponential functions need to match. This gives

$$\hat{\imath} k_1 y\sin\theta_I = -\hat{\imath} k_1 y\sin\theta_R = \hat{\imath} k_3 y = \hat{\imath} k_2 y\sin\theta_T = \hat{\imath} k_4 y \tag{2.91}$$

From the above, the following relations can be established:

$$\sin\theta_R = -\sin\theta_I \tag{2.92}$$

$$k_3 = k_1 \sin\theta_I \tag{2.93}$$

$$\sin\theta_T = \frac{k_1}{k_2}\sin\theta_I \tag{2.94}$$

$$k_4 = k_1 \sin\theta_I \tag{2.95}$$

Substituting the relations (2.92) through (2.95) in the equations (2.87) through (2.90), the equations (2.87) through (2.90) are simplified and result in

$$R + E_1 - T - E_2 = -1 \tag{2.96}$$

$$-\hat{\imath}k_1\cos\theta_R R + k_1 E_1 - \hat{\imath}k_2\cos\theta_T T + k_2 E_2 = -\hat{\imath}k_1\cos\theta_I \tag{2.97}$$

$$-D_1{k_1}^2\cos^2\theta_R R + D_1{k_1}^2 E_1 + D_2{k_2}^2\cos^2\theta_T T - D_2{k_2}^2 E_2 = D_1{k_1}^2\cos^2\theta_I \tag{2.98}$$

$$\hat{\imath}D_1{k_1}^3\cos^3\theta_R R + D_1{k_1}^3 E_1 + \hat{\imath}D_2{k_2}^3\cos^3\theta_T T + D_2{k_2}^3 E_2 = \hat{\imath}D_1{k_1}^3\cos^3\theta_I \tag{2.99}$$

Let r_k denote the ratio of the wave numbers k_2/k_1, r_D denote ratio of flexural densities D_2/D_1, $r_R = \cos\theta_R/\cos\theta_I$, $r_{E1} = \cos\theta_{E1}/\cos\theta_I$, $r_T = \cos\theta_T/\cos\theta_I$, and $r_{E2} = \cos\theta_{E2}/\cos\theta_I$ in the above equations (2.96) through (2.99), the following set of four equations result:

$$R + E_1 - T - E_2 = -1 \tag{2.100}$$

$$-r_R R - \hat{\imath}r_{E1}E_1 - r_k r_T T - \hat{\imath}r_k r_{E2}E_2 = -1 \tag{2.101}$$

$$r_R{}^2 R - r_{E1}{}^2 E_1 - r_D r_k{}^2 r_T{}^2 T + r_D r_k{}^2 r_{E2}{}^2 E_2 = -1 \tag{2.102}$$

$$-r_R{}^3 R + \hat{\imath}r_{E1}{}^3 E_1 - r_D r_k{}^3 r_T{}^3 T + \hat{\imath}r_D r_k{}^3 r_{E2}{}^3 E_2 = -1 \tag{2.103}$$

Assuming $\theta_I = 0$, a case of normal incidence, $r_R = r_{E1} = r_T = r_{E2} = 1$, the set of equations (2.100) through (2.103) recover equations (2.55) through (2.58) from the normal incidence solution. Since the above set of equations (2.100) through (2.103) are rather involved, MATLAB has been used to solve for the coefficients and generate plots.

As a simple example, consider a thin infinite plate where both medium 1 and 2 are made of the same material. Since both the medium 1 and 2 are made of same material it is expected that there will be total transmission of the wave and no reflection.

Figure 2.9 shows the reflection coefficient varying with the incident angle for various ratios of flexural rigidities D_2/D_1= 0.001, 0.01, 100, and 1000. The density ratio is set to 1. It can be observed that as the material of medium 2 becomes less rigid compared to medium 1, the reflection coefficient increases with the angle of incidence. Critical angle is the angle of incidence above which the total reflection occurs. It is also observed that total reflection occurs and the critical angle decreases as the flexural rigidity of medium 2 increases compared to medium 1. The last two cases (D_2/D_1 = 100 and D_2/D_1 = 1000) where the material in medium 2 is rigid compared to medium 1 the total reflection happens at 19 degrees and 11 degrees respectively.

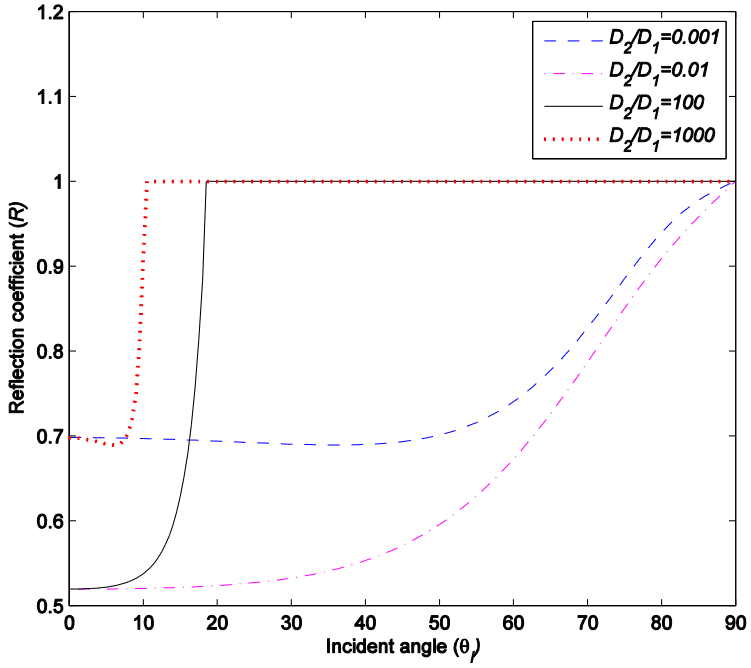

Figure 2.9: Reflection coefficient vs the incident angle for the ratio of flexural rigidities of two media, D_2/D_1=0.001, 0.01, 100, and 1000

Figure 2.10, Figure 2.11, and Figure 2.12 show the transmission coefficient and evanescent coefficients (E_1 and E_2) respectively varying with the incident angle for various ratios of flexural rigidities D_2/D_1= 0.001, 0.01, 100, and 1000. The density ratio is set to 1. It can be observed that as the material of medium 2 is less rigid compared to medium 1, the transmission coefficient decreases with the angle of incidence. As discussed total reflection happens when medium 2 becomes rigid compared to medium 1. This formulation is valid until the total reflection and so the plots of transmission coefficient and evanescent coefficients (E_1 and E_2) are truncated at the critical angle. The evanescent coefficients (E_1 and E_2) decrease with the angle of incidence when the material of medium 2 is less rigid compared to medium 1. It is also observed evanescent coefficients (E_1 and E_2) rapidly decrease when the material of medium 2 is becomes rigid compared to medium 1 up to critical angle.

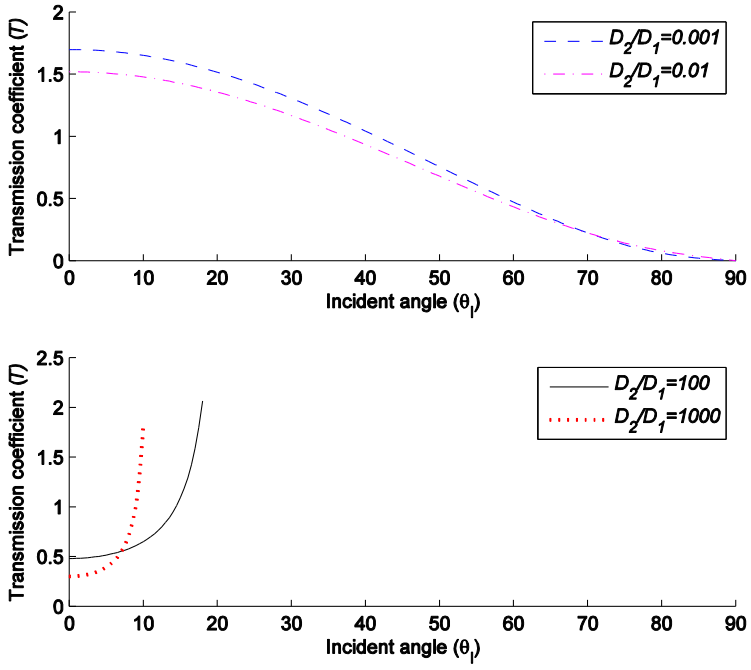

Figure 2.10: Transmission coefficient vs the incident angle for the ratio of flexural rigidities of two media, D_2/D_1=0.001, 0.01, 100, and 1000

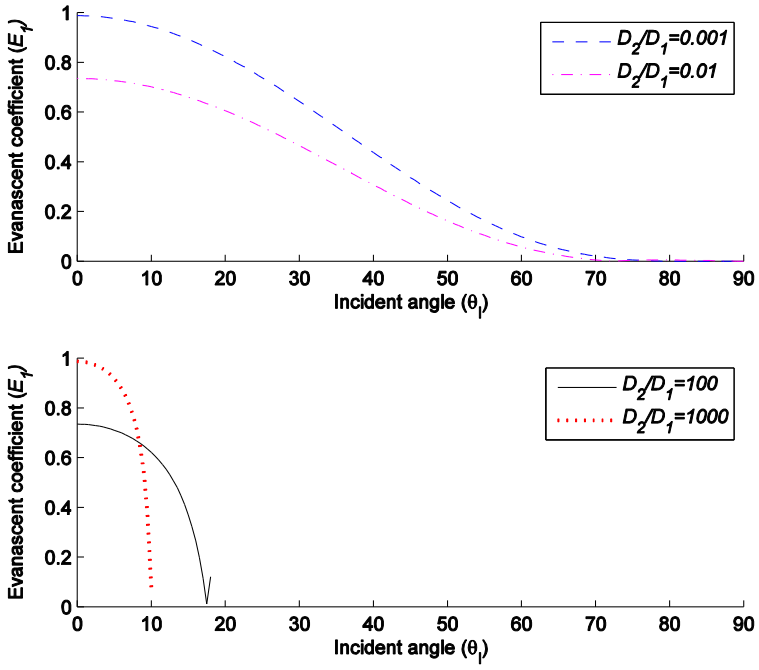

Figure 2.11: Evanescent coefficient (E_1) vs the incident angle for the ratio of flexural rigidities of two media, D_2/D_1=0.001, 0.01, 100, and 1000

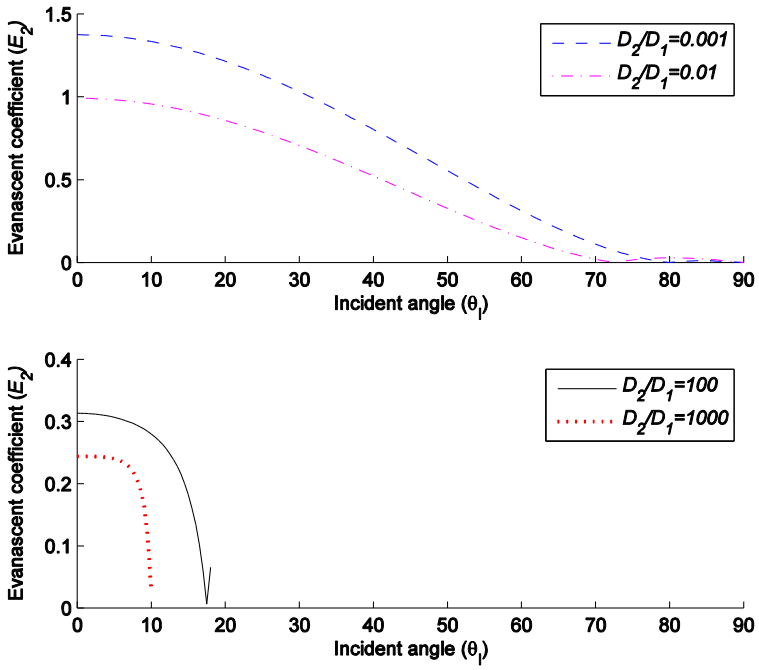

Figure 2.12: Evanescent coefficient (E_2) vs the incident angle for the ratio of flexural rigidities of two media, D_2/D_1=0.001, 0.01, 100, and 1000

Figure 2.13 shows the reflection coefficient varying with the incident angle for various ratios of densities ρ_2/ρ_1 = 0.001, 0.01, 100, and 1000. The flexural rigidity ratio is set to1. It can be observed that as medium 2 becomes less dense compared to medium 1, total reflection occurs. As medium 2 becomes less dense compared to medium 1, the critical angle decreases. For example, the first two cases (ρ_2/ρ_1 = 0.001 and ρ_2/ρ_1 = 0.01), where the material in medium 1 is denser compared to medium 2 the total reflection happens at 11 degrees and 19 degrees respectively.

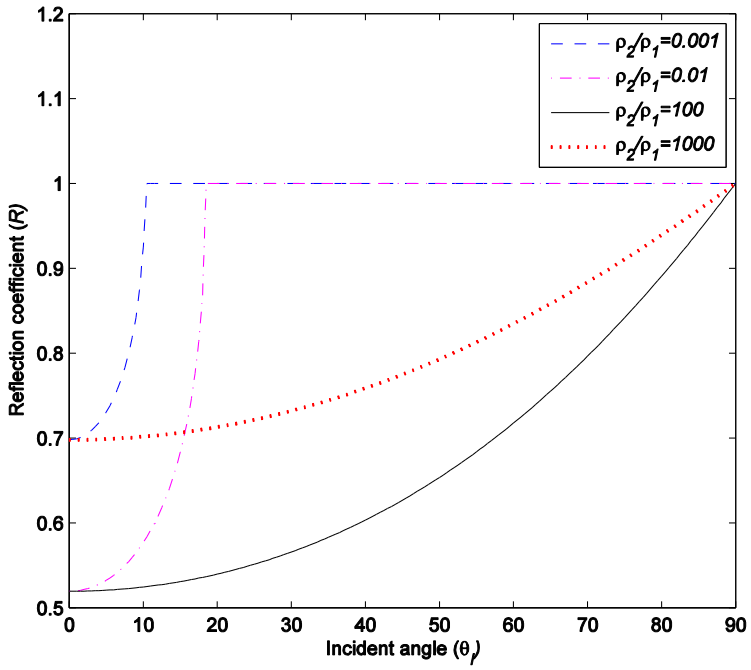

Figure 2.13: Reflection coefficient vs the incident angle for the ratio of densities of two media, ρ_2/ρ_1 = 0.001, 0.01, 100, and 1000

Figure 2.14, Figure 2.15, and Figure 2.16 show the transmission coefficient and evanescent coefficients (E_1 and E_2) respectively varying with the incident angle for various ratios

of densities ρ_2/ρ_1 = 0.001, 0.01, 100, and 1000. The flexural rigidity ratio is set to 1. It can be observed that as the material of medium 2 becomes denser compared to medium 1, the transmission coefficient decreases with the angle of incidence. As discussed total reflection happens when medium 2 becomes less denser compared to medium 1. This formulation is valid until the total reflection and so the plots of transmission coefficient and evanescent coefficients (E_1 and E_2) are truncated at the critical angle. The evanescent coefficients (E_1 and E_2) decrease with the angle of incidence when the material of medium 2 is denser compared to medium 1. It is also observed evanescent coefficients (E_1 and E_2) rapidly increase when the material of medium 2 is becomes less denser compared to medium 1 up to critical angle.

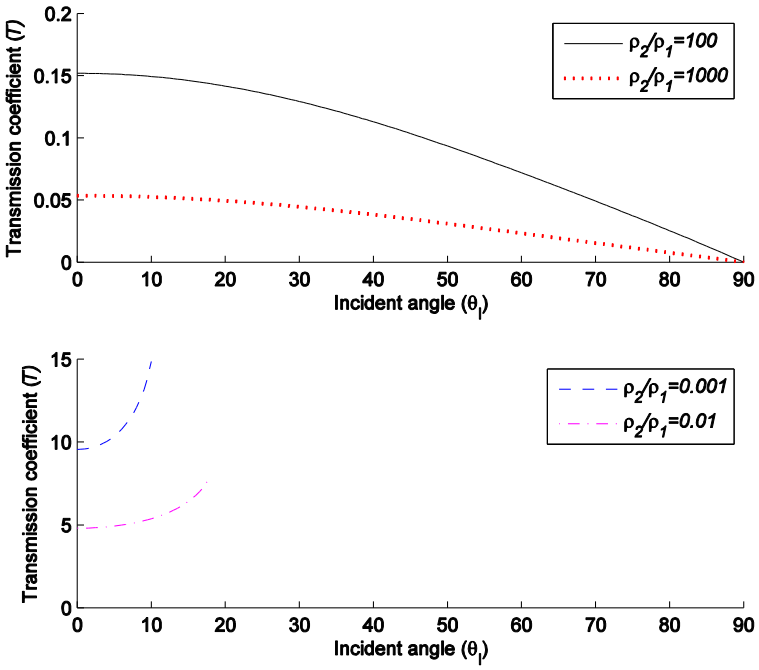

Figure 2.14: Transmission coefficient vs the incident angle for the ratio of densities of two media, ρ_2/ρ_1 = 0.001, 0.01, 100, and 1000

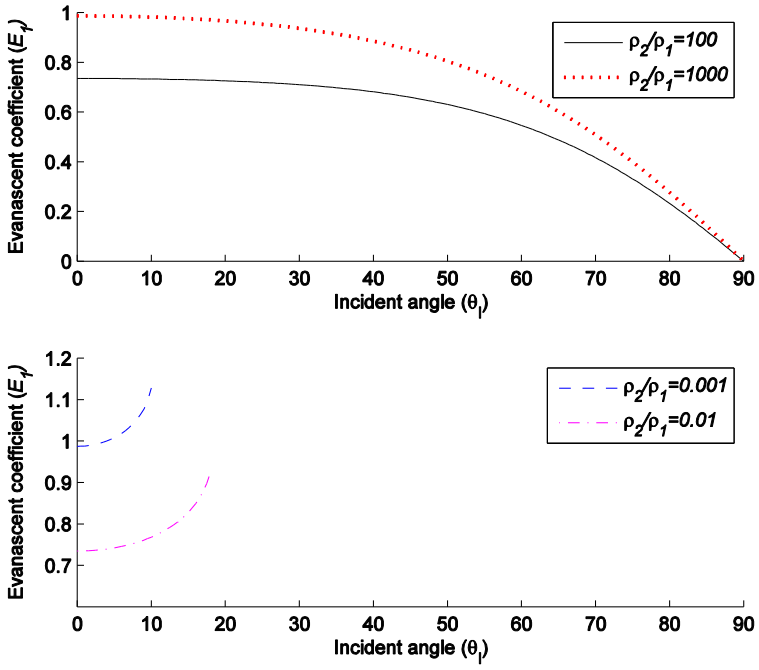

Figure 2.15: Evanescent coefficient (E_1) vs the incident angle for the ratio of densities of two media, ρ_2/ρ_1 = 0.001, 0.01, 100, and 1000

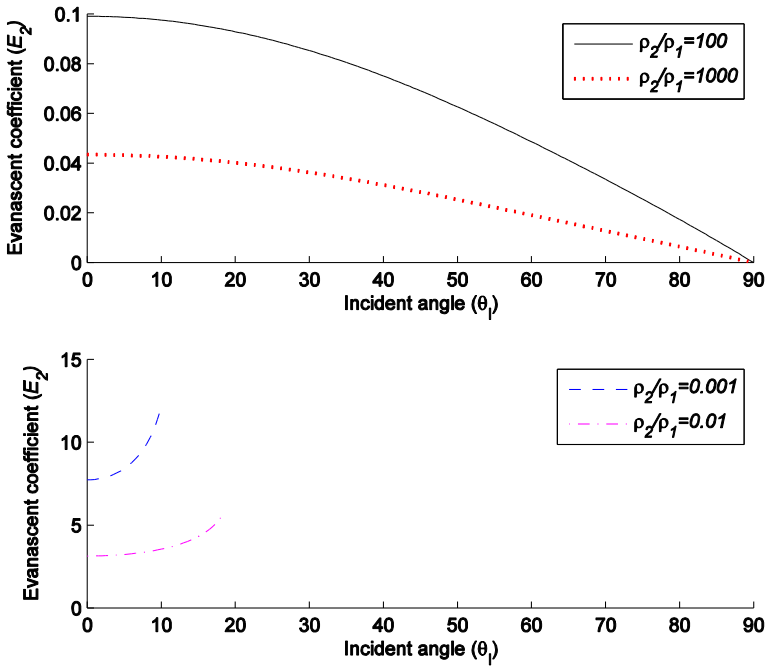

Figure 2.16: Evanescent coefficient (E_2) vs the incident angle for the ratio of densities of two media, ρ_2/ρ_1 = 0.001, 0.01, 100, and 1000

2.3 Flexural Wave Propagation in an Infinite Plate with a Thin Strip of Different Material

In this section, a method of solution to characterize the flexural wave propagation in an infinite bi-material plate with a strip inhomogeneity has been described. Closed form solutions have been obtained and the influence of the materials properties of the media on the reflection and transmission characteristics are studied.

Consider an infinite thin plate with a strip. The plate is divided into three sections: medium 1, 2 and 3. The interface between medium 1 and 2 is denoted as I-12, and the interface between medium 2 and 3 is denoted by I-23, as shown in

Figure 2.17. Medium 1 and medium 3 are made of the same material with material properties density ρ_1, Young's modulus E_1, and Poisson's ratio ν_1, and medium 2 has material properties density ρ_2, Young's modulus E_2, Poisson's ratio ν_2, and width $2b$.

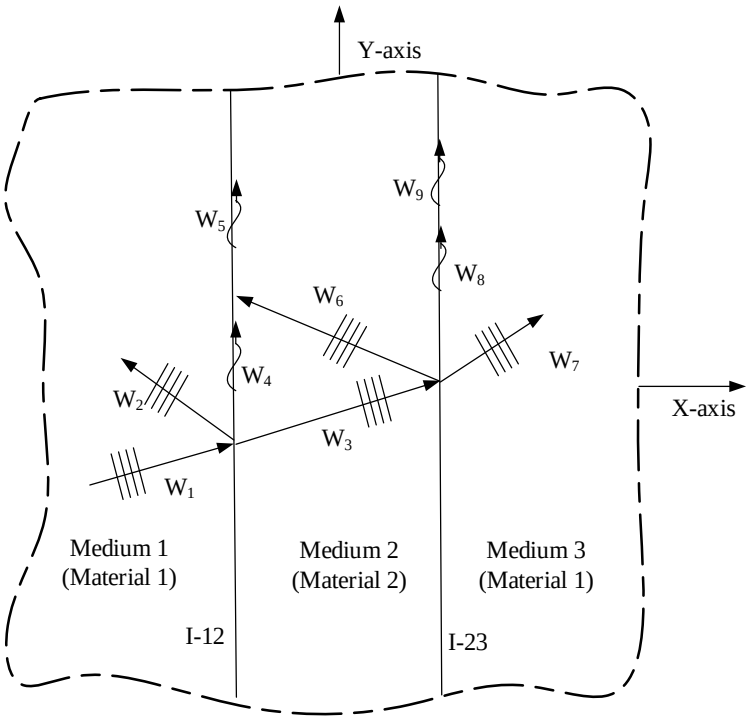

Figure 2.17: Infinite thin plate with strip of inhomogeneity

Consider a unit amplitude plane wave W_1 traveling at an angle θ_I with *x*-axis impinges onto the interface I-12. A reflected wave W_2, and a transmitted wave W_3, along with evanescent waves W_4 and W_5 along the interface, are generated as shown in

Figure 2.17. When the wave W_3 impinges onto interface I-23, a reflected wave W_6, a transmitted wave W_7 and evanescent waves W_8 and W_9 are generated. Subsequently wave W_6 impinges onto the interface I-12 and this process is continued which results in multiple reflected and transmitted waves in the strip, multiple transmitted waves in medium 3 and medium 1.

Aggregating all the different waves traveling in each of medium, W_2 represents the sum of the first reflected wave at the interface I-12 and the waves transmitted from medium 2 to medium 1. Similarly W_3 represents the total of all the forward traveling waves in medium 2 and W_6 represents the backward traveling waves. W_7 represents the aggregate of all the transmitted waves into medium 3. W_4 and W_5 represent the total evanescent wave at the interface I-12, and W_8 and W_9 represent the total evanescent wave at the interface I-23. These waves can be represented by

$$W_1 = e^{\hat{\imath}[k_1(x\cos\theta_I + y\sin\theta_I) - \omega t]} \tag{2.104}$$

$$W_2 = R_{12}e^{-\hat{\imath}[k_1(x\cos\theta_{R12} + y\sin\theta_{R12}) + \omega t]} \tag{2.105}$$

$$W_3 = T_{12}e^{\hat{\imath}[k_2(x\cos\theta_{T12} + y\sin\theta_{T12}) - \omega t]} \tag{2.106}$$

$$W_4 = E_1 e^{k_1 x} e^{\hat{\imath}k_3 y} e^{-\hat{\imath}\omega t} \tag{2.107}$$

$$W_5 = E_{12}e^{-k_2 x} e^{\hat{\imath}k_4 y} e^{-\hat{\imath}\omega t} \tag{2.108}$$

$$W_6 = R_{23}e^{-\hat{\imath}[k_2(x\cos\theta_{R23} + y\sin\theta_{R23}) + \omega t]} \tag{2.109}$$

$$W_7 = T_{23}e^{\hat{\imath}[k_1(x\cos\theta_{T23} + y\sin\theta_{T23}) - \omega t]} \tag{2.110}$$

$$W_8 = E_{23}e^{k_2 x} e^{\hat{\imath}k_5 y} e^{-i\omega t} \tag{2.111}$$

$$W_9 = E_3 e^{-k_1 x} e^{\hat{\imath} k_6 y} e^{-i\omega t} \tag{2.112}$$

where R_{12}, T_{12} are the reflection and transmission coefficients, E_1, E_{12} are the evanescent wave coefficients at the interface I-12, R_{23}, T_{23} are the reflection and transmission coefficients, E_{23}, E_3 are the evanescent wave coefficients at the interface I-23 respectively. k_1 and k_2 are the wave numbers in medium 1 and 2, k_3 and k_4 are the wave numbers of the evanescent waves along the interface I-12, and k_5 and k_6 are the wave numbers of the evanescent waves along the interface I-23. The total wave in medium 1 can be written as

$$U_1 = W_1 + W_2 + W_4 \tag{2.113}$$

$$U_1 = e^{\hat{\imath}[k_1(x\cos\theta + y\sin\theta) - \omega t]} + R_{12} e^{-\hat{\imath}[k_1(x\cos\theta_{R12} + y\sin\theta_{R12}) + \omega t]} + E_1 e^{k_1 x} e^{\hat{\imath} k_3 y} \tag{2.114}$$

The total wave in medium 2 can be written as

$$U_2 = W_3 + W_6 + W_5 + W_8 \tag{2.115}$$

$$U_2 = T_{12} e^{\hat{\imath}[k_2(x\cos\theta_{T12} + y\sin\theta_{T12}) - \omega t]} + R_{23} e^{-\hat{\imath}[k_2(x\cos\theta_{R23} + y\sin\theta_{R23}) + \omega t]} + E_{12} e^{-k_2 x} e^{\hat{\imath} k_4 y} e^{-\hat{\imath}\omega t} + E_{23} e^{k_2 x} e^{\hat{\imath} k_5 y} e^{-i\omega t} \tag{2.116}$$

The total wave in medium 3 can be written as

$$U_3 = W_7 + W_9 \tag{2.117}$$

$$U_3 = T_{23} e^{\hat{\imath}[k_1(x\cos\theta_{T23} + y\sin\theta_{T23}) - \omega t]} + E_3 e^{-k_1 x} e^{\hat{\imath} k_6 y} e^{-i\omega t} \tag{2.118}$$

At the interface I-12, the displacement, the slope, the bending moment, and the shear force must be continuous. These give the following continuity conditions at the interface I-12:

$$U_1|_{x=-b} = U_2|_{x=-b} \tag{2.119}$$

$$\left[\frac{\partial U_1}{\partial x}\right]|_{x=-b} = \left[\frac{\partial U_2}{\partial x}\right]|_{x=-b} \tag{2.120}$$

$$\left[-D_1 \frac{\partial^2 U_1}{\partial x^2}\right]|_{x=-b} = \left[-D_2 \frac{\partial^2 U_2}{\partial x^2}\right]|_{x=-b} \tag{2.121}$$

$$\left[-D_1 \frac{\partial^3 U_1}{\partial x^3}\right]|_{x=-b} = \left[-D_2 \frac{\partial^3 U_2}{\partial x^3}\right]|_{x=-b} \tag{2.122}$$

At the interface I-23, the displacement, the slope, the bending moment, and the shear force must be continuous. These give the following continuity conditions at the interface I-23:

$$U_2|_{x=b} = U_3|_{x=b} \tag{2.123}$$

$$\left[\frac{\partial U_2}{\partial x}\right]|_{x=b} = \left[\frac{\partial U_3}{\partial x}\right]|_{x=b} \tag{2.124}$$

$$\left[-D_2 \frac{\partial^2 U_2}{\partial x^2}\right]|_{x=b} = \left[-D_1 \frac{\partial^2 U_3}{\partial x^2}\right]|_{x=b} \tag{2.125}$$

$$\left[-D_2 \frac{\partial^3 U_2}{\partial x^3}\right]|_{x=b} = \left[-D_1 \frac{\partial^3 U_3}{\partial x^3}\right]|_{x=b} \tag{2.126}$$

Substituting U_1, and U_2 from equations (2.114) and (2.116) in the continuity equations (2.119) through (2.122) and $x = -b$ will result in the following equations:

$$\begin{aligned} & e^{-\hat{\imath}\omega t}[e^{\hat{\imath}k_1(-b\cos\theta_I + y\sin\theta_I)} + R_{12}e^{-\hat{\imath}k_1(-b\cos\theta_{R12} + y\sin\theta_{R12})} + E_1 e^{-k_1 b}e^{\hat{\imath}k_3 y}] \\ & \quad = e^{-\hat{\imath}\omega t}[T_{12}e^{\hat{\imath}k_2(-b\cos\theta_{T12} + y\sin\theta_{T12})} \\ & \quad + R_{23}e^{-\hat{\imath}k_2(-b\cos\theta_{R23} + y\sin\theta_{R23})} + E_{12}e^{k_2 b}e^{\hat{\imath}k_4 y} \\ & \quad + E_{23}e^{-k_2 b}e^{\hat{\imath}k_5 y}] \end{aligned} \tag{2.127}$$

$$\begin{aligned} & e^{-\hat{\imath}\omega t}[\hat{\imath}k_1\cos\theta_I e^{\hat{\imath}k_1(-b\cos\theta_I + y\sin\theta_I)} - \hat{\imath}k_1\cos\theta_{R12}R_{12}e^{-\hat{\imath}k_1(-b\cos\theta_{R12} + y\sin\theta_{R12})} \\ & \quad + k_1 E_1 e^{-k_1 b}e^{\hat{\imath}k_3 y}] \\ & \quad = e^{-\hat{\imath}\omega t}[\hat{\imath}k_2\cos\theta_{T12}T_{12}e^{\hat{\imath}k_2(-b\cos\theta_{T12} + y\sin\theta_{T12})} \\ & \quad - \hat{\imath}k_2\cos\theta_{R23}R_{23}e^{-\hat{\imath}k_2(-b\cos\theta_{R23} + y\sin\theta_{R23})} - k_2 E_{12}e^{k_2 b}e^{\hat{\imath}k_4 y} \\ & \quad + k_2 E_{23}e^{-k_2 b}e^{\hat{\imath}k_5 y}] \end{aligned} \tag{2.128}$$

$$\begin{aligned} & e^{-\hat{\imath}\omega t}[-D_1 {k_1}^2\cos^2\theta_I e^{\hat{\imath}k_1(-b\cos\theta_I + y\sin\theta_I)} \\ & \quad - D_1 {k_1}^2\cos^2\theta_{R12}R_{12}e^{-\hat{\imath}k_1(-b\cos\theta_{R12} + y\sin\theta_{R12})} \\ & \quad + D_1 {k_1}^2 E_1 e^{-k_1 b}e^{\hat{\imath}k_3 y}] \\ & \quad = e^{-\hat{\imath}\omega t}[-D_2 {k_2}^2\cos^2\theta_{T12}T_{12}e^{\hat{\imath}k_2(-b\cos\theta_{T12} + y\sin\theta_{T12})} \\ & \quad - D_2 {k_2}^2\cos^2\theta_{R23}R_{23}e^{-\hat{\imath}k_2(-b\cos\theta_{R23} + y\sin\theta_{R23})} \\ & \quad + D_2 {k_2}^2 E_{12}e^{k_2 b}e^{\hat{\imath}k_4 y} + {k_2}^2 E_{23}e^{-k_2 b}e^{\hat{\imath}k_5 y}] \end{aligned} \tag{2.129}$$

$$
\begin{aligned}
e^{-\hat{\imath}\omega t}[&-\hat{\imath}D_1{k_1}^3\cos^3\theta_I e^{\hat{\imath}k_1(-b\cos\theta_I+y\sin\theta_I)} \\
&+\hat{\imath}D_1{k_1}^3\cos^3\theta_{R12}R_{12}e^{-\hat{\imath}k_1(-b\cos\theta_{R12}+y\sin\theta_{R12})} \\
&+D_1{k_1}^3E_1e^{-k_1b}e^{\hat{\imath}k_3y}] \\
&=e^{-\hat{\imath}\omega t}[-\hat{\imath}D_2{k_2}^3\cos^3\theta_{T12}T_{12}e^{\hat{\imath}k_2(-b\cos\theta_{T12}+y\sin\theta_{T12})} \\
&+\hat{\imath}D_2{k_2}^3\cos^3\theta_{R23}R_{23}e^{-\hat{\imath}k_2(-b\cos\theta_{R23}+y\sin\theta_{R23})} \\
&-D_2{k_2}^3E_{12}e^{k_2b}e^{\hat{\imath}k_4y}+D_2{k_2}^3E_{23}e^{-k_2b}e^{\hat{\imath}k_5y}]
\end{aligned}
\tag{2.130}
$$

Substituting U_2 and U_3 from equations (2.116) and (2.118) in the continuity equations (2.123) through (2.126) and $x = b$ will result in the following equations:

$$
\begin{aligned}
e^{-\hat{\imath}\omega t}[&T_{12}e^{\hat{\imath}k_2(b\cos\theta_{T12}+y\sin\theta_{T12})}+R_{23}e^{-\hat{\imath}k_2(b\cos\theta_{R23}+y\sin\theta_{R23})}+E_{12}e^{-k_2b}e^{\hat{\imath}k_4y} \\
&+E_{23}e^{k_2b}e^{\hat{\imath}k_5y} \\
&=e^{-\hat{\imath}\omega t}[T_{23}e^{\hat{\imath}k_1(b\cos\theta_{T23}+y\sin\theta_{T23})}+E_3e^{-k_1b}e^{\hat{\imath}k_6y}]
\end{aligned}
\tag{2.131}
$$

$$
\begin{aligned}
e^{-\hat{\imath}\omega t}\big[&\hat{\imath}k_2\cos\theta_{T12}T_{12}e^{\hat{\imath}k_2(b\cos\theta_{T12}+y\sin\theta_{T12})} \\
&-\hat{\imath}k_2\cos\theta_{R23}R_{23}e^{-\hat{\imath}k_2(b\cos\theta_{R23}+y\sin\theta_{R23})}-k_2E_{12}e^{-k_2b}e^{\hat{\imath}k_4y} \\
&+k_2E_{23}e^{k_2b}e^{\hat{\imath}k_5y}\big] \\
&=e^{-\hat{\imath}\omega t}[\hat{\imath}k_1\cos\theta_{T23}T_{23}e^{\hat{\imath}k_1(b\cos\theta_{T23}+y\sin\theta_{T23})} \\
&-k_1E_3e^{-k_1b}e^{\hat{\imath}k_6y}]
\end{aligned}
\tag{2.132}
$$

$$
\begin{aligned}
e^{-\hat{\imath}\omega t}\big[&-D_2{k_2}^2\cos^2\theta_{T12}T_{12}e^{\hat{\imath}k_2(b\cos\theta_{T12}+y\sin\theta_{T12})} \\
&-D_2{k_2}^2\cos^2\theta_{R23}R_{23}e^{-\hat{\imath}k_2(b\cos\theta_{R23}+y\sin\theta_{R23})} \\
&+D_2{k_2}^2E_{12}e^{-k_2b}e^{\hat{\imath}k_4y}+{k_2}^2E_{23}e^{k_2b}e^{\hat{\imath}k_5y}\big] \\
&=e^{-\hat{\imath}\omega t}[-D_1{k_1}^2\cos^2\theta_{T23}T_{23}e^{\hat{\imath}k_1(b\cos\theta_{T23}+y\sin\theta_{T23})} \\
&+D_1{k_1}^2E_3e^{-k_1b}e^{\hat{\imath}k_6y}]
\end{aligned}
\tag{2.133}
$$

$$
\begin{aligned}
e^{-\hat{\imath}\omega t}\big[&-\hat{\imath}D_2{k_2}^3\cos^3\theta_{T12}T_{12}e^{\hat{\imath}k_2(b\cos\theta_{T12}+y\sin\theta_{T12})}\\
&+\hat{\imath}D_2{k_2}^3\cos^3\theta_{R23}R_{23}e^{-\hat{\imath}k_2(b\cos\theta_{R23}+y\sin\theta_{R23})}\\
&-D_2{k_2}^3E_{12}e^{-k_2b}e^{\hat{\imath}k_4y}+D_2{k_2}^3E_{23}e^{k_2b}e^{\hat{\imath}k_5y}\big]\\
&=e^{-\hat{\imath}\omega t}[-\hat{\imath}D_1{k_1}^3\cos^3\theta_{T23}T_{23}e^{\hat{\imath}k_1(b\cos\theta_{T23}+y\sin\theta_{T23})}\\
&-D_1{k_1}^3E_3e^{-k_1b}e^{\hat{\imath}k_6y}]
\end{aligned}
\tag{2.134}
$$

For the displacement continuity equation (2.127) to hold true for all 'y', the y factors of the exponential functions need to match. This gives

$$
\begin{aligned}
\hat{\imath}k_1y\sin\theta_I=-\hat{\imath}k_1y\sin\theta_{R12}=\hat{\imath}k_3y=\hat{\imath}k_2y\sin\theta_{T12}=-\hat{\imath}k_2y\sin\theta_{R23}=\hat{\imath}k_4y\\
=\hat{\imath}k_5y
\end{aligned}
\tag{2.135}
$$

From the above the following relations can be established

$$\sin\theta_{R12}=-\sin\theta_I \tag{2.136}$$

$$\sin\theta_{T12}=\frac{k_1}{k_2}\sin\theta_I \tag{2.137}$$

$$\sin\theta_{R23}=-\frac{k_1}{k_2}\sin\theta_I \tag{2.138}$$

$$k_3=k_4=k_5=k_1\sin\theta_I \tag{2.139}$$

For the displacement continuity equation (2.131) to hold true for all 'y', the y factors of the exponential functions need to match. This gives

$$\hat{\imath}k_2y\sin\theta_{T12}=-\hat{\imath}k_2y\sin\theta_{R23}=\hat{\imath}k_4y=\hat{\imath}k_5y=\hat{\imath}k_1y\sin\theta_{T23}=\hat{\imath}k_6y \tag{2.140}$$

From the above the following relations can be established

$$\sin\theta_{R23}=-\frac{k_1}{k_2}\sin\theta_I \tag{2.141}$$

$$\sin\theta_{T23}=\sin\theta_I \tag{2.142}$$

$$k_6=k_1\sin\theta_I \tag{2.143}$$

Substituting the relations (2.136) through (2.139) and (2.141) through (2.143) in the equations (2.127) through (2.134) and re-arranging the terms result in the following set of eight equations:

$$R_{12}e^{\hat{\imath}k_1 b\cos\theta_{R12}} + E_1 e^{-k_1 b} - T_{12}e^{-\hat{\imath}k_2 b\cos\theta_{T12}} - R_{23}e^{\hat{\imath}k_2 b\cos\theta_{R23}} - E_{12}e^{k_2 b} - E_{23}e^{-k_2 b} = -e^{-\hat{\imath}k_1 b\cos\theta_I} \quad (2.144)$$

$$T_{12}e^{\hat{\imath}k_2 b\cos\theta_{T12}} + R_{23}e^{-\hat{\imath}k_2 b\cos\theta_{R23}} + E_{12}e^{-k_2 b} + E_{23}e^{k_2 b} - T_{23}e^{\hat{\imath}k_1 b\cos\theta_{T23}} - E_3 e^{-k_1 b} = 0 \quad (2.145)$$

$$-R_{12}\hat{\imath}k_1\cos\theta_{R12}e^{\hat{\imath}k_1 b\cos\theta_{R12}} + E_1 k_1 e^{-k_1 b} - T_{12}\hat{\imath}k_2\cos\theta_{T12}e^{-\hat{\imath}k_2 b\cos\theta_{T12}} + R_{23}\hat{\imath}k_2\cos\theta_{R23}e^{\hat{\imath}k_2 b\cos\theta_{R23}} + E_{12}k_2 e^{k_2 b} - E_{23}k_2 e^{-k_2 b} = -\hat{\imath}k_1\cos\theta_I e^{-\hat{\imath}k_1 b\cos\theta_I} \quad (2.146)$$

$$T_{12}\hat{\imath}k_2\cos\theta_{T12}e^{\hat{\imath}k_2 b\cos\theta_{T12}} - R_{23}\hat{\imath}k_2\cos\theta_{R23}e^{-\hat{\imath}k_2 b\cos\theta_{R23}} - E_{12}k_2 e^{-k_2 b} + E_{23}k_2 e^{k_2 b} - T_{23}\hat{\imath}k_1\cos\theta_{T23}e^{\hat{\imath}k_1 b\cos\theta_{T23}} + E_3 k_1 e^{-k_1 b} = 0 \quad (2.147)$$

$$-R_{12}D_1{k_1}^2\cos^2\theta_{R12}e^{\hat{\imath}k_1 b\cos\theta_{R12}} + E_1 D_1{k_1}^2 e^{-k_1 b} + T_{12}D_2{k_2}^2\cos^2\theta_{T12}e^{-\hat{\imath}k_2 b\cos\theta_{T12}} + R_{23}D_2{k_2}^2\cos^2\theta_{R23}e^{\hat{\imath}k_2 b\cos\theta_{R23}} - E_{12}D_2{k_2}^2 e^{k_2 b} - E_{23}D_2{k_2}^2 e^{-k_2 b} = D_1{k_1}^2\cos^2\theta_I e^{-\hat{\imath}k_1 b\cos\theta_I} \quad (2.148)$$

$$-T_{12}D_2{k_2}^2\cos^2\theta_{T12}e^{\hat{\imath}k_2 b\cos\theta_{T12}} - R_{23}D_2{k_2}^2\cos^2\theta_{R23}e^{-\hat{\imath}k_2 b\cos\theta_{R23}} + E_{12}D_2{k_2}^2 e^{-k_2 b} + E_{23}D_2{k_2}^2 e^{k_2 b} + T_{23}D_1{k_1}^2\cos^2\theta_{T23}e^{\hat{\imath}k_1 b\cos\theta_{T23}} - E_3 D_1{k_1}^2 e^{-k_1 b} = 0 \quad (2.149)$$

$$R_{12}\hat{\imath}D_1{k_1}^3\cos^3\theta_{R12}e^{\hat{\imath}k_1 b\cos\theta_{R12}} + E_1 D_1{k_1}^3 e^{-k_1 b} + T_{12}\hat{\imath}D_2{k_2}^3\cos^3\theta_{T12}e^{-\hat{\imath}k_2 b\cos\theta_{T12}} - R_{23}\hat{\imath}D_2{k_2}^3\cos^3\theta_{R23}e^{\hat{\imath}k_2 b\cos\theta_{R23}} + E_{12}D_2{k_2}^3 e^{k_2 b} - E_{23}D_2{k_2}^3 e^{-k_2 b} = \hat{\imath}D_1{k_1}^3\cos^3\theta_I e^{-\hat{\imath}k_1 b\cos\theta_I} \quad (2.150)$$

$$-T_{12}\hat{\imath}D_2{k_2}^3\cos^3\theta_{T12}e^{\hat{\imath}k_2 b\cos\theta_{T12}} + R_{23}\hat{\imath}D_2{k_2}^3\cos^3\theta_{R23}e^{-\hat{\imath}k_2 b\cos\theta_{R23}} - E_{12}D_2{k_2}^3 e^{-k_2 b} + E_{23}D_2{k_2}^3 e^{k_2 b} + T_{23}\hat{\imath}D_1{k_1}^3\cos^2\theta_{T23}e^{\hat{\imath}k_1 b\cos\theta_{T23}} + E_3 D_1{k_1}^3 e^{-k_1 b} = 0 \quad (2.151)$$

The above set of equations can be solved for the coefficients R_{12}, E_1, T_{12}, R_{23}, E_{12}, E_{23}, T_{23}, E_3 using relations between the angles shown in equations (2.136) through (2.139) and (2.141) through (2.143). MATLAB has been used to solve for the coefficients and generate plots.

Consider a thin infinite plate of thickness ‘a’ with a ‘2b’ wide strip where both medium 1 and 2 are made of the same material. Since both the medium 1 and 2 are made of the same

material it is expected that there will be total transmission of the wave with no reflection. Figure 2.18 and Figure 2.19 show the reflection and transmitted coefficients plotted against the incident angle at the interfaces I-12 and I-23 respectively. It can be observed that the reflection coefficients are zero at both the interfaces I-12 and I-23, and the total wave is transmitted which can be observed from the values of transmission coefficients being 1 at both the interfaces I-12 and I-23.

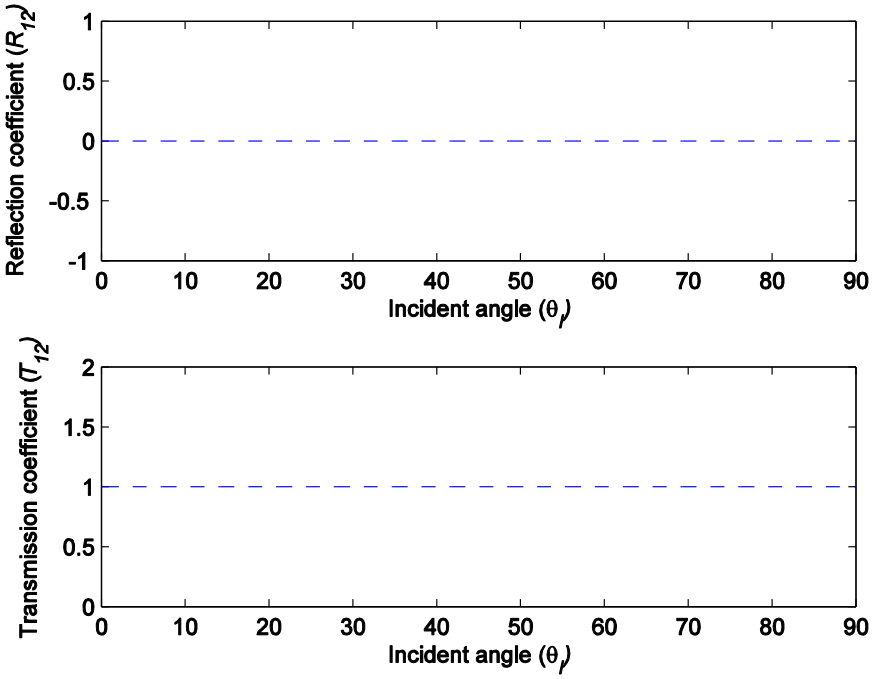

Figure 2.18 Reflection and transmission coefficients at I-12 vs the incident angle (mediums 1 & 2 are assumed to be made of same material)

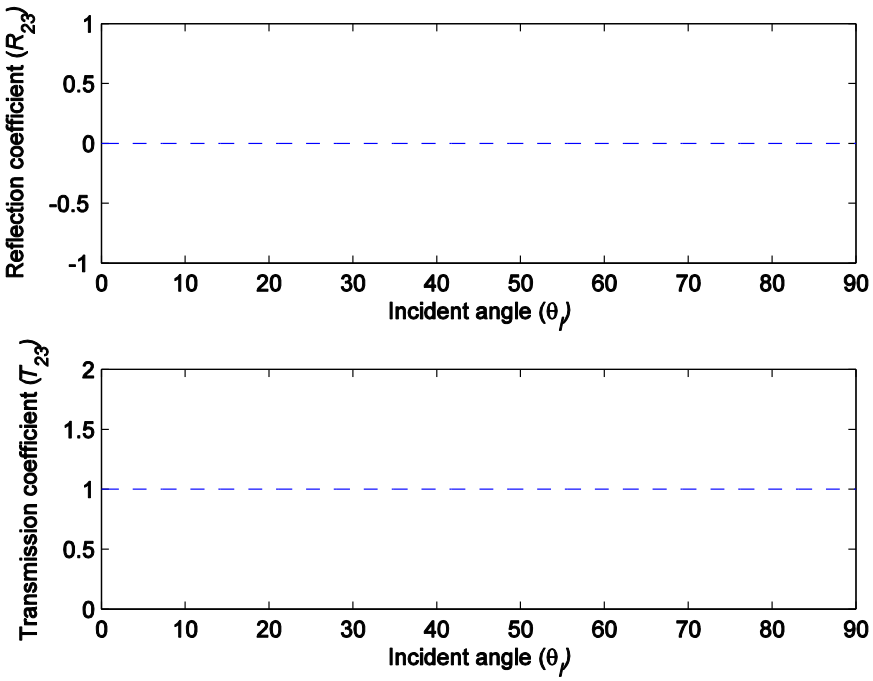

Figure 2.19: Reflection and transmission coefficients at I-23 vs the incident angle (mediums 1 & 2 are assumed to be made of same material)

Figure 2.20 shows the reflection coefficient varying with the incident angle at interface I-12, and Figure 2.21 shows the transmission coefficient against the incident angle at interface I-23 for various flexural rigidity ratios D_2/D_1 = 0.001, 0.01, 100, and 1000. The densities of both the mediums are assumed to be the same.

It can be observed that as the material of medium 2 (strip) becomes stiffer compared to the material of medium 1, there is hardly any reflected wave for lower angles of incidence as seen in Figure 2.20. Figure 2.21 shows complete transmission in for lower angles of incidence. It can also be observed that there is total reflection at higher angles of incidence when the medium 2 is stiffer compared to medium 1 (D_2/D_1 = 1000).

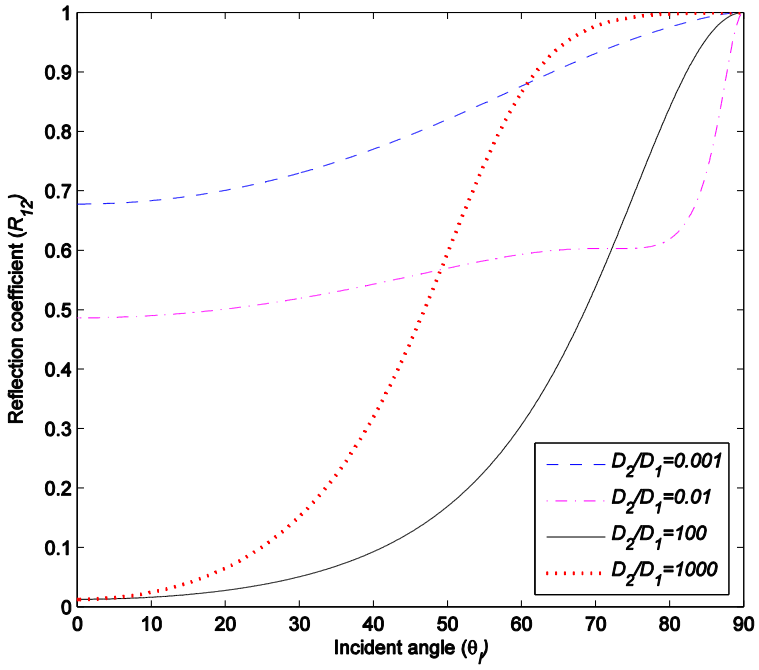

Figure 2.20: Reflection coefficient at I-12 vs the incident angle for the ratio of flexural rigidities of two media, D_2/D_1=0.001, 0.01, 100, and 1000

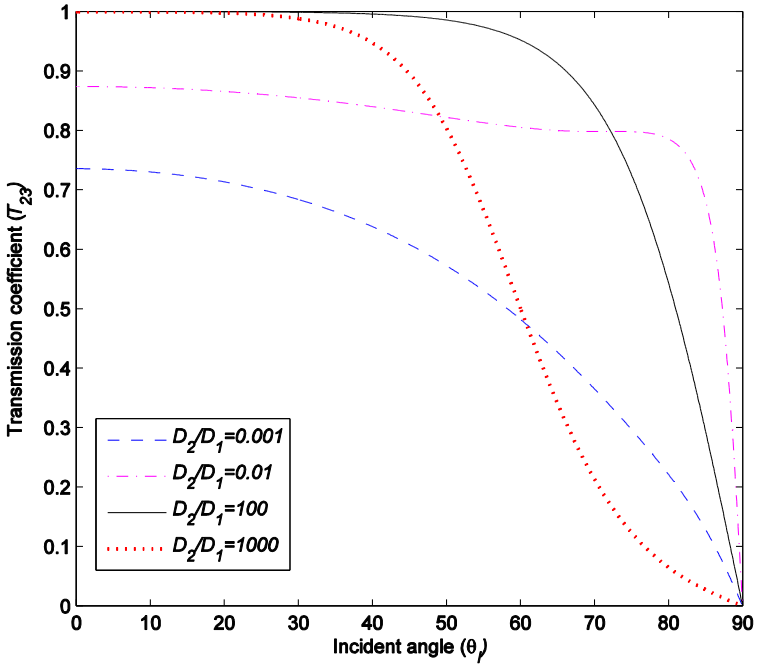

Figure 2.21: Transmission coefficient at I-23 vs the incident angle for the ratio of flexural rigidities of two media, D_2/D_1=0.001, 0.01, 100, and 1000

Figure 2.22 shows the reflection coefficient varying with the incident angle at interface I-12. Figure 2.23 shows the plots with transmission coefficients against the incident angle at interface I-23. Both the figures show plots for various density ratios ρ_2/ρ_1 = 0.001, 0.01, 100, and 1000. The flexural rigidities of both the mediums are assumed to be the same.

It is observed that as the material of medium 2 (strip) becomes denser compared to medium 1 the reflection at the interface I-12 reduces to zero as can be seen in Figure 2.22. It can be observed that there is complete transmission into medium 3 when medium 2 is denser than medium 1 as seen in and Figure 2.23.

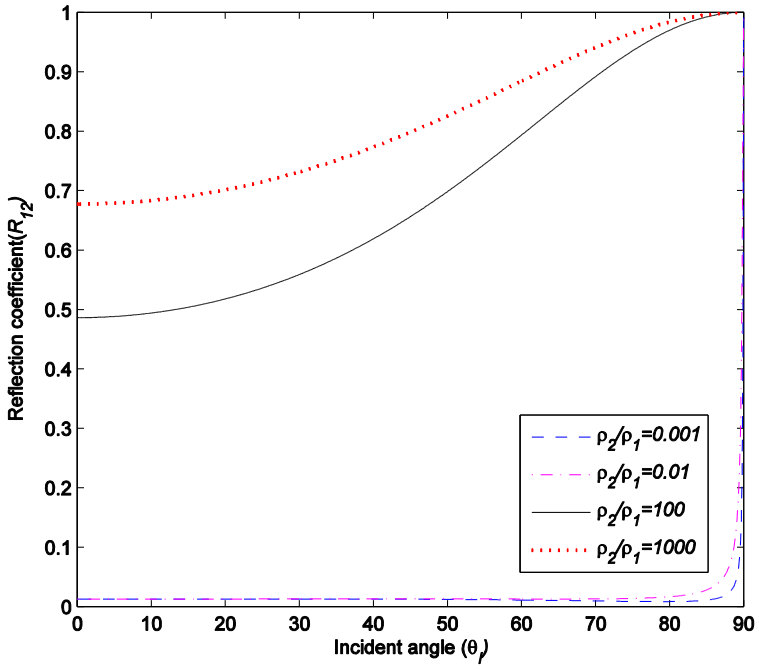

Figure 2.22: Reflection coefficients at I-12 vs the incident angle for the ratio of densities of two media, ρ_2/ρ_1 = 0.001, 0.01, 100, and 1000

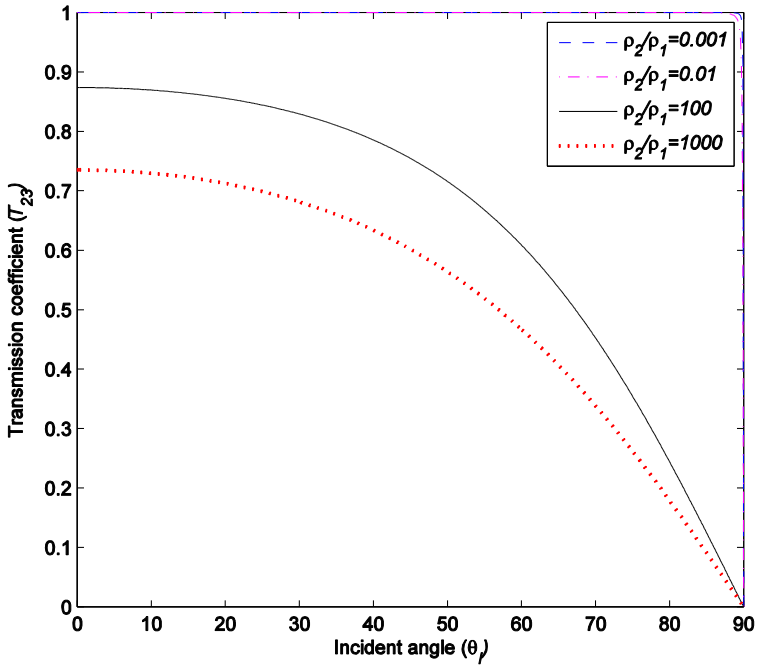

Figure 2.23: Transmission coefficients at I-23 vs the incident angle for the ratio of densities of two media, ρ_2/ρ_1 = 0.001, 0.01, 100, and 1000

Figure 2.24 shows the reflection coefficient varying with the incident angle at interface I-12 and Figure 2.25 shows the transmission coefficient varying with the incident angle at interface I-23 for two cases where medium 2 (strip) is considered as a hard elastic material (ρ_2/ρ_1 = 10 and D_2/D_1 = 100) and a soft elastic material (ρ_2/ρ_1 = 0.1 and D_2/D_1 = 0.01) compared to medium 1. It can be observed that when medium 2 is hard elastic material, reflection coefficient decreases and becomes zero and then increases shown in Figure 2.24. For lower angles of incidence, it can be observed there is complete transmission when medium 2 is made of hard elastic compared to medium 1 as shown in Figure 2.25.

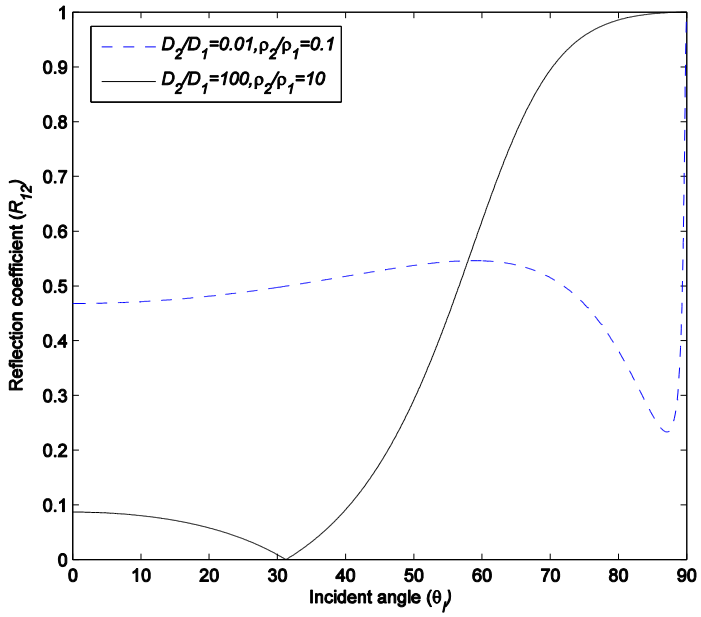

Figure 2.24: Reflection coefficient at I-12 vs the incident angle for medium 2 made of soft elastic (ρ_2/ρ_1 = 0.1 and D_2/D_1= 0.01) and hard elastic (ρ_2/ρ_1 = 10 and D_2/D_1= 100) compared to medium 1

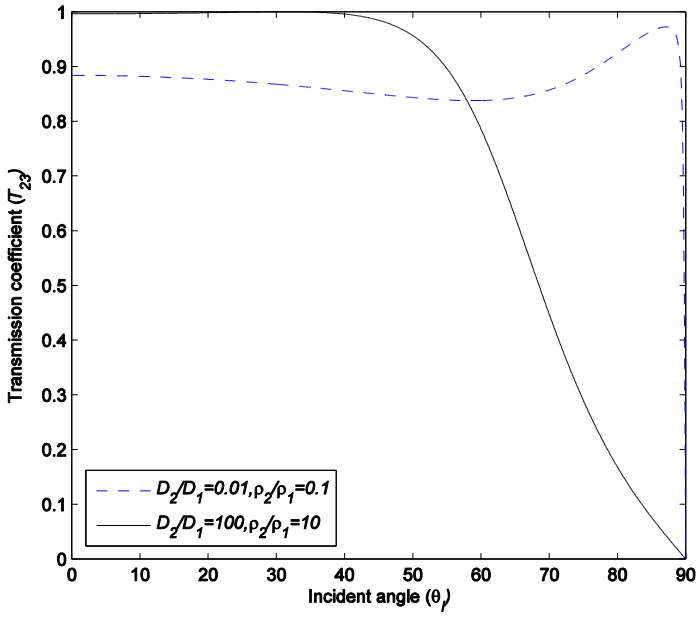

Figure 2.25: Transmission coefficient at I-23 vs the incident angle for medium 2 made of soft elastic (ρ_2/ρ_1 = 0.1 and D_2/D_1= 0.01) and hard elastic (ρ_2/ρ_1 = 10 and D_2/D_1= 100) compared to medium 1

Figure 2.26, Figure 2.27, and Figure 2.28 show the reflection coefficients at the interface I-12 against frequency ($k_2 b$) for the flexural rigidity ratios D_2/D_1 = 1, 0.01, and 100. The density ratio is set to 1. It can be observed that as the material in the medium 2 (strip) becomes softer compared to medium 1, there are many resonance peaks over the frequency range. As the material in medium 2 becomes stiffer, the resonance can be seen only at very low frequencies.

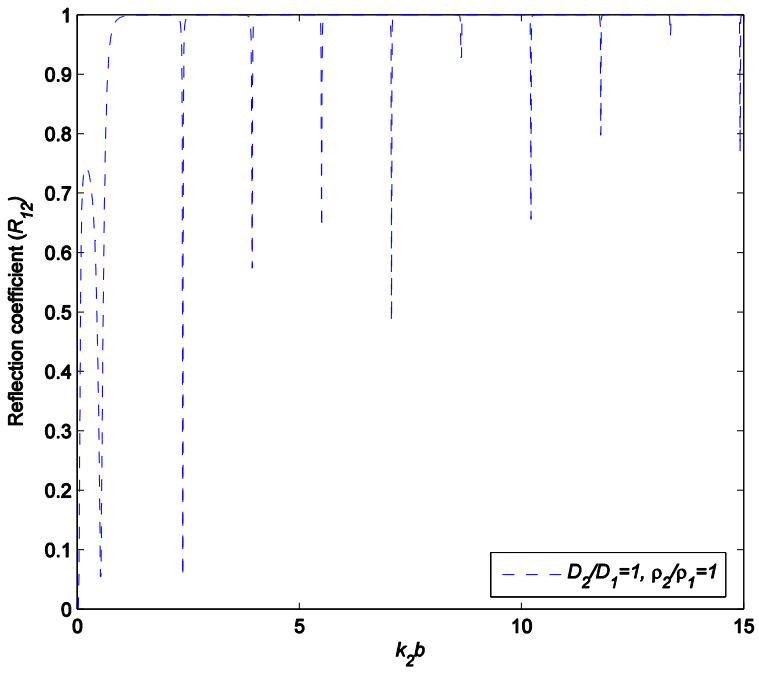

Figure 2.26: Reflection coefficient at I-12 vs k_2b (mediums 1 & 2 are assumed to be made of same material)

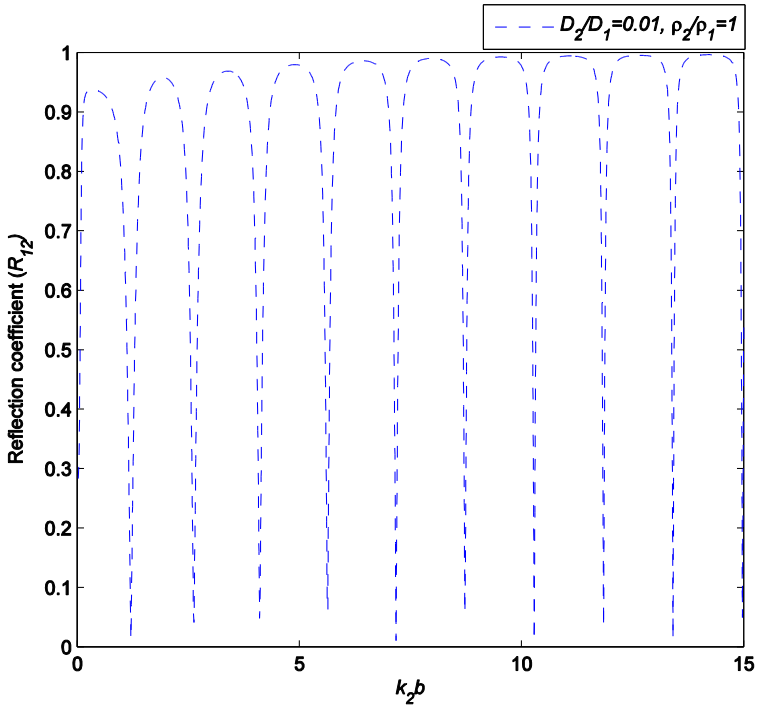

Figure 2.27: Reflection coefficient at I-12 vs k_2b (D_2/D_1= 0.01 and ρ_2/ρ_1 = 0.1)

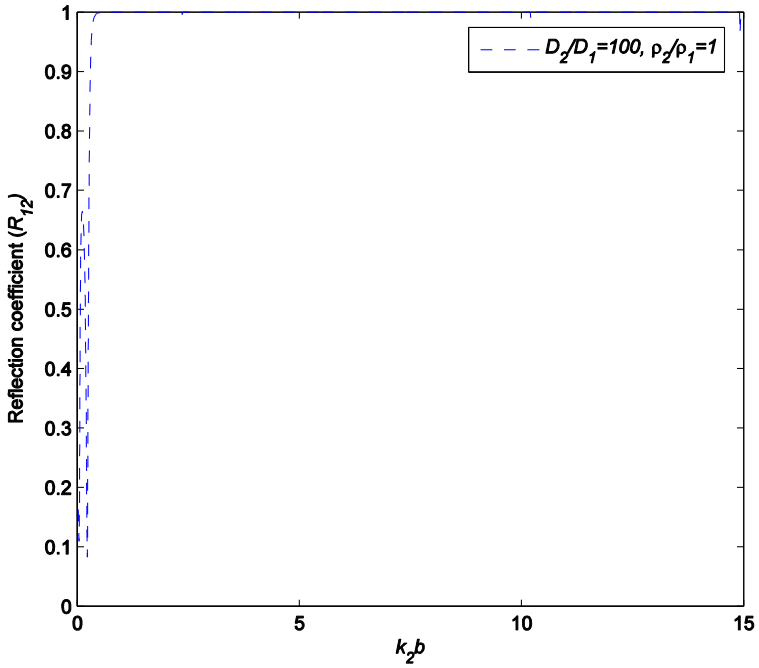

Figure 2.28: Reflection coefficient at I-12 vs k_2b (D_2/D_1= 100 and ρ_2/ρ_1 = 0.1)

Figure 2.29 and Figure 2.30 show the reflection coefficients at the interface I-12 against frequency ($k_2 b$) for the density ratios ρ_2/ρ_1 = 0.01, and 100. The flexural rigidity ratio is set to 1. It can be observed that as the material in the medium 2 becomes less denser compared to medium 1, there are more resonance peaks over frequency range. As the material in medium 2 becomes denser, the number of resonance peaks reduces.

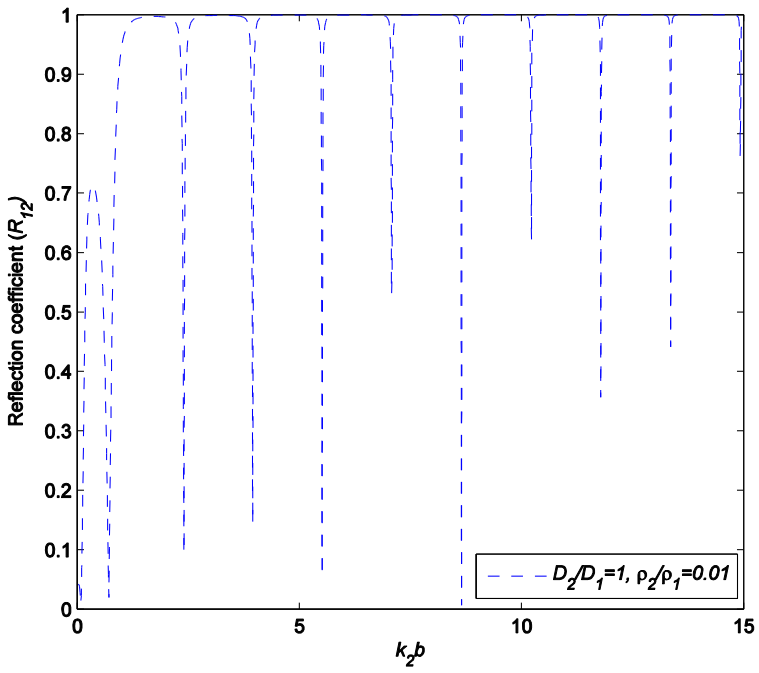

Figure 2.29: Reflection coefficient at I-12 vs k_2b (D_2/D_1= 1 and ρ_2/ρ_1 = 0.01)

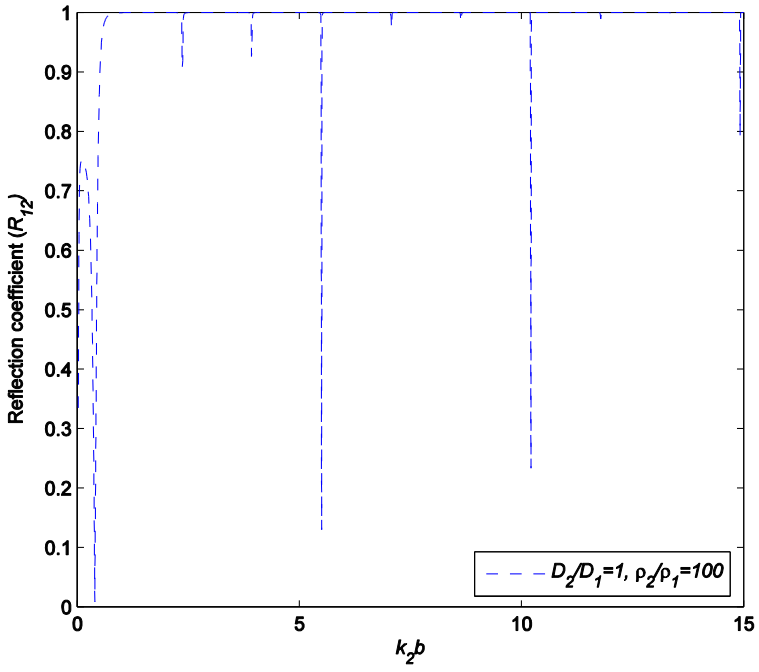

Figure 2.30: Reflection coefficient at I-12 vs k_2b (D_2/D_1= 1 and ρ_2/ρ_1 = 100)

Figure 2.31 shows the reflection coefficients at the interface I-12 against frequency (k_2b) for two cases where medium 2 (strip) is considered a hard elastic material (ρ_2/ρ_1 = 10 and D_2/D_1 = 100) or soft elastic (ρ_2/ρ_1 = 0.1 and D_2/D_1 = 0.01) compared to medium 1. It can be observed that in the case where medium 2 is soft, there are many resonance peaks all over the frequency range. There are only a few resonance peaks at the lower frequencies when the material of the strip is hard elastic compared medium 1.

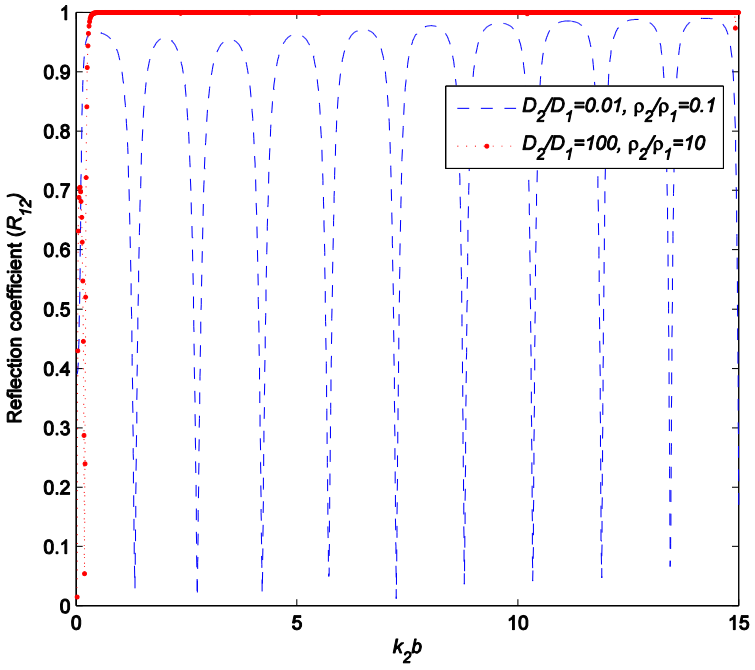

Figure 2.31: Reflection coefficient at I-12 vs k_2b for medium 2 made of soft elastic (ρ_2/ρ_1 = 0.1 and D_2/D_1=0.01) and hard elastic (ρ_2/ρ_1 = 10 and D_2/D_1= 100)

2.4 Flexural Wave Scattering by a Single Solid Cylindrical Inclusion in a Thin Plate of Infinite Size

In this section, a method of solution to characterize the multiple scattering of the flexural waves in an infinite plate with a cylindrical inclusion has been described. Closed form solutions have been obtained and validated against previously published literature. The far field scattering patterns and the dynamic stress concentration factors around the inclusions have been discussed. The effect of the material properties of the inclusion and plate on the dynamic stress concentration factor has been discussed.

Consider an infinite thin plate (medium 1) with a cylindrical inclusion (medium 2) of radius 'a' which is perfectly bonded and aligned at the origin of the coordinate system as shown in Figure 2.1. Assume medium 1 is made of material 1 with material properties density ρ_1,

Young's modulus E_1, and Poisson's ratio $\nu_1$and medium 2 has material properties density ρ_2, Young's modulus E_2, and Poisson's ratio ν_2.

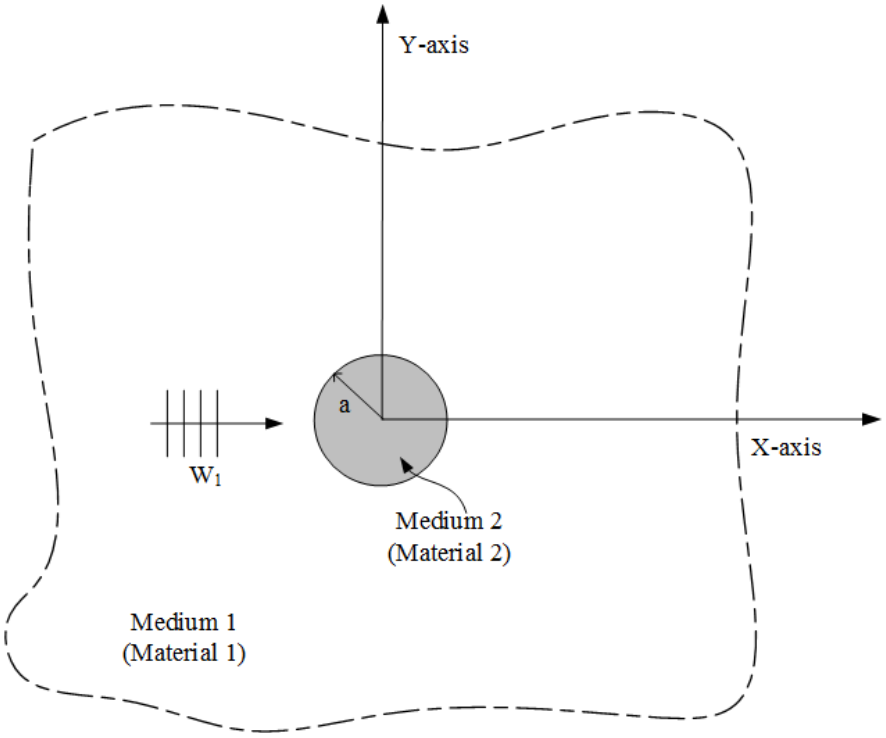

Figure 2.32: Infinite thin plate with a circular inclusion at the center

Based on the Kirchhoff's thin plate theory and its related assumptions, the governing equation of motion that describes the transverse displacement w in a thin plate shown in equation (2.30) is re-written below:

$$\mathrm{D}\nabla^4 w + \rho h \frac{\partial^2 w}{\partial t^2} = p \tag{2.152}$$

where

$$\nabla^4( ) = \frac{\partial^4}{\partial x^4} + 2\frac{\partial^4}{\partial x^2 \partial y^2} + \frac{\partial^4}{\partial y^4}$$

is called the biharmonic operator, ρ is the density, h is the plate thickness, $D = \frac{Eh^3}{12(1-\nu^2)}$ is the flexural rigidity of the plate, E denotes the Young's modulus, ν is the Poisson's ratio.

Assuming a time harmonic behavior $w(x,y,t) = w(x,y)e^{-\hat{\imath}\omega t}$ and no external force, equation (2.152) takes the form of

$$(\nabla^2\nabla^2 - k^4)w = (\nabla^2 - k^2)(\nabla^2 + k^2)w = 0 \tag{2.153}$$

where

$$k^4 = \rho h\omega^2/D$$

The solution of equation (2.153) admits to the representation

$$w = w_1 + w_2 \tag{2.154}$$

where w_1 and w_2 are the solutions of the following equations

$$(\nabla^2 + k^2)w_1 = 0 \tag{2.155}$$

$$(\nabla^2 - k^2)w_2 = 0 \tag{2.156}$$

Equations (2.155) and (2.156) represent the Helmholtz equation and the modified Helmholtz equation. The part of the flexural wave that travels in the plate is represented by w_1, while w_2 represents the wave that attenuates as it propagates. In polar coordinate system (r,θ), the general solution of the Helmholtz and modified Helmholtz are cylindrical wave functions or Bessel functions [54]. The following forms of cylindrical functions are often used: the Bessel function of the first kind $J_n(kr)$ can be used to describe source-less waves, such as the incident wave for scattering problem or waves in the region containing the origin of the coordinate system. $Y_n(kr)$ is the Bessel function of the second kind and is suitable for describing waves in the region excluding the origin. ${H_n}^{(1)}(kr)$ and ${H_n}^{(2)}(kr)$ are Hankel functions of the first and second kind of order n used to represent the outgoing and incoming waves respectively.

Consider a unit amplitude plane wave W_1 traveling along the *x*-axis impinges onto the circular inclusion (also called as a scatterer) as shown in Figure 2.32 and can be expressed as

$$w^{\text{inc}} = e^{\hat{\imath}kr\cos\theta} = \sum_{n=-\infty}^{\infty} \hat{\imath}^n J_n(kr)\, e^{\hat{\imath}n\theta} \tag{2.157}$$

The total scattered wave originating from the scatterer can be described as

$$w^{\text{scr}} = \sum_{n=-\infty}^{\infty} [A_n H_n{}^{(1)}(kr) + B_n K_n(kr)] e^{\hat{\imath}n\theta} \tag{2.158}$$

where $H_n{}^{(1)}(.)$ is the Hankel function of the first kind, and $K_n(.)$ is the modified Bessel function of the second kind of order n respectively. As discussed above, the wave consists of two parts: $H_n{}^{(1)}(.)$ represents the propagating part, and $K_n(.)$ represents the wave attenuating as it progresses. The total wave in medium 1 is the sum of the incident and the scattered wave represented by

$$w^{\text{tot}} = w^{\text{inc}} + w^{\text{scr}}$$

$$w^{\text{tot}} = \sum_{n=-\infty}^{\infty} \hat{\imath}^n J_n(k_1 r)\, e^{\hat{\imath}n\theta} + \sum_{n=-\infty}^{\infty} [A_n H_n(k_1 r) + B_n K_n(k_1 r)] e^{\hat{\imath}n\theta} \tag{2.159}$$

The total transmitted wave in medium 2 (scatterer) can be described as

$$w^{\text{trm}} = w_1^{\text{trm}} + w_2^{\text{trm}}$$

$$w^{\text{trm}} = \sum_{n=-\infty}^{\infty} [C_n J_n(k_2 r) + D_n I_n(k_2 r)] e^{\hat{\imath}n\theta} \tag{2.160}$$

At the interface between medium 1 and medium 2 ($r = a$), the displacement (w), normal derivative of the displacement ($\partial w/\partial r$), the bending moment (M_r) and the shear force(V_r) must be continuous. The bending moment (M_r) and the shear force(V_r) are

$$M_r = -D\left[\frac{\partial^2 w}{\partial r^2} + \nu\left(\frac{1}{r}\frac{\partial w}{\partial r} + \frac{1}{r^2}\frac{\partial^2 w}{\partial \theta^2}\right)\right] \tag{2.161}$$

$$V_r = -D\left[\frac{\partial}{\partial r}\nabla^2 w + (1-\nu)\frac{1}{r^2}\frac{\partial^2}{\partial \theta^2}\left(\frac{\partial w}{\partial r} - \frac{w}{r}\right)\right] \tag{2.162}$$

These give the following continuity conditions at the interface of the two materials:

$$w^{\mathrm{tot}}|_{r=a} = \ w^{\mathrm{trm}}|_{r=a} \tag{2.163}$$

$$\left[\frac{\partial w^{\mathrm{tot}}}{\partial r}\right]|_{r=a} = \ \left[\frac{\partial w^{\mathrm{trm}}}{\partial r}\right]|_{r=a} \tag{2.164}$$

$$\left[-D_1\frac{\partial^2 w^{\mathrm{tot}}}{\partial r^2} - D_1\nu_1\left(\frac{1}{r}\frac{\partial w^{\mathrm{tot}}}{\partial r} + \frac{1}{r^2}\frac{\partial^2 w^{\mathrm{tot}}}{\partial \theta^2}\right)\right]|_{r=a} = \left[-D_2\frac{\partial^2 w^{\mathrm{trm}}}{\partial r^2} - D_2\nu_2\left(\frac{1}{r}\frac{\partial w^{\mathrm{trm}}}{\partial r} + \frac{1}{r^2}\frac{\partial^2 w^{\mathrm{trm}}}{\partial \theta^2}\right)\right]|_{r=a} \tag{2.165}$$

$$\left[-D_1\frac{\partial}{\partial r}\nabla^2 w^{\mathrm{tot}} - D_1(1-\nu_1)\frac{1}{r^2}\frac{\partial^2}{\partial \theta^2}\left(\frac{\partial w^{\mathrm{tot}}}{\partial r} - \frac{w^{\mathrm{tot}}}{r}\right)\right]|_{r=a} = \left[-D_2\frac{\partial}{\partial r}\nabla^2 w^{\mathrm{trm}} - D_2(1-\nu_2)\frac{1}{r^2}\frac{\partial^2}{\partial \theta^2}\left(\frac{\partial w^{\mathrm{trm}}}{\partial r} - \frac{w^{\mathrm{trm}}}{r}\right)\right]|_{r=a} \tag{2.166}$$

Substituting the equations (2.159) and (2.160) in the continuity conditions (2.163) through (2.166) and re-arranging the terms will result in the following four set of equations shown below in the matrix form:

$$\begin{bmatrix} (AW)_n & (BW)_n & (CW)_n & (DW)_n \\ (DAW)_n & (DBW)_n & (DCW)_n & (DDW)_n \\ (AM)_n & (BM)_n & (CM)_n & (DM)_n \\ (AV)_n & (AV)_n & (AV)_n & (DV)_n \end{bmatrix}\begin{bmatrix} A_n \\ B_n \\ C_n \\ D_n \end{bmatrix} = \begin{bmatrix} T_W \\ T_{WD} \\ T_M \\ T_V \end{bmatrix} \tag{2.167}$$

where

$$(AW)_n = H_n{}^{(1)}(k_1 a)$$

$$(BW)_n = K_n(k_1 a)$$

$$(BW)_n = -J_n(k_2 a)$$

$$(BW)_n = -I_n(k_2 a)$$

$$(DAW)_n = k_1 H_n{}^{(1)\prime}(k_1 a)$$

$$(DBW)_n = k_1 K_n{}'(k_1 a)$$

$$(DCW)_n = -k_2 J_n{}'(k_2 a)$$

$$(DDW)_n = -k_2 I_n{}'(k_2 a)$$

$$(AM)_n = -D_1 {k_1}^2 {H_n^{(1)}}''(k_1 a) - \frac{D_1 \nu_1 k_1}{a} {H_n^{(1)}}'(k_1 a) + \frac{D_1 \nu_1 n^2}{a^2} H_n^{(1)}(k_1 a)$$

$$(BM)_n = -D_1 {k_1}^2 {K_n}''(k_1 a) - \frac{D_1 \nu_1 k_1}{a} {K_n}'(k_1 a) + \frac{D_1 \nu_1 n^2}{a^2} K_n(k_1 a)$$

$$(\mathrm{CM})_\mathrm{n} = \mathrm{D_2 {k_2}^2 {J_n}''(k_2 a) + \frac{D_2 \nu_2 k_2}{a} {J_n}'(k_2 a) - \frac{D_2 \nu_2 n^2}{a^2} J_n(k_2 a)}$$

$$(DM)_n = D_2 {k_2}^2 {I_n}''(k_2 a) + \frac{D_2 \nu_2 k_2}{a} {I_n}'(k_2 a) - \frac{D_2 \nu_2 n^2}{a^2} I_n(k_2 a)$$

$$(AV)_n = -D_1 {k_1}^3 {H_n^{(1)}}'''(k_1 a) + \frac{D_1 k_1}{a^2} {H_n^{(1)}}'(k_1 a) - \frac{D_1 {k_1}^2}{a} {H_n^{(1)}}''(k_1 a)$$
$$- \frac{2 D_1 n^2}{a^3} H_n^{(1)}(k_1 a) + \frac{D_1 n^2 k_1}{a^2} {H_n^{(1)}}'(k_1 a)$$
$$+ \frac{D_1 (1-\nu_1) n^2 k_1}{a^2} {H_n^{(1)}}'(k_1 a) - \frac{D_1 (1-\nu_1) n^2}{a^3} H_n^{(1)}(k_1 a)$$

$$(BV)_n = -D_1 {k_1}^3 {K_n}'''(k_1 a) + \frac{D_1 k_1}{a^2} {K_n}'(k_1 a) - \frac{D_1 {k_1}^2}{a} {K_n}''(k_1 a)$$
$$- \frac{2 D_1 n^2}{a^3} K_n(k_1 a) + \frac{D_1 n^2 k_1}{a^2} {K_n}'(k_1 a)$$
$$+ \frac{D_1 (1-\nu_1) n^2 k_1}{a^2} {K_n}'(k_1 a) - \frac{D_1 (1-\nu_1) n^2}{a^3} K_n(k_1 a)$$

$$(CV)_n = D_2 {k_2}^3 {J_n}'''(k_2 a) - \frac{D_2 k_2}{a^2} {J_n}'(k_2 a) + \frac{D_2 {k_2}^2}{a} {J_n}''(k_2 a) + \frac{2 D_2 n^2}{a^3} J_n(k_2 a)$$
$$- \frac{D_2 n^2 k_2}{a^2} {J_n}'(k_2 a) - \frac{D_2 (1-\nu_2) n^2 k_2}{a^2} {J_n}'(k_2 a)$$
$$+ \frac{D_2 (1-\nu_2) n^2}{a^3} J_n(k_2 a)$$

$$(DV)_n = D_2 {k_2}^3 I'''(k_2 a) - \frac{D_2 k_2}{a^2} I'(k_2 a) + \frac{D_2 {k_2}^2}{a} {I_n}''(k_2 a) + \frac{2 D_2 n^2}{a^3} I_n(k_2 a)$$
$$- \frac{D_2 n^2 k_2}{a^2} {I_n}'(k_2 a) - \frac{D_2 (1-\nu_2) n^2 k_2}{a^2} {I_n}'(k_2 a)$$
$$+ \frac{D_2 (1-\nu_2) n^2}{a^3} I_n(k_2 a)$$

$$T_W = -\hat{\imath}^n J_n(k_1 a)$$

$$T_{DW} = -k_1 \hat{\imath}^n {J_n}'(k_1 a)$$

$$T_M = D_1 {k_1}^2 \hat{\imath}^n J_n{}''(k_1 a) + \frac{D_1 \nu_1 k_1}{a} \hat{\imath}^n J_n{}'(k_1 a) - \frac{D_1 \nu_1 n^2}{a^2} \hat{\imath}^n J_n(k_1 a)$$

$$T_V = D_1 {k_1}^3 \hat{\imath}^n J_n{}'''(k_1 a) - \frac{D_1 k_1}{a^2} \hat{\imath}^n J_n{}'(k_1 a) + \frac{D_1 {k_1}^2}{a} \hat{\imath}^n J_n{}''(k_1 a)$$
$$+ \hat{\imath}^n \frac{2D_1 n^2}{a^3} J_n(k_1 a) - \frac{D_1 n^2 k_1}{a^2} \hat{\imath}^n J_n{}'(k_1 a)$$
$$- \frac{D_1 (1-\nu_1) n^2 k_1}{a^2} \hat{\imath}^n J_n{}'(k_1 a) + \frac{D_1 (1-\nu_1) n^2}{a^3} \hat{\imath}^n J_n(k_1 a)$$

The two limits of interest are: the rigid inclusion and the inclusion being a hole. For both these limits, only the total wave field (w^{tot}) for $r \geq a$ is meaningful. The rigid inclusion corresponds to the clamped condition at $r = a$ which corresponds to no displacement and slope at the boundary $r = a$. For the rigid inclusion case, the matrix in the equation (2.167) simplifies to the following 2×2 matrix (upper left square matrix) shown below:

$$\begin{bmatrix} (AW)_n & (BW)_n \\ (DAW)_n & (DBW)_n \end{bmatrix} \begin{bmatrix} A_n \\ B_n \end{bmatrix} = \begin{bmatrix} T_W \\ T_{WD} \end{bmatrix} \tag{2.168}$$

where

$$(AW)_n = {H_n}^{(1)}(k_1 a)$$

$$(BW)_n = K_n(k_1 a)$$

$$(DAW)_n = k_1 {H_n}^{(1)'}(k_1 a)$$

$$(DBW)_n = k_1 {K_n}'(k_1 a)$$

$$T_W = -\hat{\imath}^n J_n(k_1 a)$$

$$T_{DW} = -k_1 \hat{\imath}^n J_n{}'(k_1 a)$$

The other limit of interest is the very soft inclusion. This corresponds to inclusion being a hole, which implies no bending moment and shear force at $r = a$. So, for this case the matrix in the equation (2.167) simplifies to the following 2×2 matrix shown below:

$$\begin{bmatrix} (AM)_n & (BM)_n \\ (AV)_n & (BV)_n \end{bmatrix} \begin{bmatrix} A_n \\ B_n \end{bmatrix} = \begin{bmatrix} T_M \\ T_V \end{bmatrix} \tag{2.169}$$

where

$$(AM)_n = -D_1 {k_1}^2 {H_n}^{(1)''}(k_1 a) - \frac{D_1 \nu_1 k_1}{a} {H_n}^{(1)'}(k_1 a) + \frac{D_1 \nu_1 n^2}{a^2} {H_n}^{(1)}(k_1 a)$$

$$(BM)_n = -D_1 {k_1}^2 {K_n}''(k_1 a) - \frac{D_1 \nu_1 k_1}{a} {K_n}'(k_1 a) + \frac{D_1 \nu_1 n^2}{a^2} K_n(k_1 a)$$

$$\begin{aligned}(AV)_n = {} & -D_1 {k_1}^3 {H_n}^{(1)'''}(k_1 a) + \frac{D_1 k_1}{a^2} {H_n}^{(1)'}(k_1 a) - \frac{D_1 {k_1}^2}{a} {H_n}^{(1)''}(k_1 a) \\ & - \frac{2 D_1 n^2}{a^3} {H_n}^{(1)}(k_1 a) + \frac{D_1 n^2 k_1}{a^2} {H_n}^{(1)'}(k_1 a) \\ & + \frac{D_1 (1-\nu_1) n^2 k_1}{a^2} {H_n}^{(1)'}(k_1 a) - \frac{D_1 (1-\nu_1) n^2}{a^3} {H_n}^{(1)}(k_1 a)\end{aligned}$$

$$\begin{aligned}(BV)_n = {} & -D_1 {k_1}^3 {K_n}'''(k_1 a) + \frac{D_1 k_1}{a^2} {K_n}'(k_1 a) - \frac{D_1 {k_1}^2}{a} {K_n}''(k_1 a) \\ & - \frac{2 D_1 n^2}{a^3} K_n(k_1 a) + \frac{D_1 n^2 k_1}{a^2} {K_n}'(k_1 a) \\ & + \frac{D_1 (1-\nu_1) n^2 k_1}{a^2} {K_n}'(k_1 a) - \frac{D_1 (1-\nu_1) n^2}{a^3} K_n(k_1 a)\end{aligned}$$

$$T_M = D_1 {k_1}^2 \hat{\imath}^n {J_n}''(k_1 a) + \frac{D_1 \nu_1 k_1}{a} \hat{\imath}^n {J_n}'(k_1 a) - \frac{D_1 \nu_1 n^2}{a^2} \hat{\imath}^n J_n(k_1 a)$$

$$\begin{aligned}T_V = {} & D_1 {k_1}^3 \hat{\imath}^n {J_n}'''(k_1 a) - \frac{D_1 k_1}{a^2} \hat{\imath}^n {J_n}'(k_1 a) + \frac{D_1 {k_1}^2}{a} \hat{\imath}^n {J_n}''(k_1 a) \\ & + \hat{\imath}^n \frac{2 D_1 n^2}{a^3} J_n(k_1 a) - \frac{D_1 n^2 k_1}{a^2} \hat{\imath}^n {J_n}'(k_1 a) \\ & - \frac{D_1 (1-\nu_1) n^2 k_1}{a^2} \hat{\imath}^n {J_n}'(k_1 a) + \frac{D_1 (1-\nu_1) n^2}{a^3} \hat{\imath}^n J_n(k_1 a)\end{aligned}$$

The above set of equations for each of the cases of general, rigid inclusion and hole inclusion have been programmed in MATLAB and the results were obtained. One of the important far-field measures is the far-field scattering amplitude and is defined as the angular

distribution of the amplitude of the scattered wave field. For a generic wave field represented by ϕ, this is defined as,

$$\lim_{r\to\infty} \phi^{\text{scr}} = f(\theta)H_0(kr) \qquad \text{or} \qquad f(\theta) = \lim_{r\to\infty} \frac{\phi^{\text{scr}}}{H_0(kr)} \tag{2.170}$$

In this case as $r \to \infty$, using the relation of Hankel function of the first kind as $r \to \infty$, the scattered wave can be simplified as shown in equation below

$$\phi^{\text{scr}} = \sum_{n=-\infty}^{\infty} A_n \sqrt{\frac{2}{kr\pi}}\, e^{i(kr-(2n+1)\pi/4)}\, e^{in\theta} \tag{2.171}$$

From the properties of Bessel functions

$$\lim_{r\to\infty} H_0(kr) = \sqrt{\frac{2}{kr\pi}}\, e^{i(kr-\pi/4)} \tag{2.172}$$

Substituting the relations (2.171) and (2.172), the far-field scattering amplitude simplifies as

$$f(\theta) = \sum_{n=-\infty}^{\infty} A_n\, e^{in(\theta-\pi/2)} \tag{2.173}$$

The far-field scattering amplitude can be further simplified as,

$$f(\theta) = \sum_{n=-\infty}^{\infty} (-i)^n (A_n \cos n\theta + iA_n\, sinn\theta) \tag{2.174}$$

Comparing the equation (2.174) with far field amplitude from [55], A_n (in our case A_n) and $A_n{}'$(in our case iA_n) satisfy the following identity in equation shown below:

$$|A_0|^2 + Re\, A_0 + \sum_{n=-\infty}^{\infty} \left\{ \frac{|A_n|^2}{2} + \frac{|A_n{}'|^2}{2} + Re[(-1)^n A_n] \right\} = 0 \tag{2.175}$$

The far-field scattering amplitude has been plotted against ka for the hole inclusion for two different frequencies $ka = 1$ and $ka = 0.5$ and is shown in Figure 2.33 (a). The polar plots in Figure 2.33 (a) are compared and match with the polar plots published in Ref. [55] shown in Figure 2.33 (b).

Figure 2.34 (a) shows the plots of far-field scattering amplitude plotted against ka for a rigid inclusion for two different frequencies $ka = 1$ and $ka = 0.5$. The polar plots in Figure 2.34 (a) are compared and match with the polar plots published in Ref. [55] shown in Figure 2.34 (b).

Figure 2.35 (a) shows the plots of far-field scattering amplitude plotted against ka for both the rigid inclusion and hole cases for the same $ka = 5$. The polar plots in Figure 2.35 (a) are compared and match with the polar plots published in Ref. [55] shown in Figure 2.35 (b).

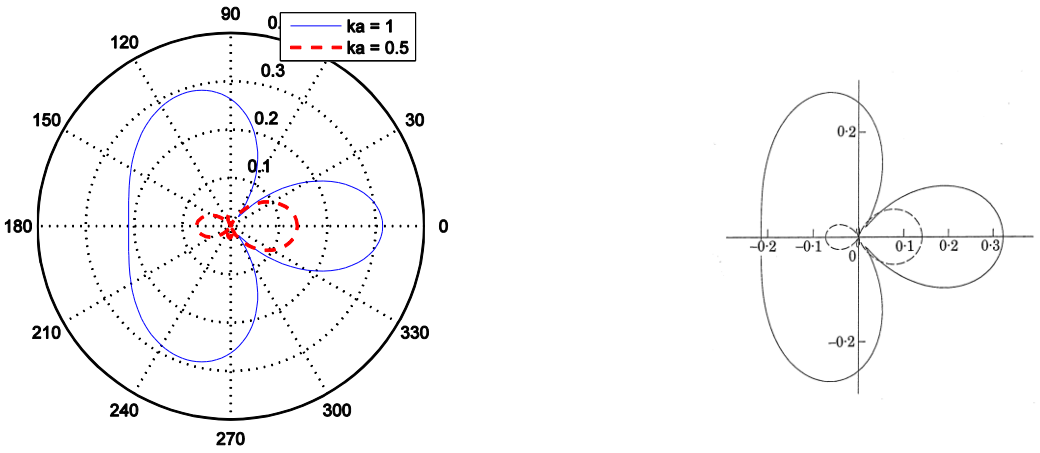

(a) Current work (b) Ref. [55]

Figure 2.33: Polar plots of the far field scattering amplitude for infinite steel plate of 1" thick with a circular hole for frequencies ka=1 (solid line) and ka=0.5 (dashed line)

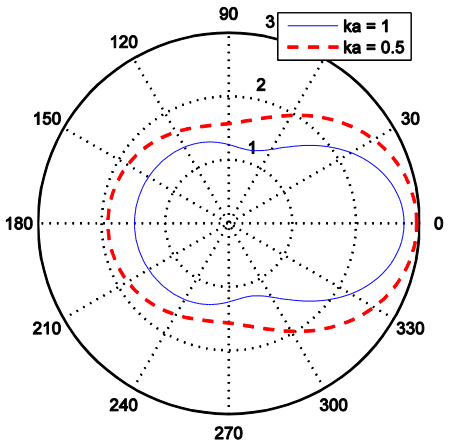

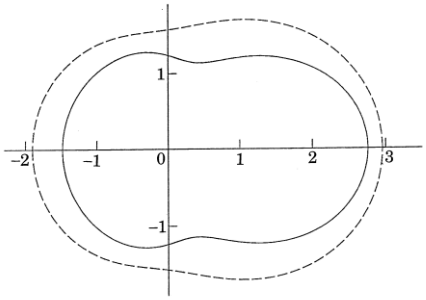

(a) Current work (b) Ref. [55]

Figure 2.34: Polar plots of the far field scattering amplitude for infinite steel plate of 1" thick with rigid inclusion for frequencies ka=0.5 (dashed line) and ka=1 (solid line)

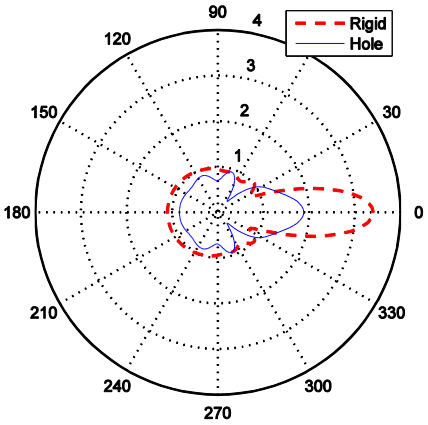

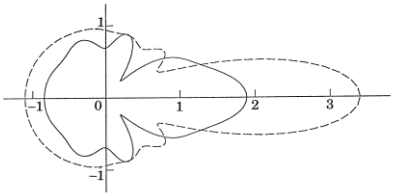

(c) Current work (d) Ref. [55]

Figure 2.35: Polar plots of the far field scattering amplitude for infinite steel plate of 1" thick with both hole (solid line) and rigid inclusion (dashed line) for ka=5

Figure 2.36 shows the polar plots of far-field scattering amplitude plotted against ka for the hole inclusion for different frequencies $ka = 5$, $ka = 1$, and $ka = 0.5$. It is observed from Figure 2.36 that the amplitude reduces to zero at lower frequencies and increases as the frequency increases on the case where the scatterer is a hole. Figure 2.37 shows the plots of far-field scattering amplitude plotted against ka for a rigid inclusion for different frequencies $ka = 5$, $ka = 2.5$, and $ka = 0.5$. Contrary to the hole as the inclusion, for the rigid inclusion case as the frequency reduces the amplitude increases. Also, the directionality of the scattered field reduces as the ka reduces. A clear directionality can be observed for the scattered field as the value of ka increases.

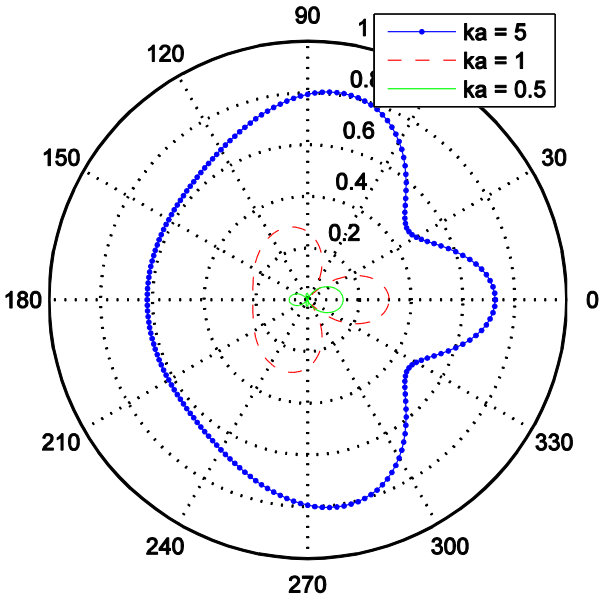

Figure 2.36: Polar plots of the far field scattering amplitude for infinite steel plate of 1" thick with a circular hole for ka=5 (dot dashed line), ka=1 (dashed line) and ka=0.5 (solid line)

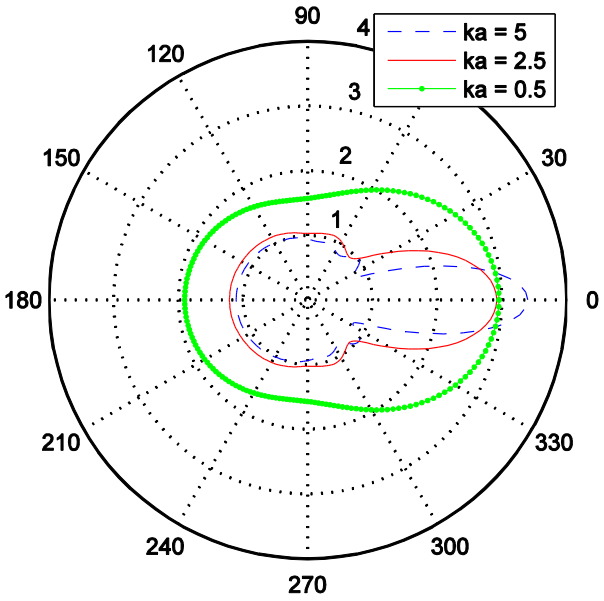

Figure 2.37: Polar plots of the far field scattering amplitude for infinite steel plate of 1" thick with rigid inclusion for ka=5 (dashed line), ka=2.5 (solid line) and ka=0.5 (dot dashed line)

The scattering cross-section is one of the scattering characteristics that is a measure of the interaction between the incident wave and the discontinuity of the medium of the propagation, i.e., the scatterer. It is defined as the ratio of the average energy flux associated with the scattered field to the average energy flux of incident wave. The scattering cross-section (σ^{sc}) is given by [55]

$$\sigma^{sc} = \frac{1}{2}\int_0^{2\pi} |f(\theta)|^2 \, d\theta \tag{2.176}$$

Using the incident wave, the scattered response and letting the contour tend to infinity, the scattered cross-section is simplified as [55]

$$\sigma^{sc} = -2\sqrt{\frac{\pi}{k}}\,\boldsymbol{Re} f(0) \tag{2.177}$$

Figure 2.38, Figure 2.39, and Figure 2.40 shows scattering cross-section over a frequency (k_1a) range of 1 to 15 for an infinite plate with hole, hard elastic and rigid inclusions respectively. The plate is made of composite material (flexural rigidity (D) = 2955.2 N.m, density (ρ) = 223.26 kg/m^3 and Poisson's ratio (ν = 0.4)) with a circular inclusion of 2" diameter. It can be observed that the scattering cross-section is zero at lower frequencies and increases with the frequency in the case of hole inclusion. The scattering cross-section increases without bound as the frequency tends to zero in both the rigid and hard elastic cases. It can be observed that at lower frequencies the scattering cross-section of the hard elastic (D_2/D_1=100 and ρ_2/ρ_1 =10) closely matches with the case of rigid inclusion. But as the frequency increases the scattering cross-section of hard elastic decreases and matches closely with the hole inclusion at higher frequencies. For the overall frequency range it can be observed that the rigid inclusion case achieves best scattering characteristics compared to the hole and hard elastic inclusion cases.

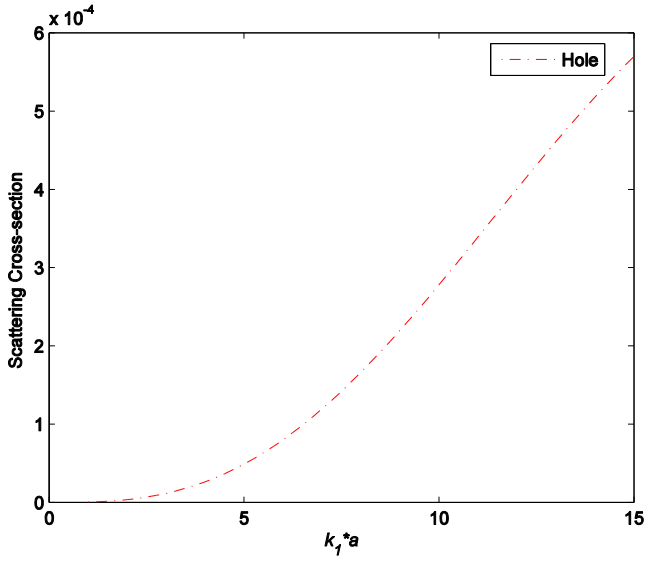

Figure 2.38: Scattering cross-section vs k_1a for composite sandwich panel with a hole inclusion

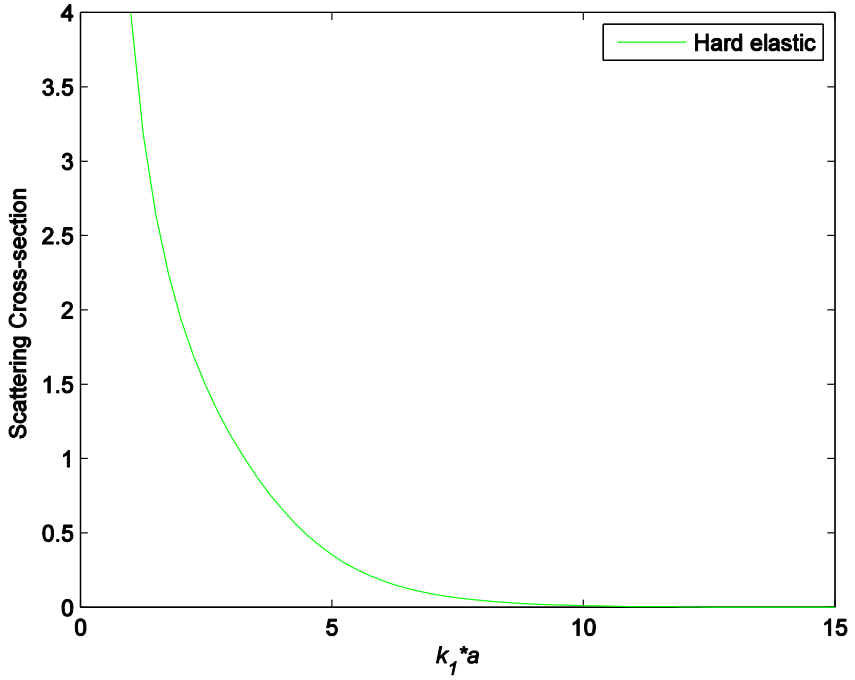

Figure 2.39: Scattering cross-section vs k_1a for composite sandwich panel with hard elastic inclusion (D_2/D_1=100 and ρ_2/ρ_1 =10)

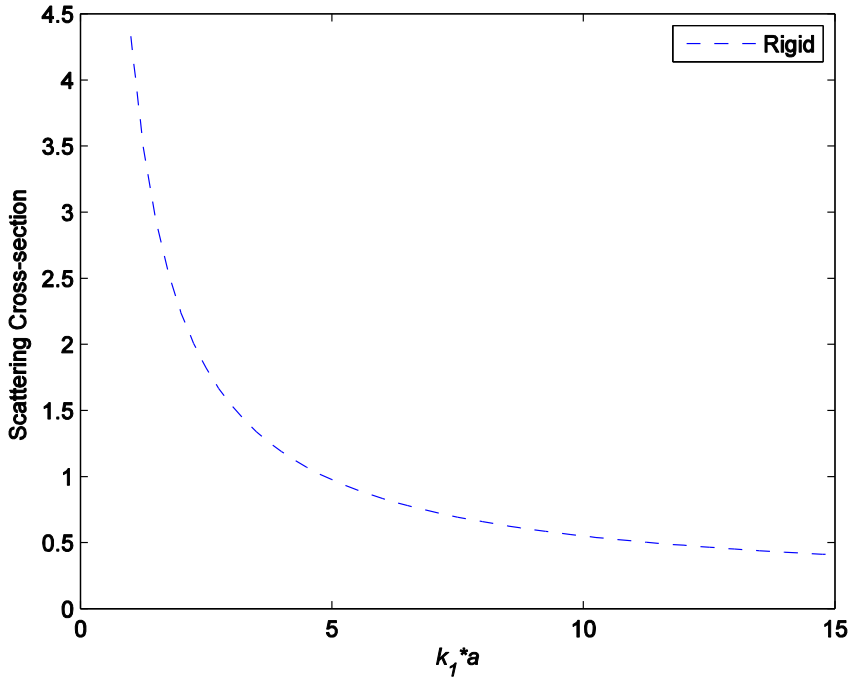

Figure 2.40: Scattering cross-section vs k_1a for composite sandwich panel with a rigid inclusion

The total wave distribution around the inclusion is explored for the cases of an hard elastic, rigid and hole inclusions to compare the reflection and attenuation of wave propagation. For this an infinite plate made of composite material (flexural rigidity (D) = 2955.2 N.m, density (ρ) = 223.26 kg/m^3 and Poisson's ratio (ν = 0.4)) with a circular inclusion of 2" diameter is considered. For the above mentioned three cases, the total wave distribution around the inclusion is plotted and compared for different frequencies. For each frequency the plots of hard elastic, rigid and hole inclusions, the same color scale is used for comparison. Figure 2.41, Figure 2.42, and Figure 2.43 show the plots of total wave distribution around the hole, elastic and rigid inclusion cases for a frequency ka=0.158 (1000Hz). In the hard elastic case, the material of the inclusion is stiffer than the plate material, D_2/D_1=100 and ρ_2/ρ_1 =10. Comparing Figure 2.41, and Figure 2.42, it can be observed that the case where the inclusion is a hole shows comparable reflection and attenuation in the direction of wave propagation with the hard elastic inclusion case. Figure 2.41, and Figure 2.43, show that the rigid inclusion has better reflection and attenuation in the direction of wave propagation compared with hole and elastic inclusion.

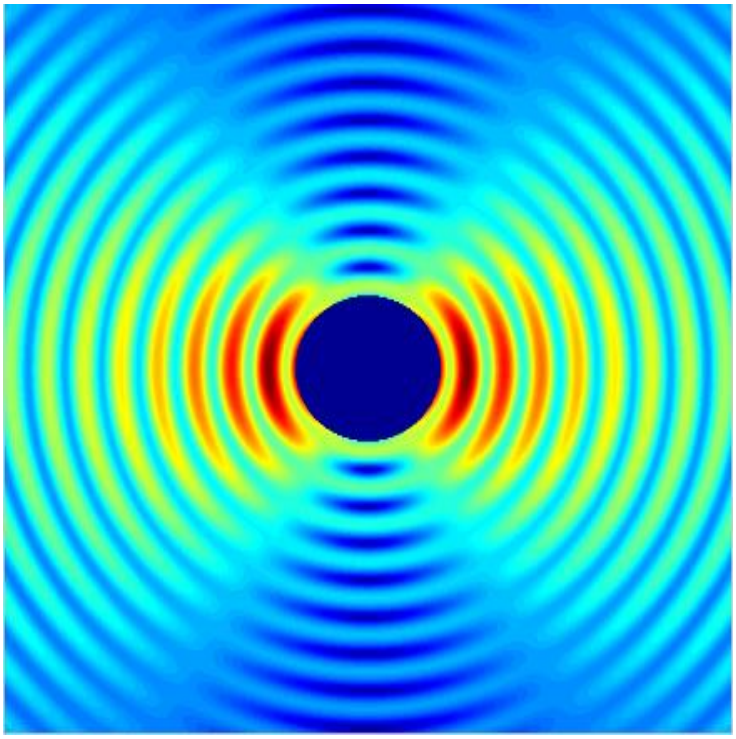

Figure 2.41: Total wave distribution around a hole inclusion for frequency ka=0.158

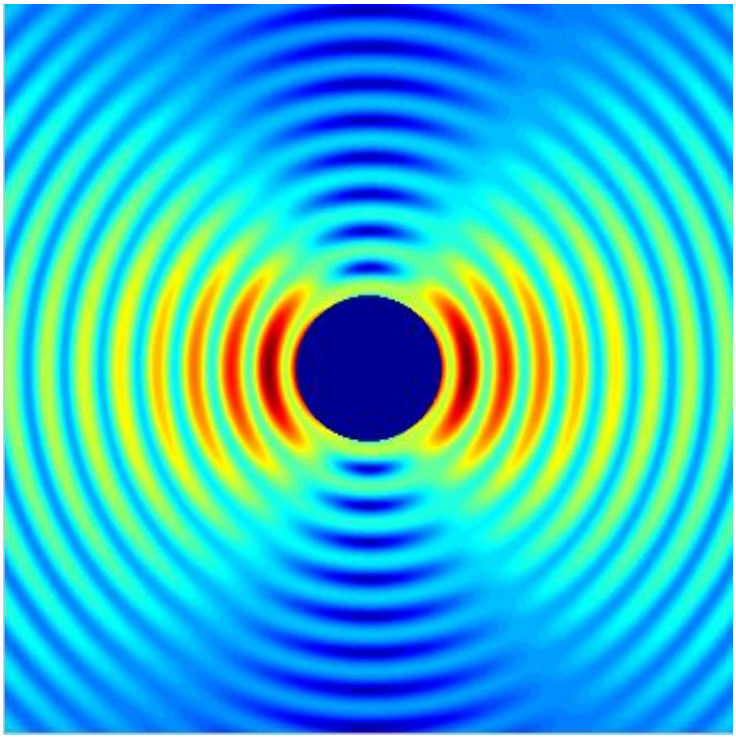

Figure 2.42: Total wave distribution around a hard elastic inclusion stiffer than the plate D_2/D_1=100 and ρ_2/ρ_1 =10 for frequency ka=0.158

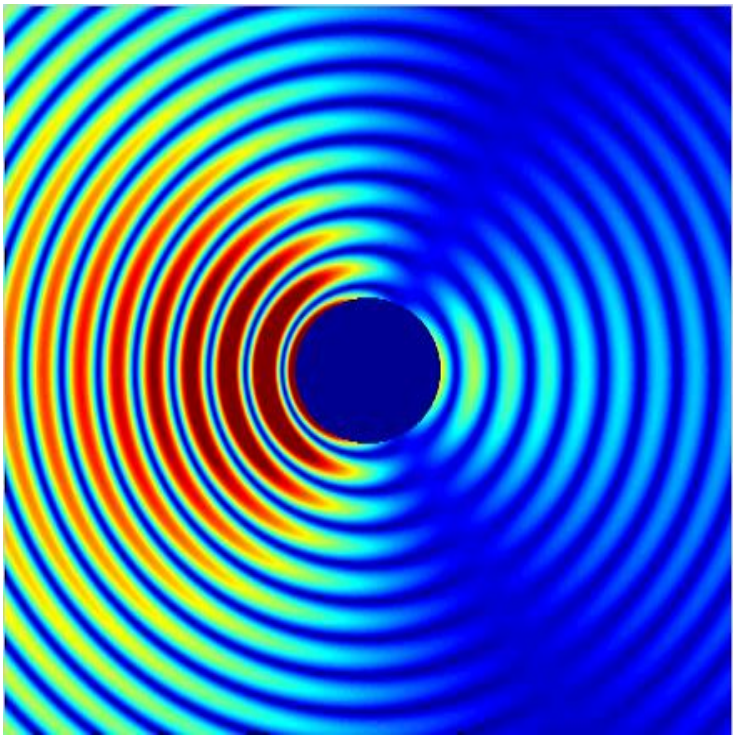

Figure 2.43: Total wave distribution around rigid inclusion for frequency ka=0.158

Figure 2.44, Figure 2.45, and Figure 2.46 show the plots of total wave distribution around the hole, hard elastic and rigid inclusion cases for a frequency ka=0.237 (3000Hz). In the hard elastic case, the material of the inclusion is stiffer than the plate material, D_2/D_1=100 and ρ_2/ρ_1 =10. Comparing Figure 2.44, Figure 2.45, and Figure 2.46, it can be observed that the rigid inclusion shows better reflection and attenuation in the direction of wave propagation compared with the hole and elastic inclusion.

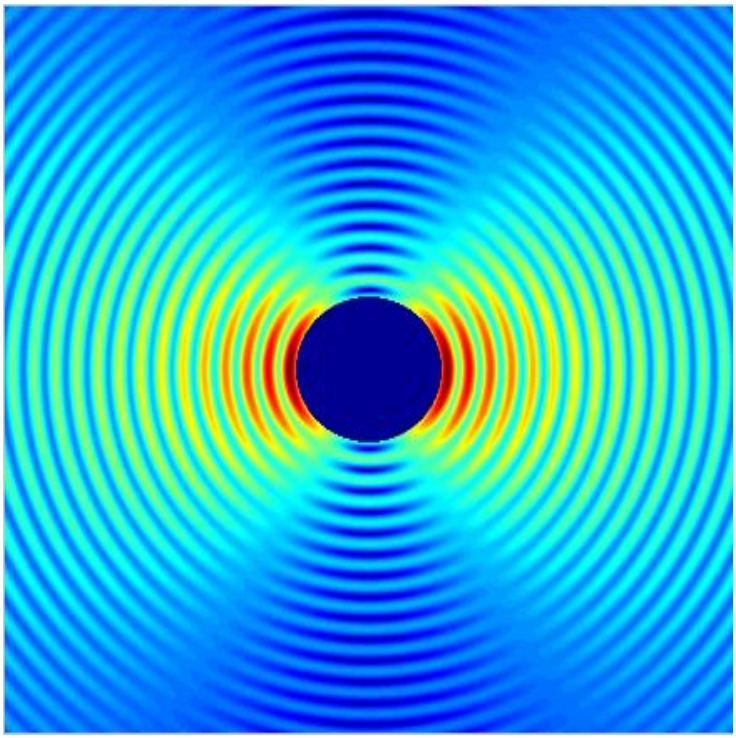

Figure 2.44: Total wave distribution around a hole inclusion for frequency ka=0.237

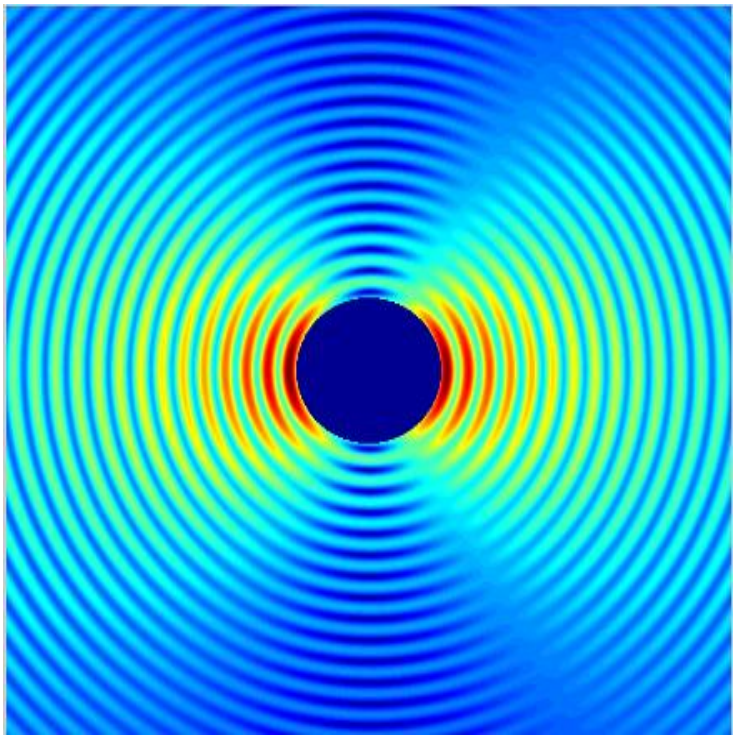

Figure 2.45: Total wave distribution around a hard elastic inclusion stiffer than the plate D_2/D_1=100 and ρ_2/ρ_1 =10 for frequency ka=0.237

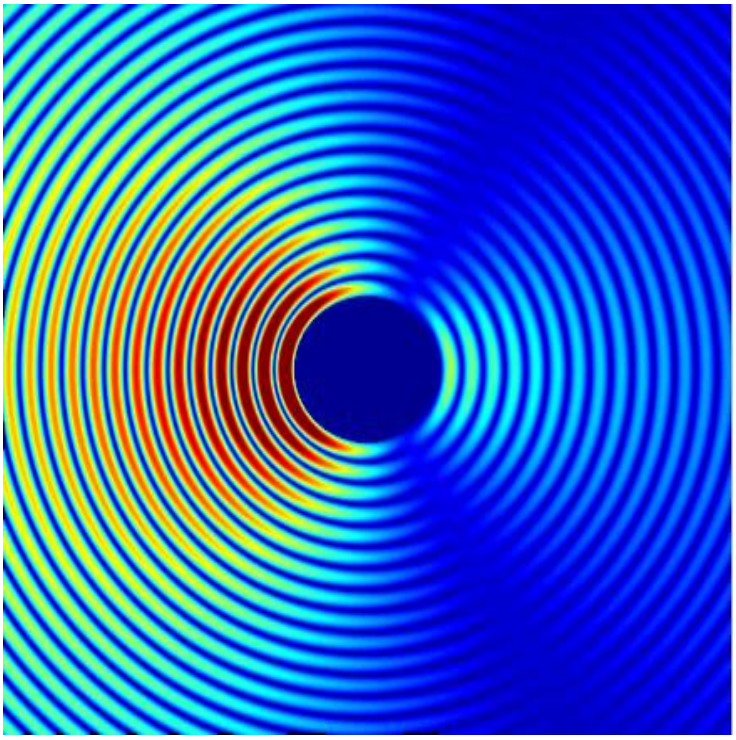

Figure 2.46: Total wave distribution around rigid inclusion for frequency ka=0.237

Figure 2.47, Figure 2.48, and Figure 2.49 show the plots of total wave distribution in the vicinity of the hole, hard elastic and rigid inclusion cases for a frequency ka=0.706 (5000Hz). In the elastic case, the material of the inclusion is stiffer than the plate material, D_2/D_1=100 and ρ_2/ρ_1 =10. Comparing Figure 2.47, Figure 2.48, and Figure 2.49, it can be observed that the rigid inclusion shows better reflection and attenuation in the direction of wave propagation compared with the hole and elastic inclusion.

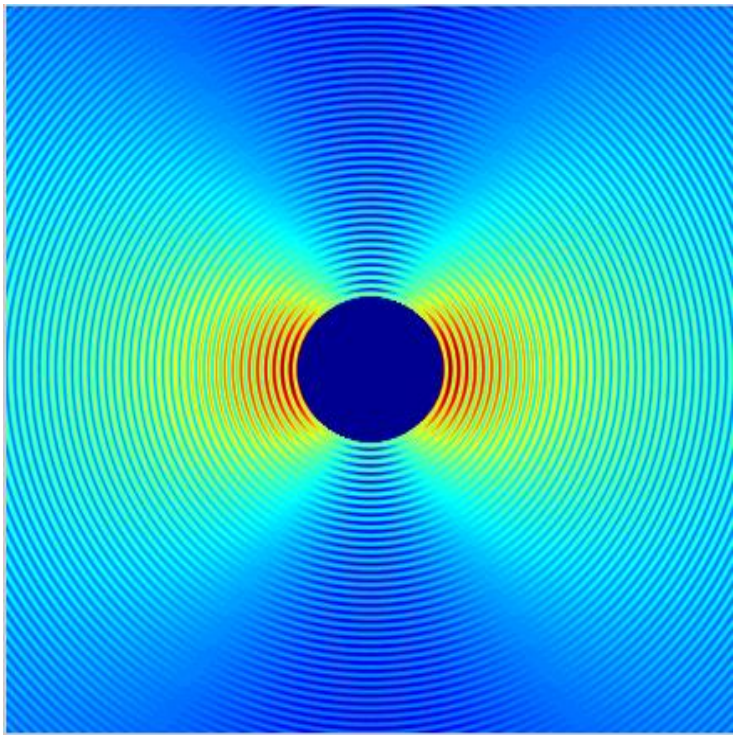

Figure 2.47: Total wave distribution around a hole inclusion for frequency ka=0.706

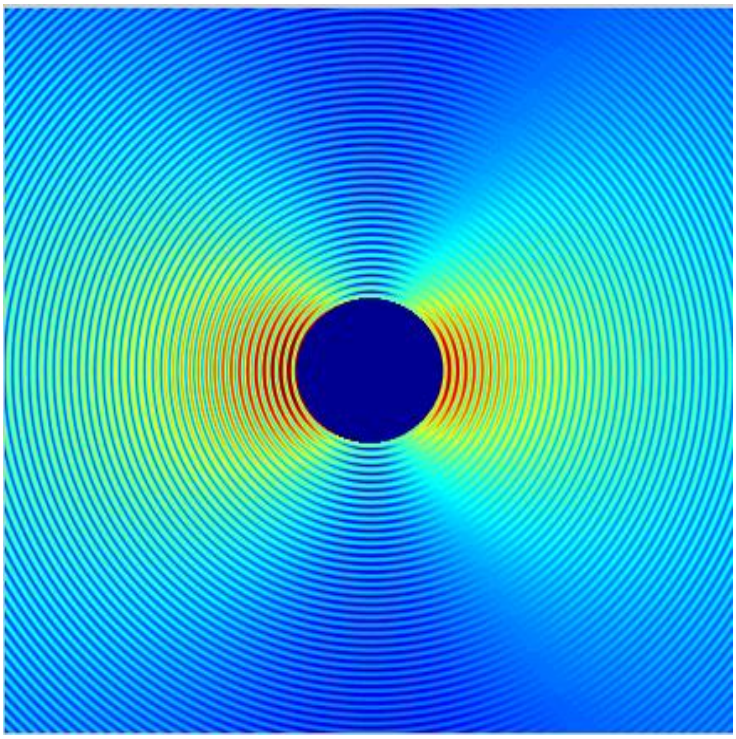

Figure 2.48: Total wave distribution around a hard elastic inclusion stiffer than the plate D_2/D_1=100 and ρ_2/ρ_1 =10 for frequency ka=0.706

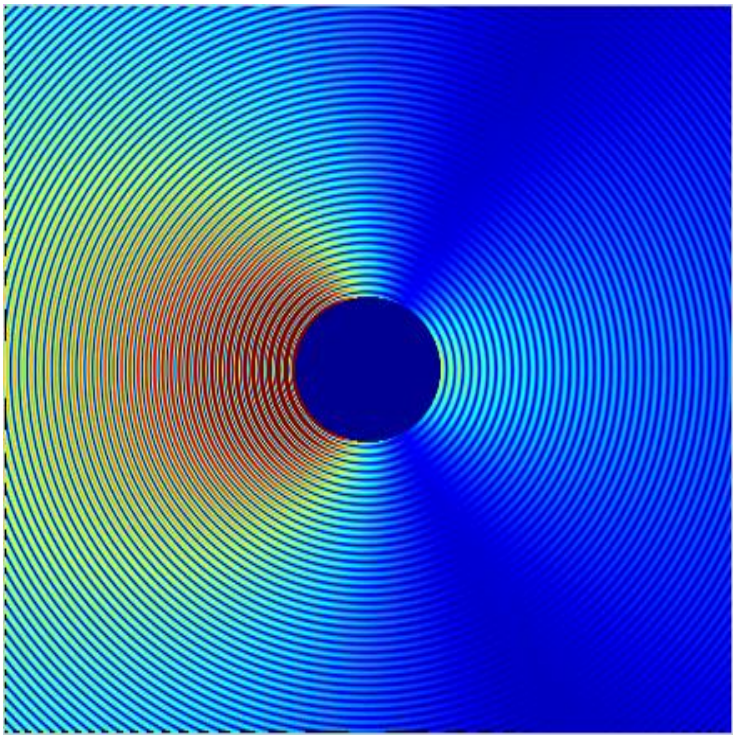

Figure 2.49: Total wave distribution around rigid inclusion for frequency ka=0.706

Based on the observations made from the total wave distribution in the vicinity of the inclusion for the cases of hole, elastic and rigid inclusion for different frequencies, the rigid inclusion achieves stronger reflection and attenuation of the waves.

All the analytical studies presented here and analytical formulations reported in the literature consider infinite plates to characterize the flexural wave propagation. This work focuses on acoustically tailoring a finite composite panel. None of the studies used damping. Characterizing the flexural propagation in finite plate with inclusions with closed form solutions is mathematically difficult process. Also with the advent of reliable and powerful commercial finite element method (FEM) software packages makes it possible to investigate the finite structures at both the fundamental as well as the applied level. So, ANSYS Finite Element Analysis software is used to conduct FEM simulations to explore the effects of different composite panel designs on the reduction of vibration transmission and flexural wave propagation.

3 Finite Element Models Representation

Finite element method (FEM) is used to explore the effects on the reduction of vibration transmission and flexural wave propagation in composite sandwich panel with different designs. The concept of phononic crystals will be used to define these designs. Phononic crystals as discussed in chapter 1 have the potential of reducing/prohibiting the transmission of the wave in a certain frequency range. This concept will be applied as a guiding principle to define the design variations that are effective in suppressing vibration transmission. These design variations will be evaluated using FEM simulations. In this work ANSYS Finite Element software is used. Various design configurations will be considered to explore the effects/contributions of different parameters like scatterer's material properties, geometry and spatial pattern. Based on knowledge gained (the effects of the parameters) through a systematic parametric study, a final design of the composite sandwich panel will be proposed, and will be further investigated to find the optimum design. The details of various parametric studies will be presented in the next chapters.

In this chapter, we will present various design configurations in the form of FEM models and the respective simulation set-ups. The first step was to come up with a reliable finite element model that would give reliable results. Some of the key variables/parameters in finite element modelling are the structure definition, contacts/bonding between the components, fixtures/constraints, material properties of each of the components, the damping ratio of the structure, mesh quality (element size, number of elements, element quality, aspect ratio, etc.), and solution set-up. For validating the finite element model and the meshing element choice, we conducted a study of modal analysis of a square plate clamped on all four sides. The results obtained from this study are compared with the well-established and published results in the

literature. The other key step to consider is how to interpret/represent the results from the simulations.

Many simulations were set up and run to characterize the different connections that can be applied between the components, mesh quality and their impact on the results. Constraints applied on the sandwich panels and choice of damping ratio are assumed based on the real world representation of the panel, the details of which will be explained in the later sections. With this information, the finite element models for the base sandwich panel and the sandwich panel with phononic crystals are set-up to explore the effects of various parameters like material properties, geometry, and spatial pattern. The goal of FEM simulations is to evaluate the effectiveness in suppressing the transmission of the vibration by various designs of panel against the unmodified sandwich panel.

The different designs configurations that are explored are:

1. The unmodified sandwich panel, which is referred as ‘Base Sandwich’ in this work.
2. Sandwich panel with sonic crystals in a one, two, and three column arrangements of scatterers. In this design, the thickness of the scatterer is equal to thickness of the composite sandwich panel.
3. Sandwich panel with sonic crystals in a one, two, and three column arrangements of extended scatterers bonded to the retaining plates. In this design, the length of the scatterers is extended beyond the thickness of the sandwich panel on both sides. The extended scatterers are bonded to the retaining plates on both sides.

In the next section, a modal analysis study is conducted with a square plate clamped on four edges and compared with the published analytical results.

3.1 Square Plate Modal Analysis - Validation Study

In this section, modal analysis is conducted in ANSYS on a square plate fixed on four sides of the plate. In this study we determine the first seven frequencies of the fixed square plate and the respective mode shapes for each of the natural frequencies are evaluated and plotted. These results are compared with the results from analytical solution published in [56].

3.1.1 FEM Model

A square plate of dimensions 48" x 48" x 0.5" is considered for the study as shown in Figure 3.1.

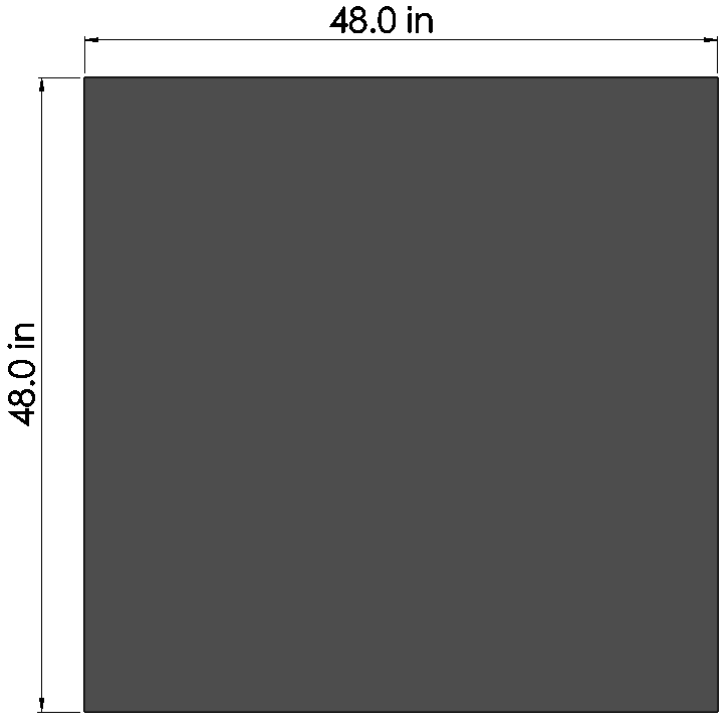

Figure 3.1: Square plate

3.1.2 Material Properties

The square plate is made of composite material whose material properties are assumed to be homogeneous, isotropic and elastic, are shown in Table 3.1.

Table 3.1: Square plate material properties

Material property	Composite material
Young's modulus (E)	2.7095×10^{8} Pa
Density (ρ)	52.862 kg/m^3
Poisson's ratio (ν)	0.4

3.1.3 Meshing

SHELL181 a four node structural shell element with six degrees of freedom at each node: translations in x, y, and z directions, and rotations about the x, y, z-axes is used. This element type is well suited for layered applications for modelling composite shells or sandwich constructions [57].

The mesh quality considered for this study is shown in Figure 3.2. For this mesh model, the total number of nodes are 1600 and the number of elements are 1521.

3.1.4 Fixtures/Constraints

The composite sandwich panel is fixed/clamped on all the four sides of the sandwich panel ABCD as shown in Figure 3.3.

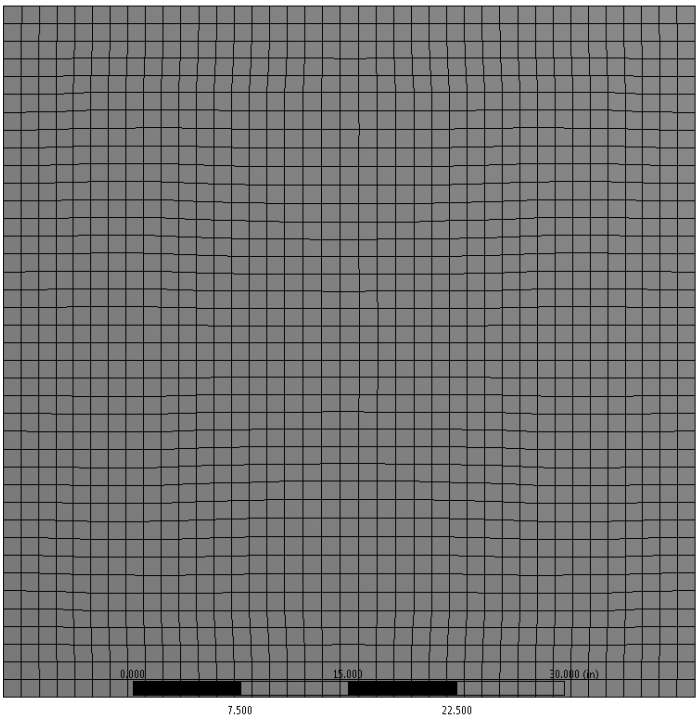

Figure 3.2: Square plate mesh

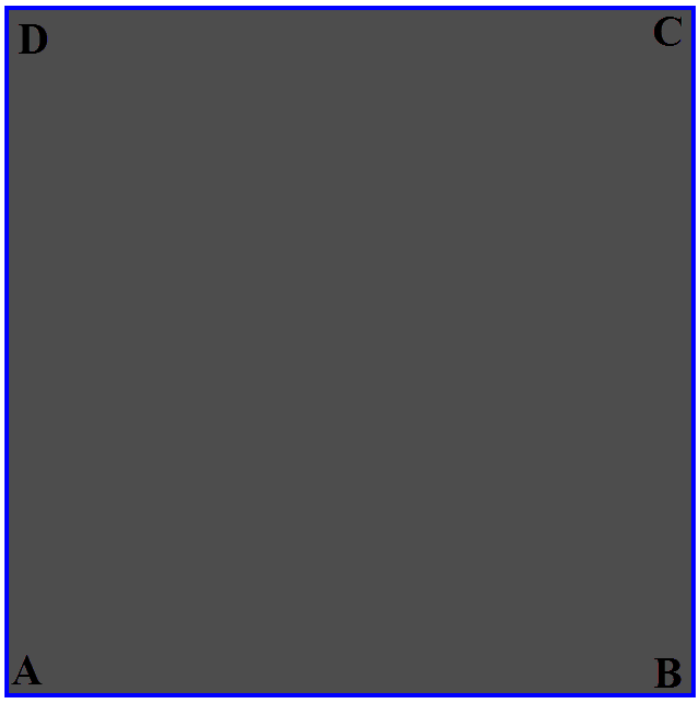

Figure 3.3: Square plate fixed on all four edges (ABCD)

3.1.5 Analysis and Results

The frequency factor is defined in the analytical solution [56] is defined as follows

$$\text{Frequency factor} = \omega a^2 \sqrt{\rho / D} \tag{3.1}$$

where, ω is frequency, a is length the plate, ρ is mass density per unit area and D is the flexural rigidity.

The frequency factors calculated from the ANSYS simulation are compared to the one listed in the analytical solution are shown below in Table 3.2 and are in very close agreement.

Table 3.2: Frequency factor comparison – ANSYS Simulation & Ref. [56]

Frequency Factor (ANSYS)	**Frequency Factor (Ref. [56])**
35.99	35.99
73.53	73.41
108.32	108.27
132.27	131.64
132.89	132.25
165.44	165.15

The mode shapes from the analytical solution in [56] is given as

$$W(x,y) = \sum_{m=1}^{p} \sum_{n=1}^{q} A_{mn} \left[\cosh\frac{\varepsilon_m x}{a} - \cos\frac{\varepsilon_m x}{a} - \alpha_m \left(\sinh\frac{\varepsilon_m x}{a} - \sin\frac{\varepsilon_m x}{a}\right)\right]\left[\cosh\frac{\varepsilon_n y}{a} - \cos\frac{\varepsilon_n y}{a} - \alpha_n \left(\sinh\frac{\varepsilon_n y}{a} - \sin\frac{\varepsilon_n y}{a}\right)\right] \tag{3.2}$$

where the A_{mn} are the amplitude coefficients and α and ε are the eigen function paremeters shown in the below Table 3.3 and Table 3.4 respectively.

Table 3.3: Amplitude coefficients

Mode 1	**Mode 2**	**Mode 3**	**Mode 4**	**Mode 5**	**Mode 6**
A_{11} = 1.0	A_{12} = 1.0	A_{22} = 1.0	A_{13} = 1.0	A_{11} = -0.0280	A_{12} = -0.0406
A_{13} = 0.0142	A_{14} = 0.0101	A_{24} = 0.0326	A_{15} = 0.0085	A_{13} = 1.0	A_{14} = -0.0105
A_{15} = 0.0020	A_{16} = 0.0020	A_{26} = 0.0073	A_{31} = -1.0	A_{15} = 0.0055	A_{16} = -0.0017
A_{31} = 0.0142	A_{32} = 0.0406	A_{42} = 0.0326	A_{35} = -0.0141	A_{31} = 1.0	A_{32} = 1.0
A_{33} = -0.0031	A_{34} = -0.0022	A_{44} = -0.0019	A_{51} = -0.0085	A_{33} = 0.1267	A_{34} = 0.0560
A_{35} = -0.0009	A_{36} = -0.0007	A_{46} = -0.0010	A_{53} = 0.0141	A_{35} = 0.0118	A_{36} = 0.0141
A_{51} = 0.002	A_{52} = 0.007	A_{62} = 0.0073		A_{51} = 0.0055	A_{52} = 0.0238
A_{53} = -0.0009	A_{54} = -0.0011	A_{64} = -0.001		A_{53} = 0.0118	A_{54} = -0.0011
A_{55} = -0.0004	A_{56} = -0.0005	A_{66} = -0.0006		A_{55} = -0.0018	A_{56} = -0.0009

Table 3.4: Eigen function parameters

m, n	$\boldsymbol{\alpha_m, \alpha_n}$	$\boldsymbol{\varepsilon_m, \varepsilon_n}$
1	0.98250222	4.7300408
2	1.00077731	7.8532046
3	0.99996645	10.9956078
4	1.00000145	14.1371655
5	0.99999994	17.2787596
6	1.0	20.4203522

The equation for the mode shapes shown in equation (3.2) from [56] using the amplitude coeffecients and teh eigen function parameters from Table 3.3 and Table 3.4, the mode shapes are computed and plotted using Matlab. These mode shapes plotted using teh analytical solution are compared with the mode shapes running the simulations in ANSYS are shown below in

Figure 3.4 through Figure 3.9. The modes shapes from the analysticals solutions match with the mode shapes obtained from the ANSYS simulation results as shown in Figure 3.4 through Figure 3.9.

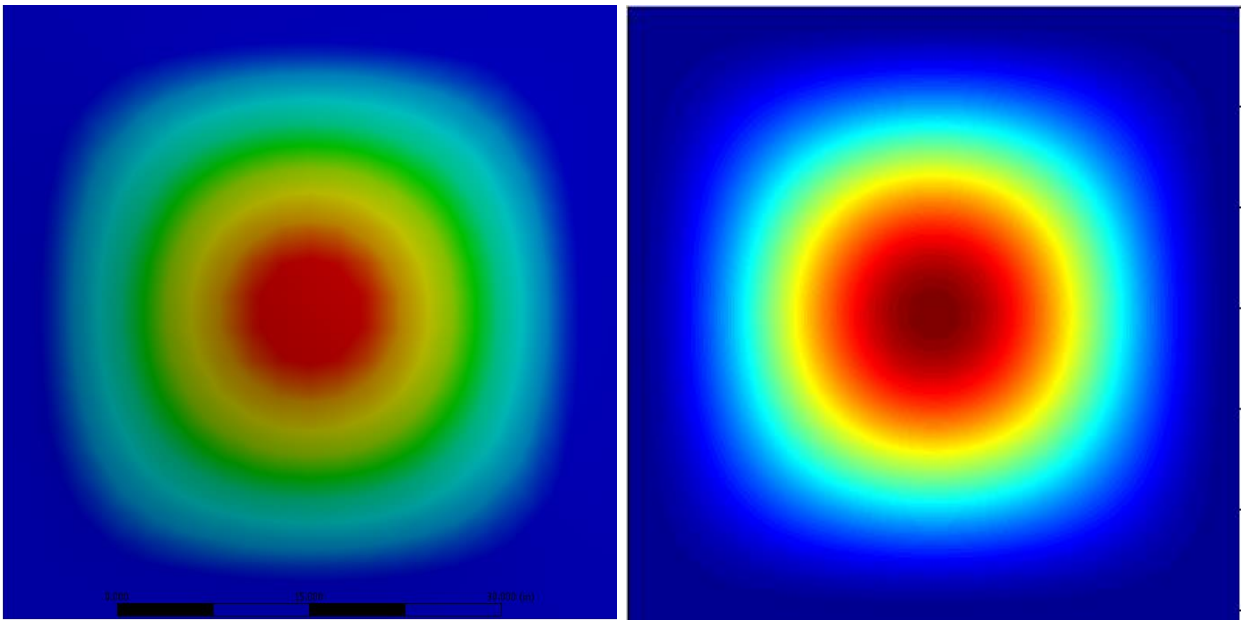

(a) Mode 1 (ANSYS Simulation) (b) Mode 1 (Ref. [56])

Figure 3.4: Mode shape 1

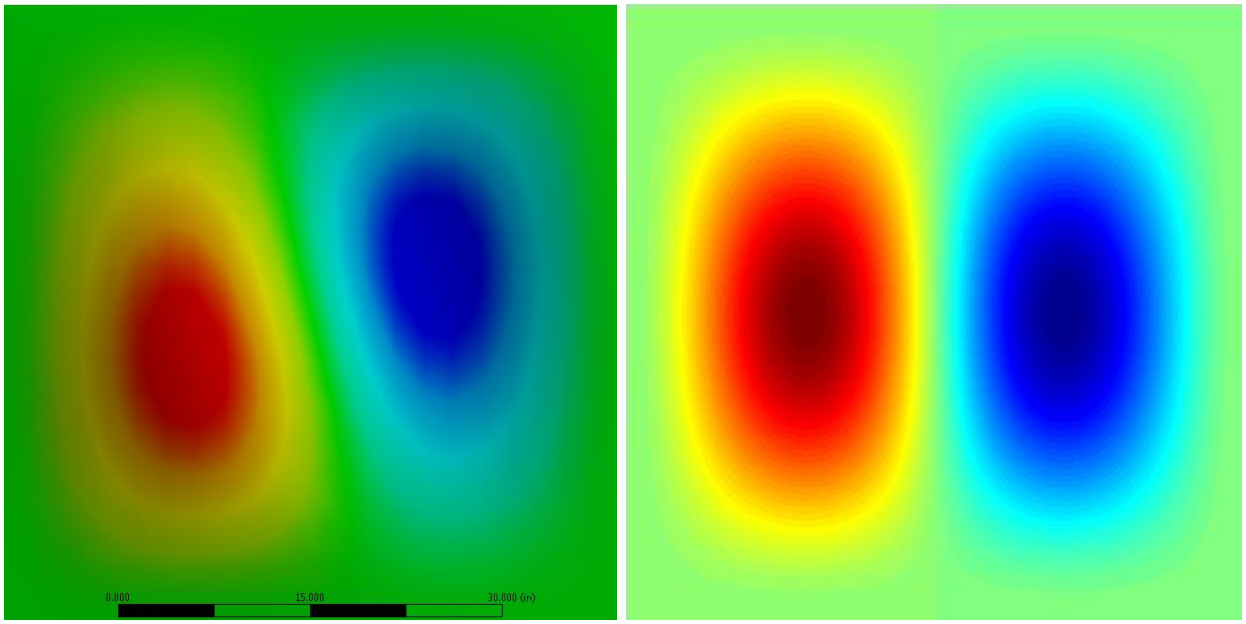

(a) Mode 2 (ANSYS Simulation) (b) Mode 2 (Ref. [56])

Figure 3.5: Mode shape 2

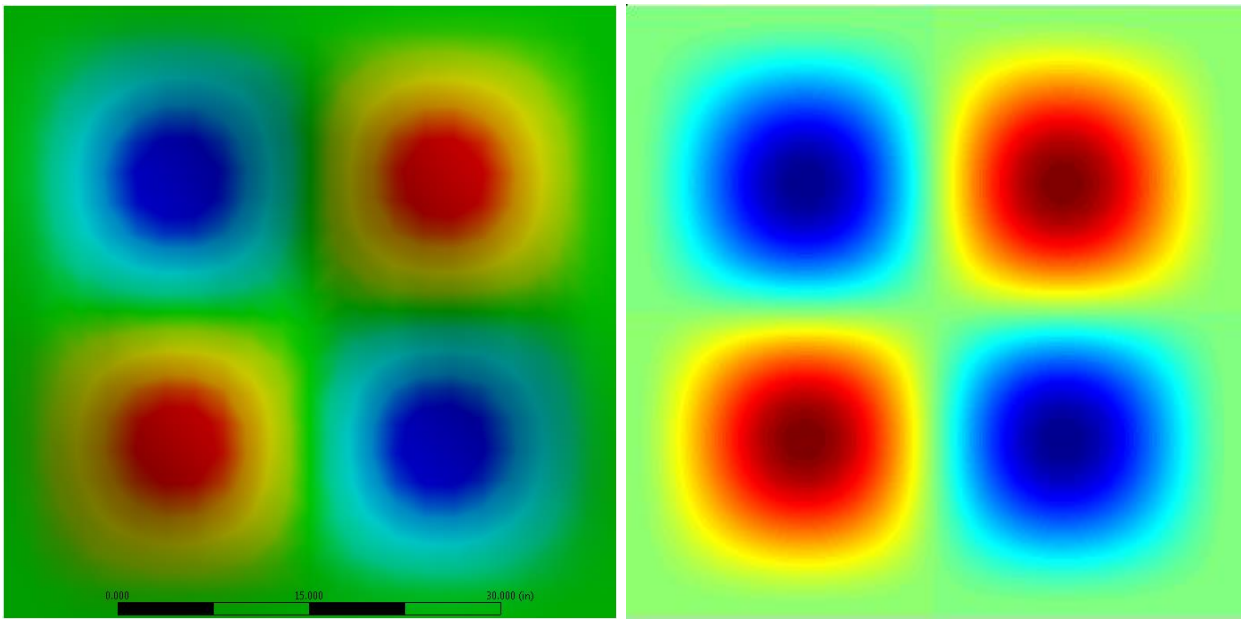

(a) Mode 3 (ANSYS Simulation) (b) Mode 3 (Ref. [56])

Figure 3.6: Mode shape 3

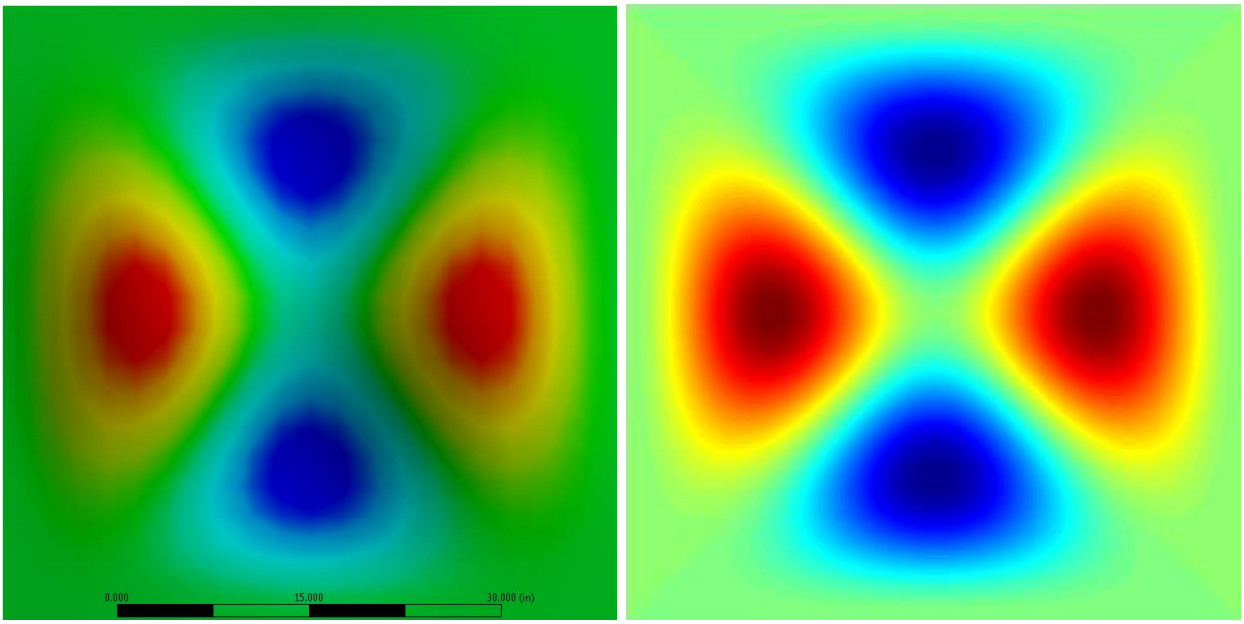

(a) Mode 4 (ANSYS Simulation) (b) Mode 4 (Ref. [56])

Figure 3.7: Mode shape 4

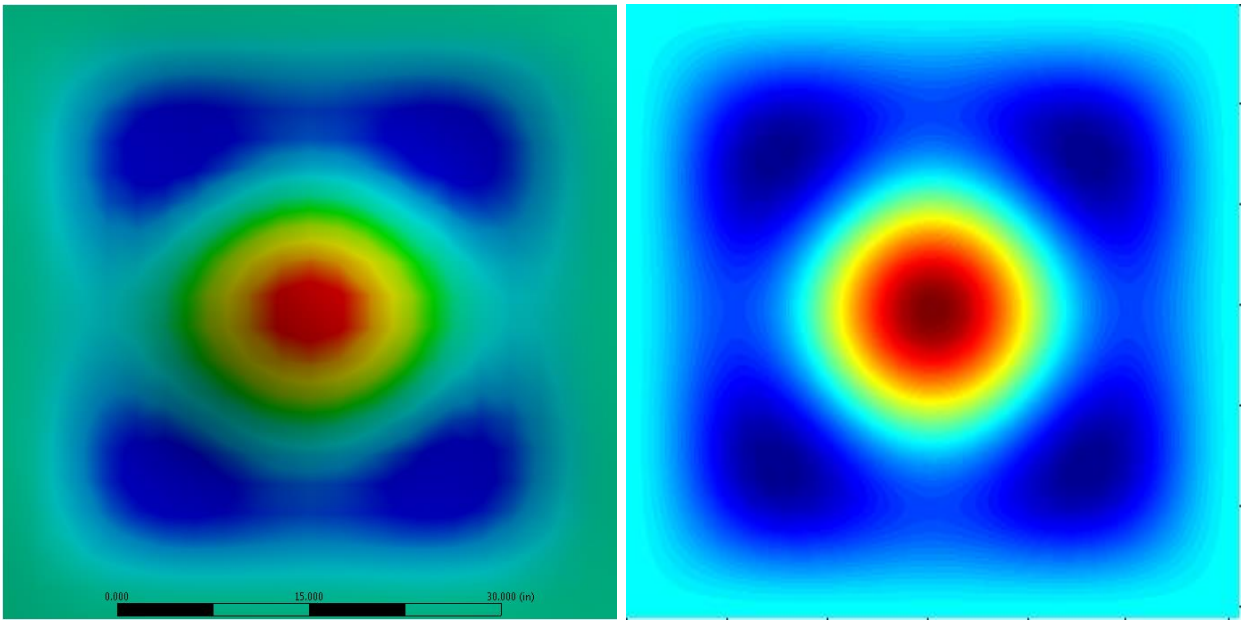

(a) Mode 5 (ANSYS Simulation) (b) Mode 5 (Ref. [56])

Figure 3.8: Mode shape 5

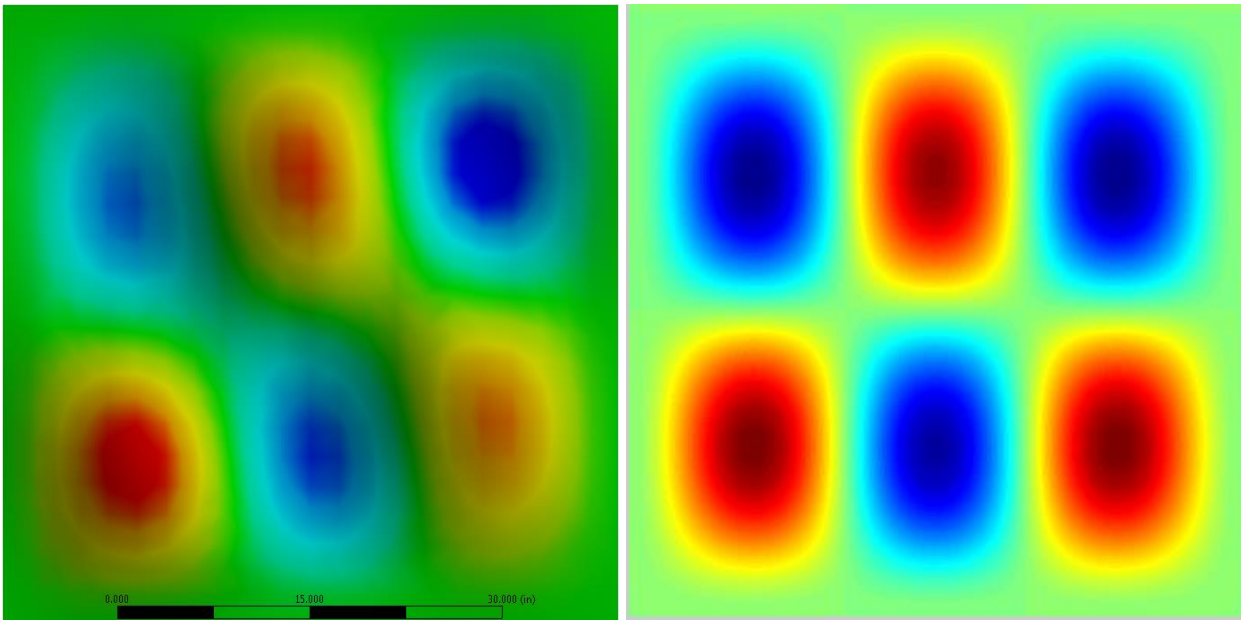

(a) Mode 6 (ANSYS Simulation) (b) Mode 6 (Ref. [56])

Figure 3.9: Mode shape 6

3.2 Base Sandwich

3.2.1 FEM Model

The base sandwich structure is a sandwich panel which consists of a core sandwiched between two face-sheets shown in Figure 3.10. The two face-sheets are assumed to be identical. The sandwich panel is 4'x4' in area. The core is 0.5" thick and the face-sheets are 0.0237" thick as shown in Figure 3.10.

The sandwich is modeled as a square surface element in ANSYS and a layered section is defined with the appropriate material properties as listed in Table 3.5 and thicknesses of the core (0.5"), top face-plate (0.0237") and bottom face-plate (0.0237").

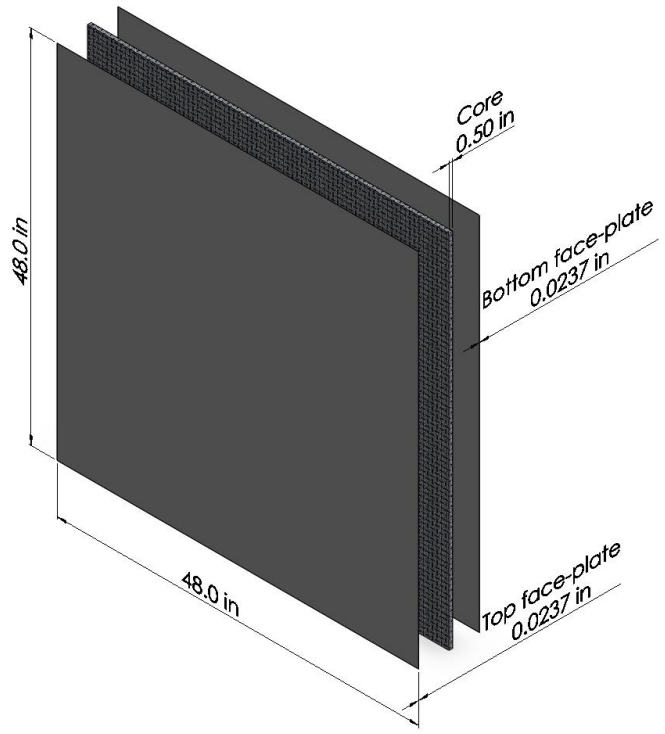

Figure 3.10: Composite sandwich panel (top face-plate, core, bottom face-plate)

3.2.2 Material Properties

The core and the face-sheet are made of composite materials which are assumed to be homogeneous, isotropic and elastic, whose material properties are shown in Table 3.5. These material properties are provided by Bell Helicopters.

Table 3.5: Sandwich panel material properties

Material property	Core	Top and Bottom face-plates
Young's modulus (E)	2.7095×10^{8} Pa	5.708×10^{10} Pa
Density (ρ)	52.862 kg/m^3	2020.7 kg/m^3
Poisson's ratio (ν)	0.4	0.211

3.2.3 Connections/Contacts

A bonded contact is applied between the three layers top face-plate, core and the bottom face-plate of the sandwich panel.

3.2.4 Meshing

Various mesh configurations were studied using modal and harmonic analysis to decide the appropriate mesh density. Mesh quality as shown in Figure 3.11 has been chosen based on considering various metrics in ANSYS (element quality, aspect ratio, Jacobian ratio, etc.) and also the variation of results based on the natural frequency analysis.

SHELL181 a four node structural shell element with six degrees of freedom at each node: translations in x, y, and z directions, and rotations about the x, y, z-axes is used. This element type is well suited for layered applications for modelling composite shells or sandwich constructions [57]. For the mesh model shown in Figure 3.11, the total number of nodes are 4225 and the number of elements are 4096.

3.2.5 Loading

The roof panels in commercial and military rotor craft fuselages are mechanically interconnected with the rotor mechanism allowing the structure-borne and acoustic-borne vibration and noise transmission into the cabins passing through these panels. In the current work, the rotor mechanism is mounted on this composite panel with the brackets that are along the lines AD and BC of the square of 3'x3' as shown in Figure 3.12 [51]. But in the first set of simulations where the influence of the parameters to reduce the vibration transmission are explored, a load amplitude of 100 lbf is applied along the line AD of 3'x3' square in negative Z-direction as shown in Figure 3.13. The full blown model will look at the loading along both the lines AD and BC.

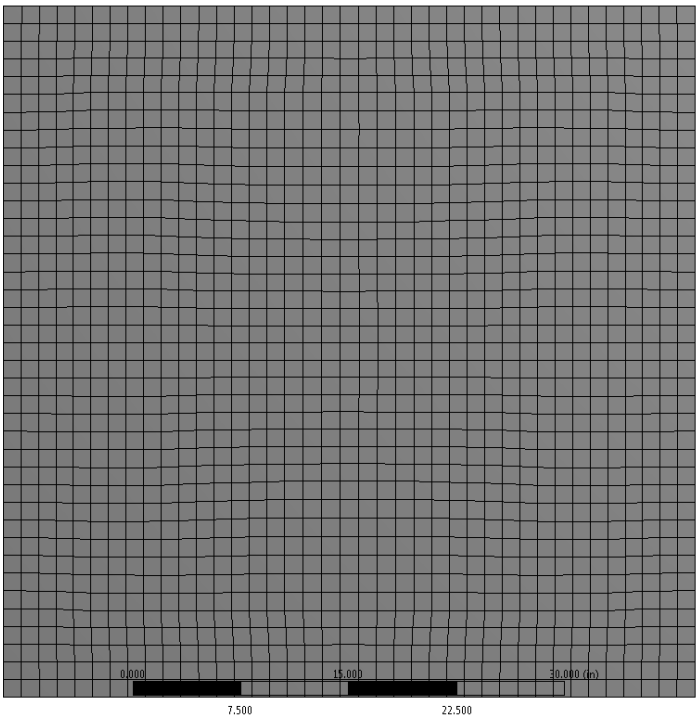

Figure 3.11: Base sandwich mesh

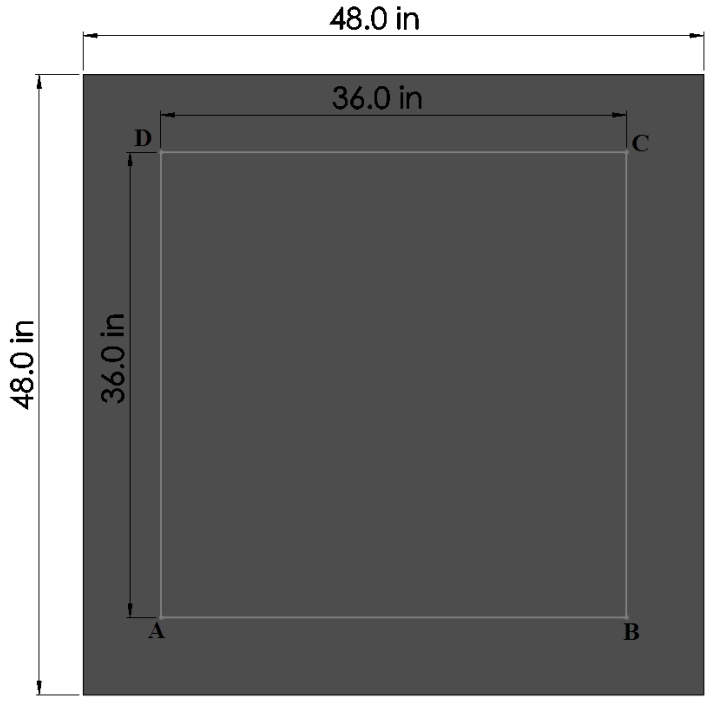

Figure 3.12: Composite sandwich panel loading lines (AD and BC)

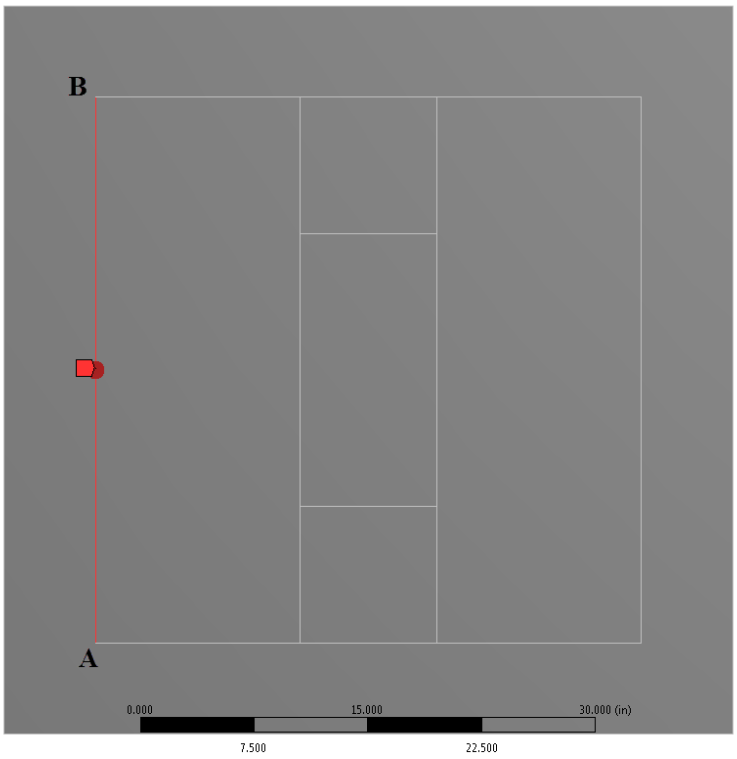

Figure 3.13: Base sandwich panel with loading line (AB)

3.2.6 Fixtures/Constraints

The composite sandwich panel is fixed/clamped on all the four sides of the sandwich panel ABCD as shown in Figure 3.14.

3.2.7 Damping

The damping ratio for the whole sandwich panel has been chosen as 0.01 close to the real world representation.

3.2.8 Analysis Set-up

Harmonic analyses are used to determine the steady-state response of a structure to the loads that vary harmonically with time. A typical harmonic analysis will calculate the response (displacements, stresses, strains, etc.) of the structure over a frequency range. In this work, a harmonic analysis is conducted for the frequency range of 2000 Hz to 4000 Hz. This range has

been chosen because Bell Helicopters was interested in minimizing the vibration transmission at 3000 Hz.

3.2.9 Post Processing

A rectangular column area ABCD as shown in Figure 3.15 is selected to record the root mean square of the displacements of all the nodes in the Z-direction over the frequency range of the study. This rectangular column ABCD which is the area of interest to capture the results will be referred as central region. The results from studies using this FEM model will be presented and discussed in the next chapter.

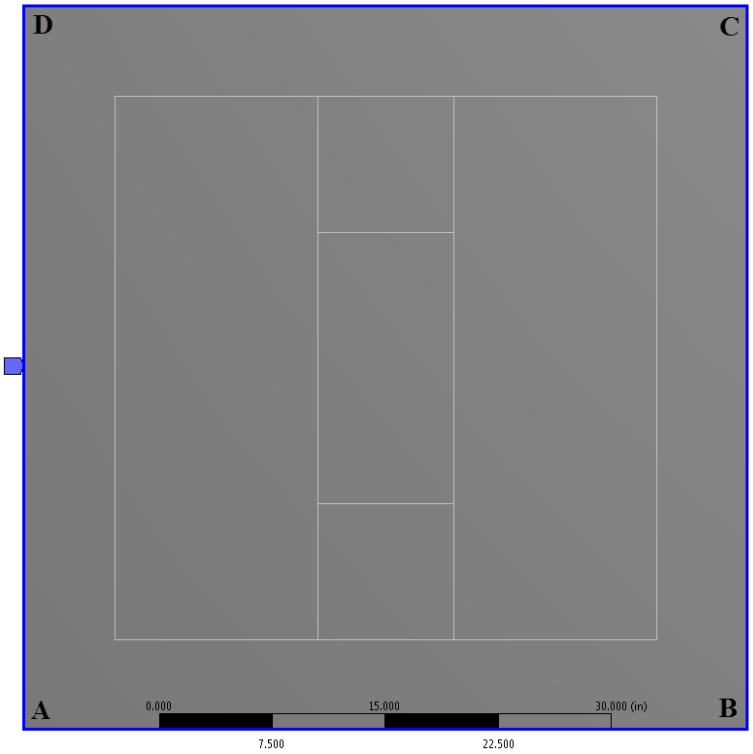

Figure 3.14: Base sandwich panel fixed on all four sides (ABCD)

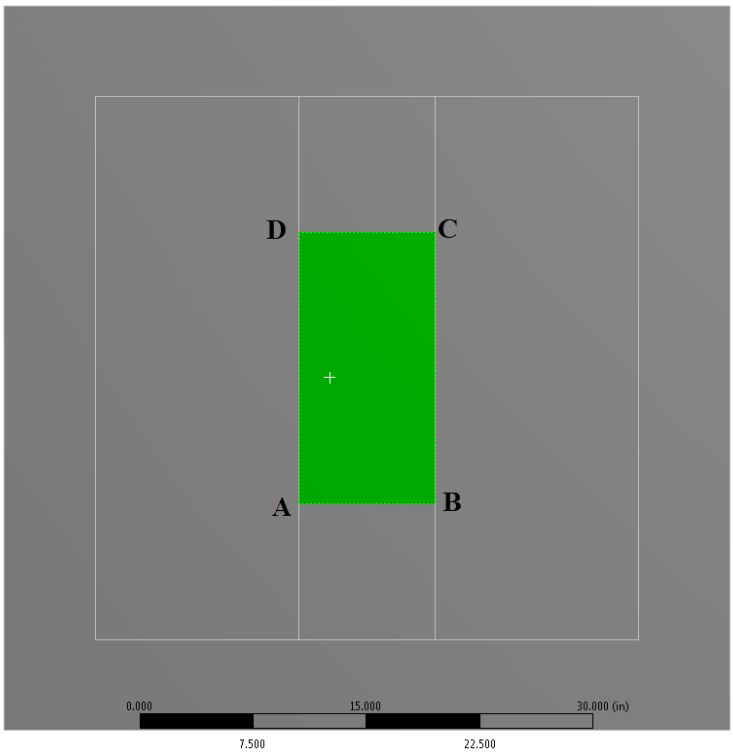

Figure 3.15: Base sandwich panel highlighting area of interest (ABCD) to capture results

3.3 Sandwich Panel with Sonic Crystals – One, Two and Three Column Scatterers

3.3.1 FEM Model

The first design variation that is considered is sandwich panel with one column of inclusions/scatterers. Figure 3.16 shows the sandwich panel with one column of scatterers where the scatterers are holes. A sandwich panel with one column of scatterers filled with a material to the thickness of the plate is shown in Figure 3.17. As can be seen in both Figure 3.16 and Figure 3.17, L is the length of the center of the scatterer from the left end of the sandwich panel, D is the diameter of the scatterer and B is the lattice constant (distance between the scatterers). B and D are the two parameters that will be varied and examined for the influence of these parameters on the vibration transmission reduction using the sandwich panel with holes as scatterers. With the

FEM model of sandwich with fillers as scatterers studies will be conducted to explore the material properties (Young's modulus and density) of the fillers along with varying B and D.

Figure 3.18 and Figure 3.19 shown the sandwich panels with a two column arrangement of scatterers where the scatterers are holes and fillers respectively. The sandwich panels with scatterers in a three column arrangement with holes and fillers as scatterers are shown in Figure 3.20 and Figure 3.21 respectively. The scatterers are arranged in a square lattice arrangement for the two and three column arrangement and the distance between the scatterers (B) is referred to as lattice constant.

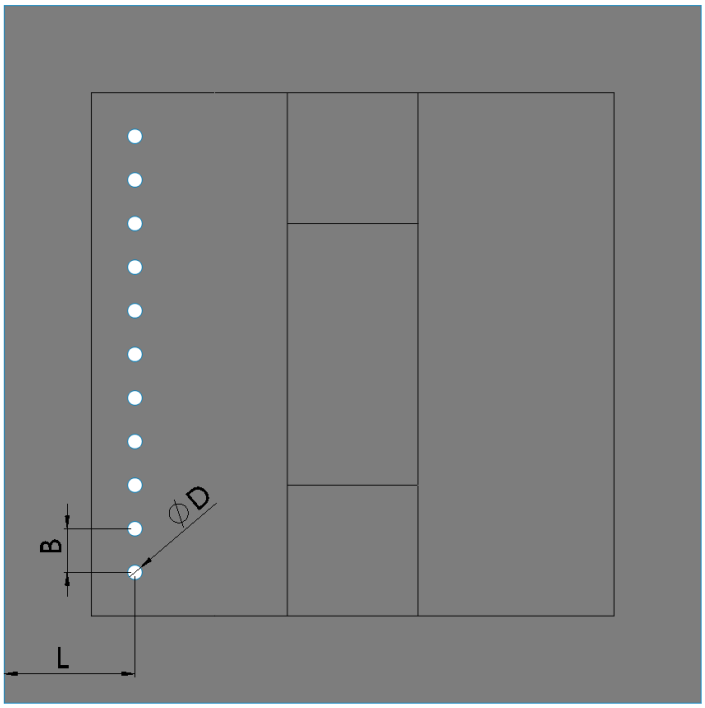

Figure 3.16: Sandwich panel with one column scatterers (holes)

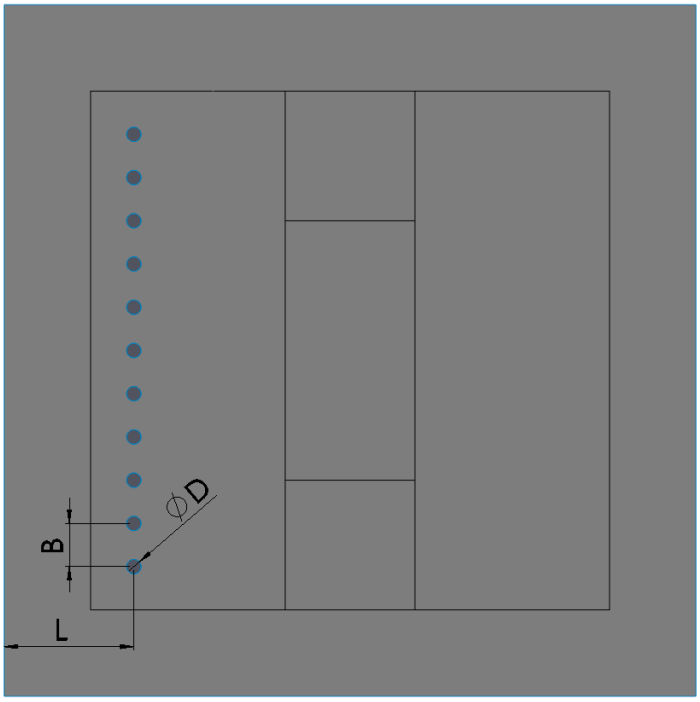

Figure 3.17: Sandwich panel with one column scatterers (fillers)

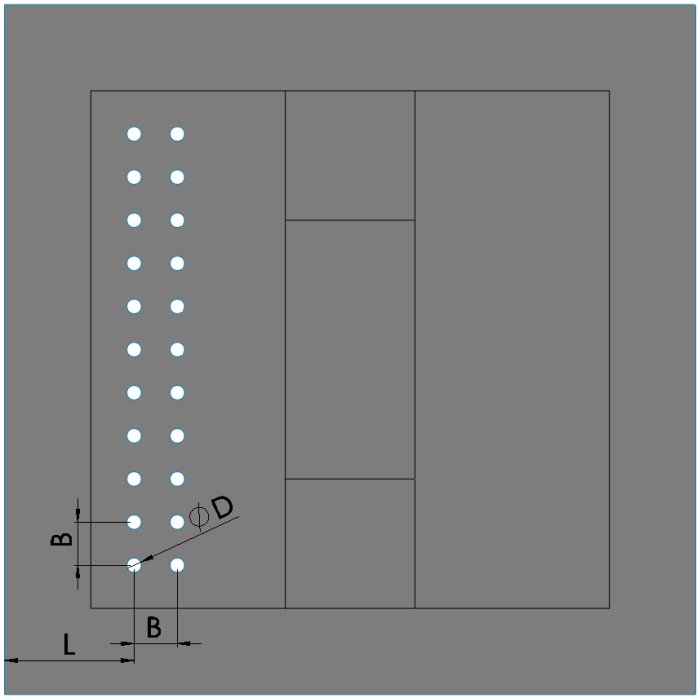

Figure 3.18: Sandwich panel with two column scatterers (holes)

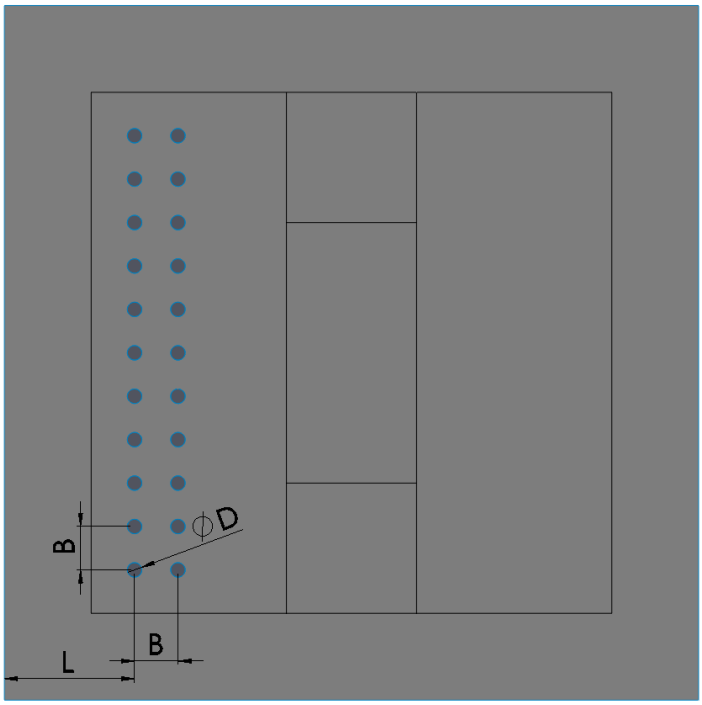

Figure 3.19: Sandwich panel with two column scatterers (fillers)

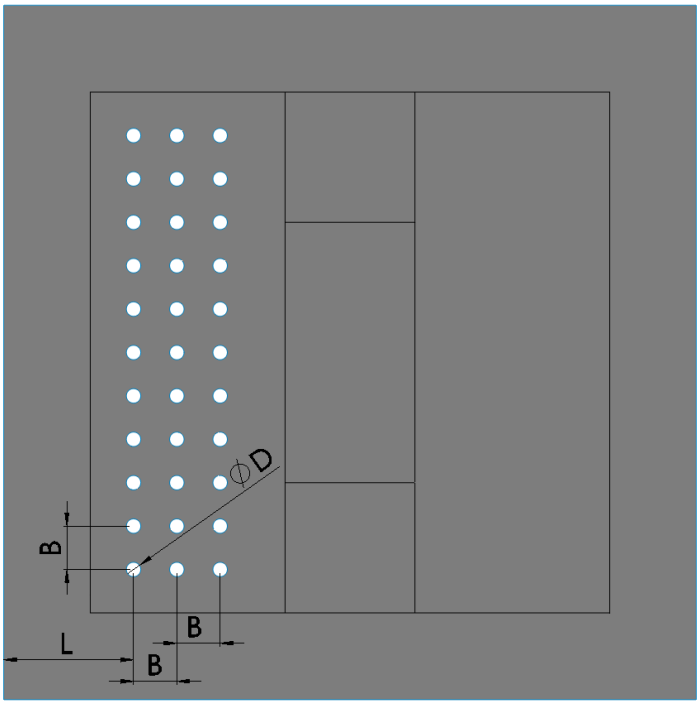

Figure 3.20: Sandwich panel with three column scatterers (holes)

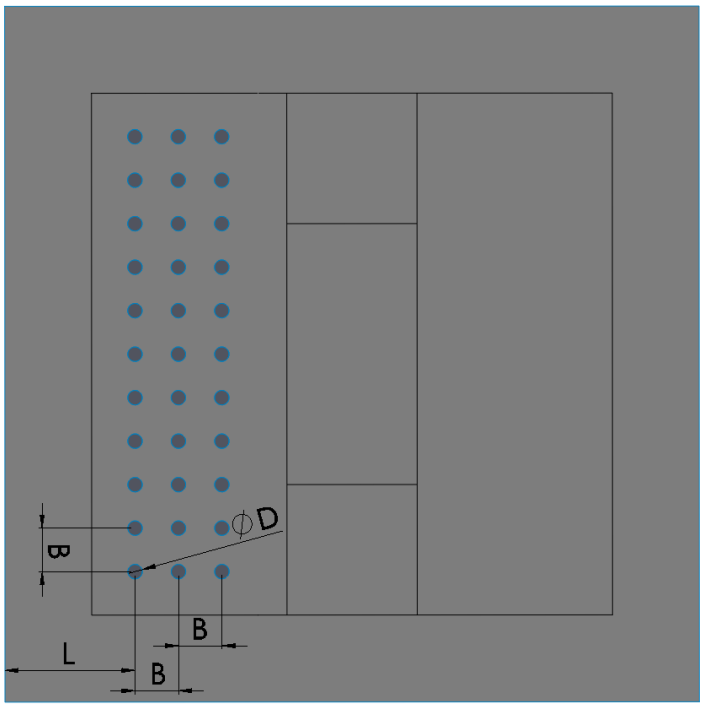

Figure 3.21: Sandwich panel with three column scatterers (fillers)

3.3.2 Material Properties

The material properties of the sandwich panel as listed in the Table 3.5 are used. The material properties (Young's modulus and density) of the fillers are also the parameters that will be altered to explore their influence on the reduction of vibration transmission.

3.3.3 Connections/Contacts

A bonded contact is applied between the three layers top face-plate, core and the bottom face-plate of the sandwich panel. The connections between the fillers and the sandwich panel is also bonded.

3.3.4 Meshing

Mesh quality for each of the models has been chosen considering various metrics in ANSYS (element quality, aspect ratio, Jacobian ratio, etc.) and also the variation of results based on the natural frequency analysis. SHELL181 a four node structural shell elements with six

degrees of freedom at each node: translations in x, y, and z directions, and rotations about the x, y, z-axes is used. This element type is well suited for layered applications for modelling composite shells or sandwich constructions [57]

For example, Figure 3.22 shows the mesh quality for the sandwich panel with one column arrangement of holes with a hole diameter (D) of 1" and lattice constant (B) of 3". For this mesh model, the total number of nodes are 3093 and the number of elements are 2958. Figure 3.23 shows the mesh quality for the sandwich panel with one column arrangement of fillers with a filler diameter (D) of 1" and lattice constant (B) of 3". For this mesh model, the total number of nodes are 5876 and the number of elements are 5617.

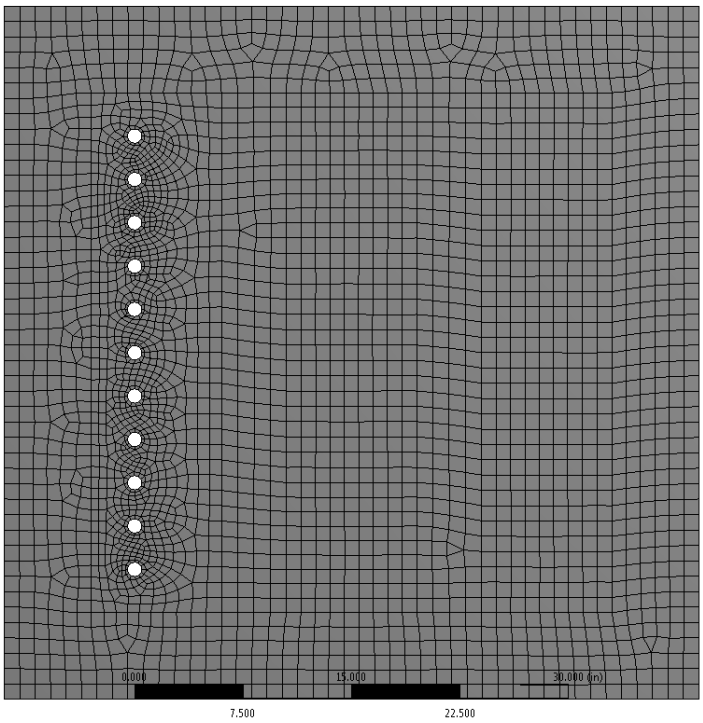

Figure 3.22: Mesh for sandwich panel with one column scatterers (holes) hole with diameter (D) of 1" and lattice constant (B) of 3"

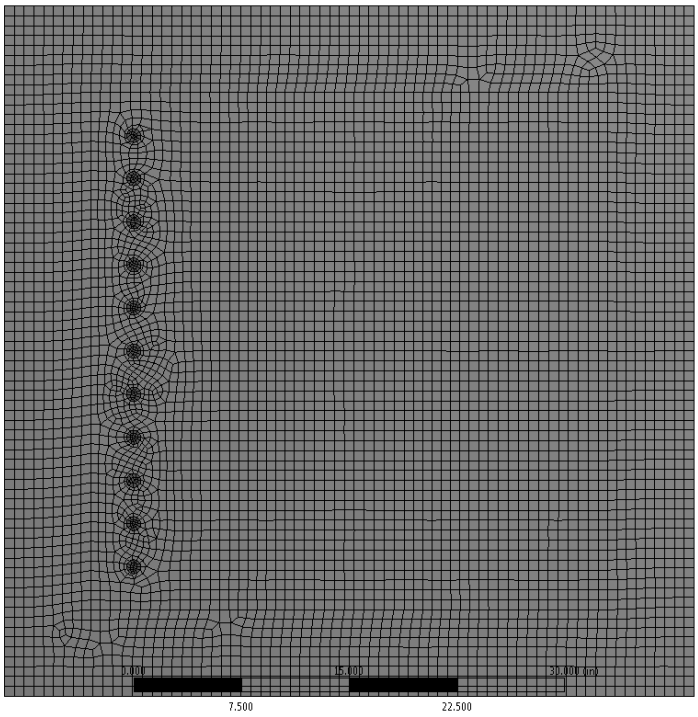

Figure 3.23: Mesh for sandwich panel with one column scatterers (fillers) with filler diameter (D) of 1" and lattice constant (B) of 3"

3.3.5 Loading

A load amplitude of 100 lbf is applied along the line AB of 3'x3' square in negative Z-direction as shown in Figure 3.24. The example shown in Figure 3.24 is for a sandwich panel with holes as scatterers in a one column arrangement. The loading line is same for the cases of sandwich panels with two and three column arrangements for holes as scatterers. The sandwich panels with fillers as scatterers in a one, two and three column arrangements also are loaded along the line AB.

3.3.6 Fixtures/Constraints

The sandwich panel is fixed/clamped on all the four sides of the sandwich panel ABCD as shown in Figure 3.25. The example shown in Figure 3.25 is for a sandwich panel with holes as scatterers in a one column arrangement. The same constraints are applied to the sandwich

panels with two and three column arrangements for holes as scatterers. The sandwich panels with fillers as scatterers in a one, two and three column arrangements also are fixed on all the four sides.

3.3.7 Damping

The damping ratio for the sandwich panel with scatterers has been chosen as 0.01 close to the real world representation.

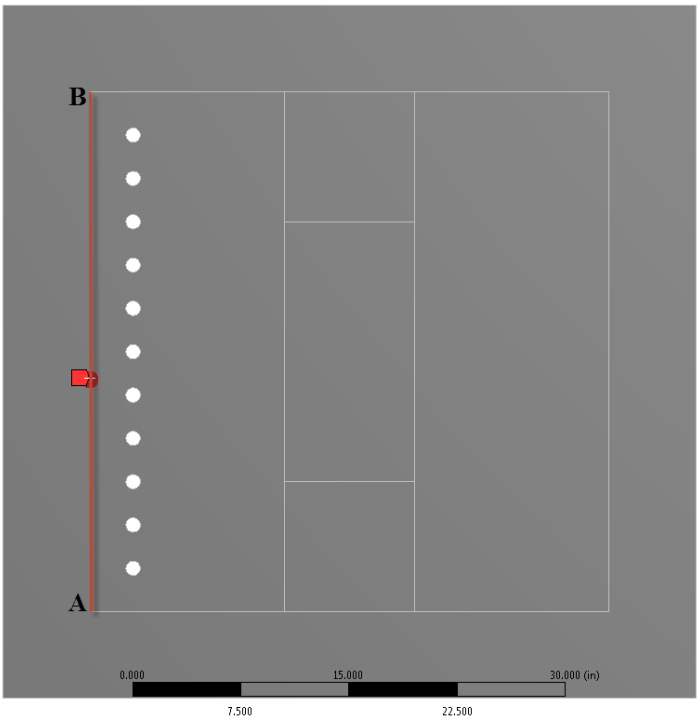

Figure 3.24: Sandwich panel with one column scatterers (holes) with the loading line (AB)

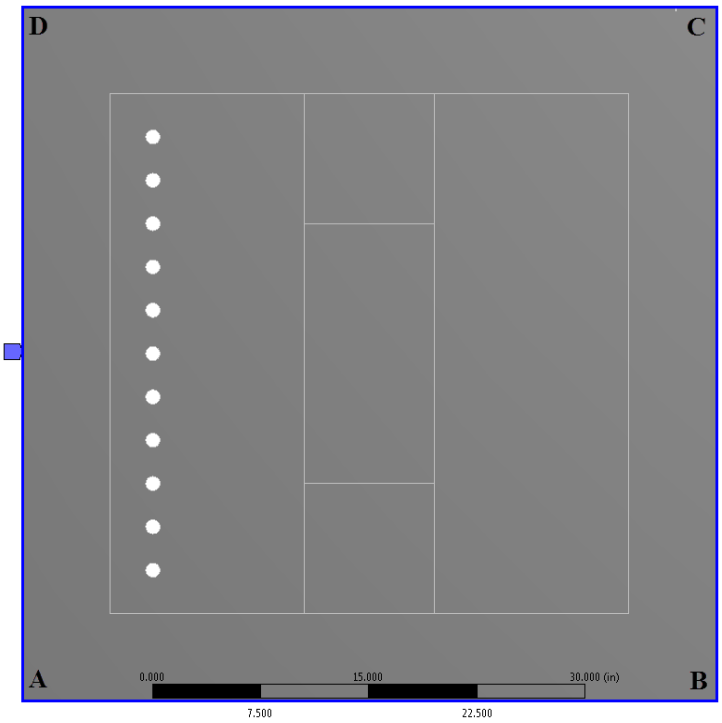

Figure 3.25: Sandwich panel with one column scatterers (holes) fixed on all four sides (ABCD)

3.3.8 Analysis Set-up

Harmonic analysis is conducted for the frequency range of 2000 Hz to 4000 Hz. This range has been chosen because Bell Helicopters was interested in minimizing the vibration transmission at 3000 Hz.

3.3.9 Post Processing

A rectangular column area ABCD as shown in Figure 3.26 is selected to record for the root mean square of the displacements of all the nodes in the Z-direction over the frequency range of the study. This rectangular column ABCD which is the area of interest to capture the results will be referred as central region. The example shown in Figure 3.26 is for a sandwich panel with holes as scatterers in a one column arrangement. The same central region is used to capture results for the two and three column arrangements for holes as scatterers. The sandwich

panel with fillers as scatterers in a one, two and three column arrangements also uses the same rectangular area to capture the results. The results from simulation studies using these FEM models will be presented and discussed in the next chapter.

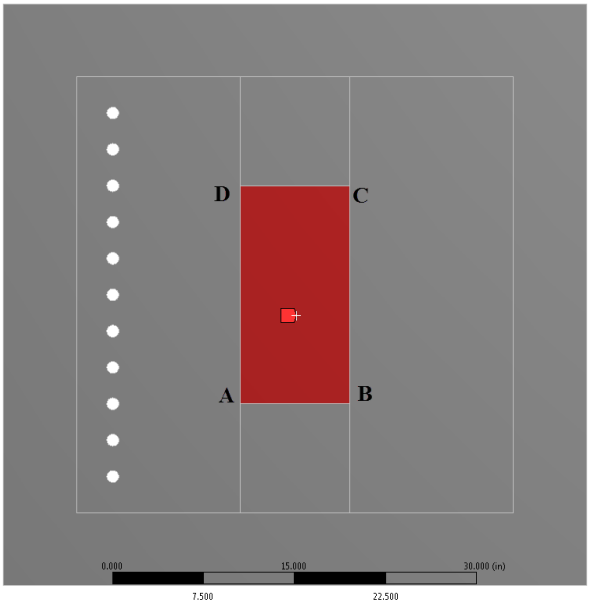

Figure 3.26: Sandwich panel with one column scatterers (holes) highlighting area of interest (ABCD) to capture results

3.4 Sandwich Panel with Sonic Crystals with Extended Scatterers Bonded to Retaining Plates - One, Two and Three Columns

3.4.1 FEM Model

From the analytical solution of infinite plate with circular inclusion, it was observed that the rigid inclusion achieved stronger reflection than the hard elastic and the hole inclusions. So, to mimic the rigid inclusions, the next design variation considered is the sandwich panel with extended scatterers (scatterers with length more than the thickness of the sandwich panel) bonded to the retaining plates on either side. The retaining plates are assumed to be a very light and made of very stiff material. This configuration is considered in one, two and three column

arrangements. The retaining plates are rectangular slabs with dimensions 36" x 9" x 0.5" covering the span of the scatterers.

Figure 3.27 shows the sandwich panel with one column extended scatterers with retaining plates. The retaining plate is highlighted with black colored edges and made transparent for visualization purposes. The retaining plates exist on either side and are bonded to the scatterers. The respective side views for better visualization are shown in Figure 3.28. As described in previous design set-ups, L is the distance between the center of the scatterer and the left edge of the sandwich panel, D is the diameter of the scatterer, B is the distance between the scatterers, and LS is the length of the scatterers as shown in Figure 3.27 and Figure 3.28. B, D, LS along with the material properties (Young's modulus and density) of the scatterers will be varied and examined for their influence on the vibration transmission reduction.

Figure 3.29 and Figure 3.30 show the sandwich panel with two column extended scatterers bonded to the retaining plates. The three column arrangement of extended fillers bonded to the retaining plates are shown in Figure 3.31 and Figure 3.32.

3.4.2 Material Properties

The material properties of the sandwich panel as listed in the Table 3.5 are used. The retaining plates are assumed to be a very light and made of very stiff homogeneous, isotropic, elastic material with the material properties as shown in Table 3.6. The material properties (Young's modulus and density) of the scatterers is one of the parameters that will be explored to understand their influence on the reduction of vibration transmission.

Table 3.6: Retaining plate material properties

Material property	Retaining plates
Young's modulus (E)	5.708×10^{13} Pa
Density (ρ)	2.0207 kg/m^3
Poisson's ratio (ν)	0.211

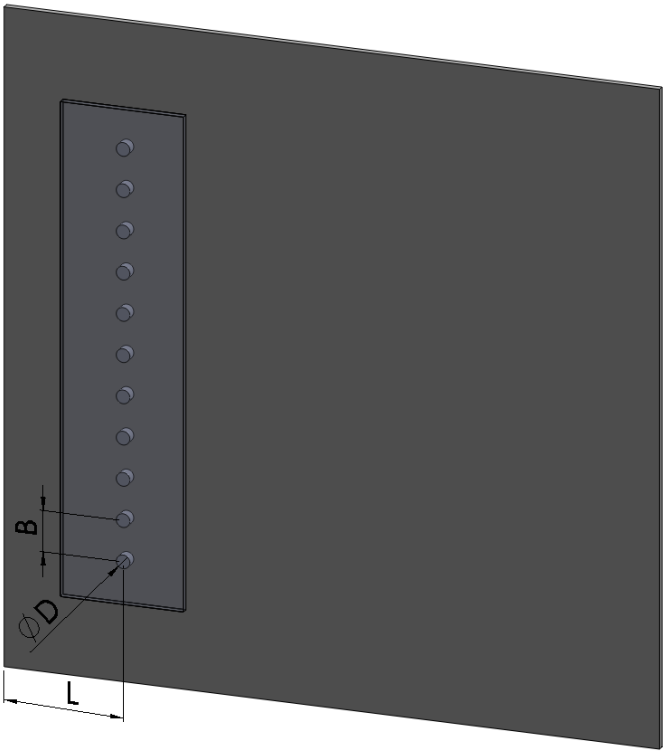

Figure 3.27: Sandwich panel with one column scatterers with retaining plates

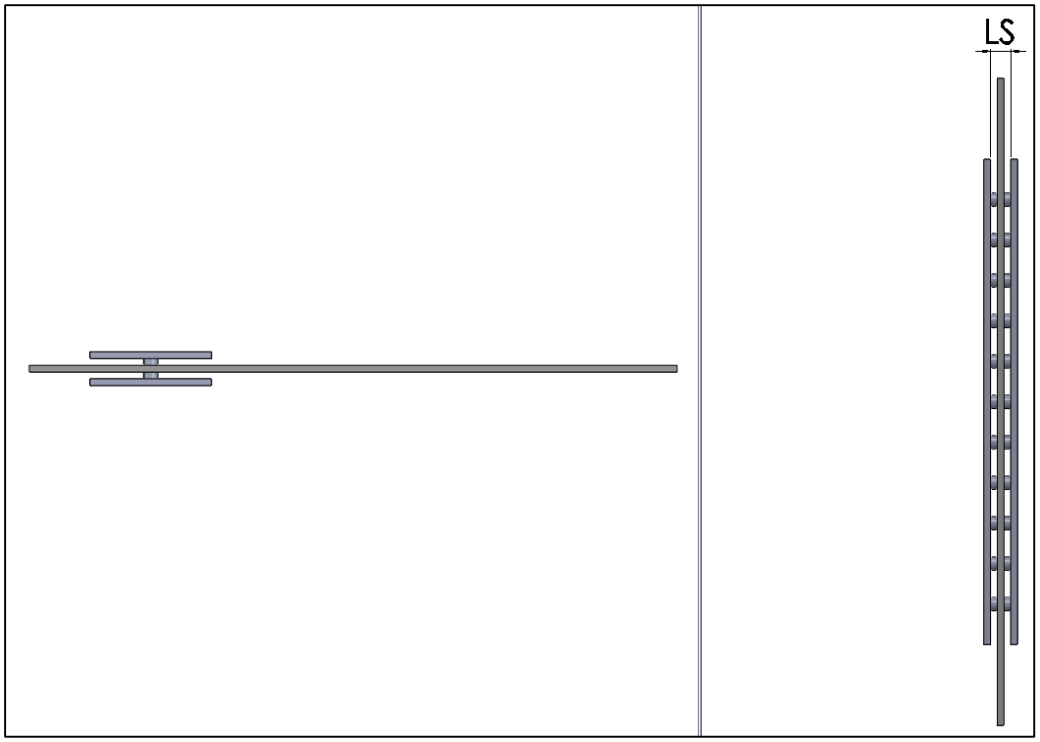

Figure 3.28: Sandwich panel with one column scatterers with retaining plates (side views)

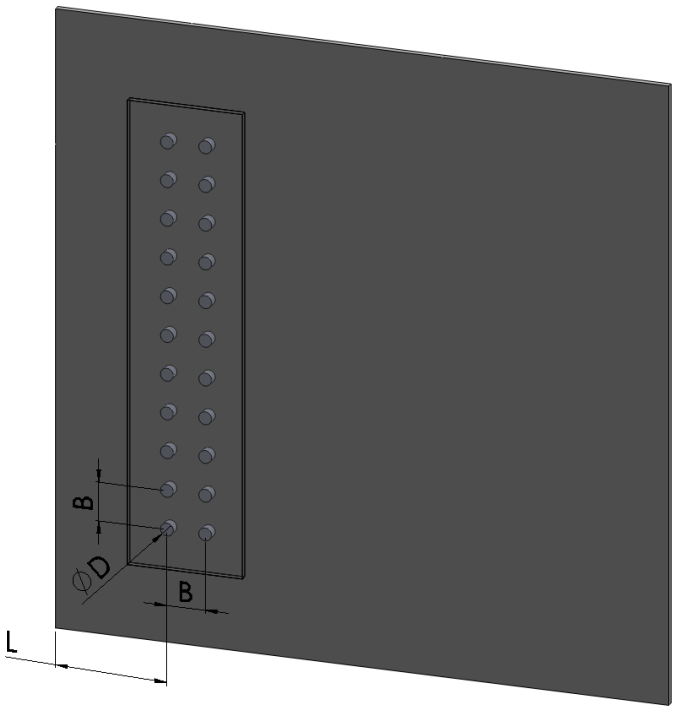

Figure 3.29: Sandwich panel with two column scatterers with retaining plates

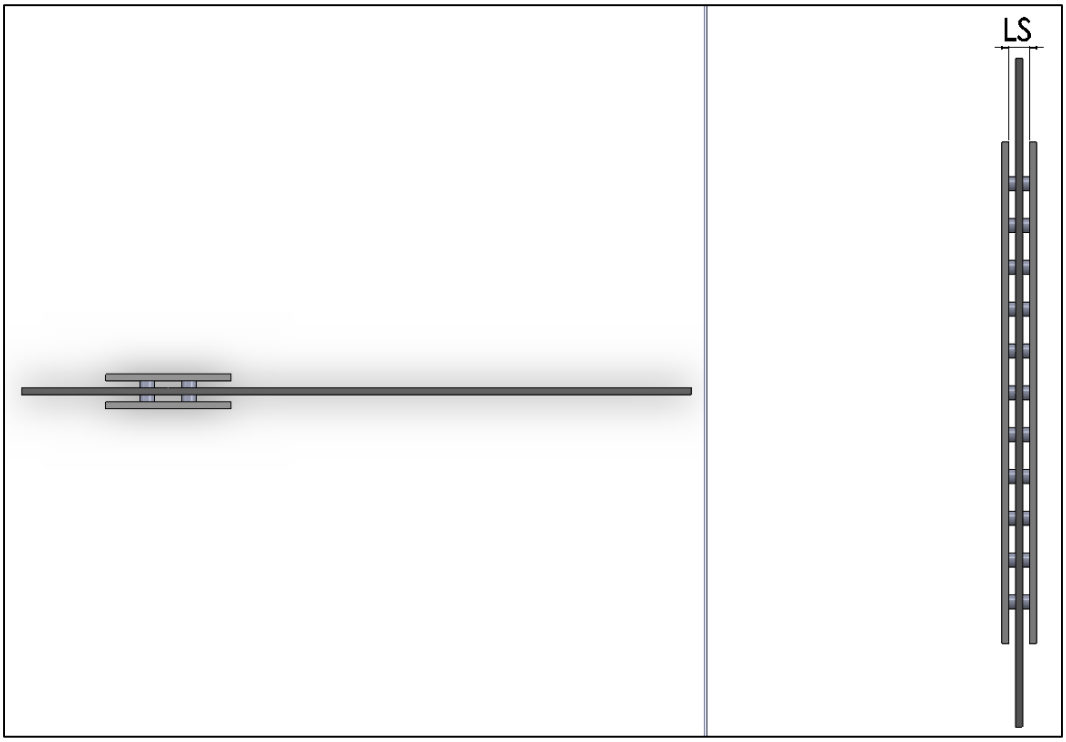

Figure 3.30: Sandwich panel with two column scatterers with retaining plates (side views)

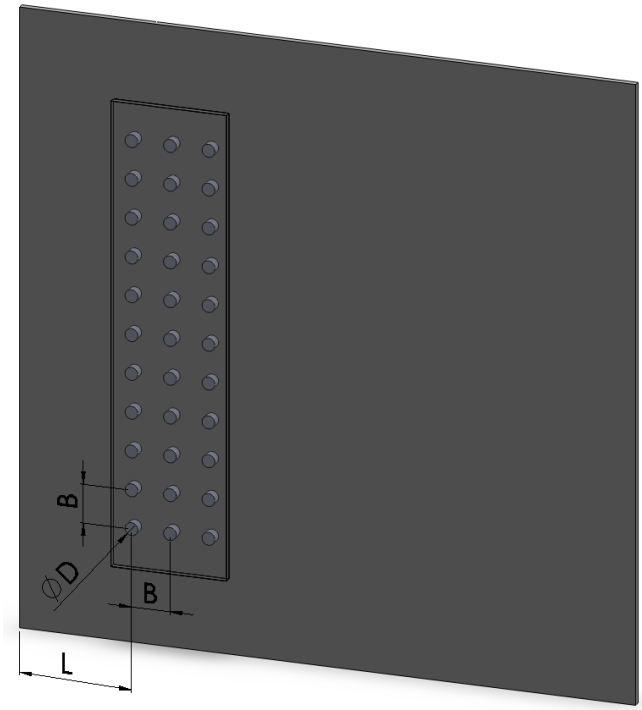

Figure 3.31: Sandwich panel with three column scatterers with retaining plates

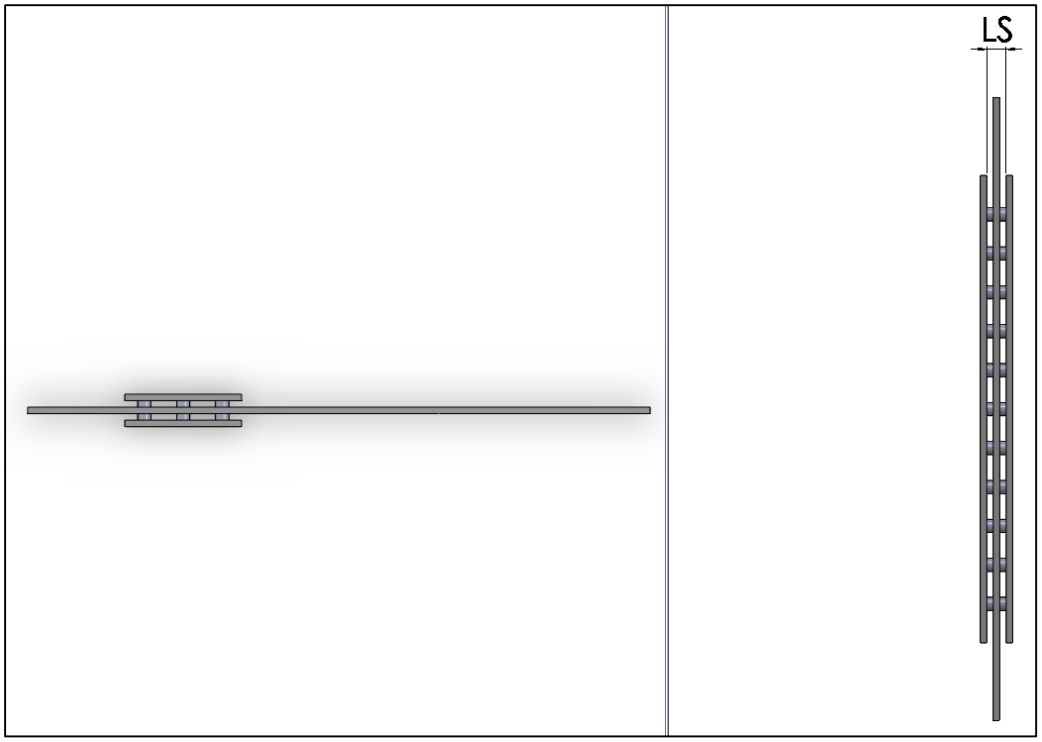

Figure 3.32: Sandwich panel with three column scatterers with retaining plates (side views)

3.4.3 Connections/Contacts

A bonded contact is applied between the three layers top face-plate, core and the bottom face-plate. The connections between the scatterers and the sandwich panel is bonded and same is the case with the connections between the scatterers and both the retaining plates.

3.4.4 Meshing

Mesh quality for each of the models has been chosen considering various metrics in ANSYS (element quality, aspect ratio, Jacobian ratio, etc.) and also the variation of results based on the natural frequency analysis. For example, Figure 3.33 and Figure 3.34 show the mesh quality selected for the sandwich panel with one column arrangement of extended scatterers with a scatterer diameter (D) of 1", lattice constant (B) of 3" and the length of scatterer (LS) of 2". For this mesh model, the total number of nodes are 30,012 and the number of elements are 21,404.

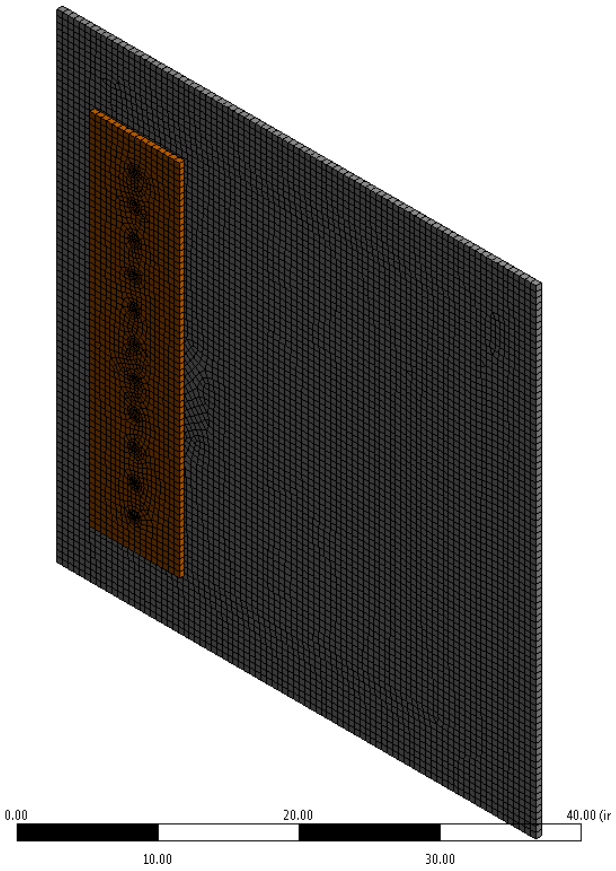

Figure 3.33: Mesh for sandwich panel with extended one column scatterers with retaining plates with scatterer diameter(D) of 1", lattice constant(B) of 3" and length of scatterer (LS) of 2"

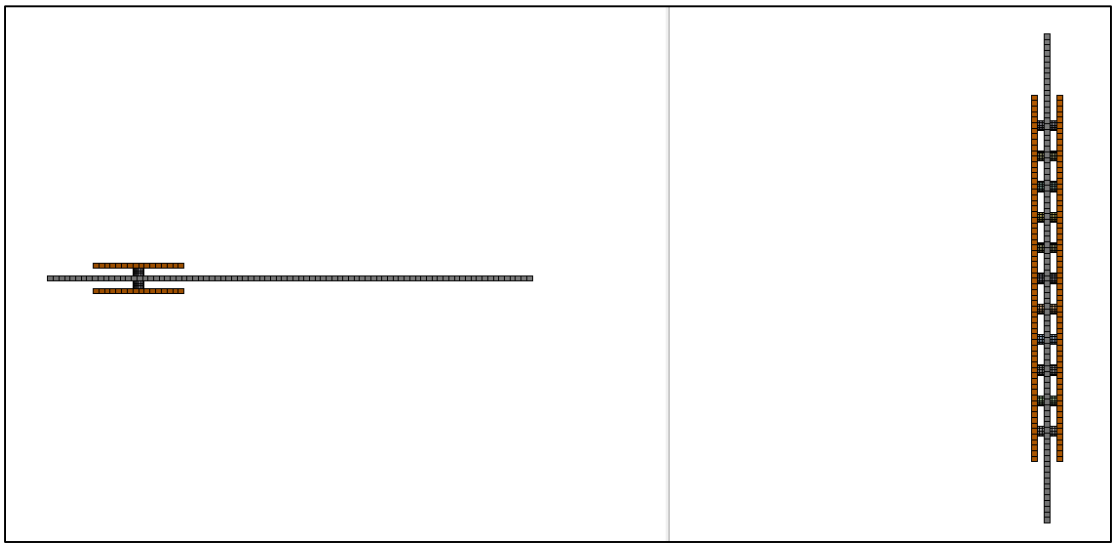

Figure 3.34: Mesh for sandwich panel with extended one column scatterers with retaining plates with scatterer diameter (D) of 1", lattice constant (B) of 3" and the length of scatterer (LS) of 2" (side views)

3.4.5 Loading

A load of amplitude 100 lbf is applied along the line AB of 3'x3' square in negative Z-direction as shown in Figure 3.35. The example shown in Figure 3.35 is for a sandwich panel with extended scatterers bonded to the retaining plates in a one column arrangement. The same is used for the two and three column arrangements. The top retaining plate is hidden in this figure for better visualization.

3.4.6 Fixtures/Constraints

The sandwich panel is fixed/clamped on all the four sides ABCD of the sandwich panel as shown in Figure 3.36. The example shown in Figure 3.36 is for a sandwich panel with extended scatterers bonded to the retaining plates in a one column arrangement. The same is used for the two and three column arrangements.

3.4.7 Damping

The damping ratio for the whole structure has been chosen as 0.01 close to the real world representation.

3.4.8 Analysis Set-up

Harmonic analysis is conducted for the frequency range of 2000 Hz to 4000 Hz for all the column arrangements. This range has been chosen because Bell Helicopters was interested in minimizing the vibration transmission at 3000 Hz.

3.4.9 Post Processing

A rectangular column area ABCD as shown in Figure 3.37 is selected to record for the root mean square of the displacements of all the nodes in the Z-direction over the frequency range of the study. This rectangular column ABCD which is the area of interest to capture the results will be referred as central region. The example shown in Figure 3.37 is for a sandwich

panel with extended scatterers bonded to the retaining plates in a one column arrangement. The same is used for the two and three column arrangements. The results from simulation studies using these FEM models will be presented and discussed in the next chapter.

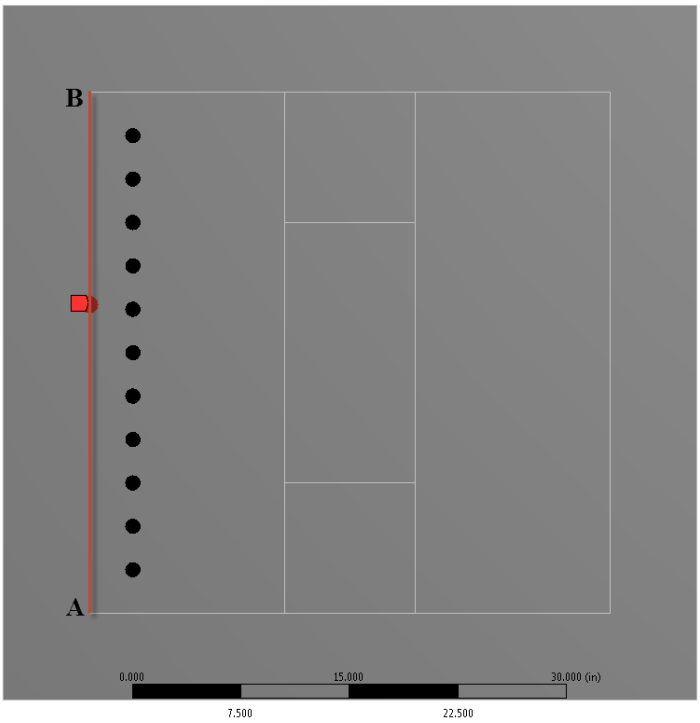

Figure 3.35: Sandwich panel with extended one column scatterers with retaining plates highlighting loading line (AB)

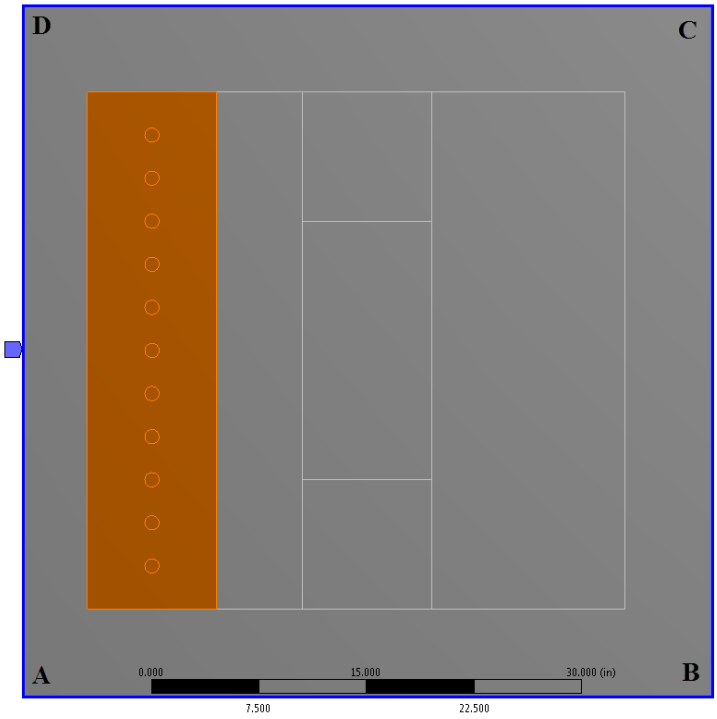

Figure 3.36: Sandwich panel with extended one column scatterers with retaining plates fixed on all four sides (ABCD)

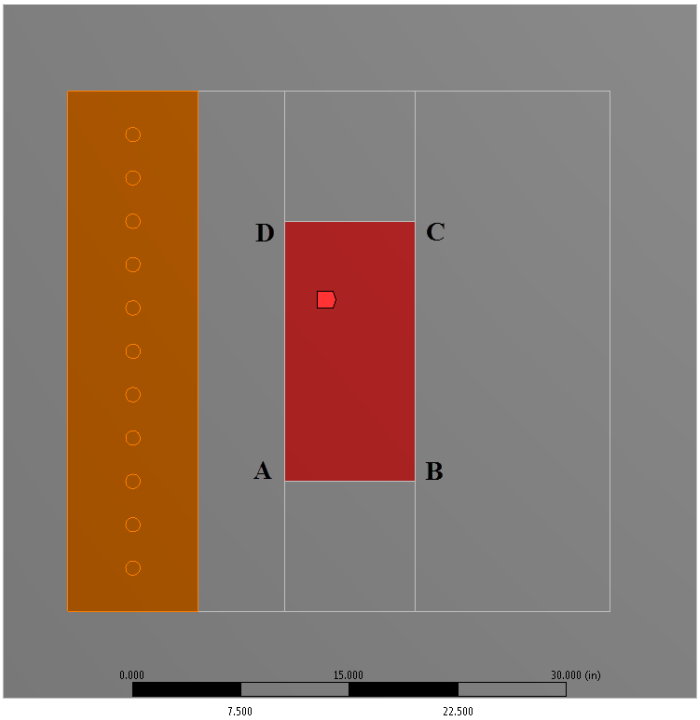

Figure 3.37: Sandwich panel with extended one column scatterers with retaining plates highlighting area of interest (ABCD)

4 Parametric Study

Results of the systematic parametric studies using different designs that were detailed in the previous chapter are presented in this chapter. Based on the learnings and knowledge gained, a final design of the composite sandwich panel is proposed and further investigated to find the optimum design. The results of the optimum design will be presented in the next chapter.

4.1 Controlling Parameters

As briefly discussed in the previous chapter, the parameters that will be explored in the simulation studies are:

1. Diameter of the scatterers
2. Number of columns of the scatterers
3. Young's modulus of the scatterers
4. Density of the scatterers
5. Lattice constant
6. Length of the scatterers

4.2 Simulations

4.2.1 Naming Convention

A parametric naming convention is followed to organize and identify the studies. Every study is named as follows: "Text-L-B-D-LS-Text1". "Text" is a descriptive string to describe the type of the study, for example "Holes1" means the simulation study is done on a sandwich panel with holes as scatterers in a one column arrangement. "L" is the distance of the scatterer from the left end of the sandwich panel, "B" denotes the lattice constant (the distance between the

scatterers), “D” is the diameter of the scatterer, and “LS” denotes the length of the scatterer and is optional. If “LS” is missing then it implies that the length of the scatterer matches the thickness of the sandwich. “Text1” is a descriptive string to describe the type of the scatterer material used in the study. The graphical representation of “L”, “B”, “D”, and “LS” are shown in all the FEM model representations in the previous chapter. Various textual descriptions (“Text”) that are part of the studies are: “Holes1”, “Holes2”, and “Holes3” represent the simulations with holes as scatterers in one, two and three column arrangements respectively; “Fillers1”, “Fillers2”, and “Fillers3” represent the simulations with scatterers where length of the scatterers match the thickness of sandwich in one, two and three column arrangements respectively; “Fillers-RP1”, “Fillers-RP2”, and “Fillers-RP3” represent simulations with scatterers whose length is extended beyond the thickness of the panel on both sides and are bonded to the retaining plates in one, two and three column arrangements respectively. For example, Holes3-9-3-1 represents the design of sandwich panel with three columns of hole scatterers where the distance between the first column of the holes and the left edge of the panel is 9", the lattice constant is 3", and the diameter of the hole is 1".

4.2.2 Results/plots

The goal of simulations is to evaluate the effectiveness in suppressing the vibration by various designs of the panel. To characterize the vibration of a design, a central region is defined as discussed in the previous chapter. A static structural study was run to capture the root mean square (RMS) of the Z-displacements of the central region denoted as SSRMSCR=0.096". The RMS of Z-displacements for the central region of a design is normalized with respect to SSRMSCR as a comparison with base sandwich panel under static loading. This normalized RMS of a design is denoted by RMSCR.

Let ARMSCR denote the averaged RMS of UZ over the frequency range of 2900 Hz to 3100 Hz (as our frequency of interest is 3000 Hz). A small range around the frequency of interest is chosen instead a single value (3000 Hz) to not miss the contribution of any natural frequency peaks in close vicinity to 3000 Hz.

To characterize the vibration reduction of a sandwich panel with scatterers compared with the base sandwich panel, a parameter 'Vibration Reduction Factor (%)' is defined as follows:

$$R = [1 - ARMSCR/(ARMSCR \text{ of base sandwich})]*100\%$$

Where ARMSCR is the averaged RMS of UZ (from 2900 Hz to 3100 Hz) for the central region for the sandwich panel with scatterers, and "ARMSCR of base sandwich" is the averaged RMS of UZ for the same central region but for the base sandwich panel (without scatterers).

The graphical plots presented in this chapter are only a subset of all simulations that are run, in order to reduce congestion in the plots and reveal trends more clearly. The first set of the plots that is presented are the normalized root means square (RMS) of the Z-displacements of the "central region" (RMSCR) vs the frequency. The second plot shows with the averaged ARMSCR vs parameter of the study. The third plot shows the Vibration Reduction Factor (%) versus the parameter of the study.

4.2.3 Circular Scatterers versus Equivalent Rectangular Slab

From the concept of phononic crystals, it was understood that multiple interferences occur due to the wave scattering through interaction with the periodicity of the circular scatterers. In the case where the multiple interferences are destructive, the waves are strongly attenuated as they travel through the periodic arrangement of scatterers.

In this section, a set of studies are conducted to verify and validate that the circular scatterers arranged periodically achieve better wave attenuation and vibration reduction compared to equivalent scatterer area replaced with a rectangular slab of same material. For this, we consider sandwich panels with a one column and two column scatterer arrangements as shown in Figure 4.1(a) and Figure 4.2(a). A scatterer diameter of 2" and lattice constant of 3" are considered for both the one and two column arrangements. These designs are compared with the sandwich panels with the scatterer area replaced by rectangular slabs as shown in Figure 4.1(b) and Figure 4.2(b). The cross-sectional area of the rectangular slab is chosen to cover the area of circular scatterers.

The material properties of the scatterers and the slabs are chosen to be the same as the face-plate material. The details of the solution set-up like mesh, connections, load, fixtures, damping, harmonic analysis and post processing are presented in section 3.3.

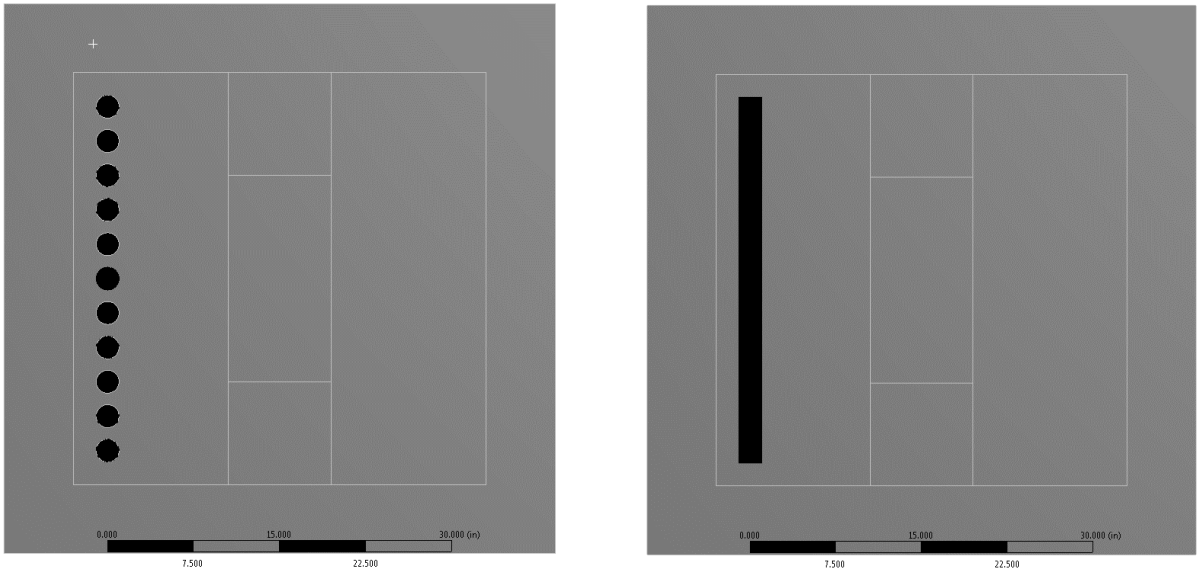

(a) (b)

Figure 4.1: (a) Sandwich panel with one column scatterers, (b) Sandwich panel with equivalent rectangular slab

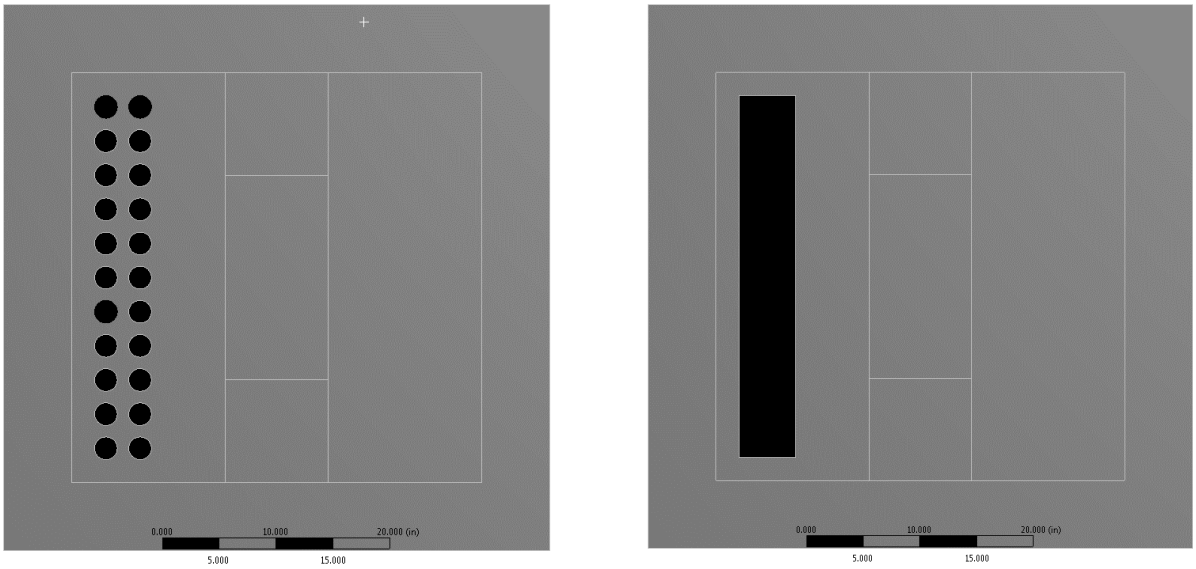

(a) (b)

Figure 4.2: (a) Sandwich panel with two column scatterers, (b) Sandwich panel with equivalent rectangular slab

Figure 4.3 shows the plots of normalized root mean square of UZ for the central region (RMSCR) against the frequency over the range of the harmonic study 2000 Hz to 4000 Hz for base sandwich panel, sandwich panel with one column scatterers and sandwich panel with a rectangular slab. It can be observed that the RMSCR of panel with a rectangular slab is greater than the base sandwich panel over the frequency range of 2600 Hz to 3100 Hz. The RMSCR of the panel with circular scatterers is consistently lower than base sandwich panel above 2500 Hz contributing to vibration reduction. The vibration reduction factor (%) for one column arrangement of scatterers is 37.9 whereas the vibration reduction factor (%) for panel with rectangular slab is -24.9 (which means the opposite of reduction, i.e., increase). So, at the frequency of interest, the sandwich panel with a rectangular slab caused an increase in vibration than the base sandwich panel instead of contributing to the vibration reduction.

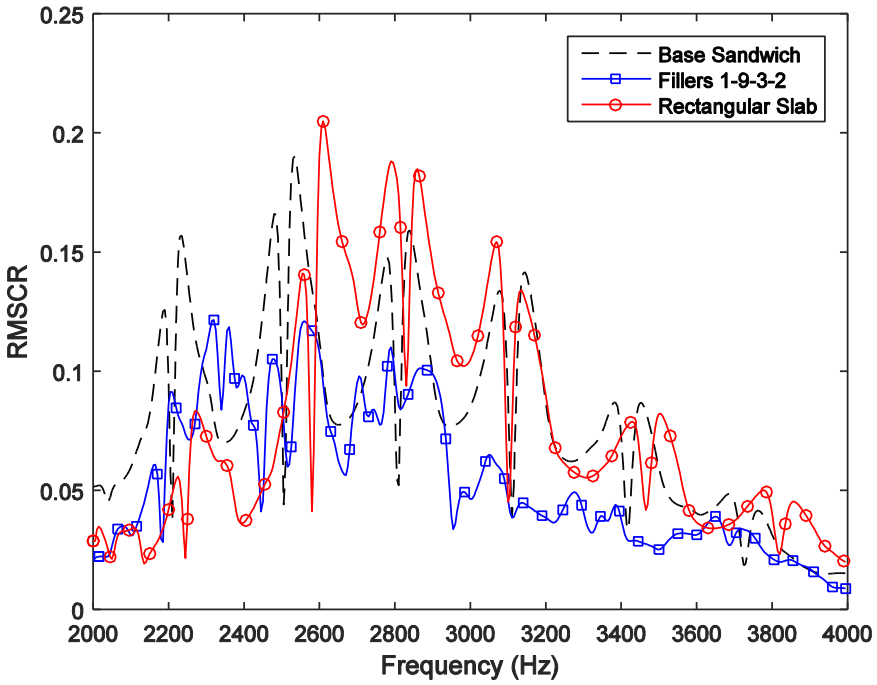

Figure 4.3: Normalized UZ (RMSCR) vs Frequency (2000 Hz-4000 Hz) for base sandwich, Fillers1-9-3-2, and sandwich panel with rectangular slab

Figure 4.4 shows the plots of normalized root mean square of UZ for the central region (RMSCR) against the frequency over the range of the harmonic study 2000 Hz to 4000 Hz for base sandwich panel, sandwich panel with two column scatterers and sandwich panel with a rectangular slab. It can be observed that the RMSCR of panel with a rectangular slab is lower than the base sandwich panel over the frequency range of study except for the range 2900 Hz to 3100 Hz which coincidently is our frequency range of interest. The RMSCR of panel with circular scatterers is consistently lower than base sandwich panel over the frequency range of study except for the range 2700 Hz to 2900 Hz. The vibration reduction factor (%) for two column arrangement of scatterers is 59.6 whereas the vibration reduction factor (%) for panel with a rectangular slab is -102.7 (i.e., vibration increase). So, at the frequency of interest, the

panel with the rectangular slab caused a significant increase in vibration than the base sandwich panel instead of contributing to the vibration reduction.

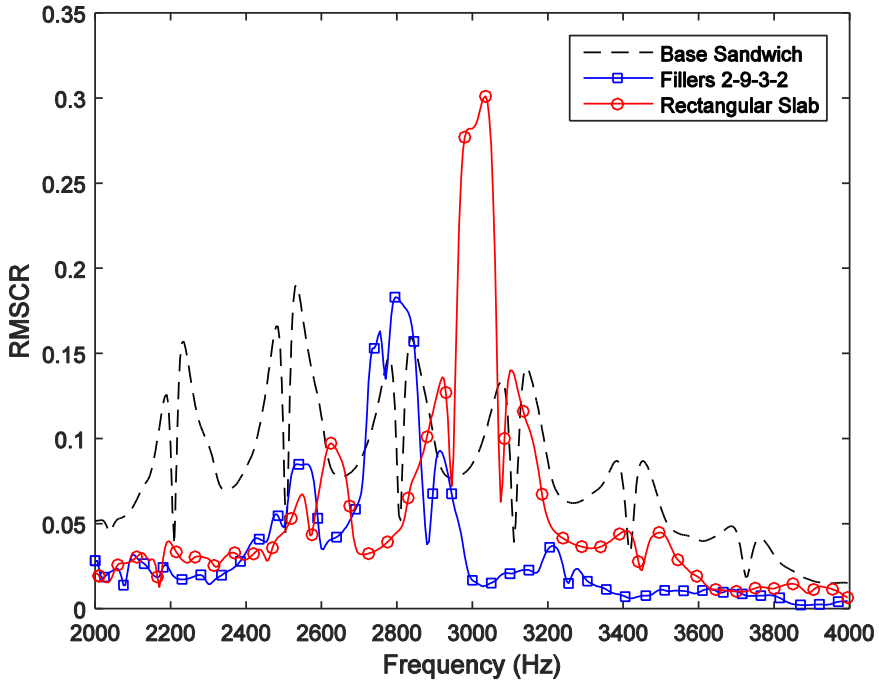

Figure 4.4: Normalized UZ (RMSCR) vs Frequency (2000 Hz-4000 Hz) for base sandwich, Fillers2-9-3-2, and sandwich panel with rectangular slab

Based on both the studies, it is clear that circular scatterers in a periodic arrangement were clearly the best choice for vibration reduction.

4.2.4 Hole Scatterers

The first set of simulations that are carried out are with sandwich panels with holes as scatterers. Three different variations were considered with holes: one column, two column and three column arrangements. The FEM models and solution set-up of these arrangements are detailed in section 3.3.

4.2.4.1 Effect of Scatterer Diameter

The one, two and three column arrangements were used to run simulations with varying diameters (0.5", 0.75", 1", 1.25", 1.5", 1.75", 2", 2.5", and 2.75") of the holes.

Figure 4.5, Figure 4.6, and Figure 4.7 show the plots of normalized UZ of the central region (RMSCR) against the frequency over the range of the harmonic study 2000 Hz to 4000 Hz. Figure 4.8 shows plots with the averaged RMS of UZ over the frequency range of 2900 Hz to 3100 Hz (ARMSCR) versus diameters of the scatterers with one column, two column and three column arrangement of holes. The dotted line represents the case of base sandwich panel. Figure 4.9 shows plots with the vibration reduction factor (%) versus diameters of the scatterers with one column, two column and three column arrangement of holes. It can be observed that vibration decreases around the frequency of interest at 3000 Hz as the diameter of the scatterer increases for the one, two and three column arrangements as can be seen in Figure 4.9. It can also be observed that the normalized UZ (RMSCR) reduces over most of the frequency range as the diameter of the scatterer increases as seen in Figure 4.5, Figure 4.6, and Figure 4.7.

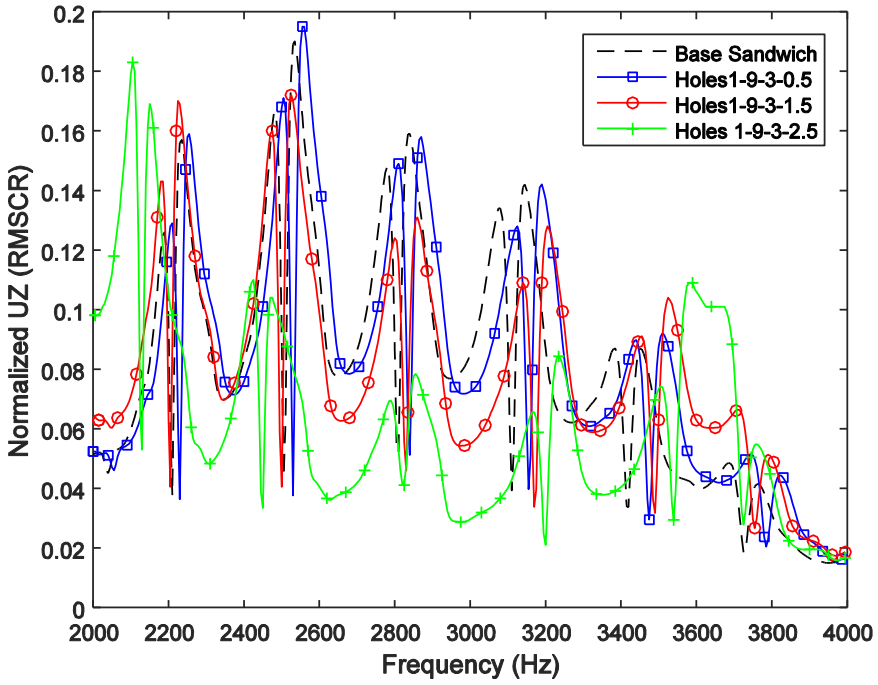

Figure 4.5: Normalized UZ (RMSCR) vs Frequency (2000 Hz-4000 Hz) for base sandwich, Holes1-9-3-X (X - 0.5", 1.5", and 2.5")

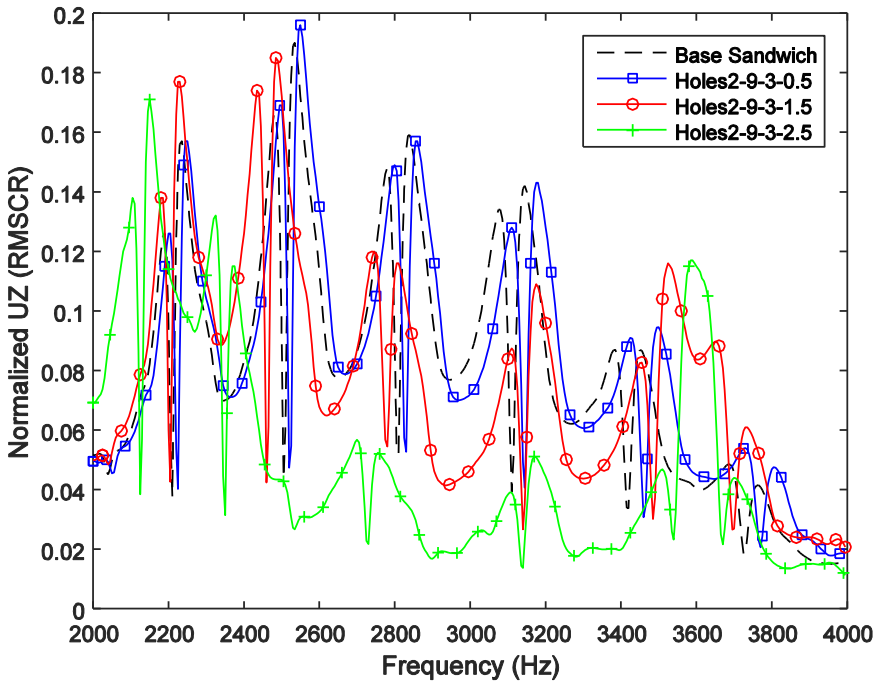

Figure 4.6: Normalized UZ (RMSCR) vs Frequency (2000 Hz-4000 Hz) for base sandwich, Holes2-9-3-X (X - 0.5", 1.5", and 2.5")

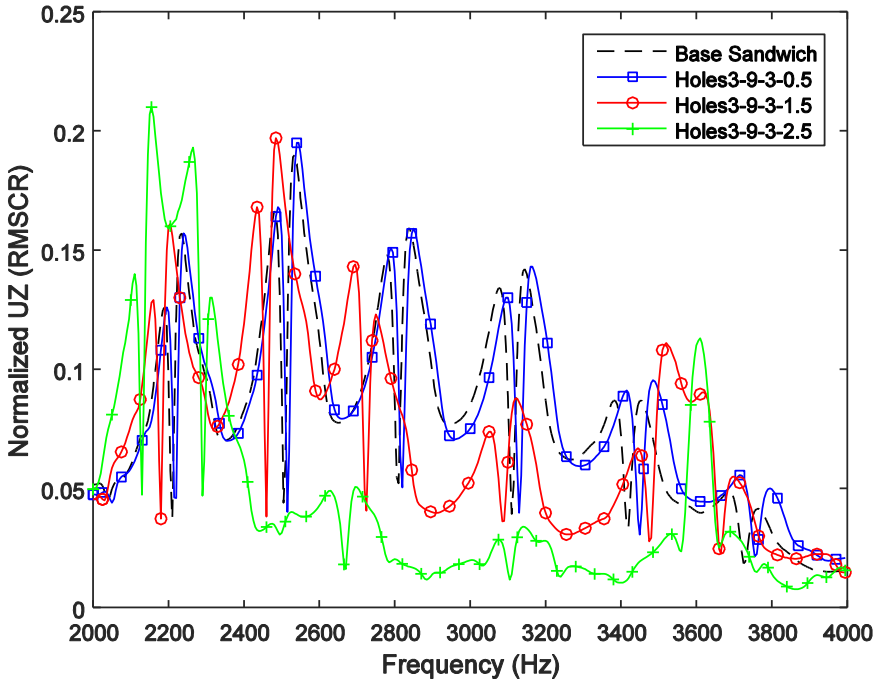

Figure 4.7: Normalized UZ (RMSCR) vs Frequency (2000 Hz-4000 Hz) for base sandwich, Holes3-9-3-X (X - 0.5", 1.5", and 2.5")

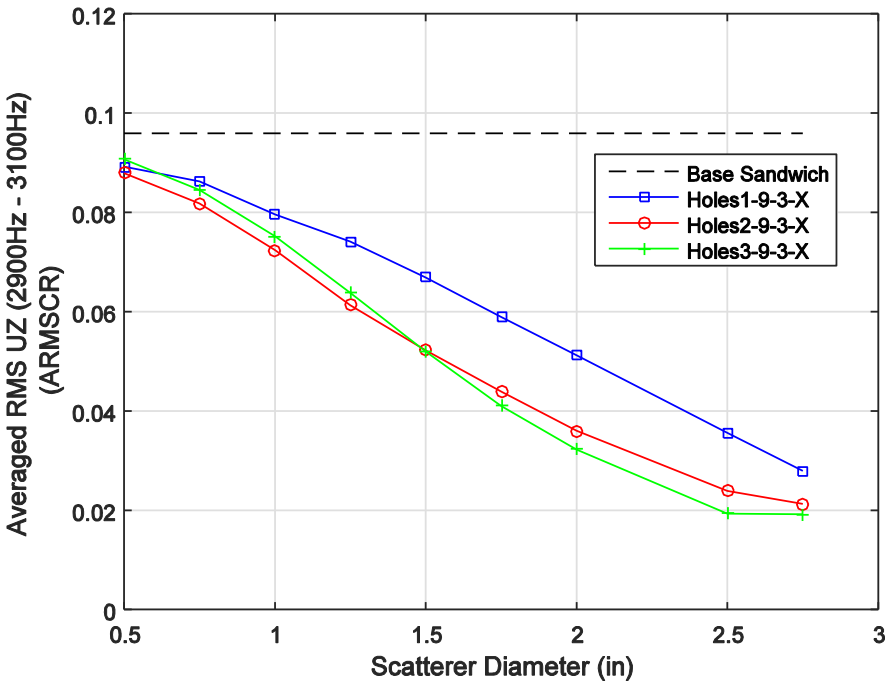

Figure 4.8: Averaged RMS UZ (ARMSCR) vs Scatterer Diameters (X - 0.5", 0.75", 1", 1.25", 1.5", 1.75", 2", 2.5", and 2.75") with Holes1-9-3-X, Holes2-9-3-X, Holes3-9-3-X

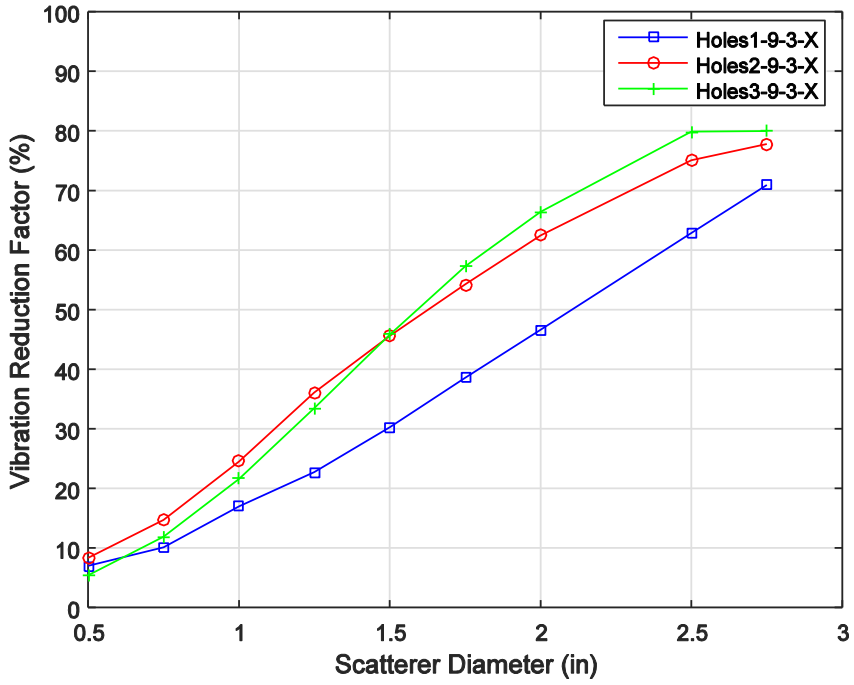

Figure 4.9: Vibration Reduction Factor (%) vs Scatterer Diameters (X - 0.5", 0.75", 1", 1.25", 1.5", 1.75", 2", 2.5", and 2.75") with Holes1-9-3-X, Holes2-9-3-X, Holes3-9-3-X

4.2.4.2 Effect of Number of Columns of Scatterers

Figure 4.5, Figure 4.6, and Figure 4.7 show the plots of normalized UZ of the central region (RMSCR) against the frequency over the range of the harmonic study 2000 Hz to 4000 Hz. Figure 4.8 shows plots with the averaged RMS of UZ over the frequency range of 2900 Hz to 3100 Hz (ARMSCR) versus diameters of the scatterers with one column, two column and three column arrangement of holes. The dotted line represents the case of base sandwich panel. Figure 4.9 shows plots with the vibration reduction factor (%) versus diameters of the scatterers with one column, two column and three column arrangement of holes. It can be observed that increasing the number of columns from one to two reduces the vibration over the frequency of interest as seen Figure 4.9. This trend of increase continue from two to three columns arrangement with the exception of smaller diameters of 0.5", 0.75", 1", and 1.25".

4.2.4.3 Effect of Lattice Constant

To explore the contribution of the lattice constant i.e., the center-to-center distance between scatterers, the two column hole arrangement has been chosen while keeping other parameters constant. The diameter of the hole chosen for these simulations is 1.5". The lattice constants 2", 2.5", 3", 3.5", and 4" are chosen for simulations.

Figure 4.10 shows plots with the vibration reduction factor (%) against different lattice constants. Figure 4.11 shows the plots of ARMSCR for different lattice constants. The dotted line represents the case of base sandwich panel. Figure 4.12 shows the plots of RMSCR against the frequency range of the harmonic studies 2000 Hz to 4000 Hz for different lattice constants. From Figure 4.10, it can be observed that increasing the lattice constant up to 3" increases the vibration reduction and then the trend reverses. This decrease for the lattice constant larger than 3" is because of the natural frequencies of the structure is changed and the peaks move to the right around frequency of interest 3000 Hz, as can be seen in Figure 4.12.

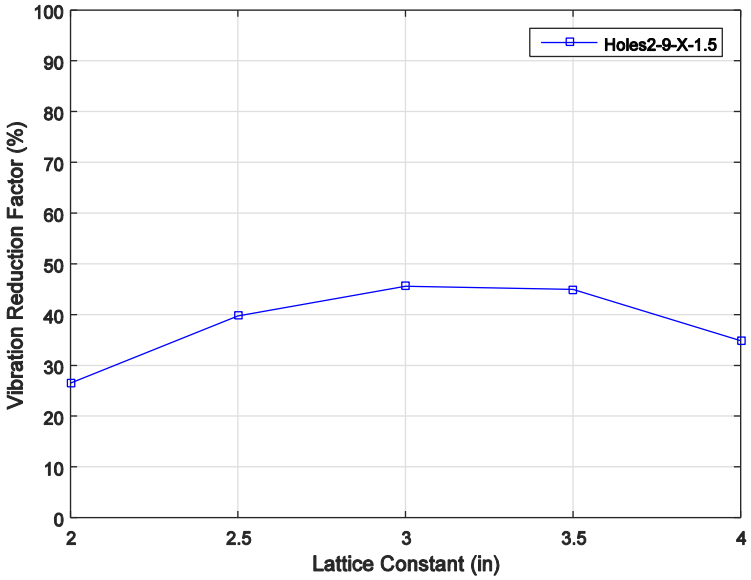

Figure 4.10: Vibration Reduction Factor % vs Lattice Constant (X - 2", 2.5", 3", 3.5", and 4") with Holes2-9-X-1.5

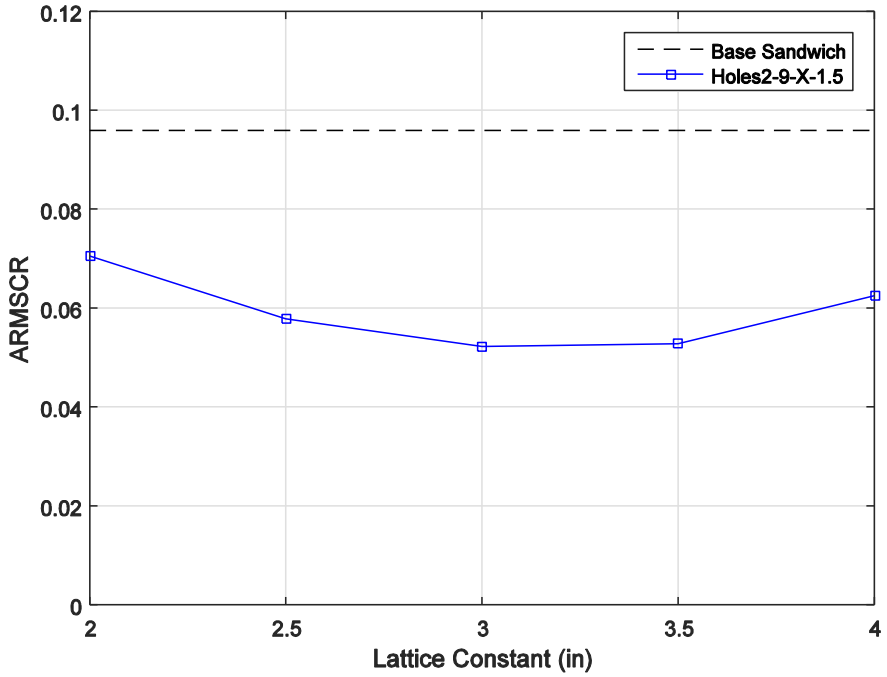

Figure 4.11: ARMSCR vs Lattice Constant (X - 2", 3", 3.5", and 4") with Holes2-9-X-1.5

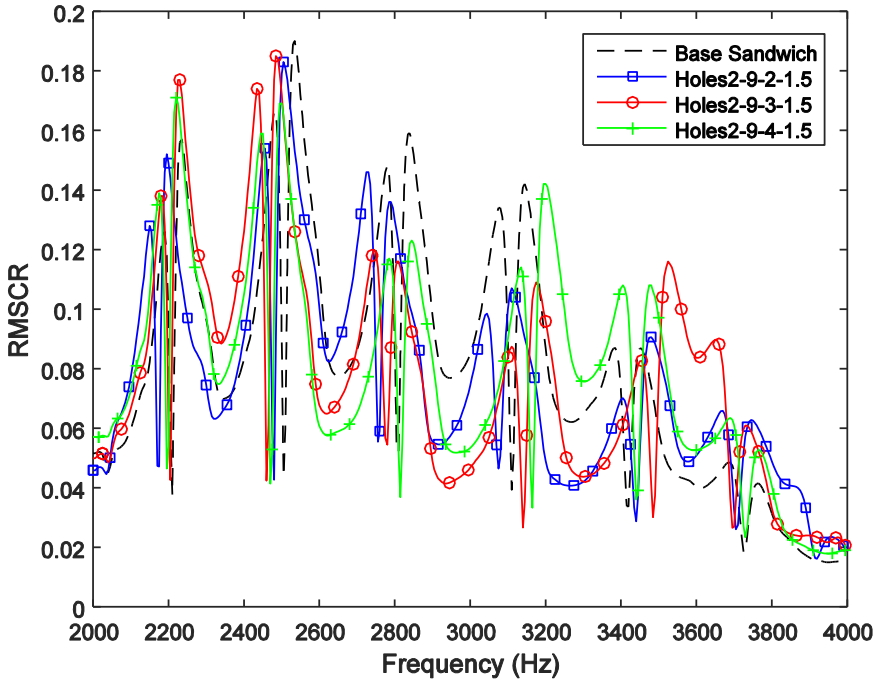

Figure 4.12: RMSCR vs Frequency (2000 Hz-4000 Hz) for base sandwich, Holes2-9-X-1.5 (X - 2", 3", and 4")

4.2.5 Filler Scatterers

The next set of simulations that are carried out are with the sandwich panel with fillers as scatterers. One column, two column and three column arrangements are considered and the respective FEM models and solution set-ups are detailed in section 3.3.

4.2.5.1 Effect of Scatterer Diameter

The one, two and three column arrangements with varying diameters (0.5", 0.75", 1", 1.25", 1.5", 1.75", 2", and 2.5") of the fillers were investigated. The material of the fillers is chosen as the same as the face-plate material as listed in Table 4.1.

Table 4.1: Sandwich panel material properties

Material property	Core	Top and Bottom face-plates
Young's modulus (E)	2.7095×10^{8} Pa	5.708×10^{10} Pa
Density (ρ)	52.862 kg/m^3	2020.7 kg/m^3
Poisson's ratio (ν)	0.4	0.211

Figure 4.13 shows vibration reduction factor (%) versus diameters of the scatterers for the simulation studies with one column, two column and three column filler arrangements. Figure 4.14 shows plots with the ARMSCR versus diameters of the scatterers for the simulation studies with one column, two column and three column filler arrangements. The dotted line represents the case of base sandwich panel. Figure 4.15, Figure 4.16, and Figure 4.17, show the plots of RMSCR against the frequency range of 2000 Hz - 4000 Hz. As can be seen in Figure 4.13, in each case of one, two and three column filler arrangements, the vibration over the frequency of

interest decreases as the diameter of the scatterer increases up to 1.5", 2", and 1.5" respectively, and then it increases. This increase after a certain diameter for each arrangement of fillers is caused by the change in the natural frequencies of the structure; the peaks move to the right around 3000 Hz, as can be seen in Figure 4.15, Figure 4.16, and Figure 4.17.

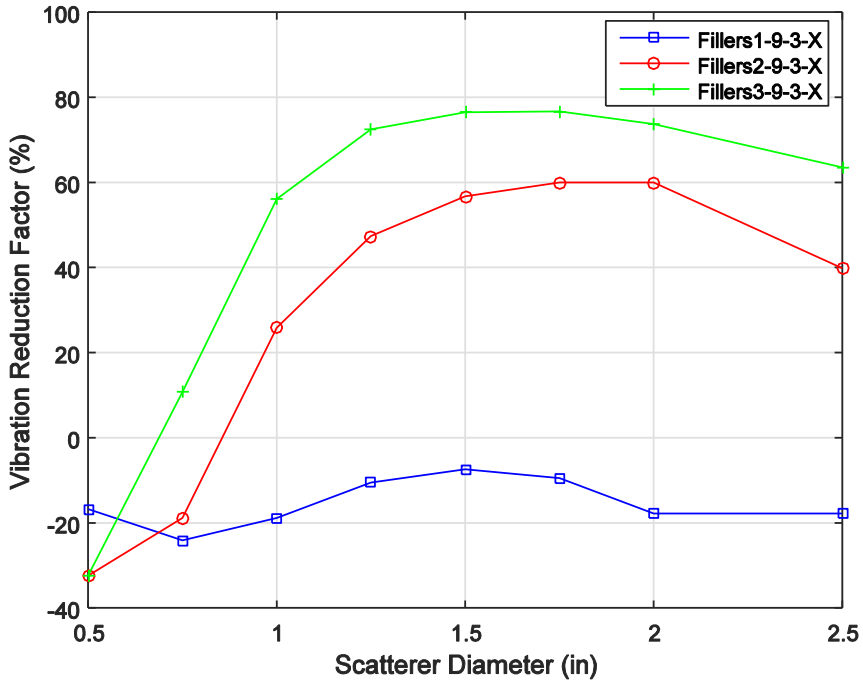

Figure 4.13: Vibration Reduction Factor (%) vs Scatterer Diameters (X - 0.5", 0.75", 1", 1.25", 1.5", 1.75", 2", and 2.5") with Fillers1-9-3-X, Fillers2-9-3-X, Fillers3-9-3-X

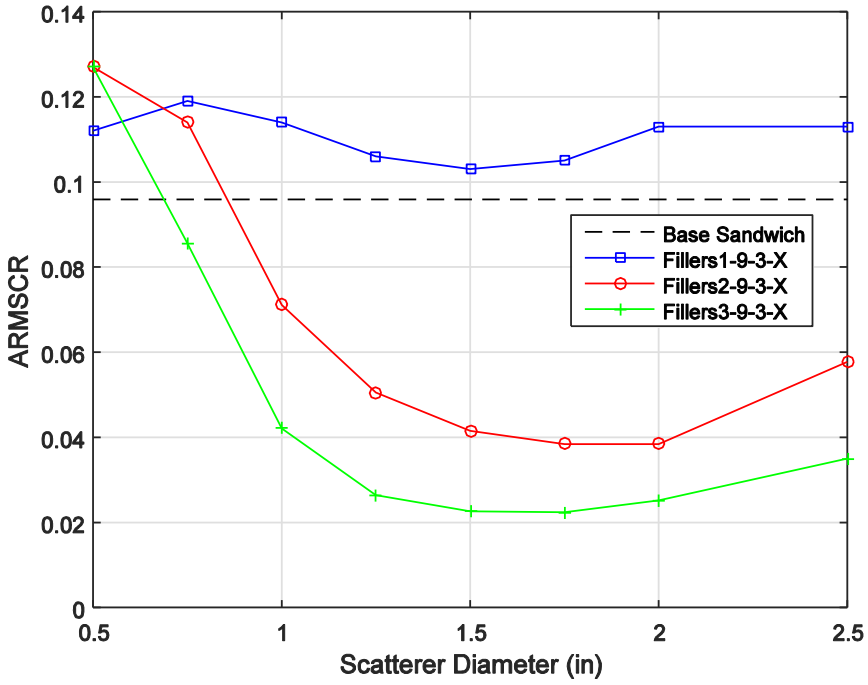

Figure 4.14: ARMSCR vs Scatterer Diameters (X - 0.5", 0.75", 1", 1.25", 1.5", 1.75", 2", and 2.5") with Fillers1-9-3-X, Fillers2-9-3-X, Fillers3-9-3-X

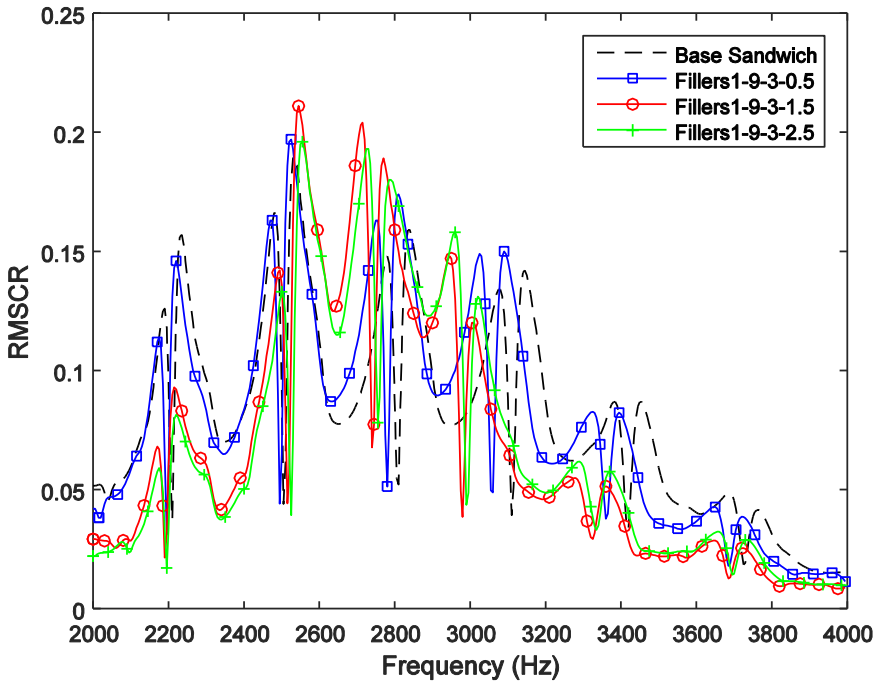

Figure 4.15: RMSCR vs Frequency (2000 Hz-4000 Hz) for base sandwich, Fillers1-9-3-X (X - 0.5", 1.5", and 2.5")

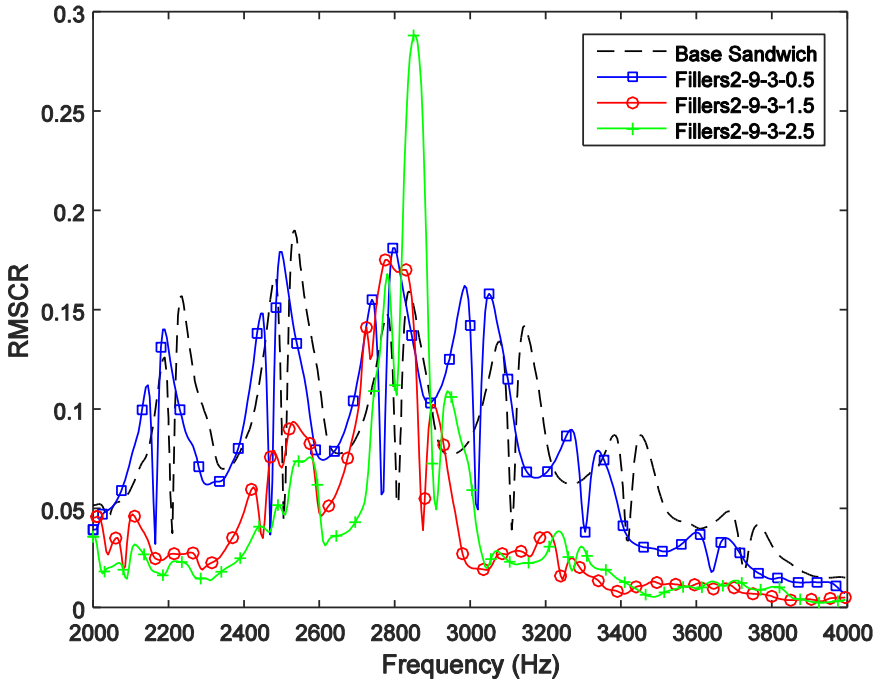

Figure 4.16: RMSCR vs Frequency (2000 Hz-4000 Hz) for base sandwich, Fillers2-9-3-X (X - 0.5", 1.5", and 2.5")

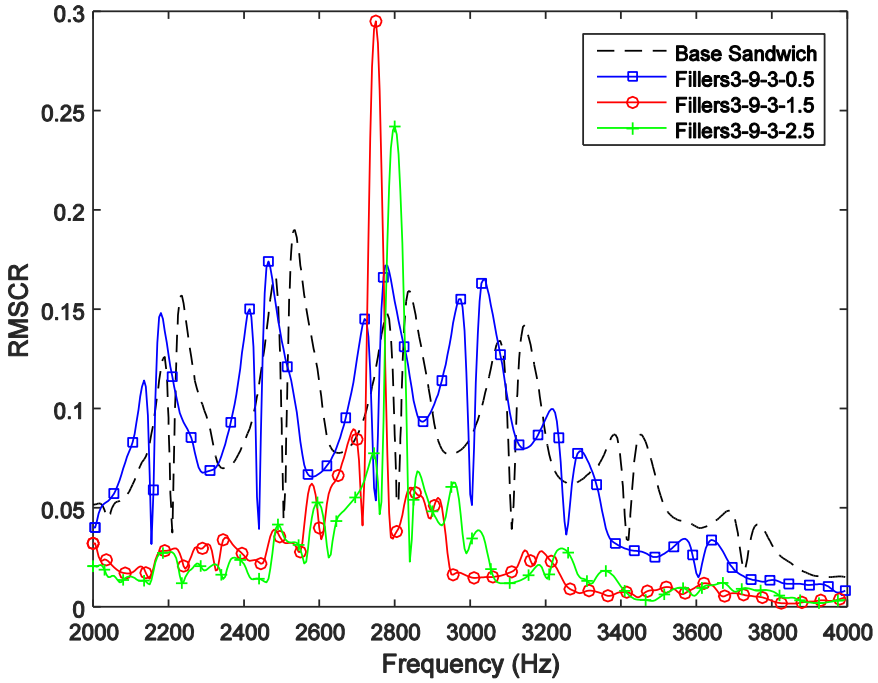

Figure 4.17: RMSCR vs Frequency (2000 Hz-4000 Hz) for base sandwich, Fillers3-9-3-X (X - 0.5", 1.5", and 2.5")

4.2.5.2 Effect of Number of Columns of Scatterers

Figure 4.13 shows vibration reduction factor (%)versus diameters of the scatterers for the simulation studies with one column, two column and three column filler arrangements. Figure 4.14 shows plots with the ARMSCR versus diameters of the scatterers for the simulation studies with one column, two column and three column filler arrangements. The dotted line represents the case of base sandwich panel. Figure 4.15, Figure 4.16, and Figure 4.17, show the plots of RMSCR against the frequency range of 2000 Hz - 4000 Hz. As can be observed in Figure 4.13, there is a vibration reduction as the number of columns increase from one to two to three for all the diameters with the exception of the lowest diameter of 0.5". This exception could be attributed to the change of natural frequencies of the sandwich panel shown in Figure 4.15, Figure 4.16, and Figure 4.17.

4.2.5.3 Effect of Material Properties

The next set of simulations looked into material variations of the fillers while keeping the other parameters constant. The Young's modulus and the density of the filler materials are explored. For these studies a sandwich panel with two column arrangement of the fillers with scatterer diameter of 1" and lattice constant of 3" is considered.

To explore the impact of Young's modulus, the rest of the material properties of the filler material were kept constant which are density (ρ) = 2020.7 kg/m^3 and Poisson's ratio (ν) = 0.211. The following Young's modulus values are considered: 5.708×10^7 Pa, 5.708×10^8 Pa, 5.708×10^9 Pa, 5.708×10^{10} Pa, 5.708×10^{11} Pa, 5.708×10^{12} Pa, and 5.708×10^{13} Pa, and each of these simulations is represented by case numbers 1, 2, 3, 4, 5, 6, and 7 in the plots.

Figure 4.18 shows the plots of RMSCR against the frequency range 2000 Hz to 4000 Hz for different filler materials described above. Figure 4.19 shows ARMSCR against the different Young's modulus values for the filler material. The dotted line represents the case of base sandwich panel. Figure 4.20 shows vibration reduction factor (%) against different Young's modulus values for the filler material. It can be observed that all the plots of RMSCR for the cases 4, 5, 6, and 7 where the Young's modulus values of the filler material are 5.708×10^{10} Pa, 5.708×10^{11} Pa, 5.708×10^{12} Pa, and 5.708×10^{13} Pa respectively, follow each other fairly closely as shown in Figure 4.18. But it can also be observed that as the Young's modulus of the filler material is reduced from 5.708×10^{10} Pa, the natural frequency peaks are moved to the left. This causes the reduction of vibration which is the trend reflected Figure 4.20.

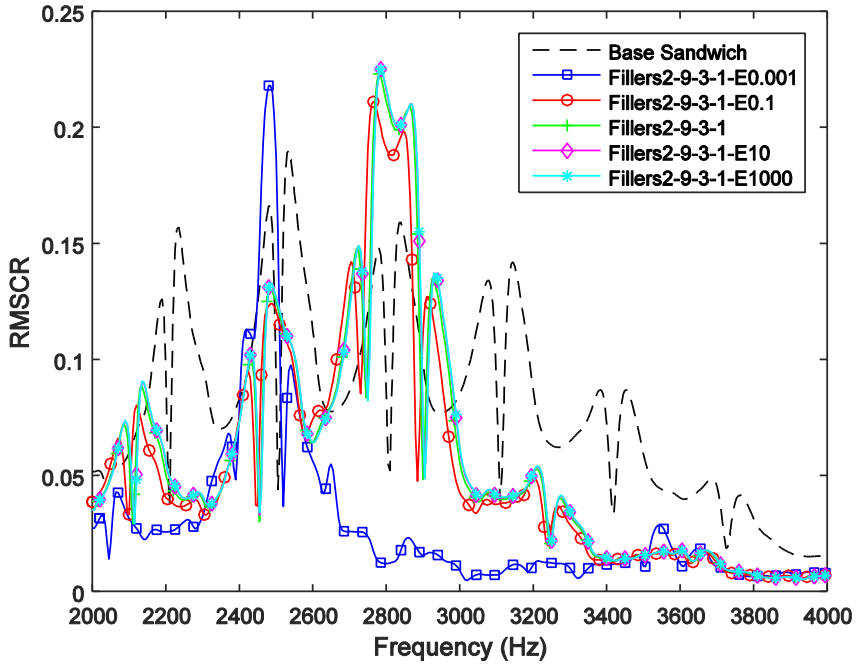

Figure 4.18: RMSCR vs Frequency (2000 Hz-4000 Hz) for base sandwich, Fillers2-9-3-1 (Filler Young's modulus - 5.708×10^{7} Pa, 5.708×10^{9} Pa, 5.708×10^{10} Pa, 5.708×10^{11} Pa, and 5.708×10^{13} Pa)

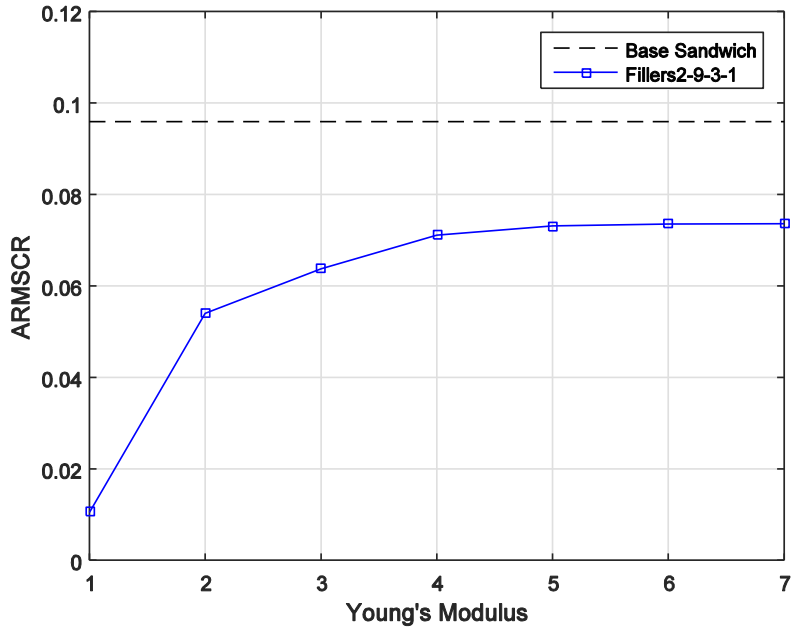

Figure 4.19: ARMSCR vs Filler Young's Modulus (5.708×10^{7} Pa, 5.708×10^{8} Pa, 5.708×10^{9} Pa, 5.708×10^{10} Pa, 5.708×10^{11} Pa, 5.708×10^{12} Pa, and 5.708×10^{13} Pa) with Fillers2-9-3-1

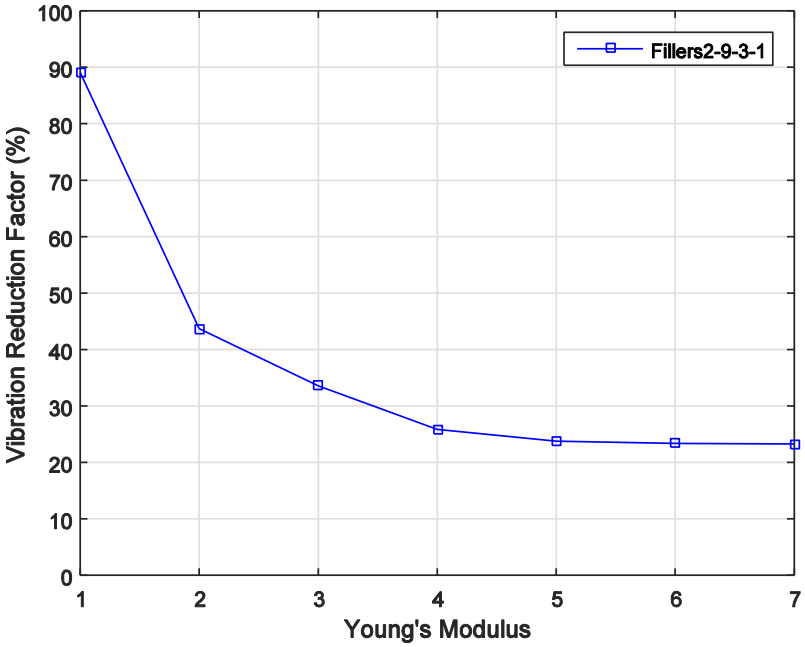

Figure 4.20: Vibration Reduction Factor (%) vs Filler Young's Modulus (5.708×10^{7} Pa, 5.708×10^{8} Pa, 5.708×10^{9} Pa, 5.708×10^{10} Pa, 5.708×10^{11} Pa, 5.708×10^{12} Pa, and 5.708×10^{13} Pa) with Fillers2-9-3-1

To explore the impact of density, the rest of the material properties of the filler material were kept constant which are Young's modulus (E) = 5.708×10^{10} Pa and Poisson's ratio (ν) = 0.211. The following density values are considered: 2.02 kg/m^3, 20.2 kg/m^3, 202.07 kg/m^3 Pa, 2020.7 kg/m^3, 2.02×10^4 kg/m^3, 2.02×10^5 kg/m^3, and 2.02×10^6 kg/m^3. Each of these simulations are represented by case numbers 1, 2, 3, 4, 5, 6, and 7 in the plots. Figure 4.21 shows the plots RMSCR against the frequency range for filler materials with different densities as mentioned above. Figure 4.22 shows ARMSCR against the different density values considered for the filler material. The dotted line represents the case of base sandwich panel. Figure 4.23 shows vibration reduction factor (%) against the different density values considered for the filler material. It can be observed that the cases with fillers of higher densities push the natural frequencies to the left as shown in Figure 4.21. A better vibration reduction is achieved over the frequency of interest and the trend plateaus for density greater than 2020.7 kg/m^3 as can be seen in Figure 4.23.

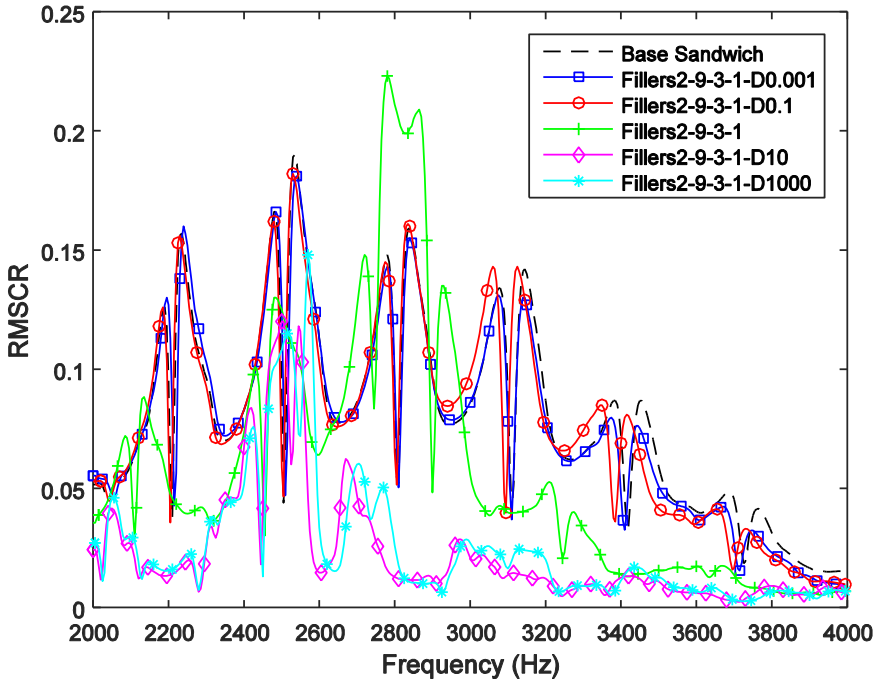

Figure 4.21: RMSCR vs Frequency (2000 Hz-4000 Hz) for base sandwich, Fillers2-9-3-1 (Filler density - 2.02 kg/m^3, 202.07 kg/m^3 Pa, 2020.7 kg/m^3, 2.02×10^4 kg/m^3, and 2.02×10^6 kg/m^3)

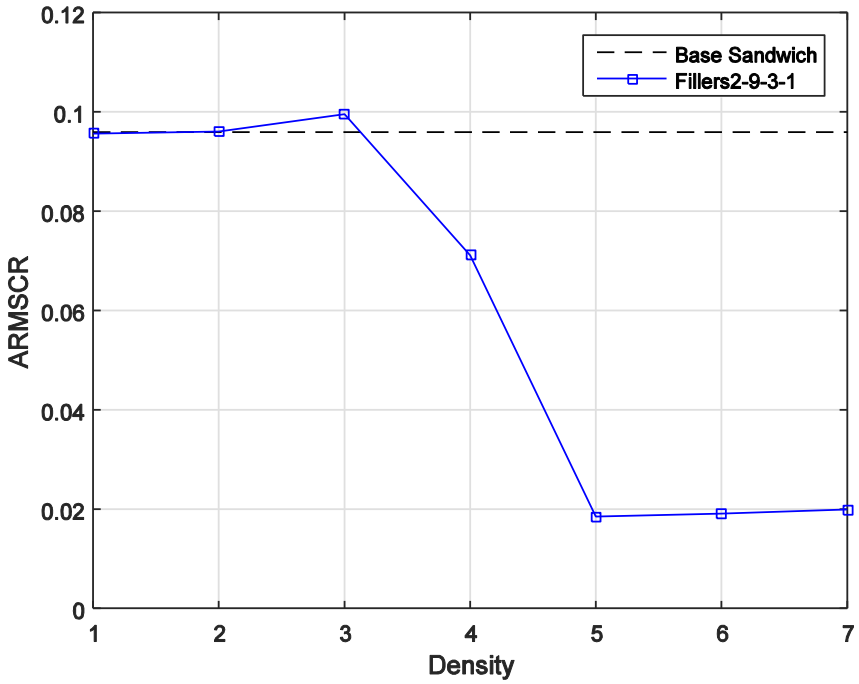

Figure 4.22: ARMSCR vs Filler Density (2.02 kg/m^3, 20.2 kg/m^3, 202.07 kg/m^3 Pa, 2020.7 kg/m^3, 2.02×10^4 kg/m^3, 2.02×10^5 kg/m^3, and 2.02×10^6 kg/m^3) with Fillers2-9-3-1

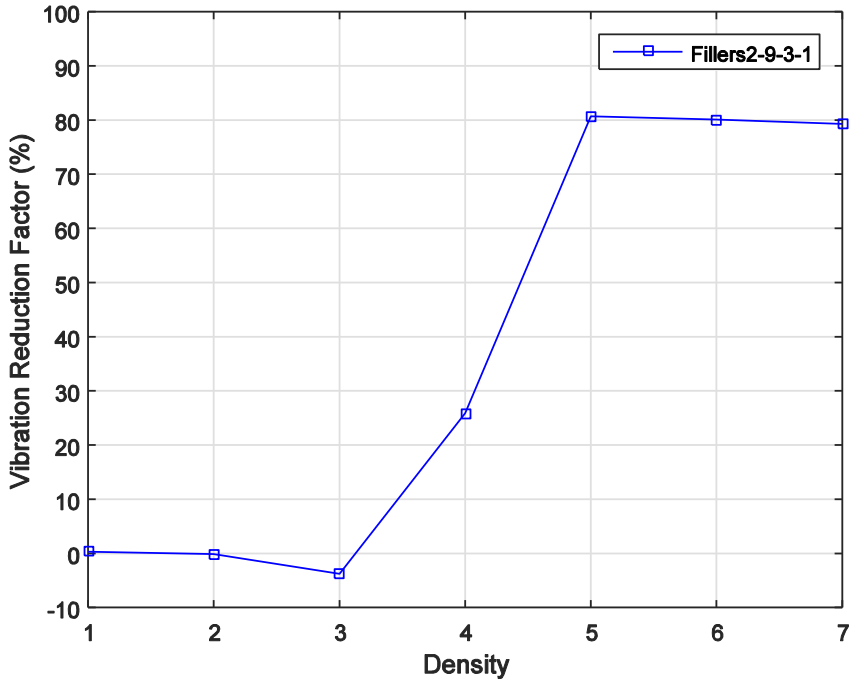

Figure 4.23: Vibration Reduction Factor (%) vs Filler Density (2.02 kg/m^3, 20.2 kg/m^3, 202.07 kg/m^3 Pa, 2020.7 kg/m^3, 2.02×10^4 kg/m^3, 2.02×10^5 kg/m^3, and 2.02×10^6 kg/m^3) with Fillers2-9-3-1

4.2.5.4 Effect of Lattice Constant

The contribution of the lattice constant was explored while keeping the other parameters unchanged. A two column filler arrangement has been chosen with the scatterer diameter as 1". The material of the fillers is chosen as the same as face-plate material as listed in Table 4.1. The lattice constants 1.5", 2", 2.5", 3", 3.5", and 4" are chosen for simulations.

Figure 4.24 shows the vibration reduction factor (%) against the different lattice constants. Figure 4.25 shows ARMSCR against the different lattice constants. The dotted line represents the case of base sandwich panel. Figure 4.26 shows the plots of RMSCR against the frequency range of 2000 Hz to 4000 Hz for different lattice constants. From Figure 4.24, it can be observed that increasing the lattice constant upto 3.5" increases the vibration reduction and the trend reverses. This increase after lattice constant of 3.5" is because of the natural frequencies of

the structure is changed, and the peaks move to the right around 3000 Hz, as can be seen in Figure 4.26.

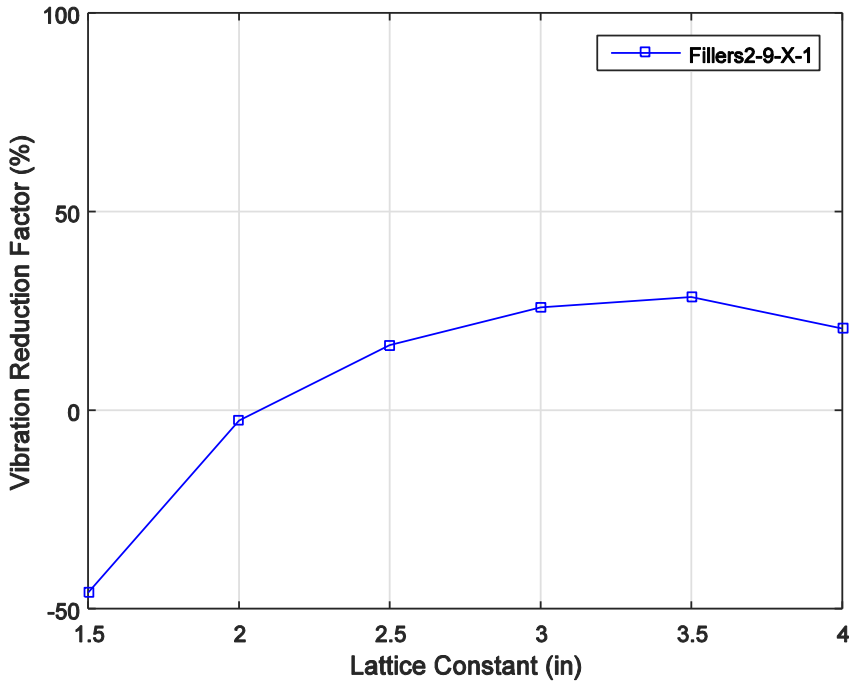

Figure 4.24: Vibration Reduction Factor (%) vs Lattice Constant (X - 1.5", 2", 2.5", 3", 3.5", and 4'') with Fillers 2-9-3-X-1

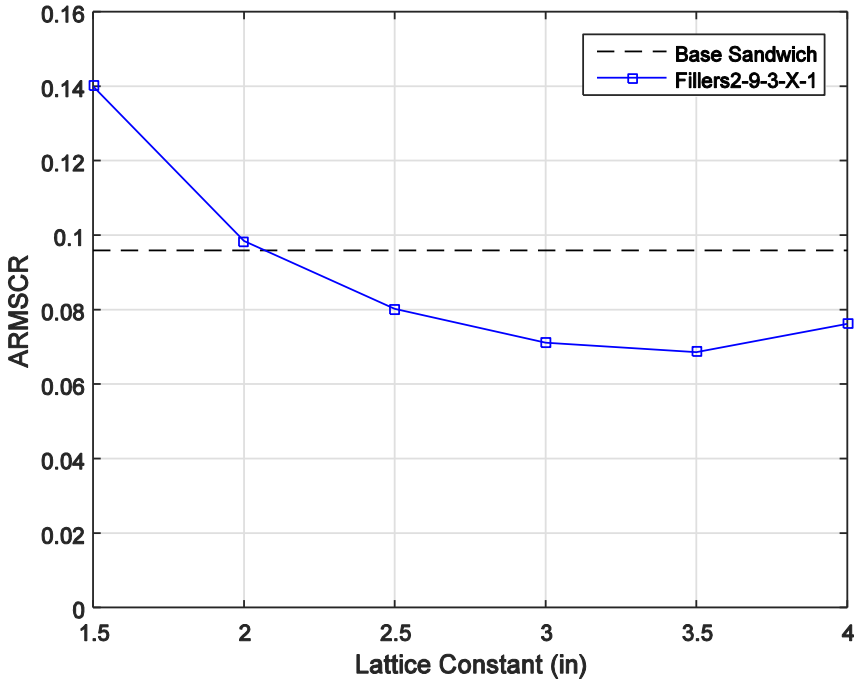

Figure 4.25: ARMSCR vs Lattice Constant (X - 1.5", 2", 2.5", 3", 3.5", and 4'') with Fillers 2-9-3-X-1

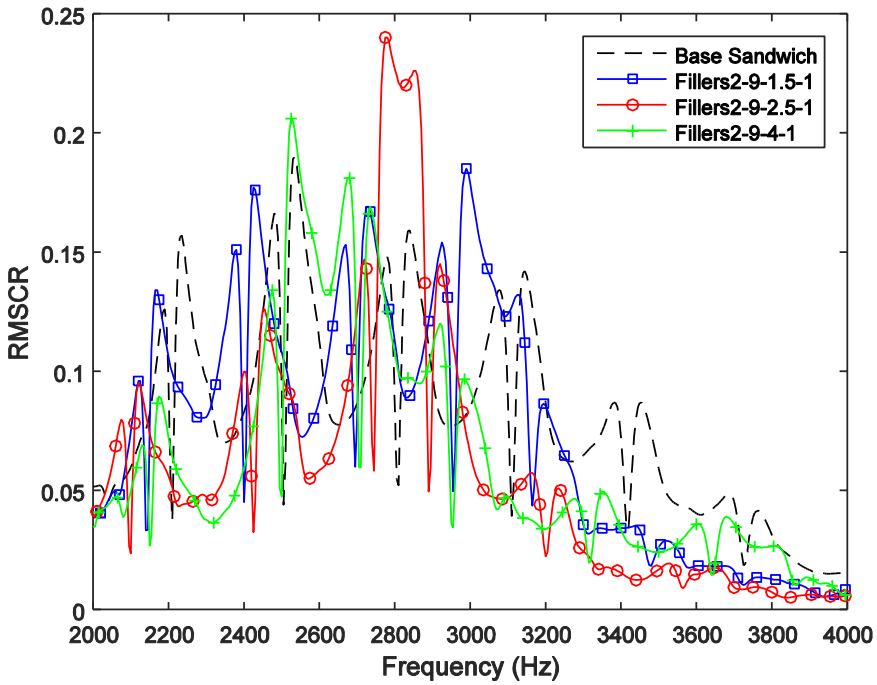

Figure 4.26: RMSCR vs Frequency (2000 Hz-4000 Hz) for base sandwich, Fillers2-9-X-1 (X - 1.5", 2.5", and 4")

4.2.6 Extended Filler Scatterers with Retaining Plates

Sandwich panel with filler rods extending beyond the thickness of the sandwich panel as scatterers which are bonded to the retaining plates on the either side is considered as another design variation for the next set of simulations. One column, two column and three column arrangements are considered and the respective FEM models and solution set-ups are detailed in section 3.4.

4.2.6.1 Effect of Scatterer Diameter

With one, two, and three column arrangements various studies were set-up with varying diameters (1", 1.25", 1.5", 2", and 2.5") of the fillers rods. The material of the filler rods is chosen as face-plate material as listed in Table 4.1 and the scatterer length is chosen to be 2". The material properties of the retaining plates chosen are shown in Table 4.2.

Table 4.2: Retaining plate material properties

Material property	Retaining plates
Young's modulus (E)	5.708×10^{13} Pa
Density (ρ)	2.0207 kg/m^3
Poisson's ratio (ν)	0.211

Figure 4.27 shows three plots with vibration reduction factor (%) versus the diameters of scatterers with one column, two column and three column arrangements. Figure 4.28 shows three plots with ARMSCR versus the diameters of scatterers with one column, two column and three column arrangements. The dotted line represents the case of base sandwich panel. Figure 4.29, Figure 4.30, and Figure 4.31 show the plots of RMSCR against the frequency range of the harmonic study 2000 Hz to 4000 Hz. It can be seen in Figure 4.27 that the vibration reduces as

the diameter of the scatterer increases to a diameter of 1.5" and then it starts increasing for all the one, two, and three column arrangements. This increase after diameter 1.5" is because the natural frequencies of the structure is changed and the peaks move to the right around 3000 Hz, as can be seen in Figure 4.29, Figure 4.30, and Figure 4.31.

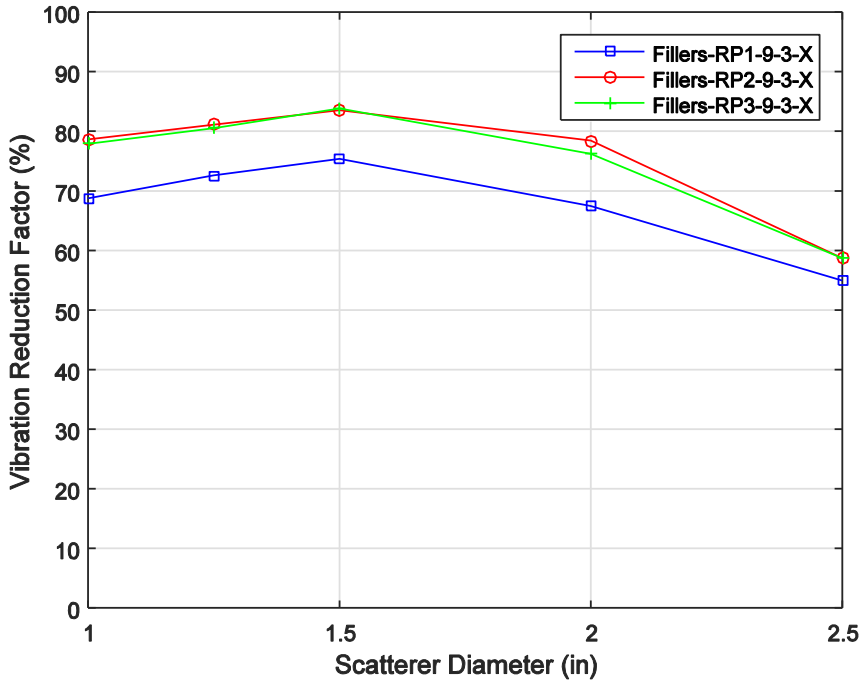

Figure 4.27: Vibration Reduction Factor (%) vs Scatterer Diameters (X - 1", 1.25", 1.5", 2", and 2.5") with Fillers-RP1-9-3-X-2, Fillers-RP2-9-3-X-2, and Fillers-RP3-9-3-X-2

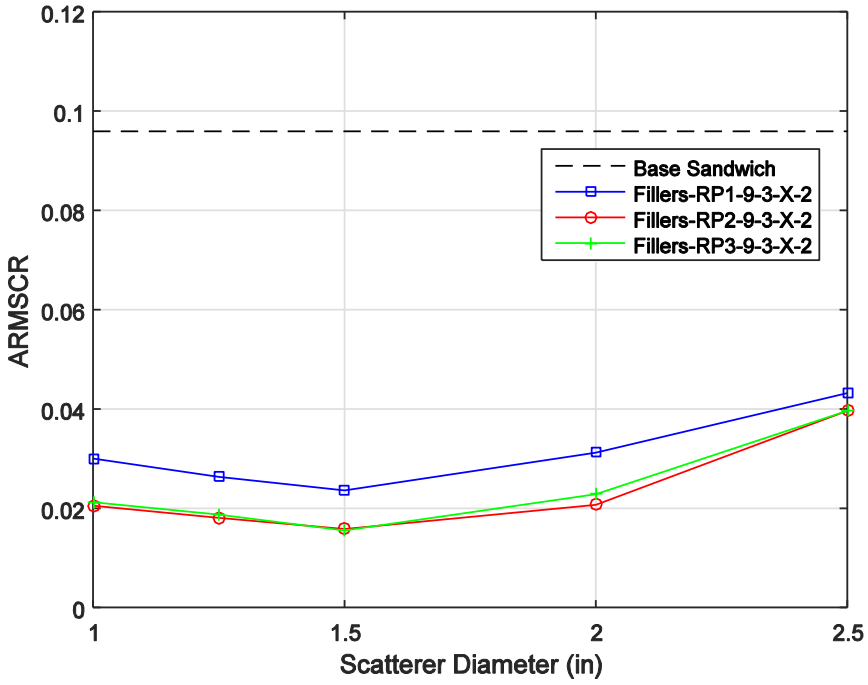

Figure 4.28: ARMSCR vs Scatterer Diameters (X - 1", 1.25", 1.5", 2", and 2.5") with Fillers-RP1-9-3-X-2, Fillers-RP2-9-3-X-2, and Fillers-RP3-9-3-X-2

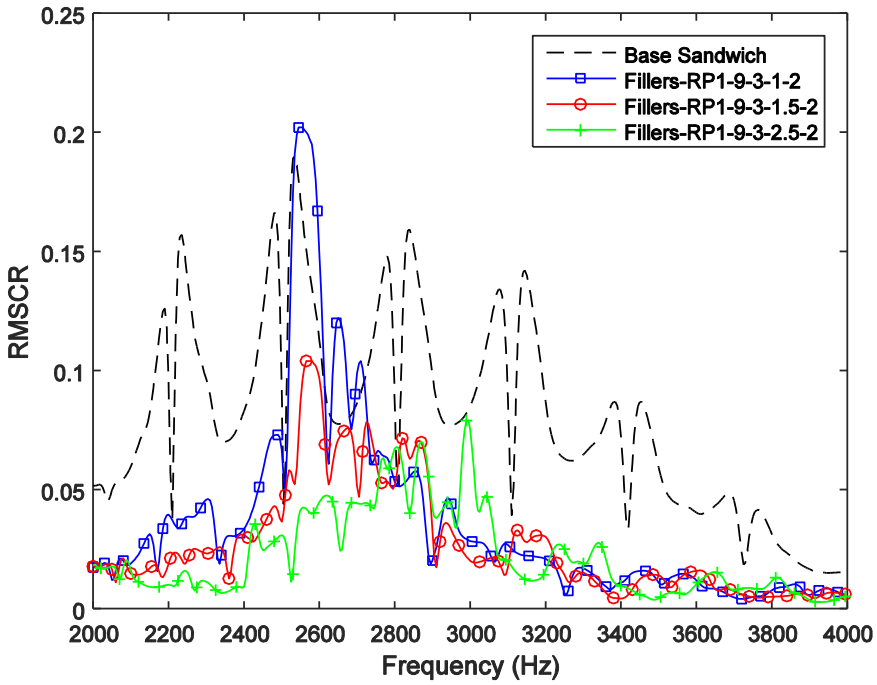

Figure 4.29: RMSCR vs Frequency (2000 Hz-4000 Hz) for base sandwich, Fillers-RP1-9-3-X-2 (X - 1", 1.5", and 2.5")

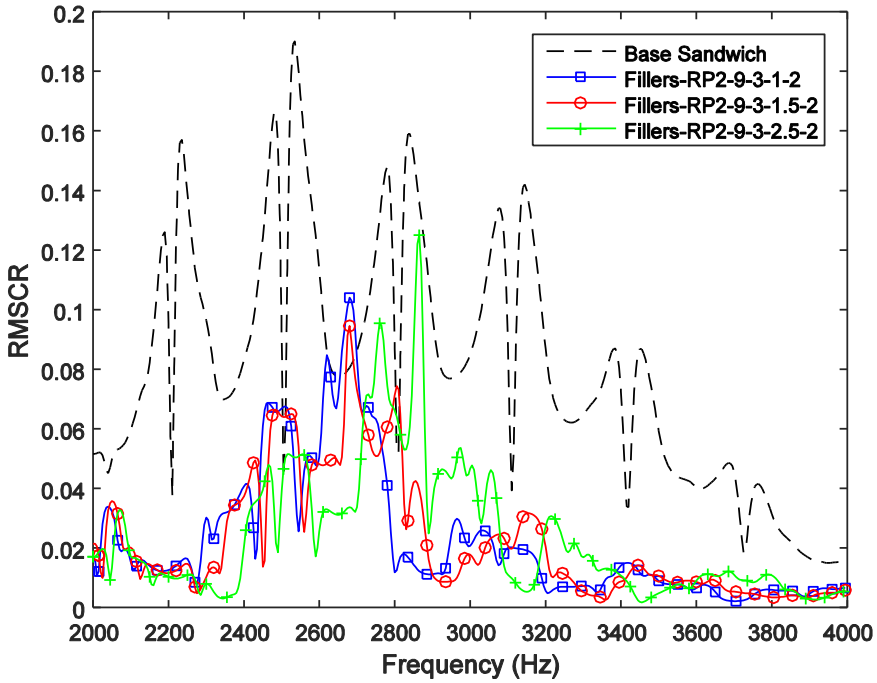

Figure 4.30: RMSCR vs Frequency (2000 Hz-4000 Hz) for base sandwich, Fillers-RP2-9-3-X-2 (X - 1", 1.5", and 2.5")

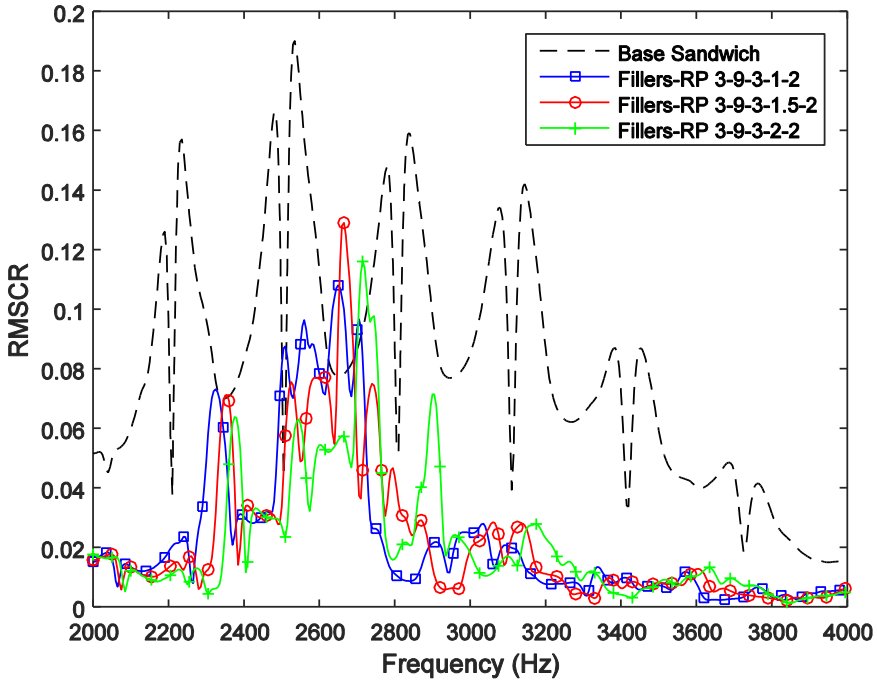

Figure 4.31: RMSCR vs Frequency (2000 Hz-4000 Hz) for base sandwich, Fillers-RP3-9-3-X-2 (X - 1", 1.5", and 2.5")

4.2.6.2 Effect of Number of Columns of Scatterers

Figure 4.27 shows three plots with vibration reduction factor (%)versus the diameters of scatterers with one column, two column and three column arrangements. Figure 4.28 shows three plots with ARMSCR versus the diameters of scatterers with one column, two column and three column arrangements. The dotted line represents the case of base sandwich panel. Figure 4.29, Figure 4.30, and Figure 4.31 show the plots of RMSCR against the frequency range of the harmonic study 2000 Hz to 4000 Hz. From Figure 4.27, it can be observed that there is some vibration reduction as the number of columns increase from one to two but the increase of number of columns from two and three does not show a significant change.

4.2.6.3 Effect of Material Properties

The next set of simulations looked into material variations of the filler rods while keeping the other parameters constant. The Young's modulus and the density properties of the filler rod materials are explored. For these studies, the sandwich panel with two column filler arrangement with scatterer diameter of 1.25" and lattice constant of 3" is considered. The retaining plates are assumed to be a very light and made of very stiff material with the material properties as shown in Table 4.2.

To explore the impact of Young's modulus, the rest of the material properties of the filler material were kept constant which are density (ρ) = 2020.7 kg/m^3 and Poisson's ratio (ν) = 0.211. The following Young's modulus values are considered: 5.708×10^7 Pa, 5.708×10^8 Pa, 5.708×10^9 Pa, 5.708×10^{10} Pa, 5.708×10^{11} Pa, 5.708×10^{12} Pa, and 5.708×10^{13} Pa. Each of these simulations is represented by the case numbers 1, 2, 3, 4, 5, 6, and 7 in the plots.

Figure 4.32 shows the plots of RMSCR against the frequency range of 2000 Hz to 4000 Hz for different filler materials of Young's modulus as mentioned above. Figure 4.33 shows

ARMSCR against the different Young's modulus values for the filler material. The dotted line represents the case of base sandwich panel. Figure 4.34 shows vibration reduction factor (%) against different Young's modulus values for the filler material. It can be observed that all the plots of the RMSCR over the frequency range follow each other closely with the exception of Young's modulus 5.708×10^{7} Pa, as shown in Figure 4.32. When the filler material is very soft with Young's modulus of 5.708×10^{7} Pa, the natural frequency peaks are moved to the left when compared with the other cases. Over the frequency range of interest, there is no significant change in the vibration reduction as shown in Figure 4.34.

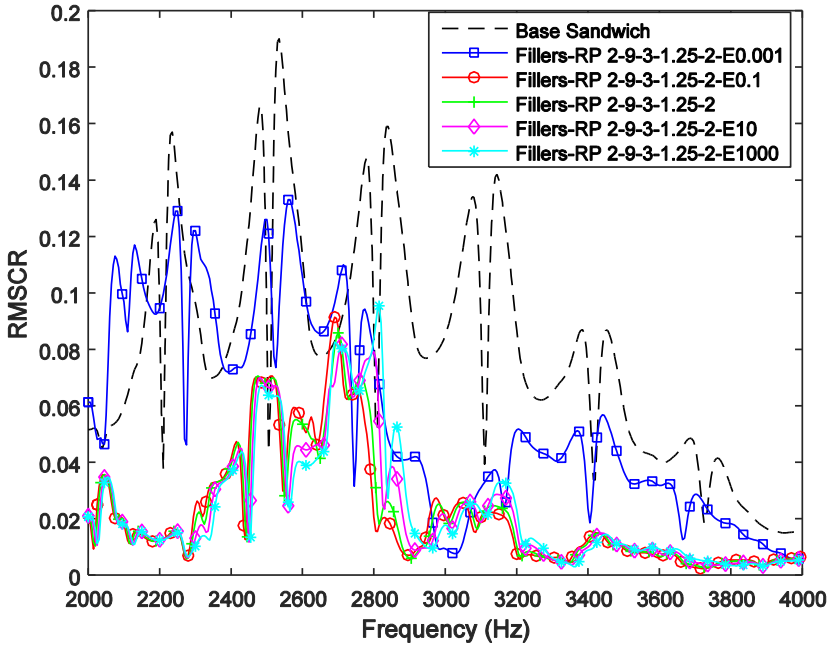

Figure 4.32: RMSCR vs Frequency (2000 Hz-4000 Hz) for base sandwich, Fillers-RP 2-9-3-1.25-2 (Filler Young's modulus - 5.708×10^{7} Pa, 5.708×10^{9} Pa, 5.708×10^{10} Pa, 5.708×10^{11} Pa, and 5.708×10^{13} Pa)

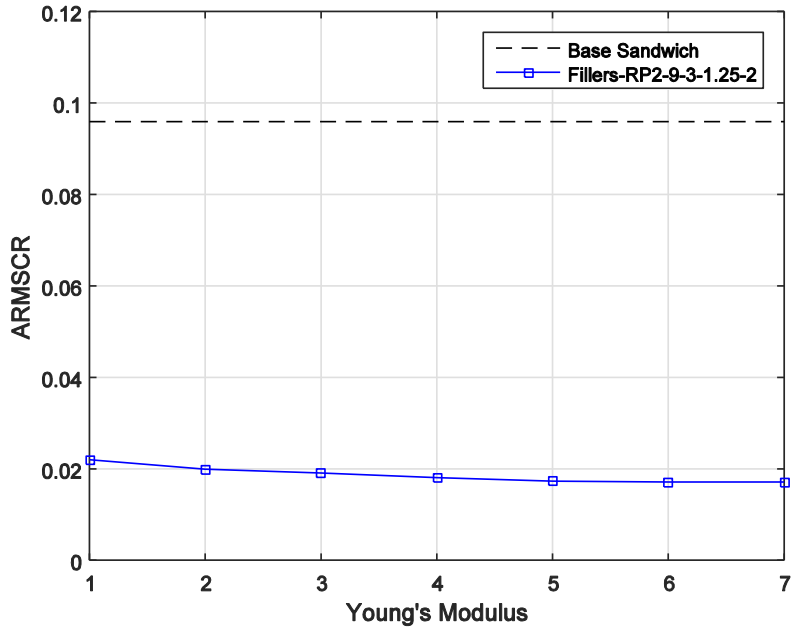

Figure 4.33: ARMSCR vs Filler Young's Modulus (5.708×10^{7} Pa, 5.708×10^{8} Pa, 5.708×10^{9} Pa, 5.708×10^{10} Pa, 5.708×10^{11} Pa, 5.708×10^{12} Pa, and 5.708×10^{13} Pa) with Fillers-RP 2-9-3-1.25-2-X

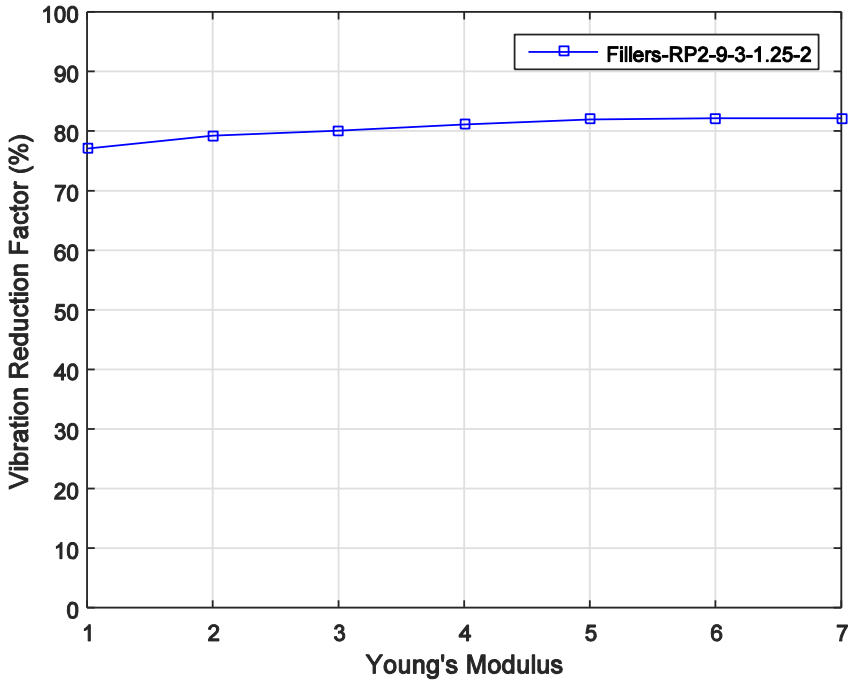

Figure 4.34: Vibration Reduction Factor (%) vs Filler Young's Modulus (5.708×10^{7} Pa, 5.708×10^{8} Pa, 5.708×10^{9} Pa, 5.708×10^{10} Pa, 5.708×10^{11} Pa, 5.708×10^{12} Pa, and 5.708×10^{13} Pa) with Fillers-RP 2-9-3-1.25-2-X

To explore the impact of density of the filler rods, the rest of the material properties of the filler rods were kept constant which are Young's modulus (E) = 5.708×10^{10} Pa and Poisson's ratio (ν) = 0.211. The following density values are considered: 2.02 kg/m^3, 20.2 kg/m^3, 202.07 kg/m^3 Pa, 2020.7 kg/m^3, 2.02×10^4 kg/m^3, 2.02×10^5 kg/m^3, and 2.02×10^6 kg/m^3. Each of these simulations is represented by the case numbers 1, 2, 3, 4, 5, 6, and 7 in the plots.

Figure 4.35 shows the plots of RMSCR against the frequency range for different filler material densities as described above. Figure 4.36 shows ARMSCR against the different filler density values. The dotted line represents the case of base sandwich panel. Figure 4.37 shows vibration reduction factor (%) against the different filler densities. It can be observed that the cases with filler rods of higher densities (2020.7 kg/m^3, 2.02×10^4 kg/m^3, 2.02×10^5 kg/m^3, and 2.02×10^6 kg/m^3) push the natural frequencies to the left as shown in Figure 4.35. A better vibration reduction is achieved over the frequency of interest and the trend plateaus with density above 2020.7 kg/m^3 which can be seen in Figure 4.37.

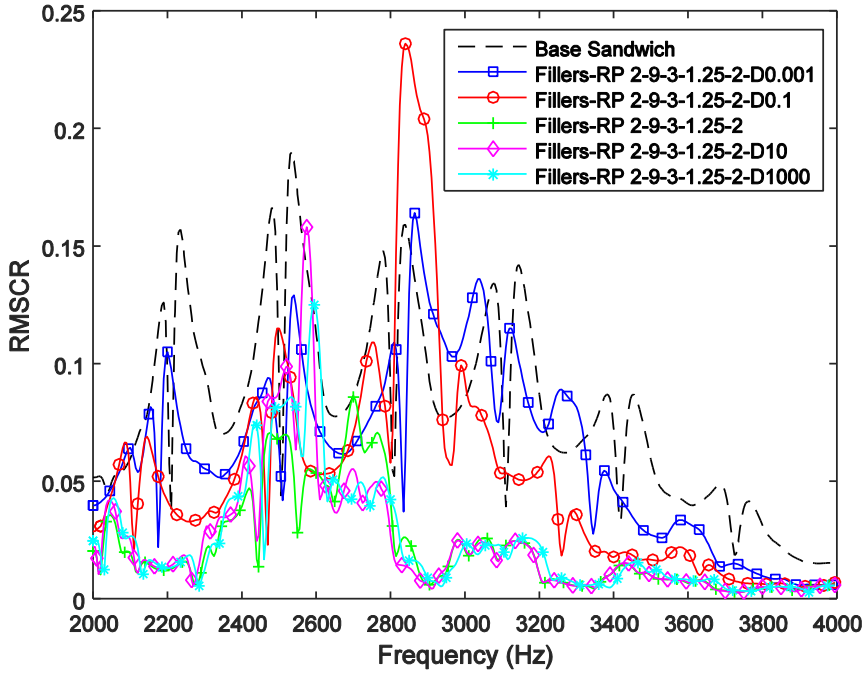

Figure 4.35: RMSCR vs Frequency (2000 Hz-4000 Hz) for base sandwich, Fillers-RP 2-9-3-1.25-2 (Filler density - 2.02 kg/m^3, 202.07 kg/m^3 Pa, 2020.7 kg/m^3, 2.02×10^4 kg/m^3, and 2.02×10^6 kg/m^3)

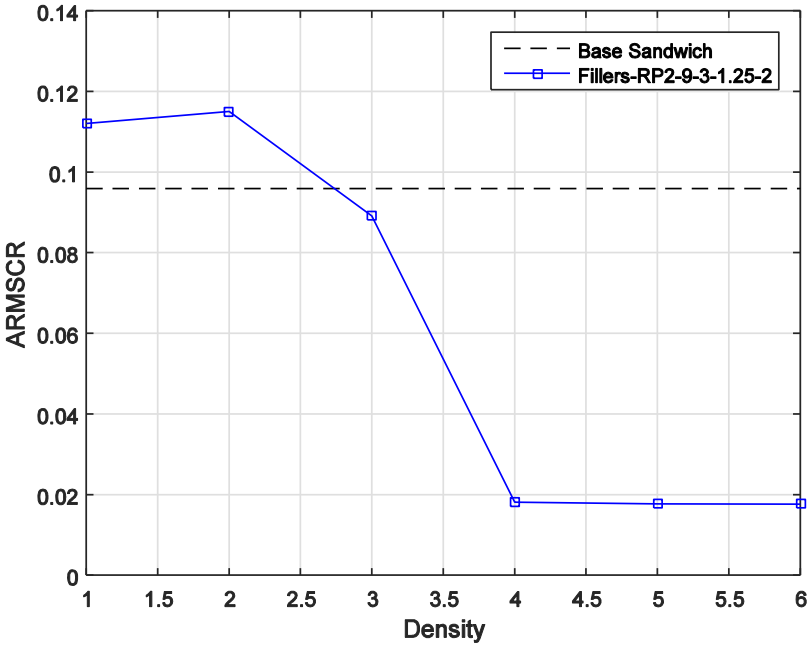

Figure 4.36: ARMSCR vs Filler Density (2.02 kg/m^3, 20.2 kg/m^3, 202.07 kg/m^3, 2020.7 kg/m^3, 2.02×10^4 kg/m^3, and 2.02×10^5 kg/m^3) with Fillers-RP 2-9-3-1.25-2

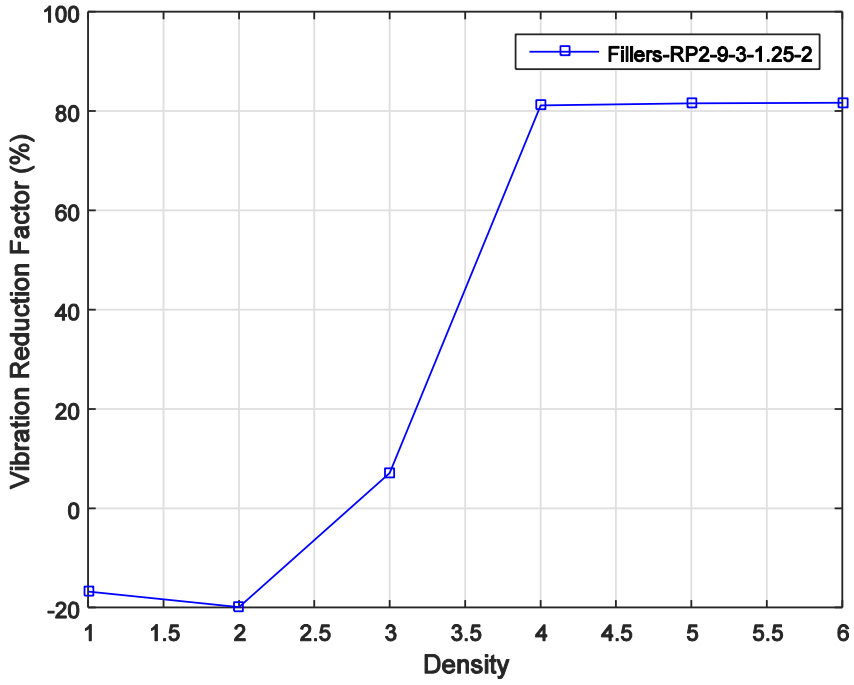

Figure 4.37: Vibration Reduction Factor (%) vs Filler Density (2.02 kg/m^3, 20.2 kg/m^3, 202.07 kg/m^3 Pa, 2020.7 kg/m^3, 2.02×10^4 kg/m^3, and 2.02×10^5 kg/m^3) with Fillers-RP 2-9-3-1.25-2

4.2.6.4 Effect of Lattice Constant

The effect of lattice constant was explored while keeping the other parameters constant. A two column filler arrangement has been chosen with the scatterer diameter as 1.25" and scatterer length as 2". The filler material is chosen the same as the face-plate material as listed in Table 4.1. The retaining plates are assumed to be a very light and made of very stiff material with the material properties as shown in Table 4.2. The lattice constants 1.5", 2", 2.5", 3", and 3.5" are chosen for simulations.

Figure 4.38 shows vibration reduction factor (%) against the different lattice constants. Figure 4.39 shows ARMSCR against the different lattice constants. The dotted line represents the case of base sandwich panel. Figure 4.40 shows the plots of RMSCR against the frequency range of 2000 Hz to 4000 Hz for different lattice constants. It can be observed that the vibration reduces as the lattice constant values decreases, as shown in Figure 4.38.

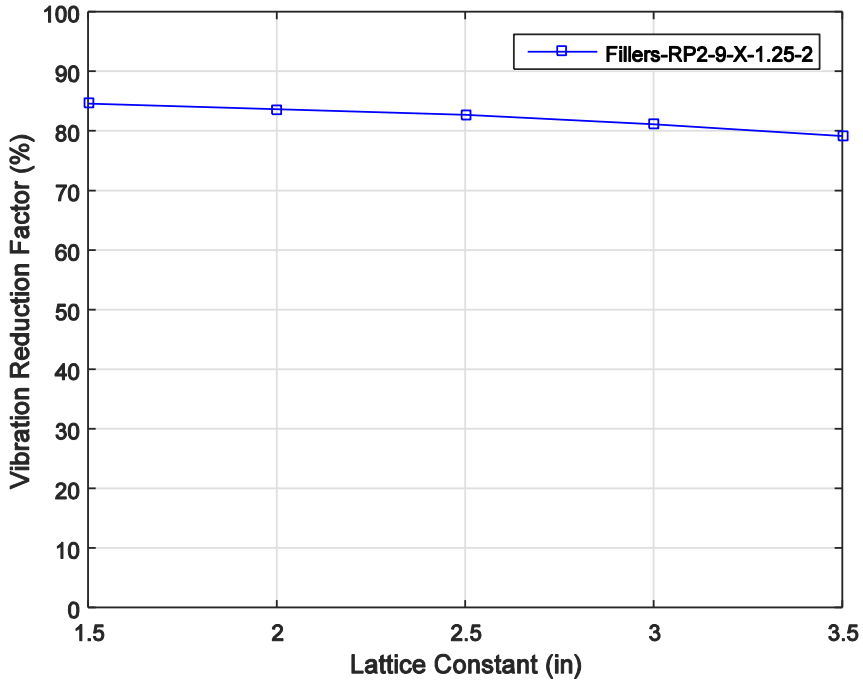

Figure 4.38: Vibration Reduction Factor (%) vs Lattice Constant (X - 1.5", 2", 2.5", 3", and 3.5") with Fillers-RP 2-9-X-1.25-2

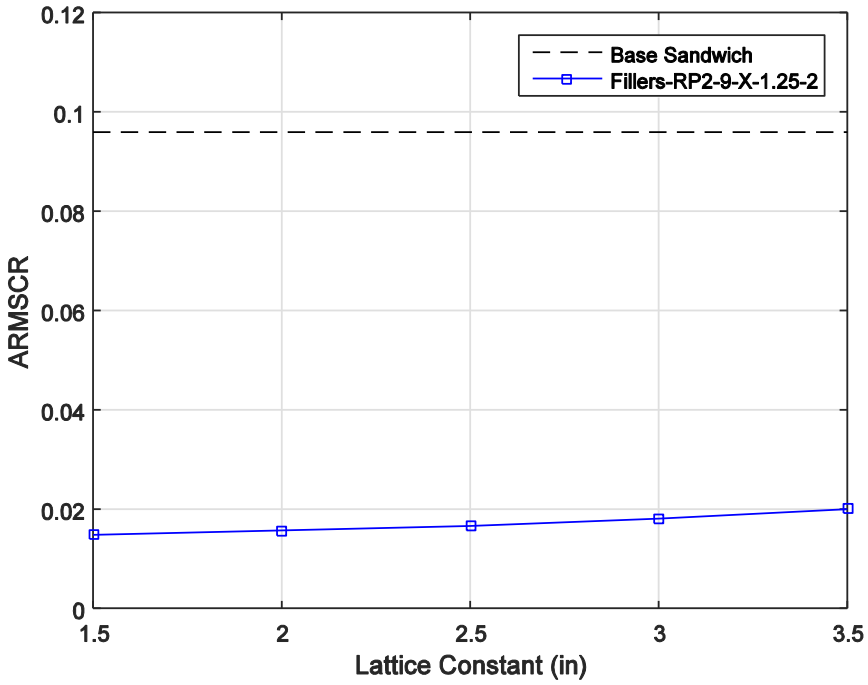

Figure 4.39: ARMSCR vs Lattice Constant (X - 1.5", 2", 2.5", 3", and 3.5") with Fillers-RP2-9-X-1.25-2

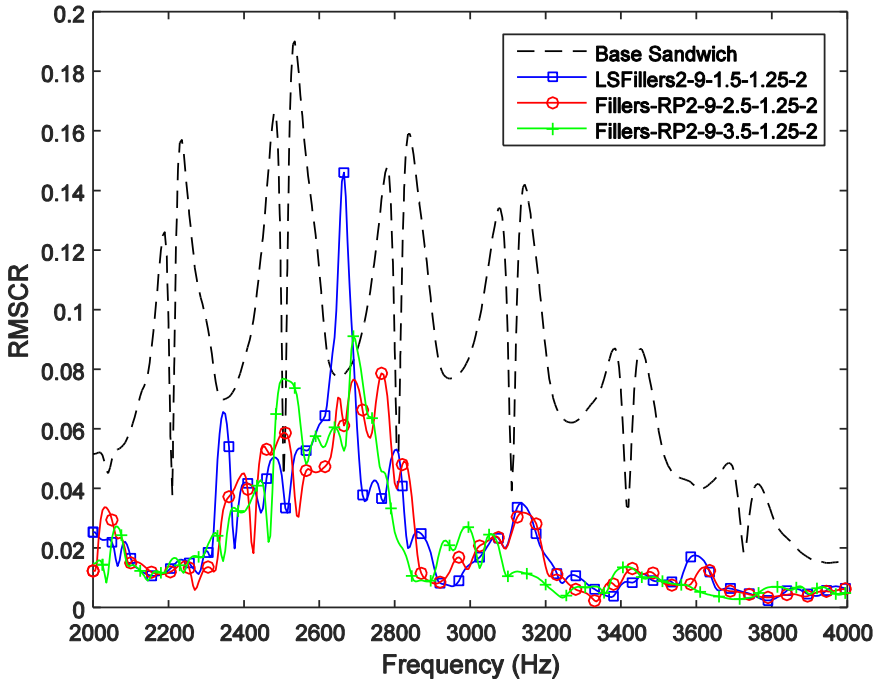

Figure 4.40: RMSCR vs Frequency (2000 Hz-4000 Hz) for base sandwich, Fillers-RP 2-9-X-1.25-2 (X - 1.5", 2.5", and 3.5")

4.2.6.5 Effect of Scatterer Length

The effect of scatterer was explored while keeping the other parameters constant. A two column filler arrangement has been chosen with the scatterer diameter as 1.25" and lattice constant as 3". The filler material is chosen the same as the face-plate material as listed in Table 4.1. The retaining plates are assumed to be a very light and made of very stiff material with the material properties as shown in Table 4.2. The scatterer lengths 1", 1.5", 2", 2.5", and 3" are chosen for simulations.

Figure 4.41 shows the plot of vibration reduction factor (%) against the different scatterer lengths. Figure 4.42 shows the plot of ARMSCR against the different scatterer lengths. The dotted line represents the case of base sandwich panel. Figure 4.43 shows the plots of RMSCR against the frequency range 2000 Hz to 4000 Hz for the different length of scatterers. From Figure 4.41, it can be observed that there is a slight reduction in vibration as the length of the

scatterers is increased from 1" to 1.5" to 2". After that, the trend plateaus. This is also confirmed by observing the plots of RMSCR over the frequency range of study as shown in Figure 4.43.

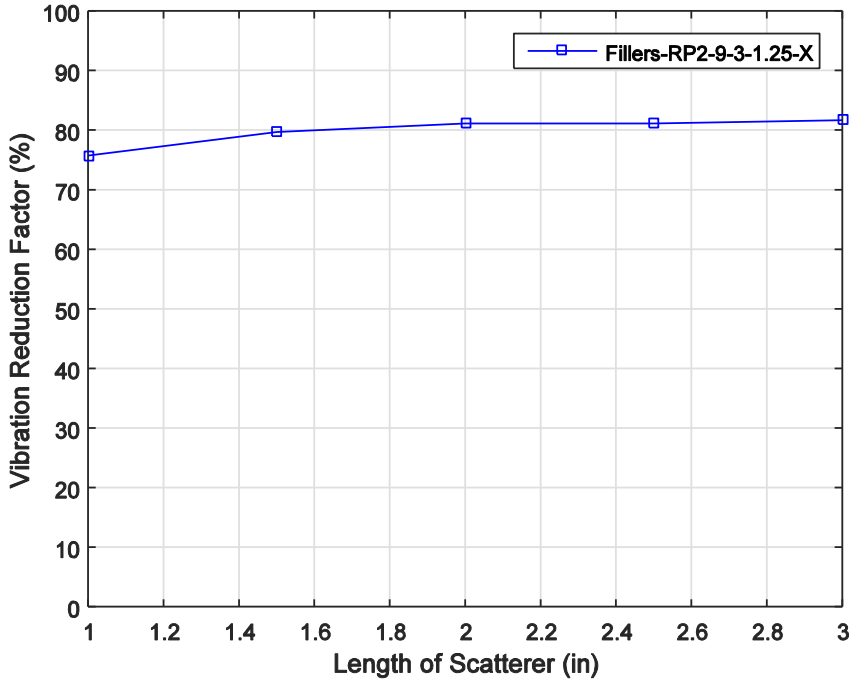

Figure 4.41: Vibration Reduction Factor (%) vs Length of Scatterer (X - 1", 1.5", 2", 2.5", and 3") with Fillers-RP 2-9-3-1.25-X

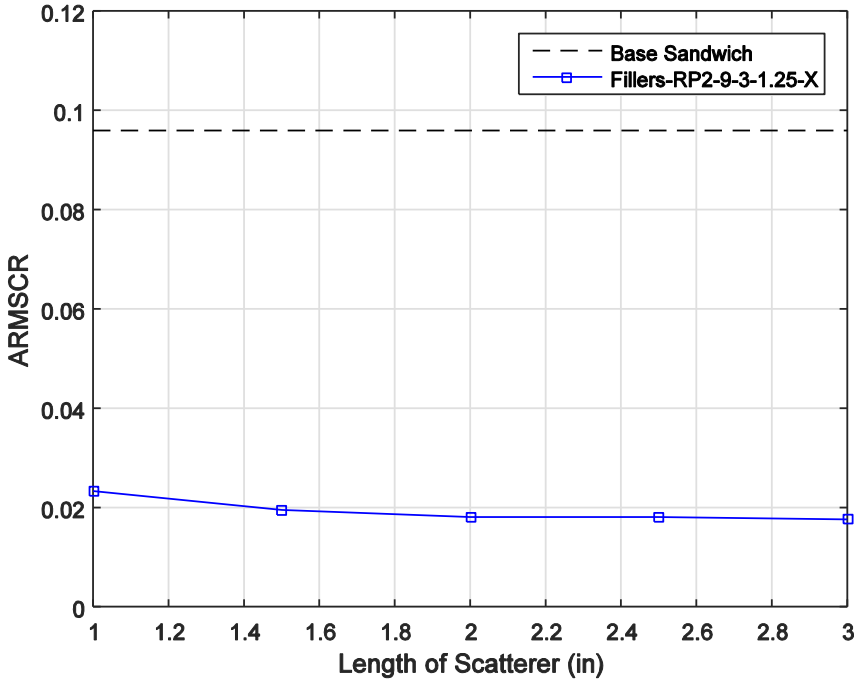

Figure 4.42: ARMSCR vs Length of Scatterer (X - 1", 1.5", 2", 2.5", and 3") with Fillers-RP 2-9-3-1.25-X

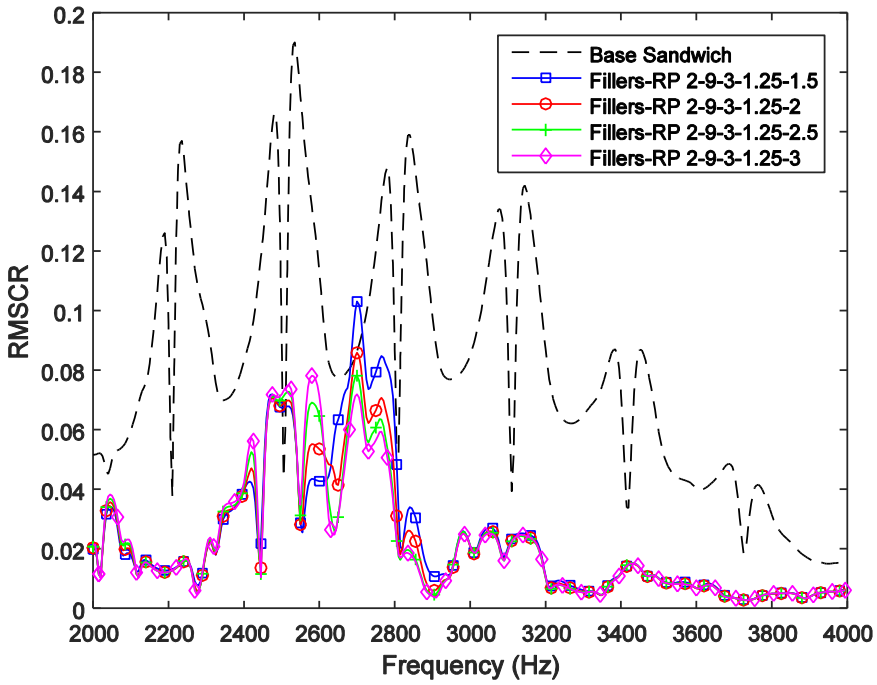

Figure 4.43: RMSCR vs Frequency (2000 Hz-4000 Hz) for base sandwich, Fillers-RP 2-9-1.25-X (X - 1.5", 2", 2.5", and 3")

4.3 Summary of Effects of Controlling Parameters

From all the simulation studies that are discussed in this chapter so far, here are some observations of the influence of the parameters on the vibration reduction.

4.3.1 Scatterer Diameter

The increase of the scatterer size contributed to the reduction of vibration over the range of frequency of interest (2900 Hz - 3000 Hz) for hole scatterers as shown in Figure 4.9. But when the increase of the diameter affects the natural frequency of the structure, the vibration reduces to a specific diameter and then starts increasing. This occurs as the peaks of natural frequencies of the structure move into the vicinity of the frequency range of interest of 3000 Hz. This trend has been observed in both designs of sandwich panels with fillers and sandwich

panels with extended scatterers bonded to the retaining plates as see in Figure 4.13 and Figure 4.27. Therefore it can be concluded that the optimum diameter for best vibration reduction is specific to a design variation under consideration.

4.3.2 Number of Columns of Scatterers

One, two, and three column configurations have been investigated. In general, the increase in the number of columns reduces the vibration, as shown in Figure 4.9 and Figure 4.13 for sandwich panel with hole scatterers and filler scatterers, respectively. But in the design where the extended scatterers are bonded with the retaining plates, there is no significant difference between two and three column arrangement, as seen in Figure 4.27.

4.3.3 Lattice Constant

For sandwich panel with holes and fillers scatterers, the increase of the lattice constant contributes to vibration reduction over the range of frequency of interest of 3000 Hz, up to lattice constant 3" and 3.5" respectively. After that the trend reverses, as the peaks of natural frequencies of the structure move into the vicinity of the frequency range of interest as seen in Figure 4.10 and Figure 4.24. For the design with extended scatterers bonded to retaining plates, a decrease of the lattice constant leads to vibration reduction, as shown in Figure 4.38.

4.3.4 Young's Modulus of the Scatterers

For sandwich panels with fillers, vibration is reduced as the material of the fillers got softer (as the Young's modulus becomes smaller) at the frequency range of interest of 3000 Hz as seen in Figure 4.20. The Young's modulus, however, has little impact on the on the vibration reduction for sandwich panels with extended scatterers bonded to the retaining plates, as seen in Figure 4.34.

4.3.5 Density of the Scatterers

For sandwich panels with fillers or with extended filler attached to retaining plates, vibration is reduced as the material of the fillers become denser at the frequency range of interest of 3000 Hz, and the trend plateaus if the density is further increased. For the sandwich panels with fillers, the trend plateaus at a density 2.02×10^4 kg/m^3 and for the sandwich panel with extended fillers, the trend plateaus at 2020 kg/m^3, as seen in Figure 4.23 and Figure 4.37.

4.3.6 Length of the Scatterers

It was observed that there was vibration reduction as the length of the scatterer increased up to 2" and then the trend plateaued as shown in Figure 4.41.

4.4 Concluding Remarks

Based on all the simulations studies that were conducted and the effects of the controlling parameters observed, here are the choice of the parameters for the final design of the sandwich panel with the realistic loading configuration:

a. No significant difference in vibration reduction was seen between the panel with two and three column arrangements of extended scatterers bonded to retaining plates. But there was vibration reduction noticed in a two column arrangement compared to a one column arrangement. Therefore, panel with a two column arrangement will be chosen. The other benefit of choosing the two columns instead of a three column will be to minimize the external structure weight (the filler rods and the retaining plate).
b. The scatterer material same as the material of face-plate will be used.
c. The length of the scatterer of 2.0" is chosen as it was observed that increasing the length beyond this length did not show any significant reduction in vibration.

d. A scatterer diameter of 1.5" will be chosen and a few variations of the diameter on both sides will be looked into to see the natural frequency pattern of the structure.

e. A few cases of lattice constants (starting with a 3") will be considered.

The next chapter will describe the final design of the sandwich panel and the results of the simulations to find the optimum design.

5 Sandwich with Optimized Sonic Crystal Design

Based on parametric studies conducted and observations made about the influence of the controlling parameters, the recommendations for value of these parameters were proposed in the preceding chapter. Using these recommendations as a guidance, the final design of the sandwich panel with applied loads that mimics the real world application is proposed and iterated to finalize the diameter of the scatterers and lattice constant for optimal performance.

5.1 FEM Model

The final design variation that is considered is the sandwich panel with extended scatterers (scatterers protruding out of the sandwich panel) in a square array arrangement with two outer rows and columns. These scatterers are bonded to the retaining plates on both sides. The retaining plates are square slabs with dimensions 36" x 36" x 0.5" covering the span of the scatterers.

Figure 5.1 shows the sandwich panel with extended two column scatterers in a square arrangement with two outer rows and columns bonded to the retaining plates. The retaining plate is highlighted with black colored edges and made transparent for visualization purposes. The retaining plates exist on both sides of the scatterers. The respective side views for better visualization are shown in Figure 5.2. As shown in Figure 5.1 and Figure 5.2, L is the distance between the center of the scatterer and the left edge of the sandwich panel, D is the diameter of the scatterer, B is the lattice constant (distance between the scatterers), and LS is the length of the scatterers.

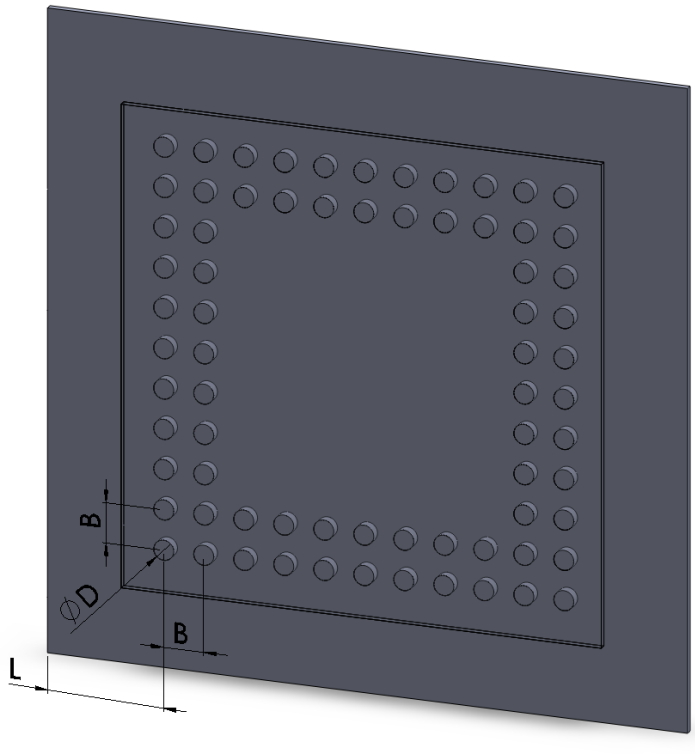

Figure 5.1: Sandwich panel with square array of scatterers with two outer rows and columns with bonded retaining plates

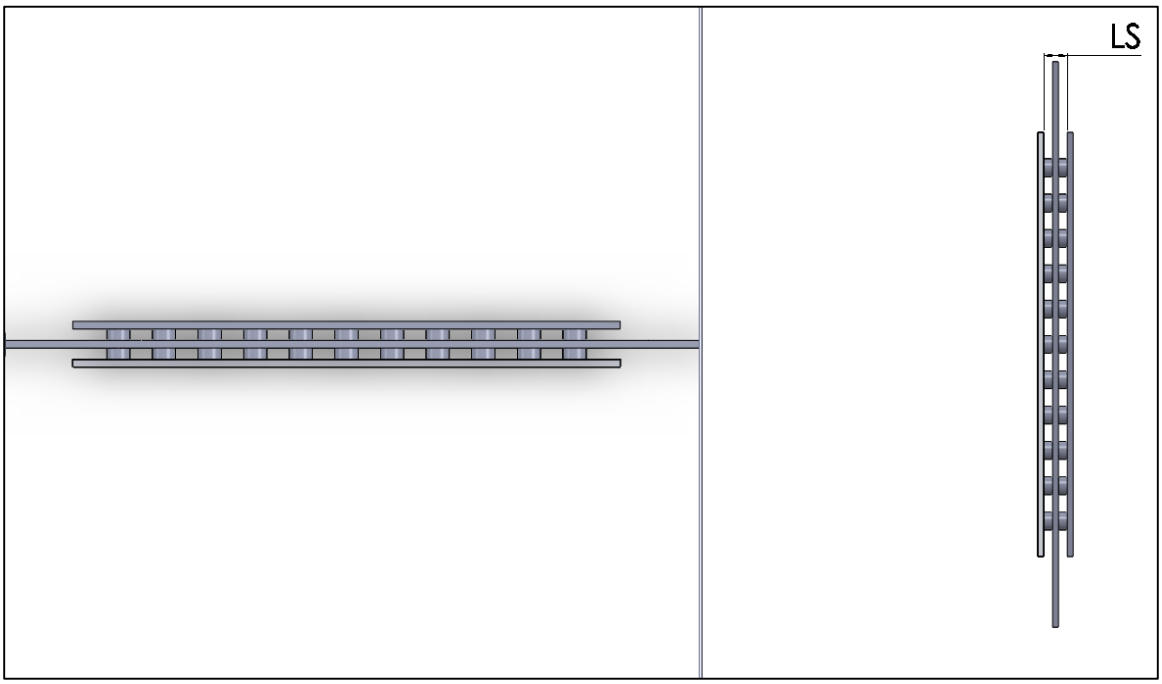

Figure 5.2: Sandwich panel with square array of scatterers with two outer rows and columns with bonded retaining plates (side views)

5.2 Material Properties

The material properties of the sandwich panel as listed in the Table 5.1 are used. The retaining plates are assumed to be a very light and made of very stiff material with the material properties as shown in Table 5.2. The material properties of the scatterers is the same as the face plate material as shown in Table 5.1. Both the materials of the sandwich panel and the retaining plates are assumed to be homogenous, isotropic and elastic materials.

Table 5.1: Sandwich panel material properties

Material property	Core	Top and Bottom face-plates
Young's modulus (E)	2.7095×10^{8} Pa	5.708×10^{10} Pa
Density (ρ)	52.862 kg/m^3	2020.7 kg/m^3
Poisson's ratio (ν)	0.4	0.211

Table 5.2: Retaining plate material properties

Material property	Retaining plates
Young's modulus (E)	5.708×10^{13} Pa
Density (ρ)	2.0207 kg/m^3
Poisson's ratio (ν)	0.211

5.3 Connections/Contacts

A bonded contact is applied to the two interfaces between the three layers: top face-plate, core, and the bottom face-plate. The connections between the extended scatterers and the sandwich panel is bonded and the case between the extended scatterers and both the retaining plates is the same.

5.4 Meshing

SHELL181, a four node structural shell element with six degrees of freedom at each node: translations in x, y, and z directions, and rotations about the x, y, z-axes is used. This element type is well suited for layered applications for modelling composite shells or sandwich constructions [57].

Mesh quality for each of the models has been chosen considering various metrics in ANSYS (element quality, aspect ratio, Jacobian ratio, etc.). For example, Figure 5.3 and Figure 5.4 show the mesh for a sandwich panel with extended scatterers with scatterer diameter (D) of 1.5", lattice constant (B) of 3", and the length of scatterers (LS) of 2". For the mesh model shown in Figure 5.3 and Figure 5.4, the total number of nodes is 148,667 and the number of elements is 72,174.

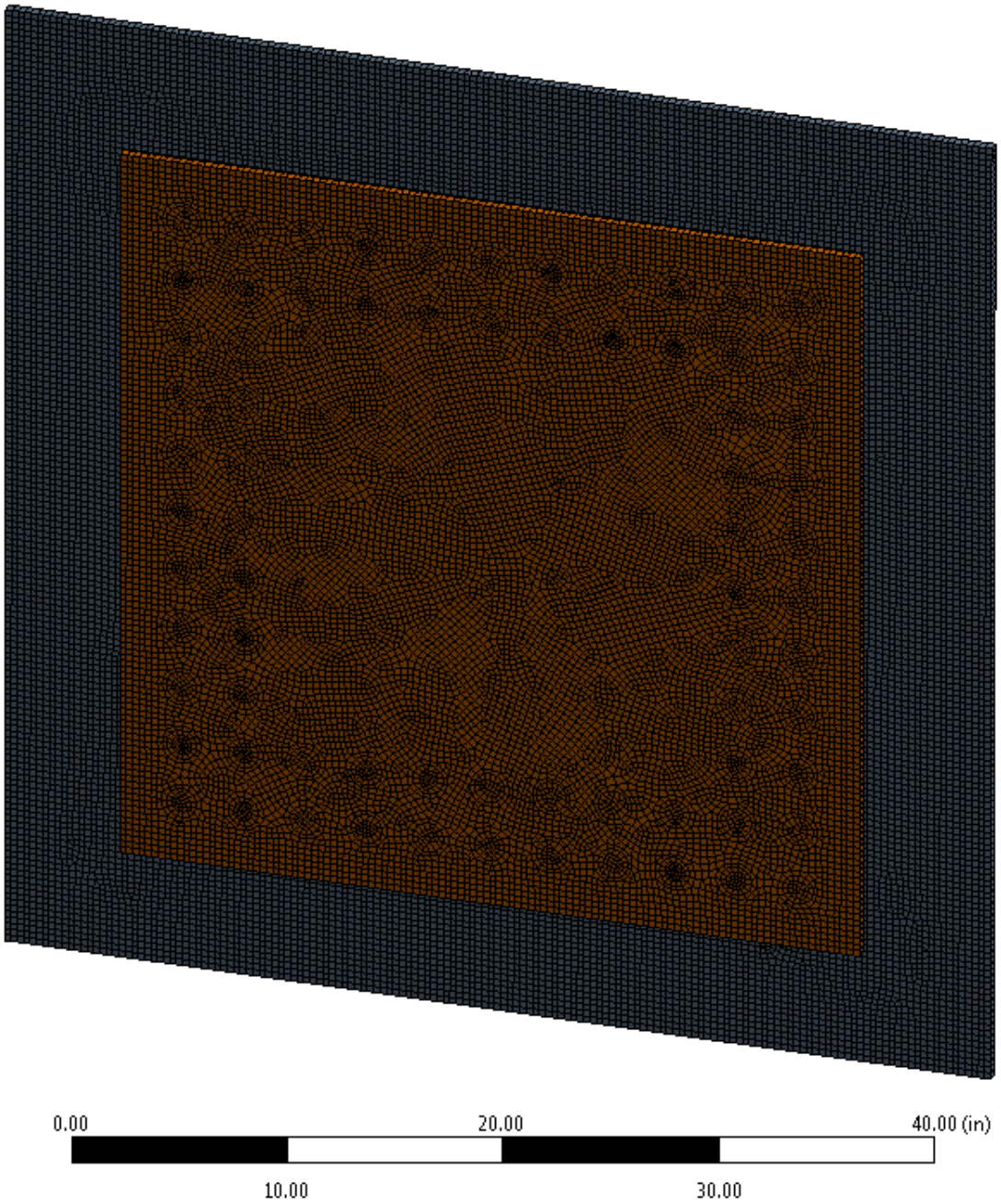

Figure 5.3: Mesh of sandwich panel with square array of scatterers with two outer rows and columns with bonded retaining plates with scatterer diameter (D) of 1.5", lattice constant (B) of 3" and the length of scatterer (LS) of 2"

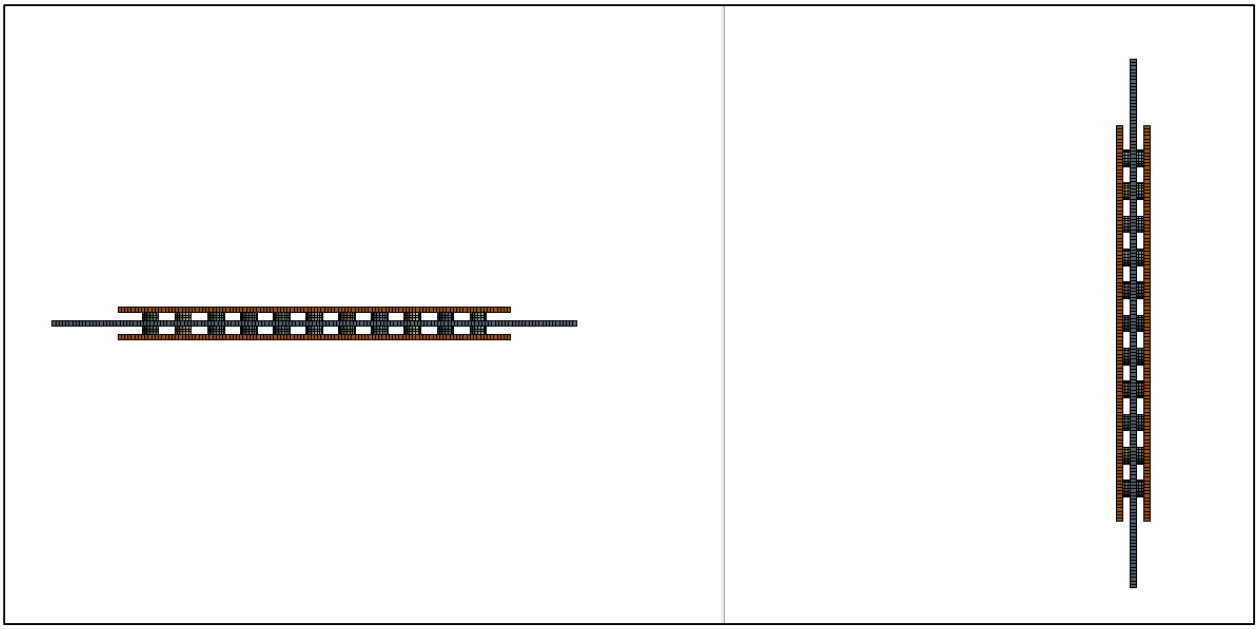

Figure 5.4: Mesh of sandwich panel with square array of scatterers with two outer rows and columns with bonded retaining plates with scatterer diameter (D) of 1.5", lattice constant (B) of 3" and the length of scatterer (LS) of 2" (side views)

5.5 Loading

The roof panels in commercial and military rotor craft fuselages are mechanically interconnected with the rotor mechanism allowing the structure-borne and acoustic-borne vibration and noise transmission into the cabins passing through these panels. In the current work, the rotor mechanism is mounted on this composite panel with the brackets that are along the lines AD and BC of the square of 3'x3' as shown in Figure 5.5 [51]. A load of 100 lbf in negative Z-direction is applied along the lines AD and BC as shown in Figure 5.5.

5.6 Fixtures/Constraints

The sandwich panel is clamped (no translation and no rotation) on all four sides of the sandwich panel ABCD as shown in Figure 5.6.

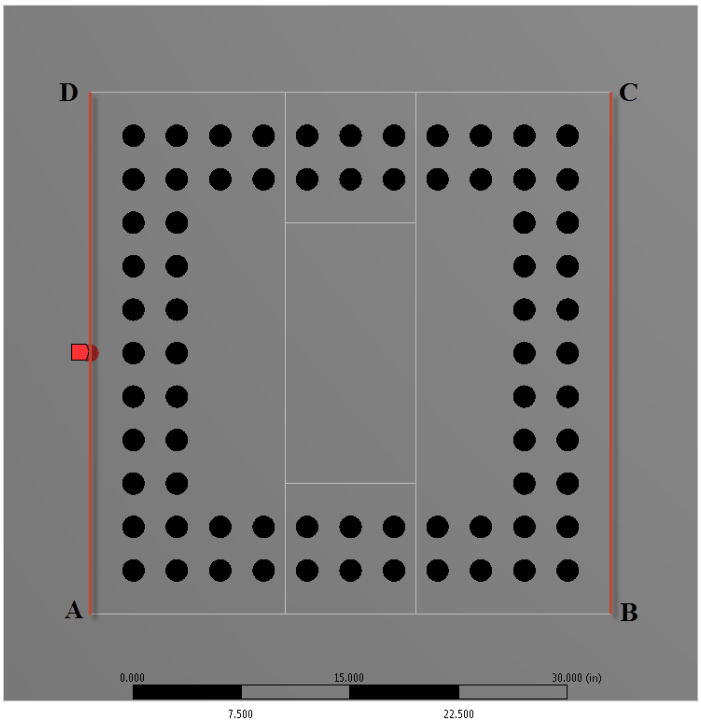

Figure 5.5: Sandwich panel with square array of scatterers with two outer rows and columns with bonded retaining plates highlighting loading lines (AD and BC)

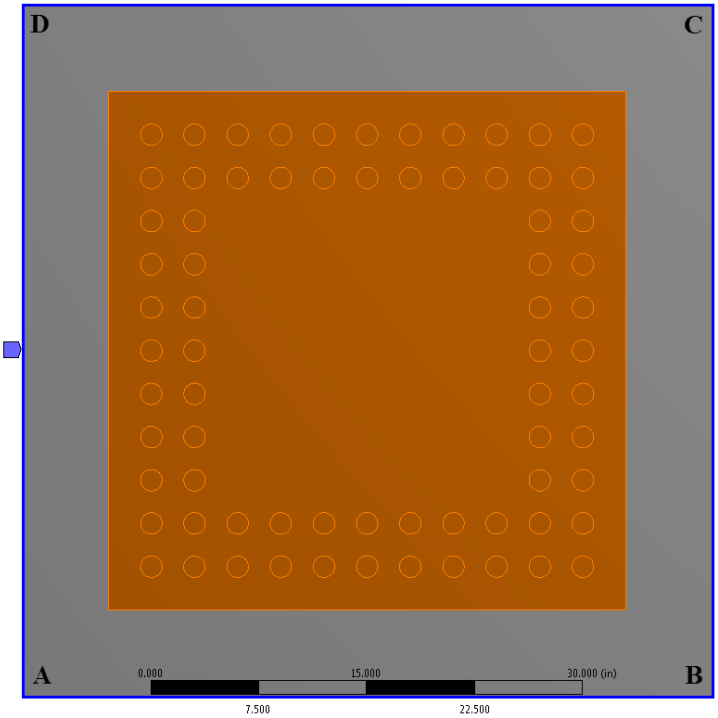

Figure 5.6: Sandwich panel with square array of scatterers with two outer rows and columns with bonded retaining plates fixed on all four sides (ABCD)

5.7 Damping

The damping ratio for the whole structure has been chosen as 0.01 close to the real world representation.

5.8 Analysis Set-up

Harmonic analyses are used to determine the steady-state response of a structure to loads that vary harmonically with time. A typical harmonic analysis will calculate the responses (displacements, stresses, strains, etc.) of the structure over a frequency range. In this work, a harmonic analysis is conducted for the frequency range of 2000 Hz to 4000 Hz. This range has been chosen because Bell Helicopters was interested in minimizing the vibration transmission at 3000 Hz.

5.9 Post Processing

A rectangular column area ABCD as shown in Figure 5.7 is selected to record the root mean square of the displacements of all the nodes in the Z-direction over the frequency range of the study. This rectangular column ABCD which is the area of interest to capture the results will be referred as central region. The results from simulation studies will be presented and discussed in the next section.

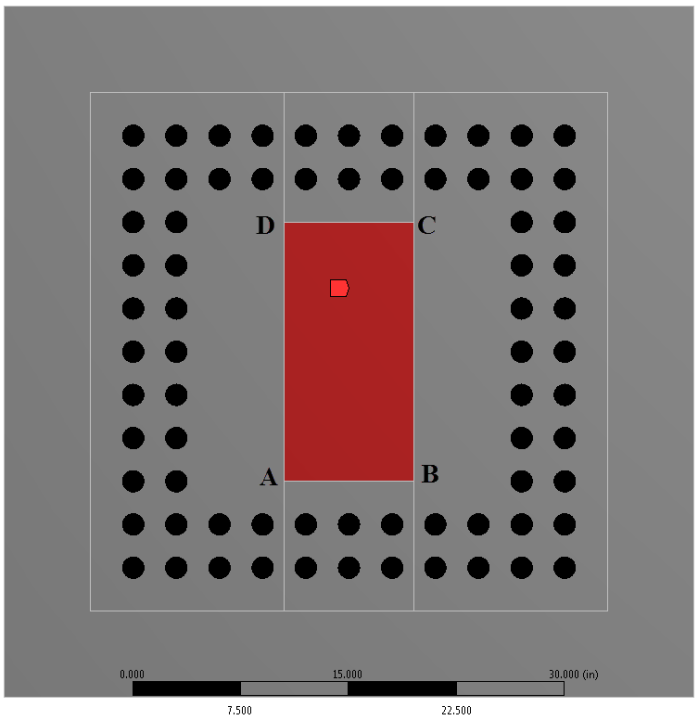

Figure 5.7: Sandwich panel with square array of scatterers with two outer rows and columns with bonded retaining plates highlighting area of interest (ABCD)

5.10 Simulation Studies

5.10.1 Effect of Scatterer Diameter

Simulations were conducted using the design described above with varying diameters (1", 1.5", 2", and 2.5") of the fillers while keeping all the other parameters constant. A scatterer length of the scatterer of 2" is chosen.

Figure 5.8 shows the plot with vibration reduction factor (%) versus diameters of the scatterers for the simulation studies. Figure 5.9 shows the plot with ARMSCR versus diameters of the scatterers for the simulation studies. The dotted line represents the case of base sandwich panel. Figure 5.10 show the plots of RMSCR against the frequency range 2000 Hz to 4000 Hz for the scatterers diameters considered in the studies. As can be seen in Figure 5.8, the vibration over the frequency of interest of 3000 Hz, decreases moderately as the diameter of the scatterer

increases up to a diameter of 2" and then it increases. This increase after a certain diameter is because of the change in the natural frequencies of the structure and the movement of the peaks closer to the frequency of interest, as can be seen in Figure 5.10. There is no significant difference between the simulation results with diameter 1.5" and 2" in terms of vibration reduction as seen in Figure 5.8. But looking at Figure 5.10, one natural frequency peak is much closer to the frequency of interest (3000 Hz) in the case of scatterer diameter 1.5", compared to the case with scatterer diameter of 2". Therefore, the sandwich panel with the scatterer diameter of 2" is chosen and is further explored to determine if further reduction of vibration is possible by changing the lattice constant.

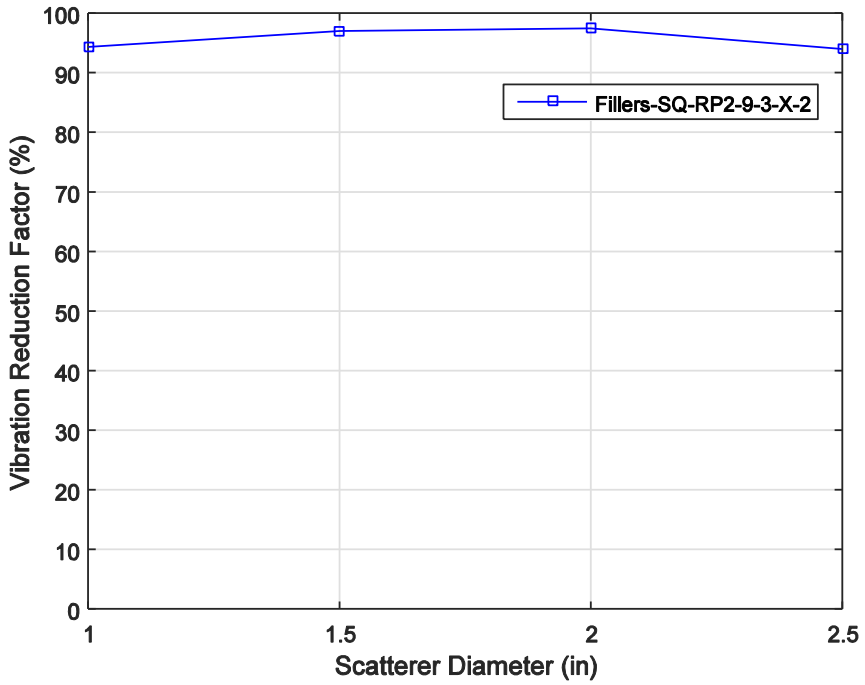

Figure 5.8: Vibration Reduction Factor (%) vs Scatterer Diameters (X - 1", 1.5", 2", and 2.5") with Fillers-SQ-RP2-9-3-X-2

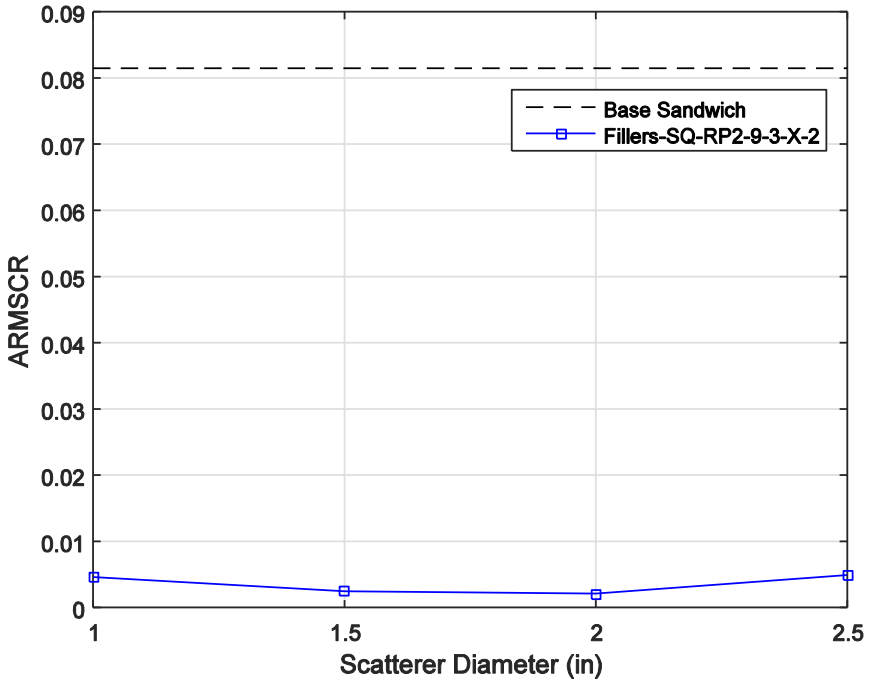

Figure 5.9: ARMSCR vs Scatterer Diameters (X - 1", 1.5", 2", and 2.5") with Fillers-SQ-RP2-9-3-X-2

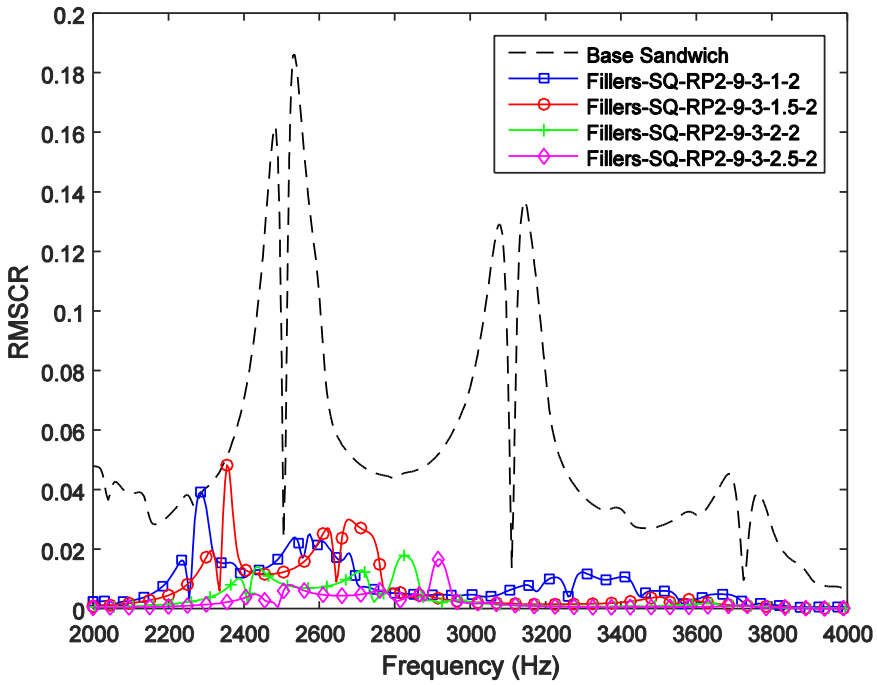

Figure 5.10: RMSCR vs Frequency (2000 Hz-4000 Hz) for base sandwich, Fillers-SQ-RP2-9-3-X-2 (X - 1", 1.5", 2", and 2.5")

5.10.2 Effect of Lattice Constant

The effect of lattice constant was explored while keeping other parameters constant. A sandwich panel with extended scatterers in a square array arrangement with only two outer rows and columns is considered with the scatterer diameter of 2" and the length of the scatterer as 2".

Figure 5.11 shows vibration reduction factor (%) against the different lattice constants (2.25", 2.5", 3", and 3.5"). Figure 5.12 shows ARMSCR against the different lattice constants. Figure 5.13 shows the plots of RMSCR of the central region against the frequency range of 2000 Hz to 4000 Hz for different lattice constants. It can be observed that the vibration reduces as the lattice constant values decreases up to the value of 2.5" and slightly increases for 2.25"as shown in Figure 5.11. So, the sandwich panel with the lattice constant of 2.5" with 2" scatterer diameter achieves the best vibration reduction.

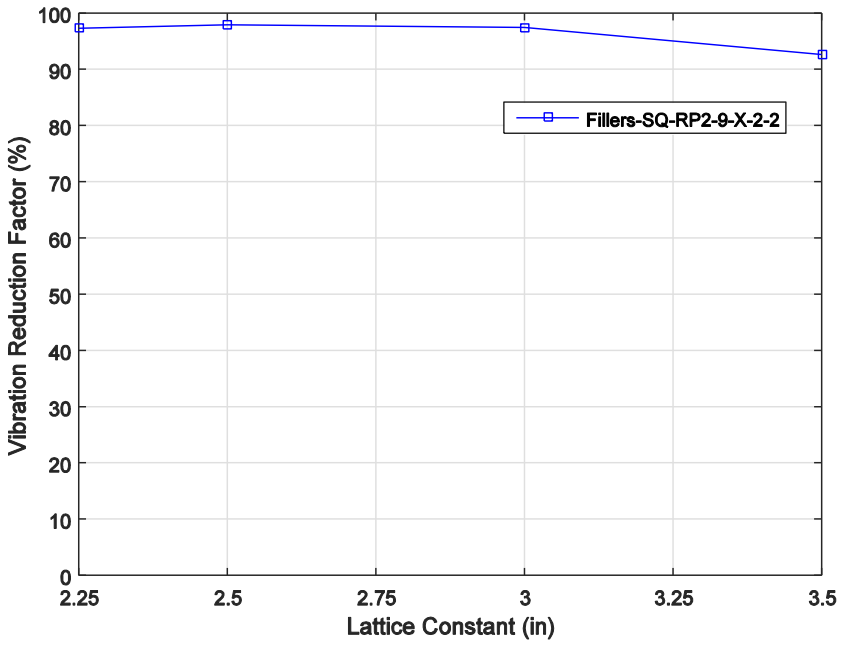

Figure 5.11: Vibration Reduction Factor (%) vs Lattice Constant (X - 2.25", 2.5", 3", and 3.5'') with Fillers-SQ-RP2-9-X-2-2

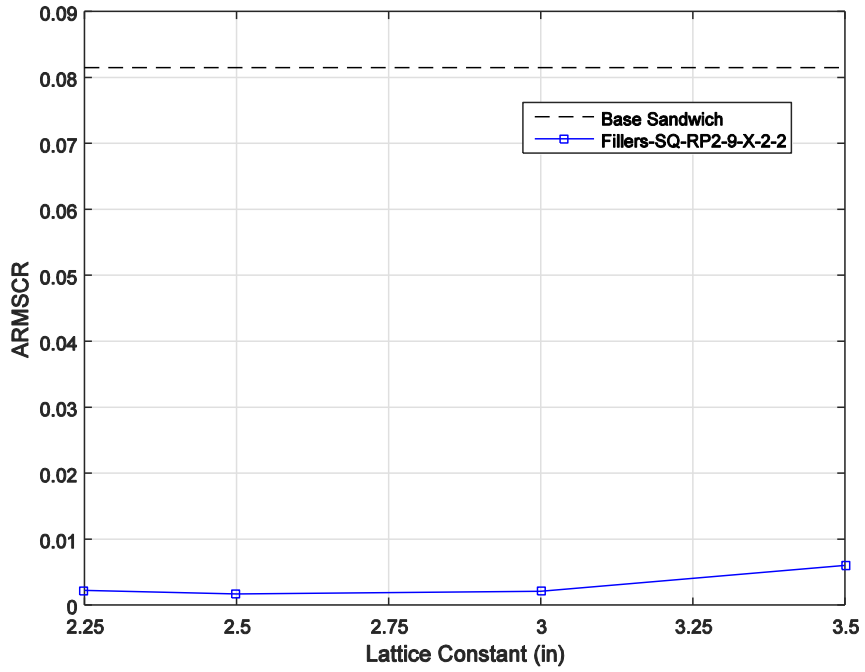

Figure 5.12: ARMSCR vs Lattice Constant (X - 2.25", 2.5", 3", and 3.5'') with Fillers-SQ-RP2-9-X-2-2

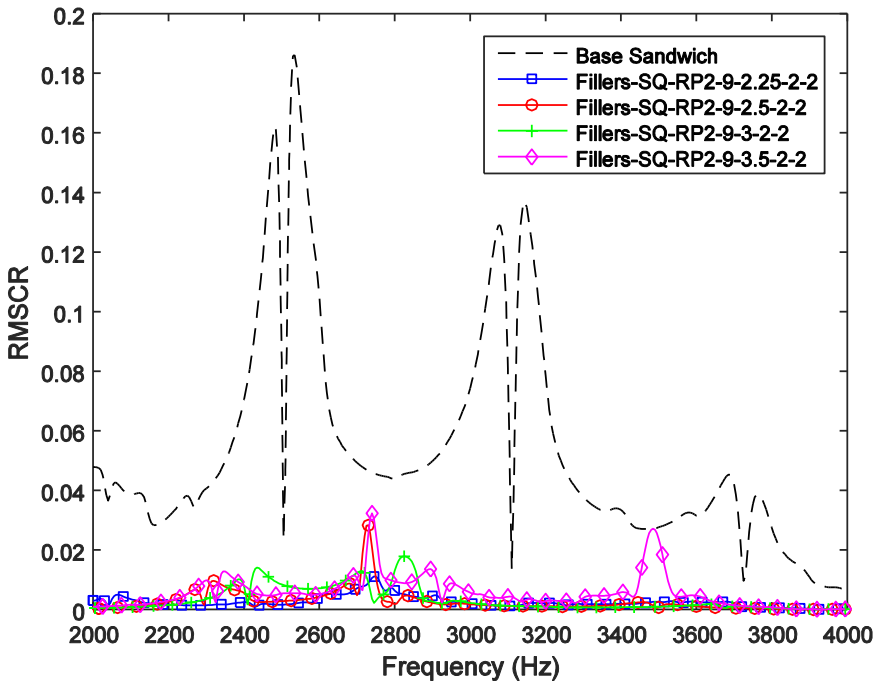

Figure 5.13: RMSCR vs Frequency (2000 Hz-4000 Hz) for base sandwich, Fillers-SQ-RP2-9-X-2-2 (X - 2.25", 2.5", 3", and 3.5")

5.11 Results and Discussion

Based on the results obtained from a systematic parametric study, the optimum sandwich panel design with the choice of parameters that achieve the best vibration reduction has been identified as follows:

a. A sandwich panel with extended scatterers (scatterers with length more than the thickness of the sandwich panel) in a square array arrangement with only two rows and columns. These scatterers are bonded to the retaining plates on both sides. The retaining plates are square slabs with dimensions 36" x 36" x 0.5" covering the span of the scatterers as shown in Figure 5.1 and Figure 5.2.
b. The extended scatterer rods material is chosen as the same as material of the face-plate material, the properties of which can be found in Table 5.1.
c. The material properties of the retaining plates chosen are listed in Table 5.2.
d. 2.0" is the length of the scatterer chosen based on the recommendations made from the simulation results obtained in the previous chapter.
e. An extended scatterer diameter of 2.0" is chosen based on the simulation results as shown in Figure 5.9.
f. A lattice constant value of 2.0" is chosen for the best vibration reduction as supported by the results shown in Figure 5.12.

Using the above sandwich panel design and the parameters of choice, it was found that the best vibration transmission reduction (98%) was achieved around the frequency of interest of 3000 Hz. Figure 5.14 shows the plots of normalized UZ of the central region against the frequency range of 2000 Hz to 4000 Hz for the unmodified base sandwich panel (dashed line) and the optimum sandwich panel design (solid line with open squares).

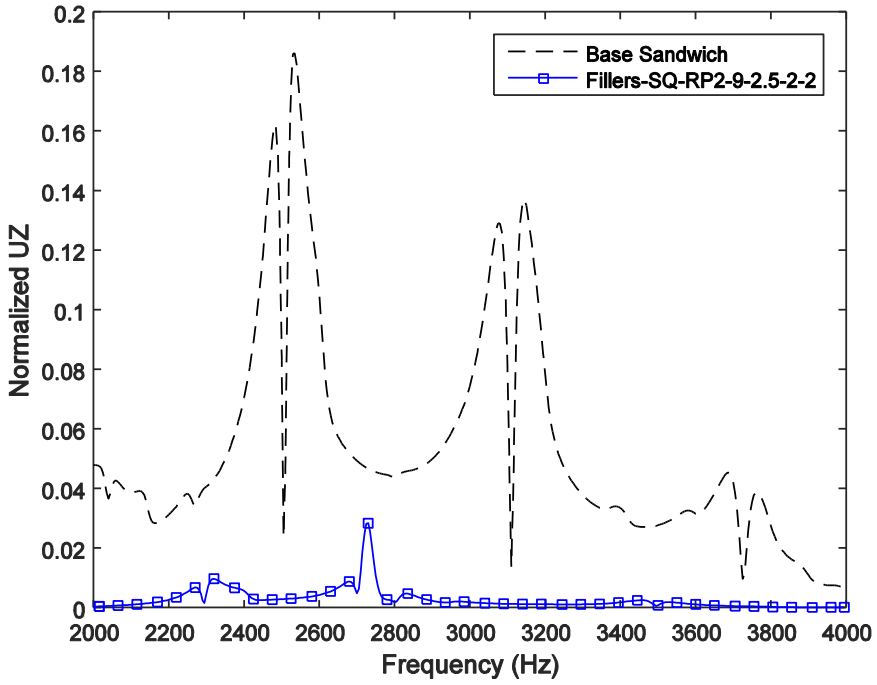

Figure 5.14: Normalized UZ vs frequency (Hz) for the base sandwich panel and the optimum sandwich panel design

6 Summary, Conclusions and Future Work

6.1 Summary and Conclusions

In this work, analytical studies of flexural wave propagation for idealized geometries are conducted and finite element method (FEM) is used to explore the effects of composite panel designs of finite size for the reduction of vibration transmission and flexural wave propagation.

In the analytical study, the governing equation for transverse deflections in a thin plate was derived to characterize flexural wave propagation. For specific cases of an infinite bi-material plate, an infinite plate with a strip inhomogeneity, and an infinite thin plate with a solid circular inclusion, closed form solutions were obtained. For an infinite bi-material plate and infinite plate with a strip inhomogeneity, the effects of material properties of the media on the reflection and transmission characteristics were explored analytically and discussed. For an infinite thin plate with a solid circular inclusion, the far and near field scattering characteristics were explored using the closed form solution. Results were also compared with published solutions, and good agreement was found. From the analytical solution of infinite plate with circular inclusion, it was observed that the rigid inclusion achieved stronger reflection than the hard elastic and the hole inclusions.

All the published analytical studies on the flexural wave propagation, and analytical study carried out here, consider infinite plates. Obtaining closed form solutions of flexural wave propagation in a finite plate with inclusions will be difficult mathematically. Finite element method (FEM) was therefore used to explore the composite panel designs. The understanding gained from the analytical study on flexural wave propagation provided guidance to finite element method investigations.

Finite element method was used to explore the effects on the reduction of vibration transmission and flexural wave propagation in composite sandwich panel with different designs. The concept of phononic crystals was used to define these designs. Phononic crystals have the potential of reducing/prohibiting the transmission of the wave in a certain frequency range. Different design variations were evaluated using FEM simulations.

The design configurations explored were:

1. The unmodified sandwich panel, which was referred as 'Base Sandwich'.
2. Sandwich panel with sonic crystals in a one, two, and three column arrangements of cylindrical scatterers. In this design, the thickness of the scatterer is equal to thickness of the composite sandwich panel.
3. Sandwich panel with sonic crystals in a one, two, and three column arrangements of extended scatterers bonded to the retaining plates. In this design the length of the scatterers is extended beyond the thickness of the sandwich panel on the both sides and the extended scatterers are bonded to the retaining plates on both sides. The retaining plates are added to mimic the rigid inclusions as it was found that the rigid inclusion achieved stronger reflection than the hard elastic and the hole inclusions from the analytical studies.

The design configurations of the sandwich panel with scatterers described above were used to explore the effects/contributions of various design parameters. The design parameters that were explored in the simulation studies are:

1. Diameter of the scatterers
2. Number of columns of the scatterers
3. Young's modulus of the scatterers

4. Density of the scatterers
5. Lattice constant
6. Length of the scatterers

Using the above discussed design configurations and the parameters, a systematic parametric study was conducted to explore the effects of these parameters on the reduction of vibration transmission. Based on the findings from the parametric study, the recommendation for the final design configuration and initial parameters (including Young's modulus and density of the scatterers, the number of columns of scatterers, and the length of the scatterers) were proposed. Following are general conclusions from the parametric study:

1. The scatterers made of hard elastic material compared to the panel material reduced the vibration at frequency of interest.
2. Two column arrangement of scatterers achieved better vibration reduction compared to one column though there was no significant reduction increasing number of columns from two to three.
3. Using retaining plates bonded to the extended scatterers achieved better vibration reduction mimicking the rigid scatterers.
4. Scatterer diameter and lattice constant showed effect on vibration reduction.

Using these recommendations as a guidance, the final design of the sandwich panel is proposed. In the final design, the sandwich panel with extended scatterers (scatterers protruding out of the sandwich panel) in a square array arrangement with two outer rows and columns is proposed. The extended scatterers are bonded to retaining plates on both sides. The scatterer material is considered same as the material of face-plate. A 2.0" length scatterers are considered.

This design is iterated to finalize the diameter of the scatterers and lattice constant for optimal performance.

With the optimum design, it was found that the best vibration transmission reduction reached 98% around the frequency of interest of 3000 Hz. The optimum sandwich panel design and the choice of parameters that achieved the best vibration reduction has been identified as follows: A sandwich panel with extended scatterers (scatterers with length more than the thickness of the sandwich panel) in a square array arrangement with two rows and columns. These scatterers are bonded to the retaining plates on both sides. The retaining plates are square slabs with dimensions 36" x 36" x 0.5" covering the span of the scatterers. The extended scatterer rods material is chosen as the same as the material of face-plate. The length of the scatterers is 2.0", and the lattice constant is 2.0".

This is the first study focused on acoustically tailoring composite rotorcraft fuselage panels using the concept of phononic crystals as a guiding principle.

6.2 Future Work

In this work, the retaining plates were chosen as a very stiff and light material and were kept constant throughout the simulations. The effects of the material properties of retaining plates can be further explored. While exploring the material properties of the retaining plates another design variation where the retaining plates with a square hole could be considered to minimize the weight of the retaining plates.

The scatterer material properties can be further explored in a narrow range to minimize the weight of the sandwich panel. In this work, we have limited the harmonic analysis from 2000 Hz to 4000 Hz. The simulations can be conducted over a wide range of frequencies to explore the bandgap formations.

References

[1] Eduard, V., and Krauthammer, T., 2001, "Thin Plates and Shells: Theory, Analysis, and Applications," Marcel Dekker, New York.

[2] Fahy, F., and Gardonio, P., 2006, "Sound and Structural Vibration Radiation, Transmission and Response," Elsevier/Academi, Amsterdam, Boston, pp. 656.

[3] Norton, M.P., and G, K.D., 2003, "Fundamentals of Noise and Vibration Analysis for Engineers," Cambridge University Press, Cambridge [England]; New York.

[4] Hambric, S. A., 2006, "Structural Acoustics Tutorial-Part 1: Vibrations in Structures," Acoustics Today, **2**(4) pp. 21-33.

[5] Rivin, E.I., 2003, "Passive Vibration Isolation," ASME Press, New York, USA.

[6] Renninger, J., 2000, "Understanding Damping Techniques for Noise and Vibration Control," Aearo Company, Indianapolis, IN.

[7] Benjeddou, A., 2001, "Advances in Hybrid Active-Passive Vibration and Noise Control Via Piezoelectric and Viscoelastic Constrained Layer Treatments," Journal of Vibration and Control, **7**(4) pp. 565-602.

[8] Campbell, R. L., and Hambric, S. A., 2004, "Acoustic Tailoring of Composite Cylindrical Shells - A Survey of Current Capability," American Society of Mechanical Engineers, Noise Control and Acoustics Division (Publication) NCA, **31**pp. 265-271.

[9] Salloway, A. J., and Millar, C. E., 1996, "Active Vibration and Noise Control," GEC Review, **11**(3) pp. 138-145.

[10] Lam, Margaretha J, Inman, Daniel J, Saunders,William R, 1997, "Vibration Control through Passive Constrained Layer Damping and Active Control," Journal of Intelligent Material Systems and Structures, **8**(8) pp. 663-677.

[11] Preumont, A., 2011, "Vibration Control of Active Structures : An Introduction," Springer, London.

[12] Baz, A., 1998, "Robust Control of Active Constrained Layer Damping," Journal of Sound and Vibration, **211**(3) pp. 467-480.

[13] Narayanan, S., 1996, "Active Vibration Control of Beams and Plates with Piezoelectric Materials," Proceedings of SPIE--the International Society for Optical Engineering, **3321**pp. 185-201.

[14] Baz, A., 1996, "Vibration Control of Plates with Active Constrained Layer Damping," Smart Materials and Structures, **5**(3) pp. 272-280.

[15] Veselago, V. G., 1968, "The Electrodynamics of Substances with Simultaneously Negative Values Of e and M
 ," Soviet Physics Uspekhi, **10**(4) pp. 509-514.

[16] Guenneau, S., Diatta, A., and Mcphedran, R. C., 2010, "Focusing: Coming to the Point in Metamaterials," Journal of Modern Optics, **57**(7) pp. 511-527.

[17] Laude, V., Khelif, A., and Benchabane, S., 2008, "An Introduction to Phononic Crystals".

[18] John, Sajeev,Rangarajan, Raghavan, 1988, "Optimal Structures for Classical Wave Localization: An Alternative to the Ioffe-Regel Criterion," Physical Review B, **38**(14) pp. 10101-10104.

[19] Economou, E. N.,Zdetsis, A., 1989, "Classical Wave Propagation in Periodic Structures," Physical Review B, **40**(2) pp. 1334-1337.

[20] Sigalas, M. M., and Economou, E. N., 1992, "Elastic and Acoustic Wave Band Structure," Journal of Sound and Vibration, **158**(2) pp. 377-382.

[21] Sigalas, M. M., and Economou, E. N., 1994, "Elastic Waves in Plates with Periodically Placed Inclusions," Journal of Applied Physics, **75**(6) pp. 2845-2850.

[22] Lu, M., Feng, L., and Chen, Y., 2009, "Phononic Crystals and Acoustic Metamaterials," Materials Today, **12**(12) pp. 34-42.

[23] Khelif, A., Achaoui, Y., and Aoubiza, B., 2013, "Locally Resonant Structures for Low Frequency Surface Acoustic Band Gap Applications,"- Springer Netherlands, Netherlands, pp. 43-59.

[24] Hsu, F., Lee, C., Hsu, J., 2010, "Acoustic Band Gaps in Phononic Crystal Strip Waveguides," Applied Physics Letters, **96**(5) pp. 051902-1-051902-3.

[25] Kushwaha, M. S.,Halevi, P., 1994, "Band-Gap Engineering in Periodic Elastic Composites," Applied Physics Letters, **64**(9) pp. 1085-1087.

[26] Kushwaha, M. S., Halevi, P., Martinez, G., 1994, "Theory of Acoustic Band Structure of Periodic Elastic Composites," Physical Review B, **49**(4) pp. 2313-2322.

[27] Caballero, D., Sánchez-Dehesa, J., Rubio, C., 1999, "Large Two-Dimensional Sonic Band Gaps," Physical Review.E, Statistical Physics, Plasmas, Fluids, and Related Interdisciplinary Topics, **60**(6) pp. R6316-R6319.

[28] Vasseur, J. O., Djafari-Rouhani, B., Dobrzynski, L., 1997, "Acoustic Band Gaps in Fibre Composite Materials of Boron Nitride Structure," Journal of Physics: Condensed Matter, **9**(35) pp. 7327-7341.

[29] Pichard, H., Richoux, O., and Groby, J., 2012, "Experimental Demonstrations in Audible Frequency Range of Band Gap Tunability and Negative Refraction in Two-Dimensional Sonic Crystal," Journal of the Acoustical Society of America, **132**(4) pp. 2816-2822.

[30] Zhou, X., Wang, Y., and Zhang, C., 2010, "Material Parameters Determining the Band Gaps of Solid-Solid Phononic Crystals," IUTAM Symposium on Recent Advances of Acoustic Waves in Solids, **26**pp. 139-148.

[31] Djafari-Rouhani, B., Pennec, Y., and Larabi, H., 2010, "Band Structure and Phonon Transport in a Phononic Crystal Made of a Periodic Array of Dots on a Membrane," IUTAM Symposium on Recent Advances of Acoustic Waves in Solids, Anonymous Springer Science, **26,** pp. 127-138.

[32] Shen, M., and Cao, W., 1999, "Acoustic Band-Gap Engineering using Finite-Size Layered Structures of Multiple Periodicity," Applied Physics Letters, **75**(23) pp. 3713-3715.

[33] Shen, M., and Cao, W., 2000, "Acoustic Bandgap Formation in a Periodic Structure with Multilayer Unit Cells," Journal of Physics D: Applied Physics, **33**(10) pp. 1150-1154.

[34] Ye, Z., and Hoskinson, E., 2000, "Band Gaps and Localization in Acoustic Propagation in Water with Air Cylinders," Applied Physics Letters, **77**(26) pp. 4428-4430.

[35] Zhang, X., Jackson, T., Lafond, E., 2006, "Evidence of Surface Acoustic Wave Band Gaps in the Phononic Crystals Created on Thin Plates," Applied Physics Letters, **88**(4) pp. 041911-1-041911-3.

[36] Xiao, Y., Wen, J., and Wen, X., 2012, "Flexural Wave Band Gaps in Locally Resonant Thin Plates with Periodically Attached Springmass Resonators," Journal of Physics.D, Applied Physics, **45**(19) pp. 195401-1-195401-12.

[37] Xiao, W., Zeng, G. W., and Cheng, Y. S., 2008, "Flexural Vibration Band Gaps in a Thin Plate Containing a Periodic Array of Hemmed Discs," Applied Acoustics, **69**(3) pp. 255-261.

[38] Pennec, Y., Vasseur, J. O., Djafari-Rouhani, B., 2010, "Two-Dimensional Phononic Crystals: Examples and Applications," Surface Science Reports, **65**(8) pp. 229-291.

[39] El-Naggar, S. A., Mostafa, S. I., and Rafat, N. H., 2012, "Complete Band Gaps of Phononic Crystal Plates with Square Rods," Ultrasonics, **52**(4) pp. 536-542.

[40] Yao, Z., Yu, G., and Li, J., 2011, "Flexural Vibration Band Gaps in a Ternary Phononic Crystal Thin Plate," Materials Science Forum, **675**pp. 1085-1088.

[41] Liu, Z., Chan, C. T., and Sheng, P., 2005, "Analytic Model of Phononic Crystals with Local Resonances," Physical Review.B, Condensed Matter and Materials Physics, **71**(1) pp. 14103-1-14103-8.

[42] Huang, H. H., Sun, C. T., and Huang, G. L., 2009, "On the Negative Effective Mass Density in Acoustic Metamaterials," International Journal of Engineering Science, **47**(4) pp. 610-617.

[43] Lee, S. H., Park, C. M., Seo, Y. M., 2009, "Acoustic Metamaterial with Negative Density," Physics Letters A, **373**(48) pp. 4464-4469.

[44] Lee, S. H., Park, C. M., Seo, Y. M., 2009, "Acoustic Metamaterial with Negative Modulus," Journal of Physics.Condensed Matter, **21**(17) pp. 175704-1-175704-4.

[45] Huang, H. H., and Sun, C. T., 2011, "Theoretical Investigation of the Behavior of an Acoustic Metamaterial with Extreme Young's Modulus," Journal of the Mechanics and Physics of Solids, **59**(10) pp. 2070-2081.

[46] Ding, Y., Liu, Z., Qiu, C., 2007, "Metamaterial with Simultaneously Negative Bulk Modulus and Mass Density," Physical Review Letters, **99**(9) pp. 093904-1-093904-4.

[47] Cai, L., 2008, "Some Preliminary Results for Highway Noise Barrier Designs Based on Acoustic Band Gap Phenomenon," ASME 2008 Noise Control and Acoustics Division Conference, pp. 415-421.

[48] Gorishnyy, T., Maldovan, M., Ullal, C., 2005, "Sound Ideas," Physics World, **18**(12) pp. 24-29.

[49] Kafesaki, M., Sigalas, M. M., and García, N., 2000, "Frequency Modulation in the Transmittivity of Wave Guides in Elastic-Wave Band-Gap Materials," Physical Review Letters, **85**(19) pp. 4044-4047.

[50] Huang, H. H., and Sun, C. T., 2010, "A Study of Band-Gap Phenomena of Two Locally Resonant Acoustic Metamaterials," Proceedings of the Institution of Mechanical Engineers; Part N; Journal of Nanoengineering and Nanosystems, **224**(3) pp. 83-92.

[51] Hambric, S. A., Koudela, K. L., Smith, E. C., 2011, "Acoustically Tailored Composite Rotorcraft Fuselage Panels," NASA.

[52] Timoshenko, S.P., and Goodier, J.N., 1970, "Theory of Elasticity," McGraw-Hill, New York, USA.

[53] Graff, K.F., 1975, "Wave Motion in Elastic Solids," Ohio State University Press, Columbus, Ohio, USA, pp. 649.

[54] Mow, C., and Pao, Y., 1973, "Diffraction of Elastic Waves and Dynamic Stress Concentrations," Crane, Russak, New York, USA.

[55] Norris, A. N., and Vemula, C., 1995, "Scattering of Flexural Waves on Thin Plates," Journal of Sound and Vibration, **181**(1) pp. 115-125.

[56] Leissa, A.W., 1969, "Vibration of plates," NASA, 19700009156, United States.

[57] ANSYS, 2012, "ANSYS Help System, ANSYS Mechanical 14.5".